2015

Utilisation of unconventional ferrous materials by sintering

Zhe Wang
University of Wollongong

UNIVERSITY OF WOLLONGONG

UTILISATION OF UNCONVENTIONAL FERROUS MATERIALS BY SINTERING

A thesis submitted to the University of Wollongong as fulfilment for the degree of

Doctor of Philosophy

from

University of Wollongong

by

Zhe Wang

School of Mechanical, Materials and Mechatronic Engineering

University of Wollongong, Australia

2015

CERTIFICATION

I, Zhe Wang, declare that this thesis, submitted in fulfilment of the requirements for award of Doctor of Philosophy, in the School of Mechanical, Materials and Mechatronics Engineering, University of Wollongong, Australia, is wholly my own work unless otherwise referenced or acknowledged. The document has not been submitted for qualifications at any other academic institution.

Zhe Wang

Signature:

April, 2015

ACKNOWLEDGMENTS

This project was financially supported by the BlueScope Metallurgical Centre Projects Grant.

I would like to express my sincere gratitude to my supervisor Dr. Guangqing Zhang and co-supervisor Prof. Brian J. Monaghan and Dr. David Pinson for their valuable guidance, support, encouragement and understanding during the project. This thesis would never have reached completion without their help.

I would like to express my great appreciation to Dr. Paul Zulli, Dr. Sheng Chew, Dr. Harold Rogers, Dr. Mark I. Pownceby and Dr. Nathan A.S. Webster. Their advice and suggestions have given a better insight into the completion of this research.

Special thanks are due to Dr. Raymond Longbottom, who devoted his precious time on helping me with experiment setting up and equipment maintenance.

Special gratitude are extended to Mr. Greg Tillman for lab training, Mr. Wayne Ireland for lab safety support, Mr. Nick Mackie for XRD analysis, Prof. Long Nghiem and Mr. Hung Cong Duong for ICP-OES analysis, Mr. Tony Romeo and Mr. Mitchell Nancarrow for SEM/EDS analysis.

My keen appreciation goes to Ms. Rhondalee Cambareri and Ms. Stacey Young for their help with general administrative issues, and Mr. Benjamin O'Brien for IT services.

It has been a great pleasure working with talented people in our group especially: Dr. Yue Ma, Mr. Xiang Li, Mr. Zhe Cui, Ms. Yujing Liu, Mr. Hao Zhang and Ms. Jingxiu Wang. Your encouragement and advice inspired this work.

Last but not least, I would like to thank all my family members specially my wife Dong Shuang for their constant support, understanding and encouragement throughout the whole course of my PhD study.

ABSTRACT

To sustain stable operation of a blast furnace, iron ore fines produced during mining and ore dressing processes need to be agglomerated into lumps. Sintering is the most economical and widely used agglomeration method for iron ore fines. Also, the sintering technology can be used for recycling of metallurgical wastes produced by the ironmaking process. The aim of the project was to study the sintering behaviour of three kinds of unconventional ferrous materials (New Zealand ironsand, mill scale and filter cake wastes) and assess the feasibility of their utilization by sintering. The effects of sintering conditions on the formation of mineral phases during iron ore sintering were investigated to gain better understanding of sintering mechanism. Raw materials used in this study were supplied by BlueScope Ltd.

Ironsand deposits along the western coast of the North Island of New Zealand are currently mined as iron ores for steel production. A detailed characterisation shows that the New Zealand ironsand sample used in this study contained about 60 wt% iron, 7.95 wt% TiO_2 and a small amount of other impurities. It was added into an industrial sinter blend in the proportion of 5 wt% and the mixture was uniaxially pressed into cylindrical tablets and sintered in a tube furnace under flowing gas with various oxygen potentials and temperatures. The sintered samples were characterised by optical and electron scanning microscopies to develop understanding of the behaviour of titanium during sintering. An industrial sinter with the addition of 3 wt% of the ironsand was also examined. Various morphologies of relict ironsand particles were present in the industrial sinter due to the heterogeneity of sintering conditions. The different morphologies observed were shown to be well simulated by bench-scale sintering experiments. The assimilation of ironsand during sintering in a reducing atmosphere started from the diffusion of calcium into the lattice of the ironsand matrix and a reacted zone was formed near the boundary within ironsand particle where a perovskite phase was generated. When sintered at higher temperatures, most of titanium moved from ironsand particles into silicate phases in a reducing atmosphere. When sintered in air, comparatively more titanium remained in the original particles.

Further investigations to elucidate the reaction mechanisms and the effects of processing parameters were then conducted. The effects of temperature, CaO/SiO_2 ratio, sintering gas atmosphere and cooling procedure on the phase composition of sintered specimens from an industrial sinter blend with addition of 5 wt% of the ironsand were examined with special focus on the formation of SFCA (silico-ferrite of calcium and aluminium) phases. The composition of mineral phases of specimens sintered at 1250 - 1325 ℃ was quantitatively examined using image analysis software. Although SFCA and SFCA-I can be formed at low temperatures by solid state reactions, they are most likely to be formed by crystallisation of the silicate melt in a relatively oxidising gas atmosphere in an industrial sintering process. Maintaining a high oxygen partial pressure favours the formation of SFCA and SFCA-I, either via solid state reactions or from a melt. This is attributed to making hematite available as a reactant of SFCA formation. Similarly, increasing CaO/SiO_2 ratio provides more CaO as a reactant for SFCA formation and promotes its formation.

To gain a better understanding of the sintering mechanism of New Zealand ironsand, two-layer interaction couples between ironsand and flux materials (reagent CaO and MgO and natural dolomite) were prepared and sintered in an atmosphere with an oxygen partial pressure of 0.5 kPa in the temperature range of 1200 - 1300 ℃ for a range of times. When the ironsand was sintered with MgO, Mg^{2+} ions can significantly diffuse into the lattice of ironsand, which stabilises the system of FeOx-MgO and hinders the assimilation of ironsand particles. During sintering of ironsand with CaO, a reaction zone consisting of perovskite and calcium ferrite occurred between the two layers. In comparison, a reacted zone consisting of perovskite, MgO-FeO solid solution and calcium ferrite formed during sintering ironsand with dolomite. Increasing sintering temperature significantly enhanced the penetration of calcium ferrite into the dolomite layer, while the perovskite phase and MgO-FeO solid solution remain stable to higher sintering temperatures due to their relatively high melting points.

A mill scale sample generated during the steel processing contained as high as 71 wt% of iron which can be used as a high quality ironmaking raw material by sintering processes. Quantitative XRD analysis of the sample shows that it consisted of about 53

wt% wustite, 35 wt% magnetite, 10 wt% hematite, 1 wt% goethite and 1 wt% green rust. The effect of mill scale additions on the phase formation of sintered specimens from an industrial sinter blend containing 0-15 wt% of mill scale was examined. Increasing mill scale addition promoted the formation of magnetite during heating stage of sintering. However, if appropriate measures are taken so that the magnetite formed during heating is allowed to be oxidised during cooling stage, the contents of SFCA and hematite will not be significantly changed and the quality of sinter can be maintained.

A large amount of filter cake wastes are produced from the flue gas cleaning systems of blast furnace (BF) ironmaking and basic oxygen furnace (BOF) steelmaking. The filter cake wastes cannot be directly recycled by the iron and steel making processes due to their high zinc contents but are stockpiled. A BOF filter cake sample (55.7 wt% Fe) and a mixture (MIX) filter cake sample (53.7 wt% Fe) from BlueScope Ltd. were investigated in this thesis. The MIX sample represents a blend of both BOF and BF filter cake. These filter cake samples were sintered at 1100 - 1300 ℃ in argon and air to evaluate the effects of temperature, gas atmosphere and carbon content on the mineral phase formation and zinc removal of sintered filter cake specimens. The fine particles in filter cake can be well agglomerated by typical ferrous sintering bonding phases (calcium ferrites and silicates) due to the presence of flux materials in the filter cakes. A certain amount of zinc removal was also obtained during sintering since zinc oxide in filter cake was reduced to zinc vapour by carbon or metallic iron present in the filter cake. Enhanced sintering temperature and carbon content as well as reducing gas atmosphere were beneficial to removing zinc from the filter cake samples.

DECLARATION ON PUBLICATIONS

This thesis includes the following chapters that have been prepared as journal manuscripts to be submitted.

Chapter 2: Zhe Wang, David Pinson, Sheng Chew, Harold Rogers, Brian J. Monaghan, Mark I. Pownceby, Nathan A. S. Webster, Guangqing Zhang, "Behaviour of New Zealand ironsand during iron ore sintering".

Chapter 3: Zhe Wang, David Pinson, Sheng Chew, Brian J. Monaghan, Mark I. Pownceby, Nathan A. S. Webster, Harold Rogers, Guangqing Zhang, "Effect of sintering conditions on the formation of mineral phases during iron ore sintering".

Chapter 4: Zhe Wang, David Pinson, Sheng Chew, Harold Rogers, Brian J. Monaghan, Guangqing Zhang, "Interaction of New Zealand ironsand and flux materials".

Chapter 5: Zhe Wang, David Pinson, Sheng Chew, Brian J. Monaghan, Mark I. Pownceby, Nathan A. S. Webster, Harold Rogers, Guangqing Zhang, "Effect of addition of mill scale on sintering of iron ores".

Chapter 6: Zhe Wang, David Pinson, Sheng Chew, Brian J. Monaghan, Harold Rogers, Guangqing Zhang, "Mineral phase formation and zinc removal during sintering of filter cake wastes".

I, Dr. Guangqing Zhang as the principal supervisor, declare that the vast majority of experiments and subsequent analysis in Chapters 2 through 6 were performed by the candidate, Mr Zhe Wang. The contributions of other co-authors to each chapter were shown as follows:

Chapters 2-3: SEM, XRF, qualitative and quantitative XRD and EPMA analysis of original New Zealand ironsand were conducted by Mark I. Pownceby and Nathan A. S. Webster. The chemical compositions of other raw materials including iron ore blend,

limestone, dolomite and silica sand examined by XRF analysis were supplied by BlueScope Ltd.

Chapter 5: Quantitative XRD analysis of original mill scale was conducted by Mark I. Pownceby and Nathan A. S. Webster. The chemical compositions of raw materials including iron ore blend, limestone, dolomite, manganese ore and mill scale examined by XRF analysis were supplied by BlueScope Ltd.

Chapter 6: The chemical compositions of filter cakes examined by XRF analysis were supplied by BlueScope Ltd. ICP-OES analysis of sintered samples were performed by Zhe Wang with the assistance of Prof. Long Nghiem and Mr. Hung Cong Duong at University of Wollongong.

All of the co-authors have participated in the regular meetings as a research team to define the scope of the research project, make research plan, review experimental results and elucidate the sintering mechanisms under different sintering conditions. All of the co-authors have involved in revision of the draft manuscripts to be submitted for publication.

Zhe Wang has reviewed the relevant literature and wrote the first draft of each manuscript. The papers were sent to the co-authors for review. After integrating their comments into the papers - mainly related to data interpretation and editorial improvements - the papers were submitted to selected journals for publication by Zhe Wang.

Zhe Wang	Dr. Guangqing Zhang
April 2015	April 2015
Candidate	Principal Supervisor

TABLE OF CONTENTS

LIST OF FIGURES

CHAPTER 1. GENERAL INTRODUCTION

CHAPTER 2. BEHAVIOUR OF NEW ZEALAND IRONSAND DURING IRON ORE SINTERING

CHAPTER 3. EFFECT OF SINTERING CONDITIONS ON THE FORMATION OF MINERAL PHASES DURING IRON ORE SINTERING

CHAPTER 4. INTERACTION OF NEW ZEALAND IRONSAND AND FLUX MATERIALS

CHAPTER 5. EFFECT OF ADDITION OF MILL SCALE ON SINTERING OF IRON ORES

CHAPTER 6. MINERAL PHASE FORMATION AND ZINC REMOVAL DURING SINTERING OF FILTER CAKE WASTES

LIST OF TABLES

CHAPTER 1. GENERAL INTRODUCTION

CHAPTER 2. BEHAVIOUR OF NEW ZEALAND IRONSAND DURING IRON ORE SINTERING

CHAPTER 3. EFFECT OF SINTERING CONDITIONS ON THE FORMATION OF MINERAL PHASES DURING IRON ORE SINTERING

CHAPTER 4. INTERACTION OF NEW ZEALAND IRONSAND AND FLUX MATERIALS

CHAPTER 5. EFFECT OF ADDITION OF MILL SCALE ON SINTERING OF IRON ORES

CHAPTER 6. MINERAL PHASE FORMATION AND ZINC REMOVAL DURING SINTERING OF FILTER CAKE WASTES

CHAPTER 1. GENERAL INTRODUCTION

1.1 Introduction

The iron and steel industry is one of the most significant production sectors all over the world. The use of blast furnace technologies has been the predominant method for producing high-grade metallic iron since the modern industrial age [1].

To sustain the stable operation of a blast furnace, iron ore fines produced during mining and ore dressing processes need to be agglomerated into lumps. Sintering is one of the most economical and widely used agglomeration methods for iron ore fines. Presently more than 70% of liquid iron in the world is produced through the sinter route [2].

In the industrial sintering process, iron ore fines are mixed with limestone flux and coke breeze. The combustion of coke breeze supplies the necessary heat to achieve partial melting of the raw materials. It also produces a locally, relatively reducing atmosphere within the sinter bed during the heating stage. Once peak temperatures are reached, the agglomerated semi-molten material slowly cools under an atmosphere with higher partial pressure of oxygen and crystallises into various mineral phases, mainly hematite, magnetite, SFCA (silico-ferrite of calcium and aluminium)/SFCA-I, calcium silicates and glass [1-3]. The formation of mineral phases in sintering is extremely important since it basically determines the mineralogy of the sinter and consequently, its quality parameters, such as strength, reducibility and low-temperature reduction degradation.

The relative proportion of mineral phases in sinter depends on the sintering conditions, such as temperature, composition, oxygen partial pressure and sintering time, etc. which are controlled by operating parameters such as sinter blend composition, coke breeze rate, humidity, windbox pressure, and sinter strand speed. Sintering is a complex process and investigations to further elucidate reaction mechanisms and the effects of processing parameters will continue into the future.

The sintering technology can also be applied to unconventional ferrous materials including low-grade iron ore or by-products from iron and steel making processes such as mill scale and collected dusts.

Ironsand deposits along the western coast of the North Island of New Zealand are currently mined as iron ore for steel production [4]. The composition of the New Zealand ironsand approximates that of titanomagnetite ($Fe_{3-x}Ti_xO_4$) containing about 60 wt% iron, 8 wt% titania (TiO_2) and a small amount of other impurities such as silica, phosphorus and lime [4-6]. Recently, BlueScope's Port Kembla sinter plant has begun incorporating 2-3% ironsand as a component of its iron ore sinter blend. The ironsand provides a cheaper, alternative source of iron and its incorporation into sinter provides an appropriate method of its utilisation in ironmaking as its small particle size precludes direct charging into a blast furnace [7]. Some investigations have provided useful information on how the addition of titanomagnetite potentially affects sinter quality, but further studies need to be performed as to how the titanomagnetite changes or reacts during the sintering process to gain a better understanding of sintering mechanism of titanomagnetite.

Mill scale is a waste product consisting of wustite, magnetite and hematite that is formed on the surface of steel as a result of oxidation of the metal that occurs during continuous casting, reheating and hot rolling operations [8]. The sintering process is considered an appropriate method of recycling mill scale. Although the composition of mill scale varies with how it is produced, mill scale usually contains a high amount of Fe (65 - 70%) and low levels of impurities like silica and alumina. Thus, it can be a high quality iron source due to its very low impurities and recycling through the sintering process can be advantageous in reducing the consumption of raw materials like iron ore and limestone. Also, the oxidation of wustite or magnetite present in mill scale during sintering provides a small fuel offset to the sintering process leading to a potential saving of fuel coke since the oxidation reactions of wustite and magnetite are exothermic [9]. However, there is limited understanding of the effect of mill scale addition on the formation of mineral phases during iron ore sintering, which requires further examination.

A huge volume of iron-rich filter cake wastes from the gas cleaning systems of the blast furnaces (BF) and basic oxygen furnaces (BOF) are produced in steelmaking industry. Although these BF and BOF filter cakes contain a high content of iron (approximately 54-70 wt%), it is not possible to directly recycle them by iron and steel making processes due to their high zinc concentrations (more than 2 wt%). Attempts to briquette filter cake for recycling were conducted by BlueScope Ltd. and trial production of briquettes have been carried out, using a small pilot plant in 2004 and 2005. But these attempts were eventually proven to be unsuccessful due to the low strength of the briquettes produced [10]. The sintering process may be an attractive way to assimilate fine particles of filter cake with partial Zn removal potentially being accomplished during sintering process.

This thesis focuses on utilisation of three kinds of unconventional ferrous materials (New Zealand ironsand, mill scale and filter cake) by sintering process. The aim of the thesis was to study the sintering behaviour of the three materials and assess the feasibility of their utilization by sintering. The structure of the thesis is as follows. A general introduction including the literature survey related to the topics of the thesis, analytical equipment and methods used in this study and an overview of the Chapters 2-6 is presented in **Chapter 1**. **Chapter 2** presents a detailed characterisation of New Zealand ironsand and the behaviour of ironsand during sintering with an iron ore blend. **Chapter 3** presents the results of a systematic study on the effects of sintering conditions on the formation of mineral phases, including temperature, CaO/SiO_2 ratio, sintering gas atmosphere and cooling procedure. To gain better understanding of the sintering mechanism of titanomagnetite, the interaction between ironsand and flux materials (CaO, MgO and dolomite) was investigated, and the results are reported in **Chapter 4**. **Chapter 5** presents the effect of addition of mill scale on the formation of mineral phases during iron ore sintering. The mineral phase formation and zinc removal during sintering of filter cake wastes are reported in **Chapter 6**. **Chapter 7** summarises the major conclusions and some recommendations for the further work.

1.2 Literature Review

This section briefly reviews the iron and steelmaking processes and industrial sintering process along with the mineralogy and mechanism of mineral formation during sintering. Previous investigations of the utilisation of three unconventional ferrous materials, New Zealand ironsand, mill scale and filter cake wastes by sintering are summarised.

1.2.1 A Brief Description of Iron and Steelmaking Processes

The iron and steel industry is one of the world's most significant production sectors all over the world [1]. The production of steel is usually accomplished at an integrated iron and steel plant using several processes. The major operations are as follows: (1) coke production, (2) sinter production, (3) iron making process, (4) steel making process and (5) casting and rolling. Figure 1-1 depicts a general flow diagram of a typical integrated steelworks.

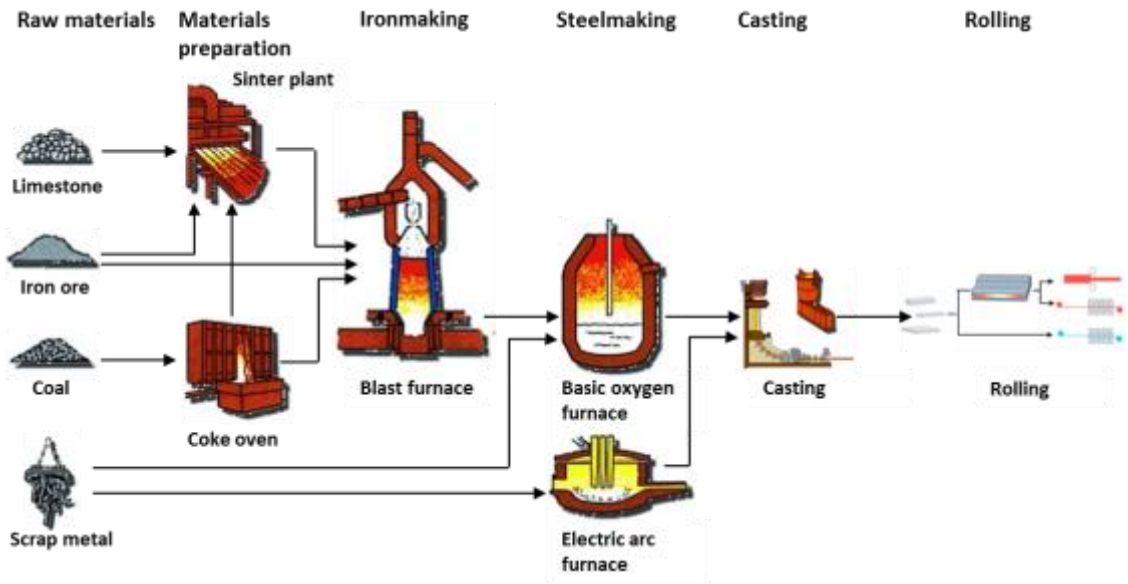

Figure 1-1 General flow diagram for the iron and steel industry. (Modified from Ref. [11])

The raw materials for producing molten iron are iron ore, coking coal and fluxes (mainly limestone). The coal is crushed, blended and fed into coke ovens where it is heated to up to 1000-1100℃ without air access to remove most of coal's volatiles and converted to coke. Coke particles do not break down as much in a blast furnace and, consequently forms a more permeable bed. [12]. Today almost all blast furnaces operate using coke.

To sustain the stable operation of a blast furnace, fine-sized ore is first mixed with coke and fluxes and heated in a sinter plant. The high temperature generated due to coke combustion partially melts the ore particles and fluxes and makes larger particles bond together to form a porous clinker called sinter.

Since the modern industrial age, the blast furnace has been the predominant method for producing high-grade metallic iron [1]. Iron ore lumps, coke, sinter and possibly extra flux are continuously charged into the blast furnace from top. Hot air is blown into the bottom of the furnace through tuyeres. Oxygen in the air combusts the coke to form carbon monoxide, simultaneously generating a large amount of heat. Carbon monoxide flows up through the blast furnace and removes oxygen from the oxides on their way down, thereby leaving iron. The heat in the furnace melts the iron, and the resulting liquid iron is tapped at regular intervals by opening tapping holes in the bottom of the furnace and allowing it to flow out. The fluxes combine with the impurities in the coke and ore to form a molten slag, which floats on the iron and is also removed (tapped) at regular intervals [13].

The molten iron from the blast furnace is sent to a basic oxide furnace (BOF) where high purity oxygen is blown into the furnace and combusts carbon and silicon in the molten iron. Some steel scrap is also recycled via BOF to utilise the waste material for steelmaking. The BOF is fed with fluxes to remove any final impurities. After the steel has been refined, the furnace is tilted and molten steel is poured out into a preheated ladle. Alloys are added to the ladle before casting to give the steel the desired composition.

The electric arc furnace (EAF) is another modern way of making steel. Unlike the BOF, EAFs are mainly used for melting and refining of steel scrap rather than molten iron. EAFs can also use direct reduced iron as part of the charge to better control alloy content. An electric current is passed through the electrodes in the furnace to form an arc. The heat generated by the arc melts the scrap. During the melting process, other metals (ferro-alloys) are added to the steel to give it the required chemical composition. As with the basic oxygen process, oxygen is blown into the furnace to purify the steel, and lime and fluorspar are added to combine with the impurities and form slag.

A significant amount of flue dusts are generated in steelmaking plants. These dusts are removed from the off-gases of BF, BOF and EAF either in the form of dry dusts by dry separation methods, or in the form of sludge or filter cake from wet separation methods [14]. Typically the off-gases are ducted to scrubbers for cleaning so that the cleaned gas can be reused within the steelworks and the collected dusts can be dewatered for stockpiling (or further processing) in the form of filter cake.

In continuous casting, the molten steel from the steelmaking operation is poured into a tundish and ducted into a water-cooled mould. The steel is drawn downwards into a series of rolls and water sprays, which ensures that it is both rolled into shape and fully solidified at the same time. At the end of the machine, it is straightened and cut to the required length. Fully formed slabs, blooms and billets emerge from the end of this continuous process and are then transported to the hot rolling mill for rolling into steel products which can be used by the manufacturing industry [15]. During continuous casting and hot rolling operations, mill scale which is a waste product containing wustite (FeO), magnetite (Fe_3O_4) and hematite (Fe_2O_3) is formed on the surface of steel as a result of oxidation of the metal [16]. Mill scale is a valuable ferrous raw material, containing 65 - 70% iron [17] and often recycled through the sintering process [8].

1.2.2 Industrial Process of Iron Ore Sintering

Up to 80 wt% of iron ore is produced as fines during mining and ore dressing processes [1]. It is necessary to agglomerate them into lumps, since the fines will be blown out by

the off gas it they are charged directly into a blast furnace. Sintering is one of the most economical and widely used agglomeration methods for iron ore fines. Presently more than 70% of liquid iron in the world is produced through the sinter route [2]. The sintering technology also can be used for recycle of metallurgical wastes such as mill scale, collected dusts and sludge.

Dwight and Lloyd invented the first continuous sintering machine that is a chain grate design [18]. The first sinter strand with suction area of 8 m^2 was operated at Birdsboro in USA in 1911 [19]. As positive relations between ferrous burden sinter ratio and blast furnace performance were established, the application of sintering process quickly became popular around the 1950's [18].

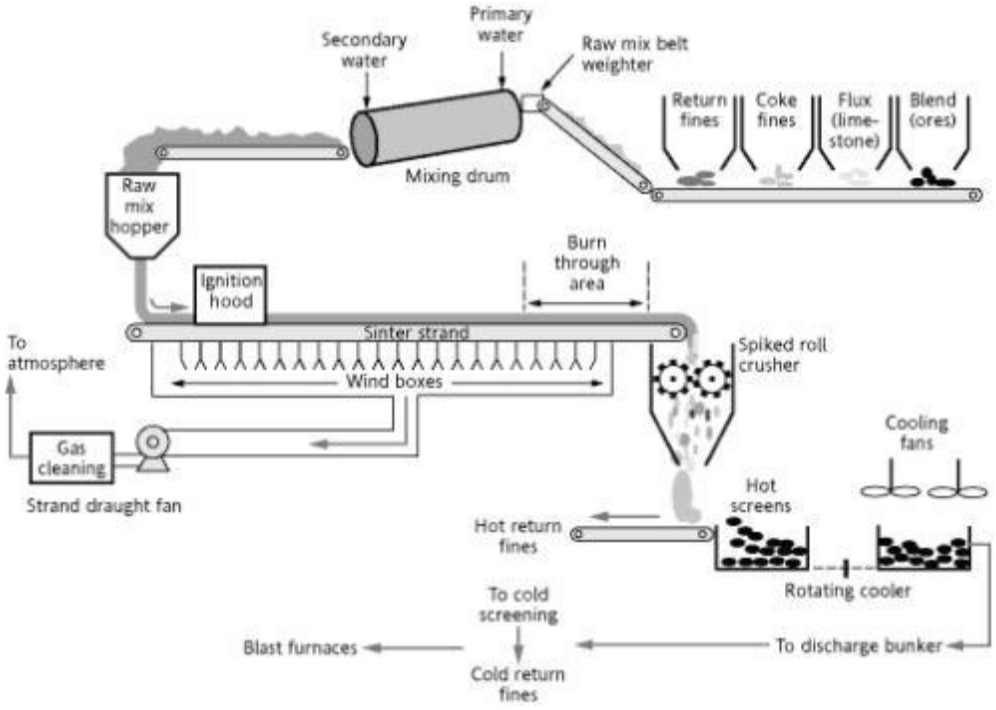

Figure 1-2 Material flow in a sinter plant [20].

Figure 1-2 shows a typical layout for a modern sinter plant. Raw materials consisting of iron ore fines, flux, coke breeze, "return fines" (sinter smaller than the minimum size specification) and recyclable waste materials filter cake and mill scale are firstly granulated with 6-8 % water in a rotating drum for several minutes to get appropriate homogenisation and agglomeration of the raw materials mix [21]. Figure 1-3(a) shows

an idealised schematic of a mixture of iron ore fines, flux and coke breeze [22]. The resulting granules are then charged onto the sintering grate. The fine coke breeze on the surface of the charged materials is ignited using gas or oil burners. Free air is drawn through the bed from below the grate to maintain combustion of the coke breeze to supply heat energy for sintering process [1]. With continuous strand movement, the sintering of the material bed on the grate proceeds downward. At the end of the strand, the fully sintered bed falls onto a spike roll crusher. After cooling, the crushed sinter is discharged to the screening section where the sinter product and return fines are separated. Return fines which are not suitable for downstream processing can be recycled again in the sintering process [23].

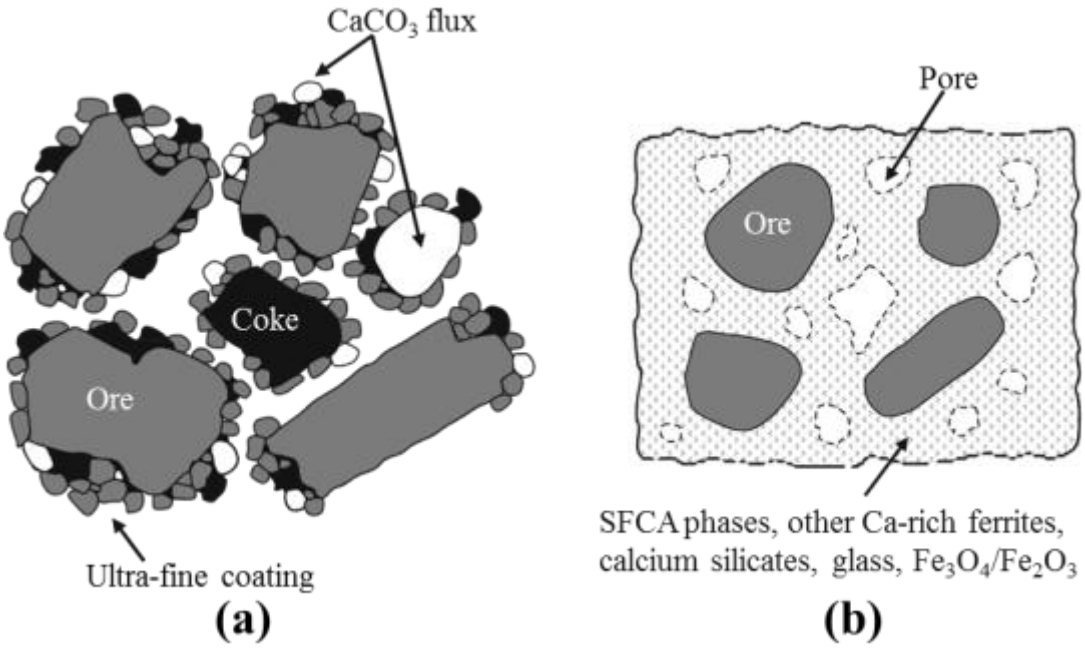

Figure 1-3 Schematic of (a) a typical presenter mixture of iron ore fines, flux, and coke, and (b) typical final iron ore sinter [22, 24].

Due to the complete combustion of carbon, the materials loaded on the sintering grate can be easily heated to 1300 ℃ to achieve partial melting of raw materials. It also produces a low oxygen partial pressure within the sinter bed during the heating stage. Once the peak temperature has been reached, the semi-molten material then slowly cools under an atmosphere with higher oxygen partial pressure [1, 3]. The final sinter shown in Figure 1-3(b) mainly contains hematite, magnetite, complex calcium-rich

ferrite(s), glassy silicate phases and unreacted coarse ores. Their relative proportion depends on the sintering conditions, such as temperature, composition, oxygen partial pressure and sintering time, etc. which are controlled by operating parameters such as sinter blend composition, coke breeze rate, humidity, windbox pressure, and sinter strand speed.

1.2.3 Thermal and Chemical Processes during Sintering

The sinter mixture is subjected to different thermal and chemical reactions during sintering. It is possible to divide the sinter bed into different zones (Figure 1-4) that coexist during the sintering process:

- Cooling zone
- Combustion zone
- Drying and preheating zone
- Wet zone

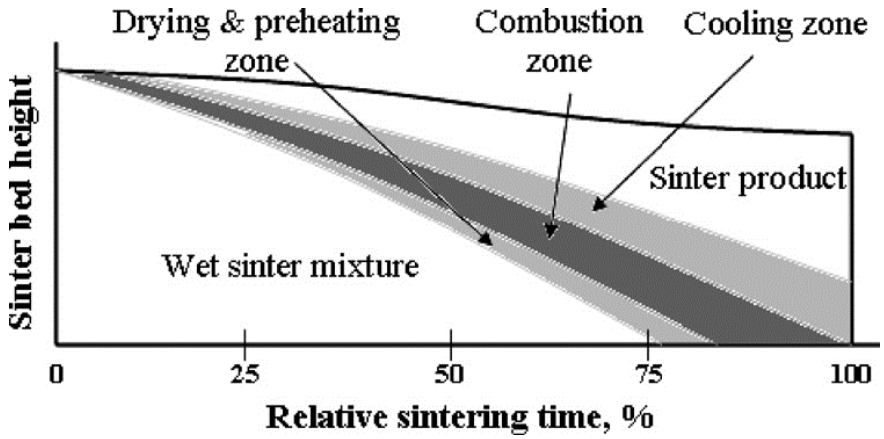

Figure 1-4 Illustration of changing sintering zones during the sintering progress [25].

There is no doubt that the formation of phases in sintering is extremely important because it basically determines the mineralogy the sinter and consequently, its quality parameters [26]. The process of formation of phases in sinter can be described schematically in Figure 1-5, where it can be seen to have the basic structure of a large core particle with a layer or coating of adhering fines initially. The fines with different chemical composition are the first to fuse by solid state reactions and to subsequently

melt. With increasing heat supply, the amount of the melt increases and the fusion proceeds through reactions between the melt and the larger particles. Once all the carbon is totally consumed, crystallisation and reoxidation of the melt occurs during cooling. The detailed process of phase formation in each sintering zone is discussed below.

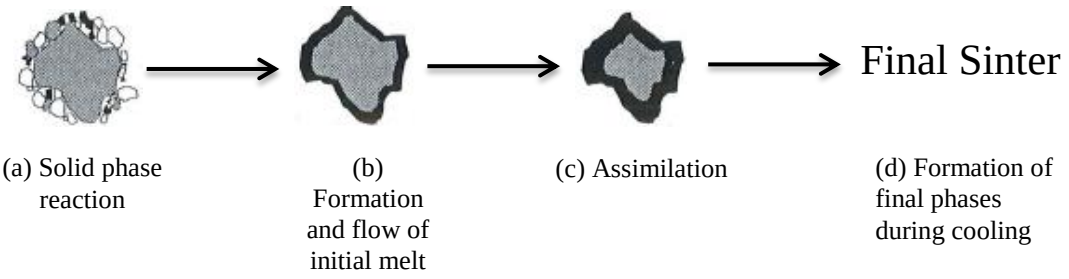

Figure 1-5 Schematic process of formation of phases in sinter (Modified from Ref. [26]).

1.2.3.1 Wet zone

The hot flowing gases are dehumidified as it flows through the lower section of the unsintered bed. Flowing air from the upper drying zone is cooled and becomes oversaturated by moisture and so partial water is condensed in this zone. This zone disappears when the combustion zone has moved low enough down the sinter bed [27].

1.2.3.2 Drying and preheating zone

The wet zone is followed by the drying and preheating zone. The hot gaseous products from the combustion layer preheat the materials in the layer below with itself cooling down in the process. In this zone, the mixture in front of the combustion zone is firstly dried by the heat from the warm gas leaving the combustion zone. During heating decomposition of dolomite and limestone occurs at 800-900 ℃ by Reactions (1-1) and (1-2).

$$CaMg(CO_3)_2 = CaO + MgO + 2CO_2 \quad (1\text{-}1)$$

$$CaCO_3 = CaO + CO_2 \quad (1\text{-}2)$$

The solid state reactions also occur in this zone. As charged to the strand, green feed granules have the basic structure of a large core particle with a layer of coating of adhering fines, as shown in Figure 1-3(a). The first product of sintering is formed by solid state reactions mainly within the layer of adhering fines, where fine and, consequently, highly reactive ores, fluxes and gangue are in intimate contact. The primary complex compounds with relatively low melting points formed by the solid state reactions can be the precursors of liquid phase and consequently decrease the liquidus temperature of the system. It is also possible for some products from solid state reactions to participate in formation of the melt and so may possibly exist in the final sinter microstructure due to the heterogeneity of sintering conditions. Therefore, the types of solid state reactions and primary products will be of vital importance to the sintering process.

During sintering, the solid state reactions start when the CaO contacts acidic oxide compounds contained in the mixture such as Fe_2O_3, SiO_2 and Al_2O_3. The reaction between CaO and Fe_2O_3 is observed to occur at temperatures as low as 600 ℃ and is known to be substantially faster than the reaction between CaO and SiO_2 or between CaO and Al_2O_3 [28]. The formation of fayalite Fe_2SiO_4 ($t_{melting}$ = 1216 ℃) also occurs during sintering due to the solid state reaction between Fe_3O_4 and SiO_2.

Extensive study on the solid state reactions in CaO-Fe_2O_3 system has been performed [29-36]. Figure 1-6 shows the phase diagram of CaO-Fe_2O_3. It can be seen that three pure compounds can be formed as a result of the reactions between CaO and Fe_2O_3. The pure CaO·Fe_2O_3 (CF) phase has a melting point of 1216 ℃ while 2CaO·Fe_2O_3 (C_2F) melts at 1448 ℃. CaO·2Fe_2O_3 (CF_2) exists within a rather narrow temperature range between 1155 and 1226 ℃ in air.

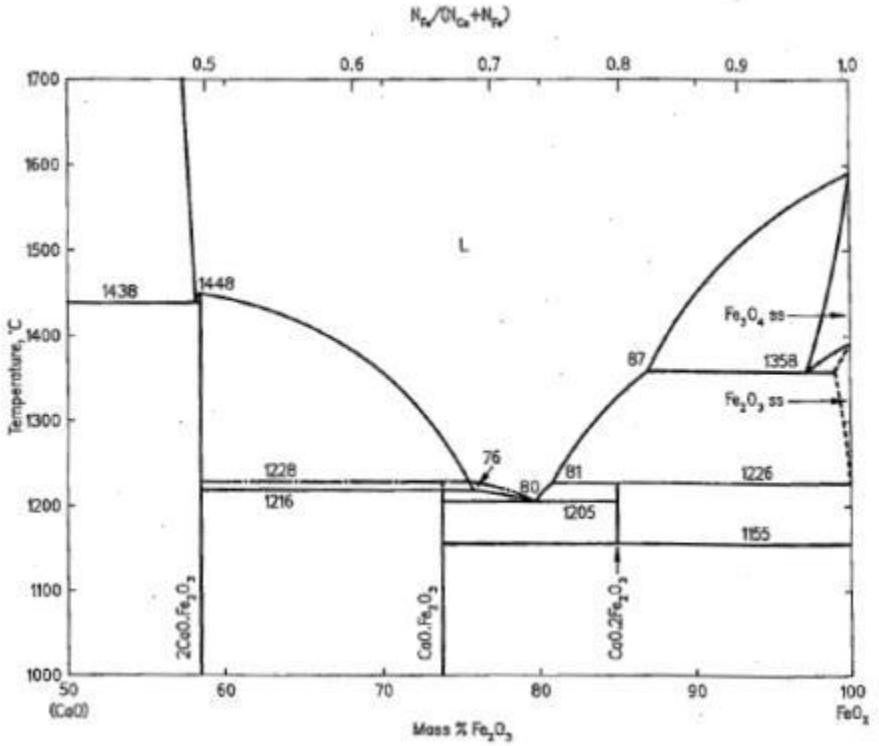

Figure 1-6 The phase diagram of CaO-Fe_2O_3 system [37].

Mazanek and Jasienska [29] investigated the rate of formation of different binary calcium ferrites by sintering mixed CaO and Fe_2O_3 powders at various temperatures and times. A more detailed study was later conducted by van Sandwijk and Koopmans [30, 31]. However, no consistent conclusion has been drawn so far on the reaction sequences in the formation of binary calcium ferrites. Guo and Ono [33] investigated the solid-state reactions between CaO and Fe_2O_3 using a diffusion-couple method. It was reported that at 1190 ℃ in air, CF was initially formed at the interface of the two layers. C_2F was then produced between the CF layer and CaO layer; while CF_2 was formed at the interface between CF and Fe_2O_3. Similar results were found by Jeon et al. [34] who studied the formation of different calcium ferrites by sintering different iron oxides and CaO under controlled atmospheres at 1000 ℃. It was observed that CF and $CaFe_3O_5$ were formed prior to the C_2F formation when Fe_2O_3 and Fe_3O_4 were used as starting materials, respectively. In comparison, in the investigation by Scarlett et al. [35] on the formation of SFCA and its intermediate phases using *in situ* powder X-ray diffraction (XRD) under vacuum condition using a heating rate of 10 ℃/min, it was found that C_2F was formed initially at about 750-780 ℃ and then it reacted with hematite to produce

CF, which is consistent with the observation by Yin et al. [36] that the formation of C_2F was prior to CF when the temperature was below 900 ℃. The differences observed in the sequence and rates of formation of calcium ferrites may be attributed to variations in experimental methods, materials composition, heating rate, etc. Further work is required to examine the effects of sintering temperature and heating rate on the reaction sequences in $CaO\text{-}Fe_2O_3$ systems.

1.2.3.3 Combustion zone

Coke can be ignited at 900 ℃ in air. The combustion of coke breeze supplies the necessary heat to achieve partial melting of the raw materials. In local regions, it also produces a relatively reducing atmosphere within the sinter bed during the heating stage. The range between the ignition of coke and the maximum temperature is defined as combustion zone. Theoretically, about 4-8wt% coke breeze in the sinter mix should be sufficient to raise the sintering temperature to 1400 ℃ [1].

In this zone, as the temperature increases, the low-melting point compounds produced in solid state reactions melt gradually and more complex systems are formed as gangue materials such as SiO_2 and Al_2O_3 dissolve into the melt [38]. First liquid imbibes into the large grains of the mixture, which are dissolved progressively [39]. The boundaries of iron ore and flux particles are penetrated by the slag melt and this process is referred to as nuclei assimilation, i.e. reaction between liquid melt and solid, resulting in dissolution of the solid. The degree of assimilation depends on the properties of the initial melt and nucleus [26]. The greater the reactivity of the melt, the greater its ability to digest the solid nucleus, while the greater the assimilation resistance of the solid nucleus, the less the amount that would be assimilated. The assimilation process terminates when the liquidus temperature of the melt increases above the sintering temperature due to the saturation of the melt mainly caused by iron oxide assimilation or when the sintering temperature decreases sufficiently to cause solidification of the melt or when the nucleus is completely assimilated [26, 40].

1.2.3.4 Cooling zone

Once all the carbon is totally consumed, the agglomerated semi-molten material then slowly cools under an atmosphere with higher partial pressure of oxygen. Crystallisation and reoxidation of the semi-molten material occurs during cooling [41].

The melt generated in combustion zone is usually saturated in Fe^{3+} and Fe^{2+} ions of hematite and magnetite respectively [42]. These two iron oxides precipitate first during cooling. The nature of the oxide which precipitates depends on the Fe^{3+}/Fe^{2+} ratio in solution. Mg ions preferably dissolve in magnetite rather than in other phases [43]. An increasing MgO input can increase the amount of magnetite spinel phase and consequently decrease the amount of hematite. When magnetite is cooled at a low rate under oxidising conditions, it may react with oxygen and form so-called secondary hematite [24, 44, 45].

Silico-ferrites of calcium and aluminium (SFCAs) precipitate at lower temperatures after magnetite and hematite. SFCA crystallises from the melt as acicular SFCA-I and then grows into columnar SFCA [24]. If the maximum temperature does not exceed 1300 ℃ during sintering or the residence time at the high temperature is extremely short, the microstructure of the sinter on cooling will be acicular SFCA-I with silicate in solid solution and unmelted hematite ore particles. In the cooling cycle, it is possible for both hematite and magnetite to be reabsorbed by reaction with the silicate melt to form SFCA [46]. If the basicity (mass ratio of CaO to SiO_2) of sinter mix is lower than 1.8, silicates tend to form either a glass or crystals such as gehlenite, dicalcium silicate instead of calcium ferrites during cooling [47-49].

1.2.4 Sinter Mineralogy

The final sinter is generally composed of ~40 to 70 vol% iron oxides (hematite and magnetite), ~20 to 50 vol% ferrites (most of which are SFCA and SFCA-I), up to 10 vol% glassy phase (quenched melt) and up to 10 vol% dicalcium silicate [50]. For the primary blast furnace requirements of sinter, especially a good reducibility and high strength, the types of minerals produced are of great importance. It is noted that the sinter

composition varies from place to place due to the heterogeneity of sintering conditions. The relative proportions of mineral phases in the final sinter depend on different parameters, such as sintering temperature, composition, oxygen partial pressure and sintering time. A brief discussion of each phase follows.

1.2.4.1 Hematite

As one of the most abundant phases in sinters, hematite can be present as either primary hematite or secondary hematite. The primary hematite, also called relict hematite, is present due to incomplete assimilation of the original hematite in iron ore with other components in sinter mix and can be recognised by its irregular shape and corroded grain boundaries. The secondary hematite is usually formed as a result of direct precipitation or the oxidation of a magnetite precipitation; it can be identified by its euhedral crystal shape. Secondary hematite is often observed around the edges of open pores in sinter [51]. Figure 1-7 presents the microstructure of a secondary hematite rich zone in a sinter from BlueScope's sinter plant. Hematite is characterised by its high reflectance (bright white colour) and its anisotropic nature.

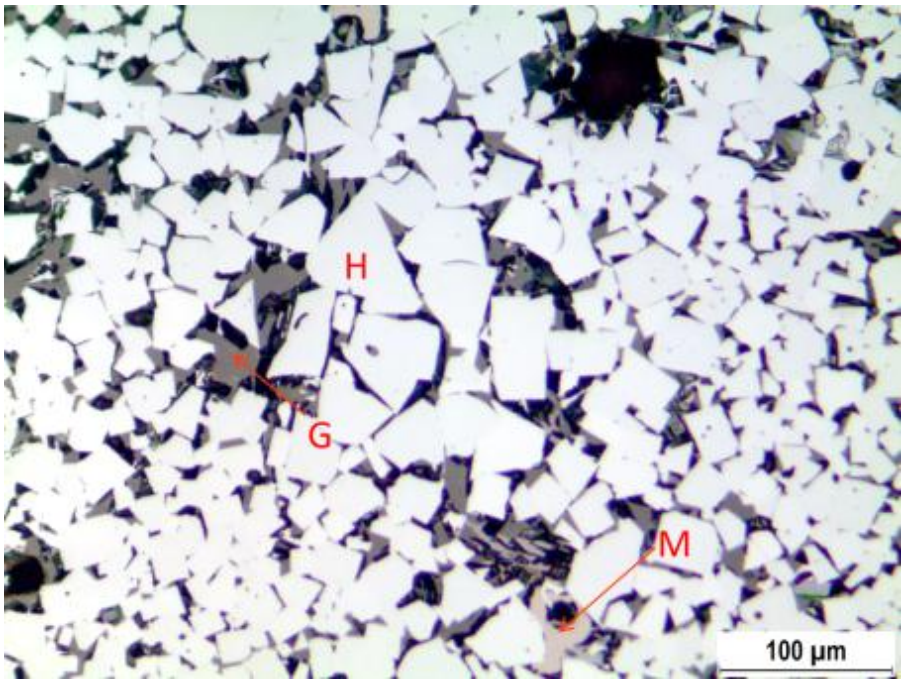

Figure 1-7 Optical micrograph of secondary hematite (H) with magnetite (M) and glass (G).

1.2.4.2 Magnetite

Magnetite is an important component in the sinter; its presence greatly influences the sinter properties. There are two generic types, unassimilated magnetite and crystallised magnetite from the melt. The unassimilated type is found in a number of ways depending on the nature of the original ore. The hematite in original ore can be easily reduced to magnetite due to the low oxygen partial pressure during heating stage of sintering. If the volume of liquid phase formed is limited, magnetite reduced from hematite can be retained in the final sinter without assimilation. Magnetite also can be crystallised from the melt, which depends on the Fe^{2+} content in the melt. A relatively reducing atmosphere during sintering increases the Fe^{2+} content of the melt which correspondingly leads to increased magnetite precipitation during cooling.

Figure 1-8 presents shows grains of magnetite bonded by SFCA and glass phases in a sinter sample from BlueScope. The reflectivity of magnetite is relatively low in comparison with hematite. The colour of magnetite in reflected light is grey with faint red tinge.

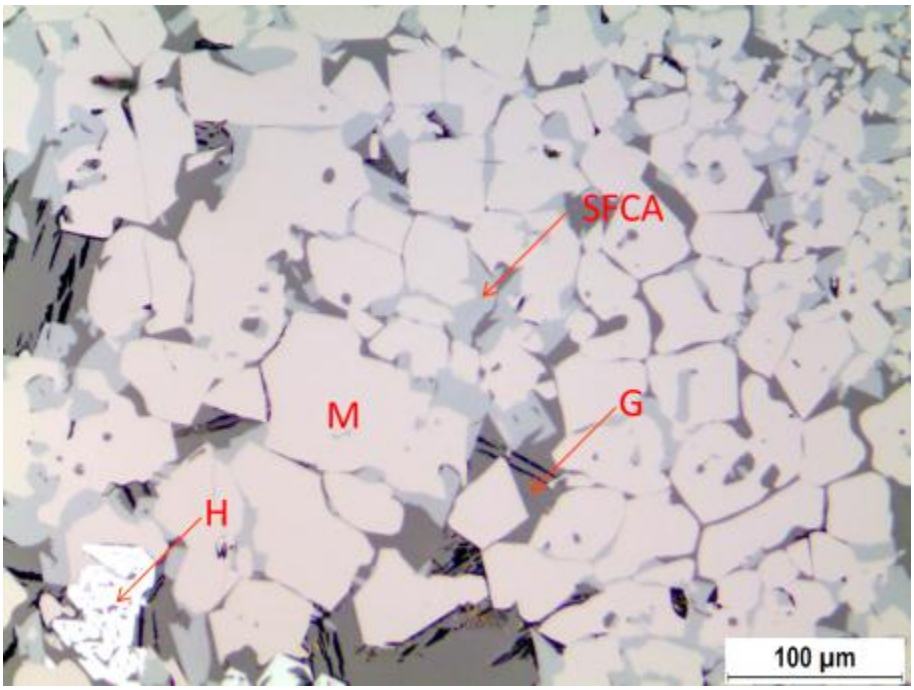

Figure 1-8 Optical micrograph of magnetite (M) associated with SFCA, glass phase (G) and hematite (H).

Sintering temperature and gas atmosphere are key factors to the conversion of hematite to magnetite. Hematite decomposes to magnetite at about 1390 ℃ in air but the temperature decreases by about 200 ℃ when the oxygen partial pressure is reduced to 0.2 kPa. Therefore, increasing sintering temperature and reducing the pO_2 by increasing coke addition favours the formation of magnetite in sinter.

Magnetite phase in iron ore sinter often contains a certain amount of MgO. Generally one ion may replace another to form a solid-solution if the difference in their ionic radii does not exceed 15% of the radius of the samller ion [52]. The ionic radius of Fe^{2+} ion is 92 pm which is close to that of Mg^{2+} ion (86 pm). Due to their similar size and identical charge, Fe^{2+} ions can replace Mg^{2+} ions without distorting the overall structures of minerals such as olivine and spinel [53]. The introduction of magnesia-bearing minerals has a large impact on magnetite content in final sinter. The reason is that the diffusion of Mg^{2+} into hematite results in its transformation to a magnetite-magnesio-ferrite (Fe_3O_4-MgO-Fe_2O_3) solid solution which is considered to be more stable than magnetite (FeO·Fe_2O_3) [54]. The mechanism involved could be explained as follows: the presence of Mg^{2+} lowers the decomposition temperature of hematite to magnetite because diffusing Mg^{2+} in hematite causes a charge imbalance which can be alleviated by the hematite giving up O^{2-} i.e. converting to magnetite, and the hematite structure cannot accommodate the Mg^{2+} unless it transforms to magnetite [54].

1.2.4.3 SFCA and SFCA-I

Calcium ferrite, as a mineral generated during iron ore sintering, usually contains some silica and aluminium as well as small amount of FeO, MnO and MgO, which is known as silicoferrite of calcium and aluminium (SFCA) [55, 56]. SFCA is the major bonding phase in iron ore sinter and has been extensively investigated on its key role in influencing sinter quality. SFCA can be divided on the basis of composition, morphology and crystal structure into two main types. The first is a low-Fe form called SFCA. Its morphology has often been referred to as columnar, blocky, or lath shape [3, 49]. SFCA found in industrial sinters typically consists of 60 to 76 wt% Fe_2O_3, 13 to 16 wt% CaO, 3 to 10 wt% SiO_2, 4 to 10 wt% Al_2O_3, and 0.7 to 1.5 wt% MgO [49]. The

second ‘SFCA’ type is a high-Fe, low-Si form named SFCA-I. It is a higher-order homologue of SFCA that appears needle-like or acicular in cross section. Mumme et al. [55] claimed that an SFCA-I phase in industrial sinter contained 84 wt% Fe_2O_3, 13 wt% CaO, 1 wt% SiO_2, and 2 wt% Al_2O_3, and a synthesised SFCA-I material had the composition 83.2 wt% Fe_2O_3, 12.6 wt% CaO, and 4.2 wt% Al_2O_3. Typical compositional ranges exhibited by SFCA and SFCA-I are shown in Figure 1-9.

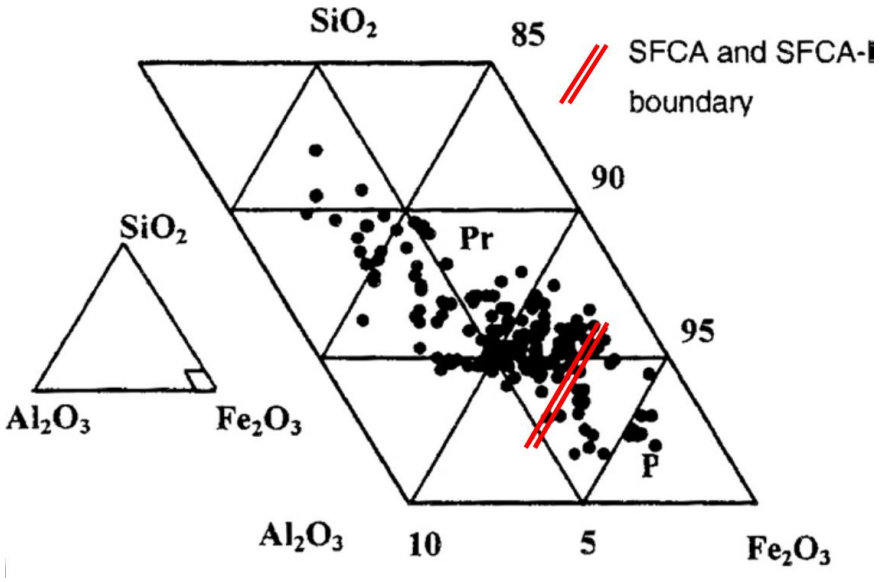

Figure 1-9 Ternary plot showing the ranges in composition of SFCA and SFCA-I measured in p ot grate sinter [57].

Typical SFCA-I and SFCA textures found in an industrial sinter from BlueScope are shown in Figure 1-10. The typical fine fibrous form of SFCA-I is indicated in Figure 1-10(a), which is a highly desirable structure. Figure 1-10(b) shows that the large, columnar SFCA was surrounded by glass. Previous work [58, 59]demonstrated that the SFCA-I phase is the most desirable bonding phase in iron ore sinters since a sinter composed entirely of SFCA-I microstructure shows higher physical strength and higher reducibility than that predominantly of SFCA. Umadevi [58] conducted pot grate sintering experiments using various raw mix and indicated that with increasing the content of SFCA-I in sinter from 6% to 20% the reducibility index of sinter increased from 63% to 80%, and there was a corresponding increase in the tumbler index (+6.3mm) of sinter from 60% to 73%.

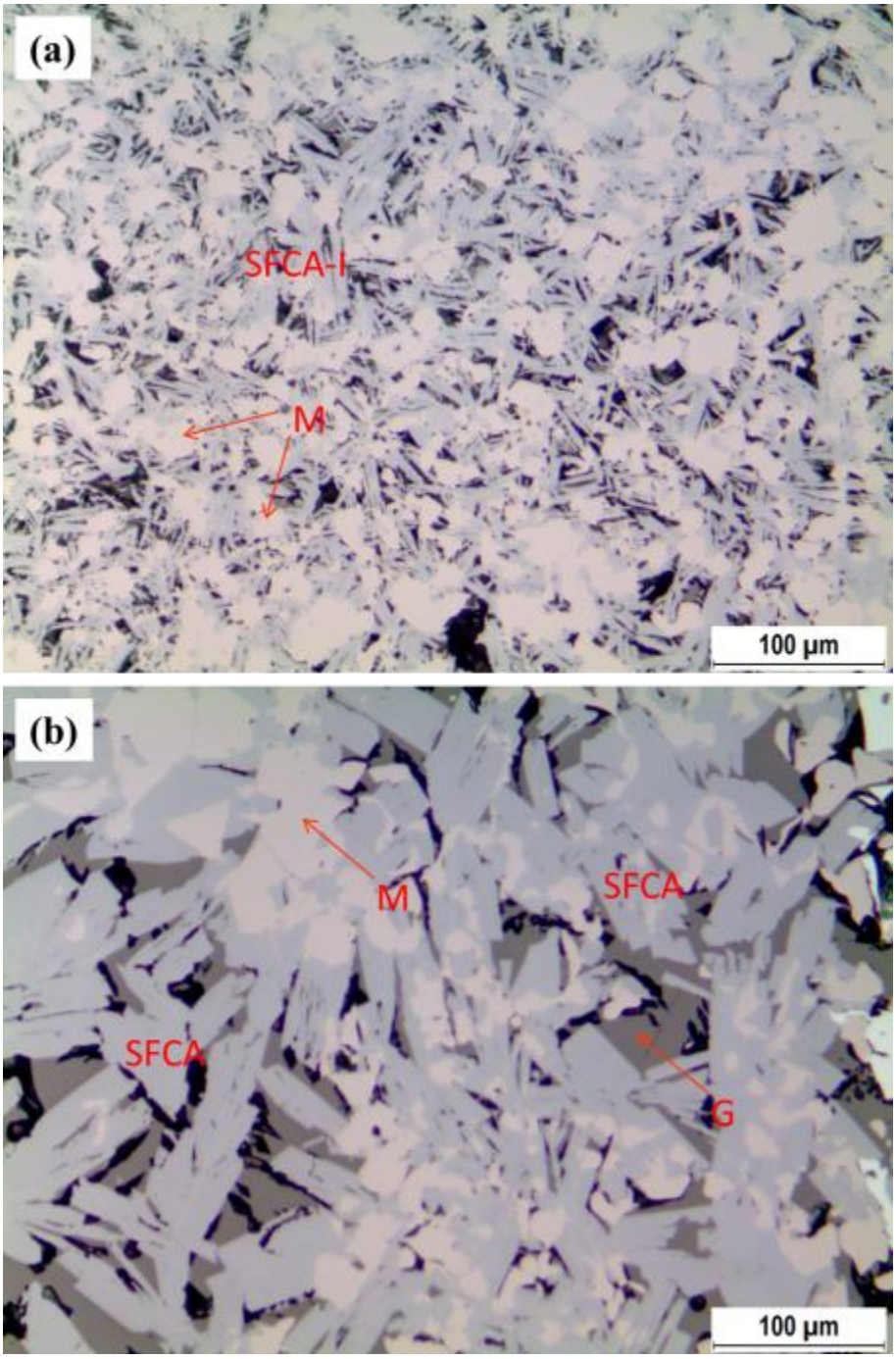

Figure 1-10 Optical micrographs showing typical (a) needle-like SFCA-I and (b) columnar SFCA morphologies in iron ore sinter. M = magnetite, G = glass.

Attempts have been made by many investigators to study how SFCA and SFCA-I are developed in a sinter. M atsuno [47] and Matsuno and Harada [48] conducted sintering experiments under equilibrated oxidising conditions which do not correspond to the real sintering process in a sinter plant. Similarly, Ahsan et al. [49] attempted to deduce the

sintering mechanism from the structure of industrial sinters. However, little information was obtained as to how initial and intermediate phases were developed during the sintering process.

Egundebi and Whiteman [60] found that the total SFCA (including SFCA-I) forms more slowly at lower temperatures but is retained longer, while at higher temperatures it forms and disappears more rapidly. As shown in Figure 1-11, more SFCA can be obtained at a lower temperature if there is enough time for sintering to take place than at high temperatures. They also proposed that the effects of time, temperature, and composition on the evolution of mineral phases in sinters were associated with change in the viscosity of the melt. High viscosity melts sintered at low temperatures (<1300 ℃) and short sintering time produced assemblages consisting of SFCA-I, calcium silicates, glass and relict hematite whereas high sinter temperatures (>1300 ℃) and long sintering time produced SFCA, calcium silicates, glass, magnetite and hematite.

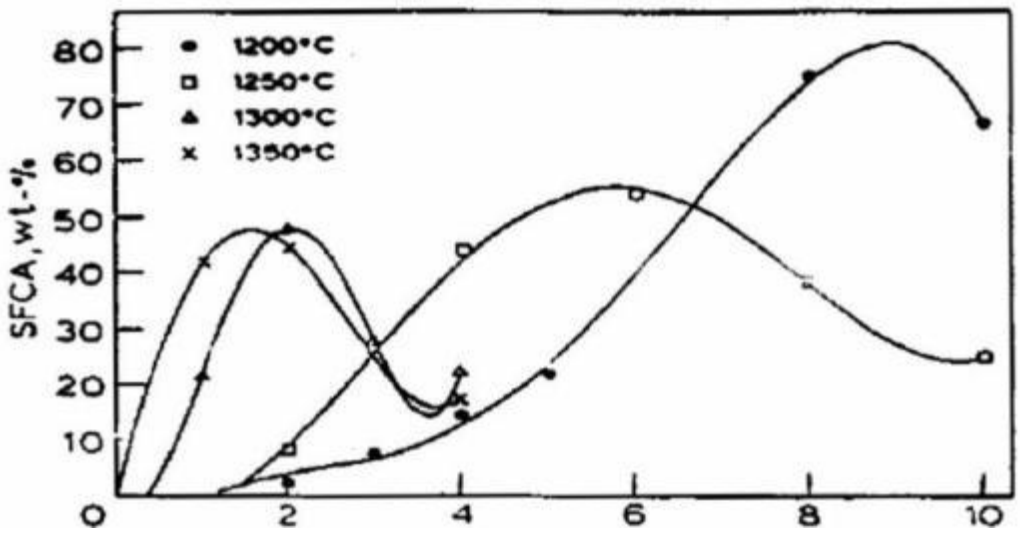

Figure 1-11 Variation of the proportion of total SFCA with time (min) at different temperatures [60].

A more detailed study by Sasaki and Hida [24] concluded that complex calcium ferrites such as SFCA-I, are present in iron ore sinter if the temperature remained below 1300 ℃. If, however, the sintering temperature exceeded 1300 ℃, the early formed SFCA-I would breakdown to a calcium silicate melt and either Fe_3O_4 at low oxygen

partial pressure (pO_2) or Fe_2O_3 at high pO_2. Upon cooling, Sasaki and Hida [24] observed that a different complex calcium ferrite (now termed SFCA), crystallised. This was distinguished from SFCA-I by its coarse-grained columnar crystal morphology, and its lower Fe and higher Si content.

To examine the effect of oxygen partial pressure on sinter phase formation, Hsieh and Whiteman [61, 62] conducted experiments in which small tablet specimens made from powdered materials were rapidly heated in a tube furnace under controlled gas atmospheres to a temperature in the range of 1180 - 1255 ℃. They found that a medium pO_2 of 0.5 kPa maximised the formation of SFCA-I in the heating stage. In the cooling stage, magnetite magnetite could be oxidised to hematite and also react with the silicate melt to produce a large amount of columnar calcium ferrite (SFCA).

Wang et al. [63] terminated the sintering process during pot tests and analysed specimens taken in different layers by optical microscopy and scanning electron microscopy (SEM). They found that the high temperature oxidation zone in the sintering process was very important for SFCA formation. A longer residence time in this zone was critical for improving sinter quality, especially in the sintering of magnetite.

Pownceby and Clout [57] examined the relations of iron ore chemical composition to the formation of high temperature bonding phase during sintering. They reported that lower Fe grade (<62 wt% Fe) ores and concentrates typically generated SFCA as part of the final sinter; while medium Fe grade (62-65 wt% Fe) ores formed a mixture of SFCA and SFCA-I and high Fe grade (65-68 wt% Fe) favoured the formation of SFCA-I.

The CaO/SiO_2 mass ratio, or basicity, of the sinter blend has also been shown to be a key factor governing mineral phase formation and sinter microstructure. A CaO/SiO_2 ratio greater than 1.8 to 2.0 favours the formation of complex calcium ferrites, while a lower basicity favours the formation of calcium silicate and glassy phases [47-49].

A number of recent investigations [22, 35, 64-66] utilised *in situ* powder XRD in order to determine the formation mechanisms of SFCA and SFCA-I. Webster et al. [22] examined the formation of SFCA and SFCA-I phases during heating and cooling of synthetic iron ore sinter mixtures in the temperature range 25 to 1350 ℃ at a fixed pO_2 of 0.5 kPa, variable alumina contents between 1-10 wt% and a heating rate of 10 ℃/min. They reported that initially Fe_2O_3 reacted with CaO at 771 ℃ to form calcium ferrite C_2F ($Ca_2Fe_2O_5$). The C_2F phase then reacted further with Fe_2O_3 to produce calcium ferrite CF ($CaFe_2O_4$) in the temperature range of 968 to 979 ℃. SFCA-I formation occurred in the temperature range of 1054 to 1119 ℃, preceding SFCA formation which occurred between 1107 and 1164 ℃. The changing temperature ranges in SFCA-I and SFCA formation reflected the difference in alumina contents, with high alumina content increasing the temperature range over which SFCA-I was stable before the formation of SFCA, and stabilising SFCA to higher temperatures before it incongruently melted to produce the assemblage Fe_3O_4 and melt. Further studies by Webster et al. [64, 65] of the effect of oxygen partial pressure on SFCA and SFCA-I formation showed that if the pO_2 was too low (0.01 kPa), SFCA-I would not form, whereas both were stable under an oxidising regime. Webster et al. [66] also investigated the effect of basicity on SFCA and SFCA-I formation and found that higher basicity favoured the formation of SFCA-I.

1.2.4.4 Dicalcium silicate and glass

Dicalcium silicate, also called larnite, is a phase which precipitates from the melt at high temperatures in areas where the melt is rich in lime and silica. Dicalcium silicate is the only essentially Fe-free phase in sinter. Only a minor amount of Fe can be incorporated into dicalcium silicate, with a content usually smaller than 1 wt%. The formation of dicalcium silicate often signifies that the maximum temperature during sintering has been high enough to dissolve most or all available silica in the region. It is often associated with glass and magnetite in the areas that have been very hot and where strong coalescence of melt has occurred. Mechanically, it is not a desirable phase and can lead to loss of sinter strength due to the volume expansion accompanying the phase

transformation of β- to γ-dicalcium silicate during cooling which generates points of weakness and cracks.

Glass phase generally represents the last material to solidify during cooling. It is high in silica and contains considerable amount of iron and other species (such as K_2O) that have been taken into solution by extensive local melting but have then been rejected into the liquid by the precipitation of near pure exsolution species. Glass phase is also not a desirable phase since it is brittle by nature and lack of porosity resulting in very low reducibility for the iron contained.

1.2.5 Utilization of New Zealand Ironsand by iron ore sintering

The New Zealand ironsand provides a cheaper, alternative source of iron. Addition of the ironsand into sinter blend can provide an appropriate method of its utilisation in ironmaking as its small particle size hinders direct charging into a blast furnace.

1.2.5.1 Introduction to New Zealand Ironsand

New Zealand ironsand was formed 2.5 million years ago from rock deposited by volcanic activity along the west coast of the North Island of New Zealand. Ironsand deposits at Waikato North Head and Taharoa in New Zealand have been mined currently as iron ores for iron and steel production [4].

The composition of the New Zealand ironsand is similar to titanomagnetite ($Fe_{3-x}Ti_xO_4$). It contains about 60 wt% iron and 8 wt% titania (TiO_2). Other notable impurities in the ore include aluminium, magnesium and silicon, which occur in varying amounts [4-6].

There are two types of titanomagnetite particles: homogeneous grains and those containing exsolution lamellae. Exsolution lamellae texture is a common feature in titanomagnetite in vocanic rocks [67]. Point counting made by Cocker et al. [4] indicates that 90 to 95 vol% of the titanomagnetite particles are homogenous. Figure 1-12(a) is a back-scattered electron microscopic (BSE) image presenting a homogeneous

titanomagnetite particle (uniform medium grey). Figure 1-12(b) shows the BSE image of a particle containing hematite-ilmenite exsolution lamellae which appears as darker grey coloured bands of variable thickness in a trellis-like pattern.

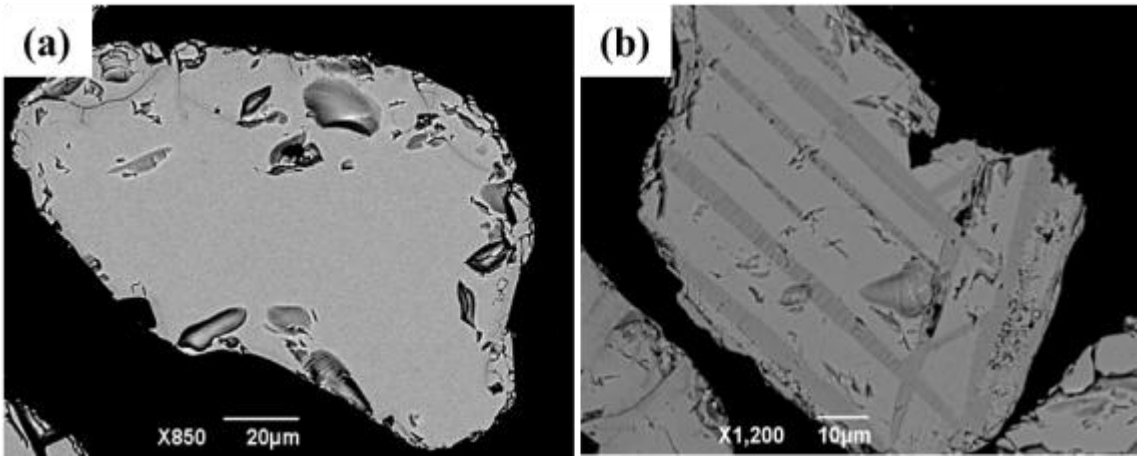

Figure 1-12 Back-scattered electron microscopic (BSE) images of typical ironsand particles. Image (a) shows a homogeneous titanomagnetite particle (uniform medium grey). Image (b) is a titanomagnetite particle with thick hematite-ilmenite (white-grey bands).

The lamellae exsolution has different composition from the titanomagnetite matrix in a particle. Cocker et al. [4] estimated the contribution of Ti in different mineral phases of the feed to the Glenbrook steel mill combining the petrographic information and electron microprobe analyses of minerals from New Zealand ironsand. It was found that homogeneous titanomagnetite particles are relatively enriched in Ti, containing up to 8.2 wt% TiO_2, and their composition fall on the tie-line that represents solid solution between ulvospinel ($Fe^{2+}{}_2TiO_4$) and magnetite ($Fe^{2+}Fe^{3+}{}_2O_4$) shown in Figure 1-13(a). By contrast, the magnetite matrix of particles with exsolution lamellae texture contains much less Ti than homogeneous titanomagnetite particles, and consequently, its composition distributes close to a pure end-member magnetite (Figure 1-13(b)). The magnetite matrix of the particles with exsolution lamellae has an overall low TiO_2 content of 1.5 wt% and the hematite-ilmenite lamellae whose composition falls on the tie-line that represents solid solutions between ilmenite ($FeTiO_3$) and hematite (Fe_2O_3) have an overall high TiO_2 content of 13.1 wt%. High-temperature oxidation of Fe^{2+} to Fe^{3+} in titanomagnetite produces vacancies in octahedral sites of the {111} crystal

planes, allowing for increased diffusion of Ti to these regions. The oxidation process leads to the formation of hematite-ilmenite lamellae (1-10 μm) along the original {111} planes of the titanomagnetite host [67].

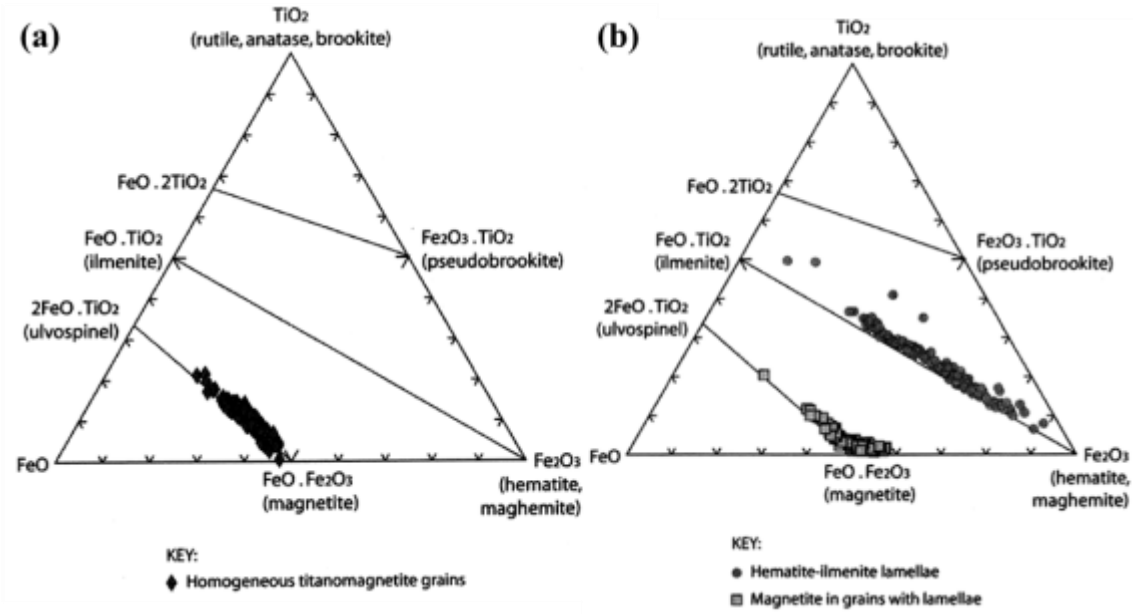

Figure 1-13 FeO-TiO_2-Fe_2O_3 diagram showing compositions of (a) homogeneous titanomagnetite and (b) magnetite matrix in particles with lamellae, and hematite-ilmenite lamellae [4].

1.2.5.2 Sintering of Iron Ore with Titanomagnetite

Recently, BlueScope's Port Kembla sinter plant has begun incorporating 2-3% ironsand as a component of its iron ore sinter blend. The ironsand provides a cheaper, alternative source of iron and its incorporation into sinter provides an appropriate method of its utilisation in ironmaking [7]. The introduction of a small amount of titanium-bearing burden into blast furnaces has been demonstrated to be beneficial to the operation of blast furnace through forming titanium carbonitride precipitates that deposit on the hearth lining and, consequently, extend operating campaigns [68].

A survey of the literature shows that the study on the sintering of iron ore with New Zealand ironsand is very limited [7]. Relevant references on the sintering of titanomagnetite ores are also summarised in this section.

1.2.5.2.1 Titanium Distribution in Sinter Containing Titanomagnetite

During sintering of iron ore with titanomagnetite, the titanomagnetite particles can be dissolved into melt and the titanium will diffuse out of the grains and be distributed into different mineral phases in the final sinter after solidification.

An important feature of the sinter containing titanium was perovskite ($CaO \cdot TiO_2$) phase formation [69]. It is often distributed in the silicate slag phase or among the hematite and magnetite particles. The morphology can be referred to be as granular, dendritic and skeletal shapes. Figure 1-14 presents the standard Gibbs free energy changes of the reactions between CaO and several oxides at 700 - 1300 ℃. It can be seen that thermodynamically CaO preferably combines with TiO_2 rather than Fe_2O_3. Perovskite is not a desirable phase in sinter since it cannot bond the iron ore and is brittle by nature.

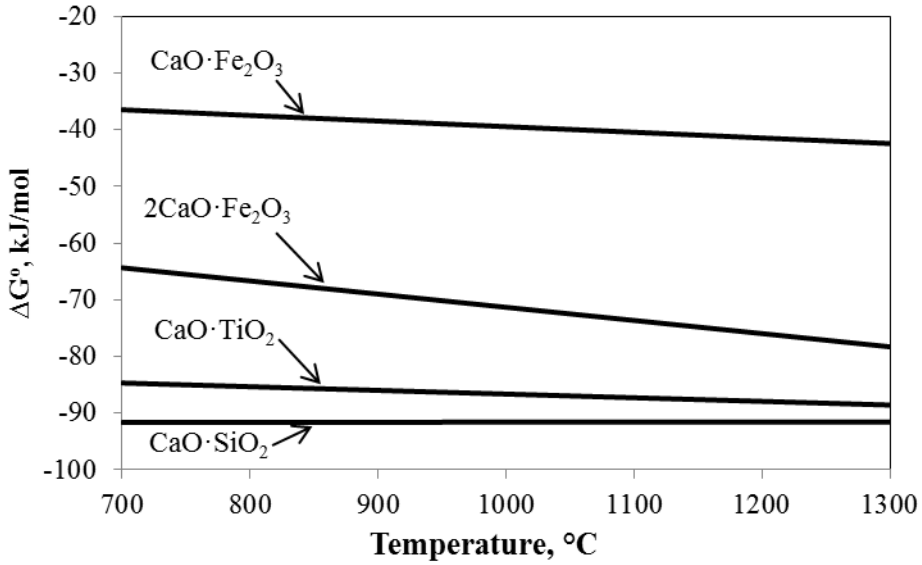

Figure 1-14 The standard Gibbs free energy change of reactions between CaO and several oxides at 700 – 1300 ℃ [70].

Bristow and Loo [7] examined the effect of addition of Taharoa ironsand from New Zealand into two iron ore blends containing 10% and 20% pisolitic limonite respectively, on the properties of sinter prepared using a pilot scale sintering facility. Most of Ti was found in the glass phase. Other exsolution phases (SFCA, secondary hematite, and magnetite) were also found to contain Ti. The Ti contents in different

mineral phases in final sinter as obtained by EDS analysis are shown in Figure 1-15. As the addition of ironsand was increased to 6%, the Ti content in the glass phase increased gradually to about 3.5 wt%. The Ti contents in secondary hematite and SFCA also increased with increasing ironsand addition, but the overall levels were much lower. The perovskite phase was not reported in that study [7] perhaps due to the low content of ironsand added into the sinter mix.

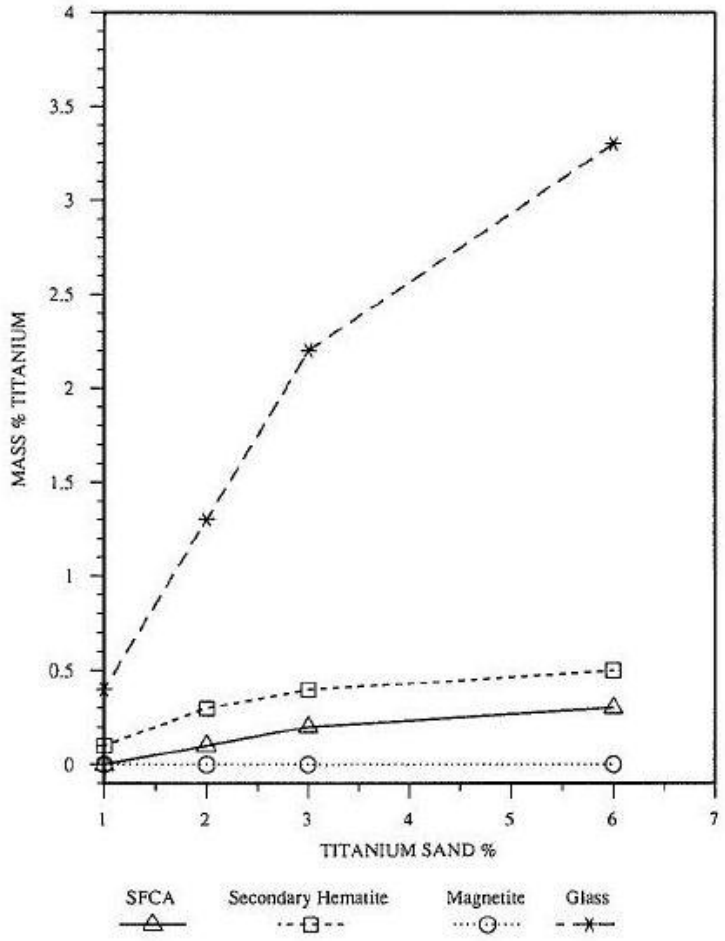

Figure 1-15 Titanium distribution in sinter examined by Bristow and Loo [7].

1.2.5.2.2 Properties of Iron Ore Sinter containing Titanomagnetite

The influence of titanium on ore sintering has been investigated previously. It is not possible to draw quantitative relationships on the influence of sinter titanium content, since the raw materials used in these reported studies are very different. However, there

appears to be general agreement that increasing the level of titanium in the sinter mix can reduce sinter strength and result in deterioration in sinter reducibility.

- **Strength**

The amount of titanomagnetite introduced into the sinter mix affects the sinter strength. Generally, addition of titanomagnetite into a sinter mix can decrease sinter strength, although the effect is insignificant when the amount of titanomagnetite is low.

Wei et al. [71] carried out sintering pot tests with Indonesia vanadium-bearing titanomagnetite (containing TiO_2 over 1.40%). It is reported that while the proportion of Indonesia iron ore was less than 15%, the strength of sinter had little fluctuation. Further increasing its proportion from 15% to 45%, the drum index was decreased from 66% to 48%, giving a decline of 18%. The authors suggest that with increasing Indonesia iron more than 15%, the perovskite phase with inferior strength becomes the main binding phase of sinter [72], resulting in the deterioration of sinter strength. Similar phenomenon is present in the work by Bristow and Loo [7]. The introduction of 6% Taharoa ironsand to iron ore blends did not significantly influence tumbler strength. It is worthy to note that an addition of 45% of Indonesia titanomagnetite ore is equivalent to about 8% of New Zealand ironsand to produce similar overall Ti content in the sinters (ignoring possible Ti in other iron ores).

- **Reduction Disintegration**

Compared to sinter strength, the effect of adding Ti-bearing materials on the low temperature reduction degredation properties (RDI) of sinter is more significant [73]. The study at BHP's Slag and Plate Products Division (SPPD) indicates that the RDI of sinter was very dependent on sinter titania level: for every 0.1% increase in TiO_2, sinter JSM RDI increased by 2.5%. In a case, increasing the sinter TiO_2 concentration from 0.12 to 0.35% using ilmenite sand increased RDI from about 38 to over 43% [7]. Paananen and Kinnunen [74] also found increasing TiO_2-content caused deterioration in the RDI of sinter in their tests using both rutile and crushed hematite pellets containing TiO_2 as additives. When the TiO_2 content increased from the original 0.43% to 0.88%, RDI increased from 18.3% to 50.8%.

Although the negative effect of titanium oxide on RDI has been demonstrated, the degradation mechanism of sinter caused by TiO_2 is ambiguous. The amount of hematite and secondary hematite in particular is widely regarded as the main cause of disintegration of sinter in low temperature reduction. The loss of sinter strength can be initiated through cracks and fissures caused by volume changes during the reduction of hematite [1]. Paananen and Kinnunenalso [74] found the TiO_2 addition to test sinter mix increased the amount of hematite phase in the sinter and the higher the TiO_2 content of doped hematite briquettes, the more significant their disintegration, which was detected visually and also by microscope.

Other phases containing titanium in some mineralogical structures in sinter may also lead to deterioration in sinter reducibility. Bristow and Loo [7] found addition of more than 3% titanomagnetite caused a significant increase in RDI of the sinters. It was postulated that the addition of titanium decreased the fracture toughness of glass phase which is the weakest phase in a sinter and would increase the vulnerability of the sinter to crack propagation, thereby resulting in deterioration in sinter RDI.

1.2.6 Utilisation of Mill Scale by iron ore sintering

Iron oxides can form on the surface of the metal during the processing of steel in mills. These oxides, known as mill scale, contain a high level of iron (about 65-70% [17]) and are valuable metallurgical raw materials. Its introduction into iron ore sinter provides an appropriate method of its recycle in ironmaking.

1.2.6.1 Introduction to Mill Scale

Mill scale is a waste product containing wustite (FeO), magnetite (Fe_3O_4) and hematite (Fe_2O_3) that is formed on the surface of steel as a result of oxidation of the metal that occurs during continuous casting, reheating and hot rolling operations [16]. Figure 1-16 displays an optical microscope picture of a typical mill scale particle supplied by BlueScope Ltd. The mill scale contains three layers of iron oxides. Hematite layer

(white) is very thin and the middle layer is magnetite showing pinkish colour in reflected light. The thickest layer is wustite (uniform mid-grey).

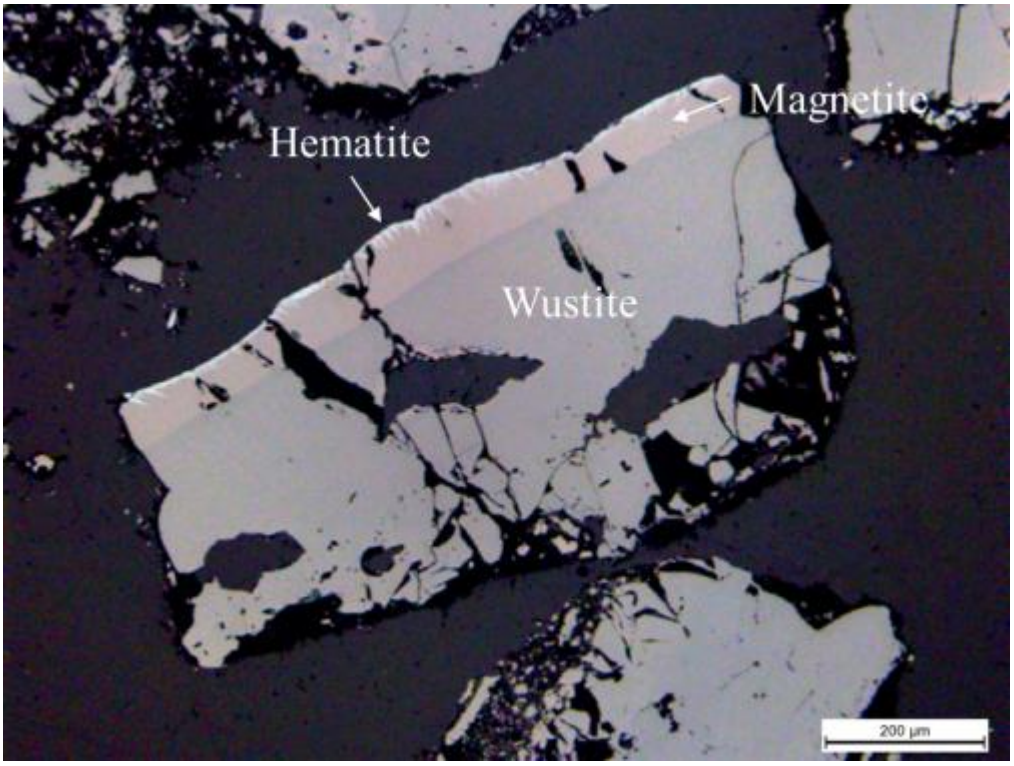

Figure 1-16 Optical microscope image of a typical mill scale particle.

The mechanism of oxidation of iron has been investigated extensively and well understood. When iron is oxidised in air at high temperatures, it grows a scale containing layers of FeO, Fe_3O_4 and Fe_2O_3 [75]. Figure 1-17 presents the phase diagram of the iron-oxygen system. It can be seen that FeO does not form below 570 ℃. Therefore, Fe oxidised below this temperature would be expected to form a two-layer scale of Fe_3O_4 and Fe_2O_3 with the Fe_3O_4 next to the metal. Above 570 ℃ the oxide layer in the scale would be FeO, Fe_3O_4 and Fe_2O_3, with the FeO next to the metal [76].

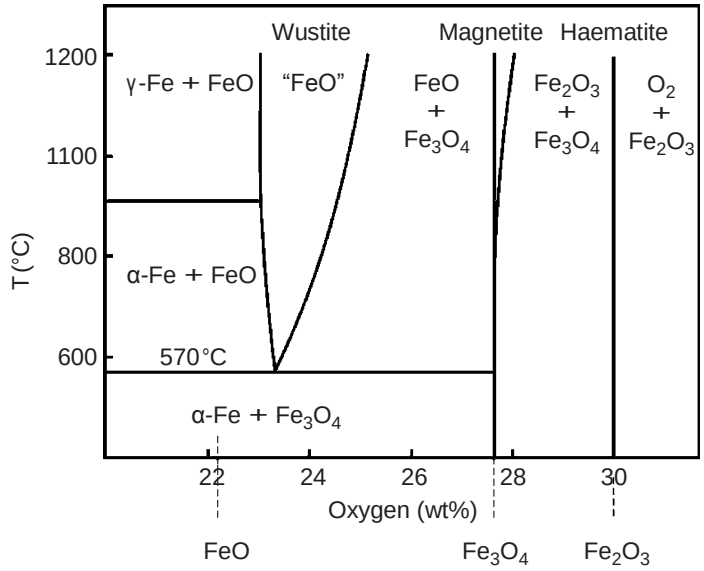

Figure 1-17 Iron-oxygen phase diagram [76].

A relatively simple mechanism of oxidation of iron is presented in Figure 1-18 on the basis of the knowledge of the structure and diffusion properties on the iron oxides. Fe ions diffuse within the scale towards hematite layer; while oxygen ions diffuse in the opposite direction into scale. Reactions occur in the interfaces between different layers. Increased mobility of oxygen causes greater defects in the wustite layer. As a result the wustite layer is thicker than the magnetite and hematite layers. It is reported that the relative thicknesses of FeO : Fe_3O_4 : Fe_2O_3 are in the ratio of roughly 95:4:1 at 1000 ℃ [76].

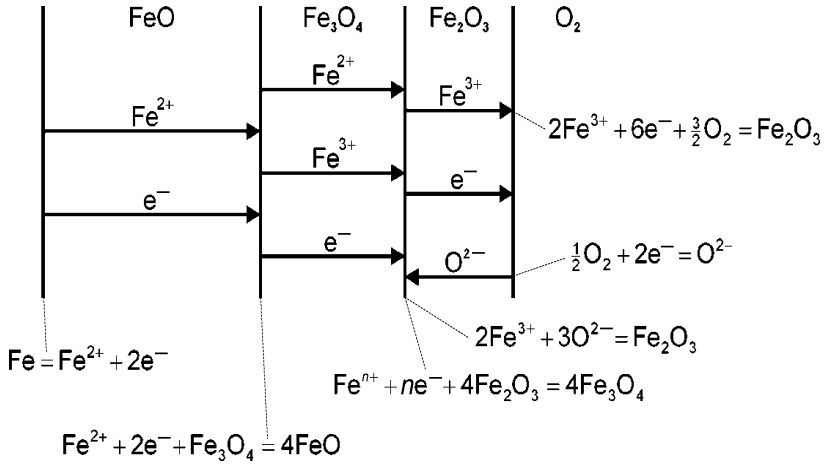

Figure 1-18 Oxidation mechanism of iron to form a three-layered scale of FeO, Fe_3O_4, and Fe_2O_3 above 570 ℃ showing diffusion steps and interfacial reactions [16].

1.2.6.2 Sintering of Iron Ore with Mill Scale

The sintering process is considered to be an appropriate method for recycling mill scale. The mill scale contains a high amount of Fe and very low amounts of silica and alumina. Thus, recycling it through the sintering process helps in the saving of raw materials like iron ore and limestone.

A further advantage in the use of mill scale is that as it is assimilated during sintering, the oxidation of wustite or magnetite provides a small fuel offset to the sintering process leading to a potential saving of fuel coke since the oxidation reactions of wustite and magnetite are exothermic [9]. The oxidation of magnetite ore to reduce coke consumption has been proved by several investigators. Button and Lundh [77], using ore blend containing 30 wt% magnetite in pot tests, found that compared to 100 wt% hematite ore blend, the maximum sintering temperature at the same coke rate was about 60 ℃ higher, which was equivalent to about 0.75 wt% coke breeze. Panigrahy et al. [78] studied the effect of blending 7 and 23 wt% of magnetite (Carol Lake concentrate) on sintering of hematite ore in pilot scale test. It was found 10 wt% coke breeze saving was achieved by blending 23 wt% magnetite.

Although there have been a number of sintering and oxidation of magnetite ore studies [45, 79-81], there have not been many focused on understanding the effect of mill scale addition on the sintering process largely due to the complexity of the raw materials and variation of sintering conditions.

JSW Steel Ltd [9] in India conducted pot grate sintering experiments to investigate the influence of mill scale addition on sintering. The mill scale in the sinter mix was varied from 0 to 70 kg/t sinter. Figure 1-19 shows the effect of mill scale addition on the mineral phase formation in sinter. It can be seen that with increasing mill scale addition, the magnetite and FeO phases increased, with a simultaneous decrease in hematite and calcium ferrites. It is also reported the sinter productivity decreased with an increase in the amount of mill scale addition due to a decrease in sinter bed permeability. The sinter strength initially increased and reached a maximum at mill scale addition of 40-50kg/t sinter and declined afterwards. The RDI and reducibility of the sinter decreased with the

increase in mill scale addition due to the increase in FeO content. El-Hussiny et al. [8] similarly found that replacement of the initial iron ore concentrate with 5 wt% mill scale increased the overall sinter strength, but the productivity decreased due to mill scale addition. This distinction in conclusions on the productivity change is likely caused by the difference in the physical form of the mill scale used.

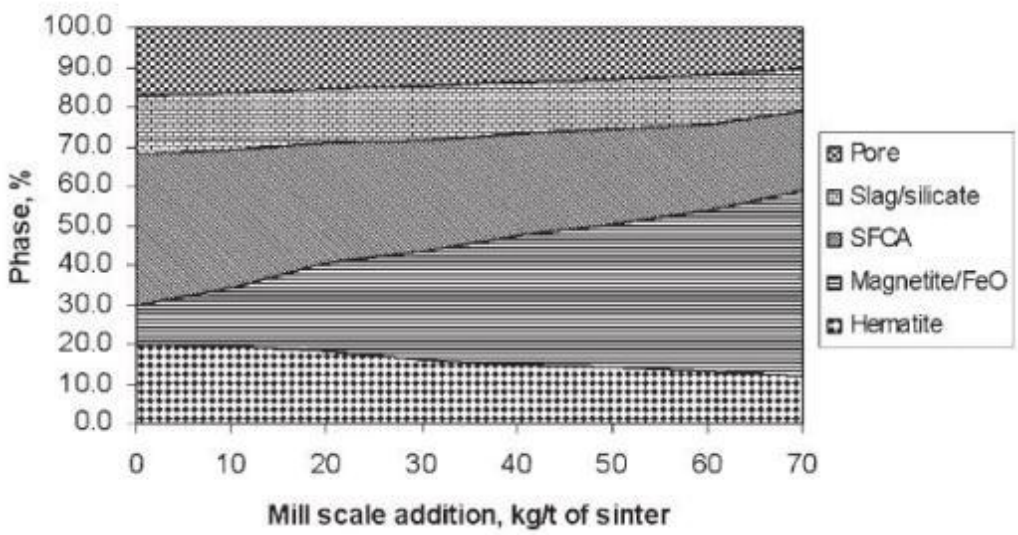

Figure 1-19 Effect of mill scale addition on phase formation in sinter [9].

1.2.7 Recycling of Iron and Steel Making Dusts

1.2.7.1 Introduction to Iron and Steel Making Dusts

For over a century, with iron and steel industry booming worldwide, a significant amount of iron and steel making dusts have been generated inevitably during iron and steel making processes. These dusts are removed from the off-gases of blast furnaces (BF), basic oxygen furnaces (BOF) and electric arc furnaces (EAF) either in the form of dry dusts by dry separation methods, or in the form of sludge or filter cake from wet separation methods [14]. If the off-gases are ducted to scrubbers for cleaning where the cleaned gas is reused in iron or steel making processes and remaining dusts in water can be filtered, dried and disposed into a stockpile in a form of filter cake.

These dusts usually contain large amounts of Fe, Zn and other harmful elements like Cd, Pd, Na and K. In iron and steel making processes, temperature of 1600 ℃ or even higher can be achieved and many components of the charge including Zn and Pd are evaporated and accumulated in the dusts in the off-gases from furnaces [82], while others mainly iron or its oxides are carried out by the off gases as fine particles. Mineralogical analysis shows that zinc is present in oxide forms as zincite ZnO and franklinite $ZnFe_2O_4$. Iron can be found mostly as hematite Fe_2O_3, magnetite Fe_3O_4, wustite FeO, franklinite and metallic iron. Typically, EAF dust contains higher level of zinc (about 15-30%) compared to BF and BOF dusts (1-5%). The brief remarks on the phases containing the major elements in BOF dusts are presented in Table 1-1 [14].

Table 1-1 Mineral phase distribution of the major elements present in BOF dusts [14].

Element	Phase Containing Element
Fe	Fe_3O_4 is most prevalent phase. Portions of Fe cations in Fe_3O_4 are replaced by Zn, Mg, Ca, Cr, Mn, etc. Some Fe is as metal iron, wustite and hematite.
Zn	50-80% as ZnO. Balance mainly associated with Fe in a mixed zinc-iron ferrite spinel. Very small amounts of zinc can be as a sulphide, silicate or aluminate.
Ca	As CaO and $CaCO_3$ mainly. The balance may occur as a fluoride, ferrite, or silicate.
Cd	Distribution not well established, but possibly as for Zn considering the similarities in most properties of the two elements.
Pd	Mostly as an oxide. $PdSO_4$ and $PdCl_2$ are also present.
Cr, Ni	Replace Fe in Fe_3O_4 spinel phase. Some Cr could be as Cr_2O_3.

Although the iron content in the dusts is high, its direct utilisation in iron or steelmaking is however not possible for a number of reasons.

In ironmaking, the major problem is that the dust contains unacceptable levels of zinc which has been found to be the main cause of many troubles in blast furnace operation, such as refractory failure and scaffold formation in the stack. Consequently, feed to an iron blast furnace must have a very low zinc concentration (less than 0.01% [83]). Other undesired trace elements like Pb, Cu, S, Na, and K are similarly unwanted even at low

levels since they also reduce the furnace life or its efficiency [84], or are hard to remove from the steel bath and result in the poor quality of steels [14]. Recycling of the dusts via steelmaking can lead to the volatile components to recirculate. This not only increases operating costs, but also gives rise to the build-up of impurities in the melt. The direct recycling in steelmaking process also can increase the concentration of non-ferrous metals in the dust in the off-gases [14].

1.2.7.2 The Processing of Iron and Steel Making Dusts

Attempts have been made by many investigators to recycle the dusts generated from the iron and steel making processes, however the information on the treatment of BF and BOF dusts is limited. Processes investigated include pyrometallurgical [85-87] and hydrometallurgical processes [88-90]. After decades of process development, the problem is still not well solved.

- **Pyrometallurgical Methods**

The majority of the pyrometallurgical technologies are based on high temperature reduction and volatilisation of the heavy metal followed by gas phase recovery. Temperatures used are in excess of 1100 ℃. Solid carbonaceous materials are the more usual reductants, but gaseous reductants (CO or H_2) are also used. ZnO is reduced to gaseous zinc; $ZnFe_2O_4$ is reduced to gaseous Zn and Fe_3O_4; Fe_3O_4 goes to FeO or Fe, while PbO is reduced to Pb [14]. Depending on the process, Zn may be recovered as elemental Zn in liquid form in a Zn condenser such as in the Imperial Smelting Process (ISP) [86] or in solid form as ZnO in bag houses [87].

The inert slags produced during the pyrometallurgical technologies can be used as subsurface material in construction or dumped as a non-hazardous solid waste. Another common advantage of the processes is that they are suitable to treat different zinciferous materials. Even zinc initially present as a ferrite is recoverable at the high temperatures in use. In addition, the reactions of pyrometallurgical processes are fast. Both purposes of de-toxifying the filter cake and removing Zn from it for subsequent recovery are rapidly accomplished.

However, a common disadvantage of pyrometallurgical technologies is that the iron rich slag is generally not appropriate for iron or steelmaking. For example in terms of Waelz Kiln slag, even after grinding to -300 μm and using magnetic concentration, impurity elements like S and Cu are still at intolerable levels. Metallic iron produced in some of the processes is similarly contaminated [91]. Also, pyrometallurgical processes usually requiring capital investments of several tens to hundreds of millions dollars, and the relatively low Zn levels in BF and BOF dusts had meant most of the established processes would not be economically feasible. Besides, the environmental issues caused by pyrometallurgical processes such as air pollution and noise pollution would hinder its wide commercial application.

- **Hydrometallurgical Methods**

Vast amount of research efforts have been invested in the development of a suitable hydrometallurgical process which could potentially recover valuable metal like zinc from the flue dusts and have the residual suitable for recycling in steel plant or detoxified such that it becomes an acceptable ordinary waste material for landfill.

The majority of the hydrometallurgical technologies are based on leaching and can be categorised into the several lixiviants used for leaching, namely; sulphuric acid [92-94], hydrochloric acid [89], sodium hydroxide [95] and ammonium salts [96, 97].

However, available information indicates that up to now none of the proposed hydrometallurgical processes achieved commercial success. One common problem encountered with all leaching processes in terms of Zn removal is that mild acid and caustic solutions readily dissolve ZnO, whereas $ZnFe_2O_4$ can only be soluble in very strong H_2SO_4 or HCl. The use of strong acids will dissolve the Fe into the solution which in turn created problem for Zn recovery via electrowinning. And the produced residuals are not suitable for recycling via iron and steel making due to S and Cl contaminants from the leaching process.

1.2.8 Summary and Project Objectives

Sintering is the most economical and widely used agglomeration method for iron ore fines in ironmaking. The mineral phases formed in sinter which determine the sinter quality depend on the sintering conditions, such as temperature, composition, oxygen partial pressure and sintering time, etc. Sintering is a complex process and investigations to further elucidate reaction mechanisms and the effects of processing parameters will continue into the future.

The sintering technology also can be used for utilisation of unconventional ferrous materials including low-grade iron ore or by-products from iron and steel making processes such as mill scale and collected dusts.

The composition of the New Zealand ironsand approximates that of titanomagnetite ($Fe_{3-x}Ti_xO_4$) containing about 60 wt% iron, 8 wt% titania (TiO_2). The influence of titanium on iron ore sintering has been previously investigated and there is a general agreement that increasing the level of titanium in the sinter mix can reduce sinter strength and result in deterioration in sinter reducibility. However, little information is known about how titanomagnetite changes during sintering process. More detained work needs to be done to gain better understanding of sintering mechanism of titanomagnetite.

Mill scale is a mixture of iron oxides (wustite, magnetite and hematite) and is formed by the oxidation of the surface of steels during continuous casting, reheating and hot rolling. Sintering process is believed to be one of appropriate methods of recycling mill scale. However, there has been no satisfactory conclusion on the effect of mill scale addition in different contents on the formation of mineral phases during iron ore sintering.

During iron and steel production, a large amount of filter cake wastes is produced from the fine dust captured in the gas cleaning systems of BF and BOF and deposited in settling ponds. The filter cake cannot be directly recycled by iron and steel making processes due to its small particle size and high zinc concentration. Sintering process is

believed to be an attractive agglomeration method to assimilate fine particles of filter cake and improve its strength consequently. Besides, the high temperature reduction and volatilisation of zinc can potentially be achieved during sintering.

The aim of the project was to study the sintering behaviour of three unconventional ferrous materials (New Zealand ironsand, mill scale and filter cake wastes) and assess the feasibility of their utilisation by sintering. The project will study:

1) Characterisation of New Zealand ironsand, including raw New Zealand ironsand and relict particles in industrial sinters with addition of 3 wt% of New Zealand ironsand from BlueScope Ltd.

2) The behaviour of New Zealand ironsand during iron ore sintering.

3) Systematic study on the effect of sintering conditions on the formation of mineral phases, including temperature, CaO/SiO_2 ratio, sintering gas atmosphere and cooling procedure.

4) Study on the interaction behaviour of New Zealand ironsand with the flux materials (CaO, MgO and dolomite).

5) Comprehensive study on the effect of various levels of mill scale addition on the formation of mineral phases during iron ore sintering.

6) Mineral phase formation and zinc removal during sintering of filter cake materials.

1.3 Experimental Methods

1.3.1 Sample Preparation for Morphology

The sintered samples were firstly placed in a mould where epoxy resin was then pour over the top of samples. The samples were also held within a vacuum chamber for around 30 minutes to ensure that the resin impregnated the inner of samples, before being left to harden for 24 hours at ambient temperature.

The mounted samples were cut perpendicular to the top surface by a diamond blade on the Struers Accutom-50 precision cut-off machine (Struers Inc., United States). The cross-section was then ground using SiC paper, from 500 to 1200 grade; followed 9 μm, 3 μm and 1 μm diamond paste on a polishing wheel of a Struers TegraPol-21 automatic polishing machine (Struers Inc., United States). The polished samples were coated with a carbon film at high vacuum to guarantee good conductivity for SEM/EDS and EPMA analysis.

1.3.2 Optical Microscopy

Optical photomicrographs of polished samples were obtained in reflected light using a Leica DM6000 (Leica Microsystems, Germany) optical microscope with an attached Leica DFC295 digital camera. Images were captured using the Leica Application Suite (LAS) V4.3 software package.

1.3.3 Determination of the Volumetric Fractions of Mineral Phases

The obtained digital optical photomicrographs were analysed using Leica Phase Expert (Leica Microsystems, Germany) software to determine the volumetric fractions of mineral phases which is equal to the area fractions of the corresponding phases in the cross sections of the sintered samples. Different phases (hematite, magnetite and SFCA) as well as pores in a sintered sample were identified respectively by regions of homogeneous reflectivity. The key phases were then differentiated by coloured overlays

to show their distribution, and the volumetric fractions of the phases present in the sinter were determined using the software.

The silicate phase in a sintered sample was difficult to be distinguished from pores by the software due to their similar contrast, so it was not counted in the phase composition of the samples in this study. Hematite phase can be accurately identified by Leica Phase Expert due to its sharp contrast with other phases. In comparison, there is not sharp contrast between SFCA and magnetite phases. Therefore, to obtain accurate volumetric fractions of SFCA and magnetite phases, the image was firstly turned over to two different extremes and the corresponding volumetric fraction of each phase was recorded. The average volumetric fractions of individual phases in two extremes were taken as the fractions of the phases in the image. It is found that the relative errors of the volume fractions of SFCA and magnetite phases were in the range of ±5% of the corresponding values. The data of hematite fractions have significantly smaller error than that of SFCA and magnetite.

An example of the processing of the optical photomicrographs of sintered samples by Leica Phase Expert was given in Figure 1-20. Figure 1-20 (a) shows an original reflected light optical photomicrograph of one sintered sample. Figure 1-20 (b) and (c) present the same image processed using the software for determination of the volumetric fractions of SFCA and magnetite phases with two different extremes. In Figure 1-20 (b), 29.3% SFCA and 27.6% magnetite were identified, while 26.4% SFCA and 30.5% magnetite were observed in Figure 1-20 (c). The relative errors of the volume fractions of SFCA and magnetite phases were ±5.21% and ±4.99%, respectively. The fraction of each phase was obtained by taking the average of 20 images with 200x magnification from each sintered sample.

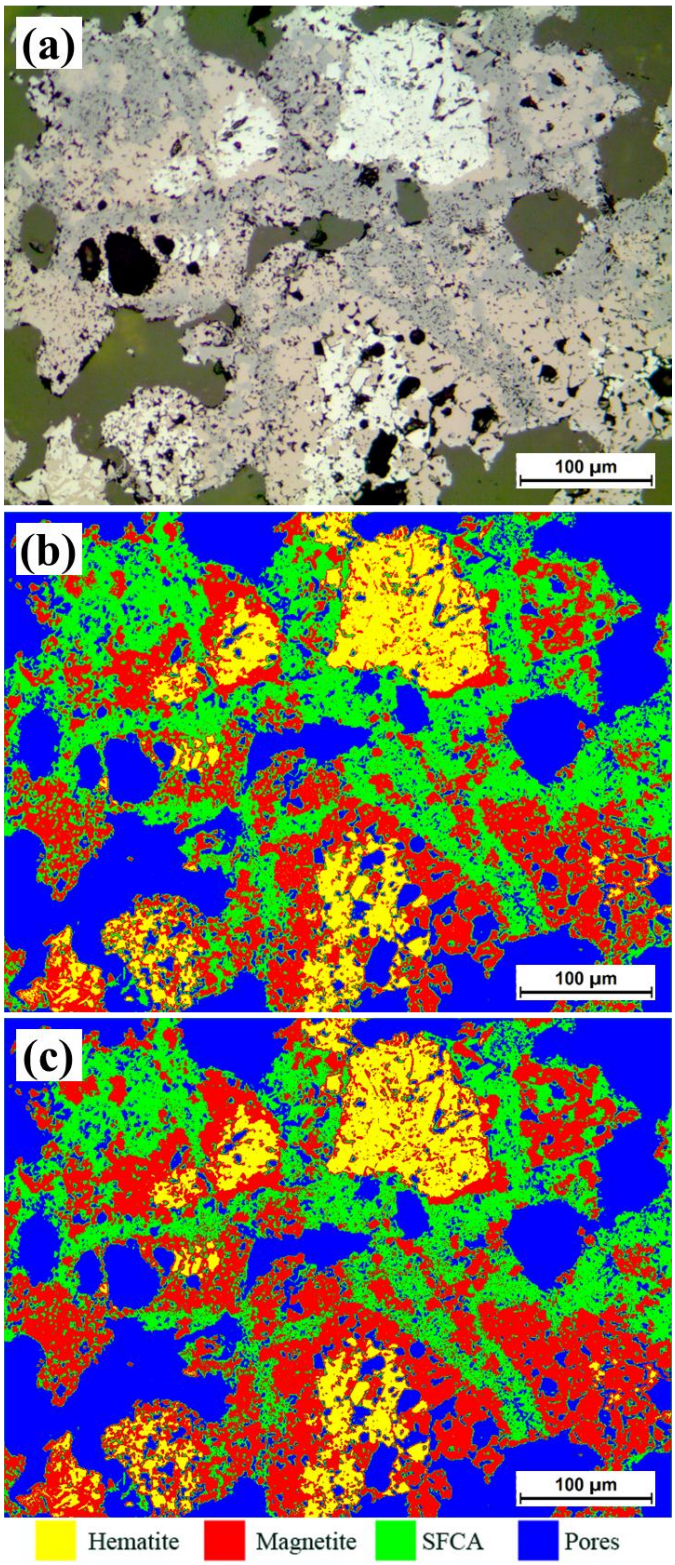

Figure 1-20 Processing of the optical microscopic images of sintered samples to determine the fractions of mineral phases. (a) Original reflected light optical microscopic image; (b) and (c) the same images processed using the Leica Phase Expert software for determination of the phase proportion with two different extremes.

1.3.4 Scanning Electron Microscopy/Energy Dispersive X-ray Spectroscopy

All scanning electron microscopy (SEM) observations reported in Chapter 2 and 6 were undertaken on a JEOL JSM – 7001F field emission scanning electron microscope (FESEM), fitted with Energy Dispersive X-ray Spectroscopy (EDS) system. The operation was carried with an accelerating voltage of 15kV and working distance of 10mm.

All SEM observations presented in Chapter 4 were done on a JEOL JCM - 6000 SEM and its linked EDS system. The operation was carried with an accelerating voltage of 15 kV and working distance of 10 mm.

1.3.5 Qualitative and Quantitative X-Ray Diffraction

All the qualitative XRD investigations were conducted using a GBC MMA XRD using a copper Kα X-ray source (λ = 1.54056 Å) with a nickel monochromator. The scans were done from 15^{o} to 85^{o} at 1^{o}/min and a step size of 0.02^{o}. The voltage used was 35 kV, with a current of 28.6 mA. Qualitative phase analysis was carried out using Traces software (Version 6.6.10).

The quantitative XRD analysis of original New Zealand ironsand presented in Chapter 2 was carried out at CSIRO Mineral Resources Flagship in Clayton using a Philips X'Pert diffractometer, fitted with a Co long-fine-focus tube operated at 40 kV and 40 mA and a curved graphite post-diffraction monochromator. Data were collected over the range $3° \leq 2\theta \leq 140°$ in steps of 0.01°, with a counting time of 5 s at each step.

A Rietveld refinement-based approach to quantitative phase analysis (QPA) [98] was performed using TOPAS software (Version 4.2) [99]. In order to determine the absolute phase concentrations via the QPA, the ironsand sample was mixed with an ultra pure and highly crystalline corundum (α-Al_2O_3; Baikalox Alumina Polishing Powder, Type GE6) internal standard.

1.3.6 Electron Probe Microanalysis

The Electron Probe Microanalysis (EPMA) of original New Zealand ironsand reported in Chapter 2 was conducted at CSIRO Mineral Resources Flagship in Clayton. Two types of EPMA information were obtained. Initially, the ironsand sample was mapped using a high resolution Field Emission Gun (FEG) equipped EPMA (JEOL 8500F Hyperprobe). Following mapping by FEG-EPMA, the samples were examined by quantitative EPMA techniques using a JEOL 8900 Superprobe to determine the composition of the titanomagnetite grains. The operating conditions for each of the techniques and the instruments are described separately below.

- **EPMA Mapping**

The JEOL Hyperprobe microanalyser used for electron microprobe mapping is equipped with five wavelength dispersive (WD) spectrometers. The carbon coated sample was mapped over a grid of analysis points covering 2 x 2 mm using a combination of WD and energy dispersive (ED) spectroscopic techniques. The elements mapped using the WD spectroscopic techniques were Fe, Nb, Cr, V and Ti. Standards used to calibrate the EPMA WD spectrometers prior to mapping were: hematite (Fe_2O_3), niobium metal (Nb), rutile (TiO_2), synthetic yttrium vanadate (YVO_4) and synthetic eskolaite (Cr_2O_3). Elements that were not measured by WD spectroscopy were measured using two energy-dispersive (ED) spectrometers operating in parallel. Operating conditions for the microprobe during mapping were an accelerating voltage of 15 kV, a beam current of 100 nA, a step size of 2 μm (in x and y), and a counting time of 30 ms per step. The choice of step size was based on a compromise between maximising the number of particles analysed and ensuring any fine-grained mineral phases were located.

Following mapping, the element distribution data obtained by mapping were manipulated using the software package CHIMAGE [100] which incorporates an automated clustering algorithm that identifies chemically alike phases [101]. These phases were then overlaid onto the mapped region to provide a “phase-patched” map showing the distribution of all chemical/mineral phases within the mapped area.

- **Quantitative EPMA**

Approximately 500 randomly selected Ti-bearing grains were analysed using a JEOL 8900 Superprobe to assess the distribution of major and minor elements. The analysis position within each grain was also random. For the quantitative analyses, the microprobe was operated at 15 kV and 40 nA and the electron beam defocused to 10 μm (to account for any within-grain inhomogeneity). Counting times were 20 s on the main peak and 10 s on the background. The suite of elements analysed included Al, Cr, Mn, Mg, Ti, V, Fe, Si and Nb. Oxygen was calculated by difference, based on valence. . All analysis positions were verified as being homogeneous and flat by viewing the secondary electron image of the area to be analysed (at 5000x magnification). Elemental analyses were corrected for atomic number (Z), absorption (A) and fluorescence (F) using the PAP procedure of Pouchou and Pichoir [102-104].

1.3.7 Carbon Content Analysis

In Chapter 6, the carbon content of sample was determined using a LECO SC-444 DR Carbon/Sulphur analyser (LECO Corporation, St. Joseph, USA). Analysis was based on a basic combustion method, where a sample is melted and combusted in an induction furnace. The CO_2 generated was measured by an infrared sensor, with the amount of CO_2 giving the carbon content.

1.3.8 Inductively Coupled Plasma- Optical Emission Spectrometry

The zinc content of samples in Chapter 6 was examined by an Inductively Coupled Plasma- Optical Emission Spectrometry (ICP-OES). Around 0.1g crashed sample after sintering was digested into a solution consisting of 6 ml HCl, 2 ml HNO_3 and 2 ml H_2O_2. After filtration through 0.1μm glass fibre filter, the solution was then diluted to an appropriate concentration for analysis.

1.3.9 Control of Oxygen Partial Pressure of Sintering Atmosphere

In Chapters 2 and 3, the sintering of iron ore blend with New Zealand ironsand was conducted at different temperatures (1250, 1275, 1300 and 1325 ℃) in atmospheres with various oxygen partial pressure. The atmospheres with pO_2 = 0.5 kPa and 5 kPa were achieved by mixing argon with air with accurately controlled flow rates. However, it is difficult to achieve a pO_2 at a very low level using the same method. A 1% CO-24% CO_2-75% Ar gas mixture was used in experiments with low oxygen potential.

The pO_2 of above CO-CO_2-Ar gas mixture can be obtained assuming the following chemical reaction reached equilibrium. The standard Gibbs free energy change of the reaction was taken from ref. [62]:

$$CO + 1/2\ O_2 = CO_2 \qquad (1\text{-}3)$$

$$\Delta G = -67500 + 20.75T\ (cal)$$

Therefore, the 1% CO-24% CO_2-75% Ar gas mixture gave equilibrium pO_2 of 2.9×10^{-6} kPa (1250 ℃), 5.9×10^{-6} kPa (1275 ℃), 1.2×10^{-5} kPa (1300 ℃), and 2.3×10^{-5} kPa (1325 ℃).

References

[1] A. K. Biswas, Principles of Blast Furnace Ironmaking: Theory and Practice, Cootha Publishing House, Brisbane, (1981), 194.

[2] Cleaner Technology Options for Sintering Plant of an Intergrated Iron & Steel Plants, Ministry of Environment & Forests, Government of India, http://www.cpcb.nic.in/.

[3] P. R. Dawson, J. Ostwald, K. M. Hayes, Influence of Alumina on Development of Complex Calcium Ferrites in Iron Ore Sinters, *Transactions of the Institution of Mining and Metallurgy Section C-Mineral Processing and Extractive Metallurgy*, **94** (1985), C71-C78.

[4] H. A. Cocker, J. L. Mauk, H. Rogers, A. B. Padya and J. Ogiliev, Where is the Titanium in the Ironsands? - Ti Partitioning in the Magnetic Fraction, Proceedings of the AusIMM New Zealand Branch 43rd Annual Conference, AusIMM New Zealand Branch, Alexandra, (2010), 165-174.

[5] J. B. Wright, Iron-titanium Oxides in Some New Zealand Ironsands, *New Zealand Journal of Geology and Geophysics*, **7** (1964), 424-444.

[6] J. B. Wright and J. F. Lovering, Electron-probe Micro-analysis of the Iron-titanium Oxides in some New Zealand Ironsands, *Mineralogical Magazine*, **35** (1965), 604-621.

[7] N. J. Bristow and C. E. Loo, Sintering Properties of Iron Ore Mixes containing Titanium. *ISIJ International*, **32** (1992), 819-828

[8] N. A. E. Hussiny, F. M. Mohamed and M. E. H. Shalabi, Recycling of Mill Scale in Sintering Process, *Science of Sintering*, **43** (2011), 21-31.

[9] T. Umadevi, A. Brahmacharyulu, P. Karthik, P. C. Mahapatra, M. Prabhu and M. Ranjan, Recycling of Steel Plant Mill Scale via Iron Ore Sintering Plant, *Ironmaking and Steelmaking*, **39** (2012), 222-227.

[10] Bluescope Community, Safety and Enviroment Report 2011, BlueScope Ltd., (2011), 32. http://www.bluescopesteel.com/sustainability/publications.

[11] Information on Steel Making and Processing, Industrial Steel Processing & Trading Group, http://www.profisol.gr/en/production/steelmaking.aspx.

[12] K. Bugayev, Y. Bychkov, Y. Konovalov, V. Kovalenko and E. Tretyakov, Iron and Steel Production, The Minerva Group, Inc., (1971), 50.

[13] A. Ghosh and A. Chatterjee, Ironmaking and Steelmaking: Theory and Practice, PHI Learning Private Limited, New Delhi, (2008), 148.

[14] R. L. Nyirenda, The Processing of Steelmaking Flue-Dust: A Review, Minerals Engineering, 4 (1991), 1003-1025.

[15] How steel is Made, UK Steel, http://www.eef.org.uk/uksteel/About-the-industry/How-steel-is-made/step-by-step/Ironmaking.htm.

[16] N. Birks, G. H. Meier, and F. S. Pettit, Introduction to the High Temperature Oxidation of Metals, 2nd edition, Cambridge University Press, Cambridge, (2006), 83.

[17] T. Umadevi, M. G. S. Kumar, P. C. Mahapatra, T. M. Babu and M. Ranjan, Recycling of Steel Plant Mill Scale via Iron Ore Pelletisation Process, *Ironmaking and Steelmaking*, **36** (2009), 409-415.

[18] A. Babich, D. Senk, H. W. Gudenau and K. T. Mavrommatis, Ironmaking: Textbook, Aachen Institut für Eisenhüttenkunde, Aachen, (2008), 50-62.

[19] K. Meyer, Pelletizing of Iron Ores, Springer-Verlag, (1980), 13.

[20] Simplified Diagram of a Sinter Plant, Eurotherm, http://www.eurotherm.com/industries/heat-treatment/metals-applications/sintering/.

[21] C. E. Loo, A Perspective of Goethitic Ore Sintering Fundamentals, *ISIJ International*, 45 (2005), 436-448.

[22] N. A. S. Webster, M. I. Pownceby, I. C. Madsen and J. A. Kimpton, Silico-ferrite of Calcium and Aluminum (SFCA) Iron Ore Sinter Bonding Phases: New Insights into their Formation during Heating and Cooling, *Metallurgical and Materials Transactions B*, **43** (2012), 1344-1357.

[23] The Sintering Process of Iron Ore Fines, Ispat Guru, http://ispatguru.com/the-sintering-process-of-iron-ore-fines-2/.

[24] M. Sasaki and Y. Hida, Consideration on the Properties of Sinter from the Point of Sintering Reaction, *Tetsu-to-Hagane*, **68** (1982), 563-571

[25] R. Shen, G. Zhang, M. Dell'Amico, P. Brown and O. Ostrovski, Sintering Pot Test of Manganese Ore with Addition of Manganese Furnace Dust, *ISIJ International*, **47** (2007), 234-239.

[26] C. E. Loo, R. P. Williams and L. T. Matthews, Influence of Material Properties on High-Temperature Zone Reactions in Sintering of Iron-Ore, *Transactions of the Institution of Mining and Metallurgy Section C-Mineral Processing and Extractive Metallurgy*, **101** (1992), C7-C16.

[27] C. E. Loo, Some Progress in Understanding the Science of Iron Ore Sintering, ICSTI/57th Ironmaking Conference Proceedings, (1998), 1299-1316.

[28] R. Freer, Self-Diffusion and Impurity Diffusion in Oxides, *Journal of Materials Science*, **15** (1980), 803-824.

[29] E. Mazanek and S. Jasienska, Formation of Binary Ferrites in Iron Ore Sinters, *J. Iron Steel Inst.*, **204** (1966), 344-348.

[30] A. van Sandwijk and K. Koopmans, The Solid State Reaction between CaO and Fe_2O_3 in Air, *Science of Ceramics*, **10** (1980), 403-409.

[31] A. van Sandwijk and K. Koopmans, The Mechanism of the Formation of Calcium Ferrites in Air. *Science of Ceramics*, **11** (1981), 327-332.

[32] B. Bergman, Solid-State Reactions between CaO Powder and Fe_2O_3, *Journal of the American Ceramic Society*, **69** (1986), 608-611.

[33] X. Guo and Y. Ono, Kinetics of Calcium Ferrites Formation from CaO and Fe_2O_3 in Solid State, Memoirs of the Faculty of Engineering, Kyushu University, **52** (1992), 7-17.

[34] J. W. Jeon, S. M. Jung and Y. Sasaki, Formation of Calcium Ferrites under Controlled Oxygen Potentials at 1273 K, *ISIJ International*, **50** (2010), 1064-1070.

[35] N. V. Y. Scarlett, M. I. Pownceby, I. C. Madsen and A. N. Christensen, Reaction Sequences in the Formation of Silico-Ferrites of Calcium and Aluminum in Iron Ore Sinter, *Metallurgical and Materials Transactions B*, **35** (2004), 929-936.

[36] J. Yin, X. Lv, S. Xiang, C. Bai and B. Yu, Influence of CaO Source on the Formation Behaviour of Calcium Ferrite in Solid State, *ISIJ International*, **53** (2013), 1571-1579.

[37] K. C. Mills, Slag Atlas, 2nd edition, Verlag Stahleisen GmbH, D-Düsseldorf, (1995).

[38] L. X. Yang and L. Davis, Assimilation and Mineral Formation during Sintering for Blends Containing Magnetite Concentrate and Hematite/Pisolite Sintering Fines. *ISIJ international*, **39** (1999), 239-245.

[39] C. Kamijo, M. Matsumura and T. Kawaguchi, Sintering Behaviour of Raw Material Bed Placing Large Particles, ISIJ international, **45** (2005), 544-550.

[40] C. E. Loo and L. T. Matthews, Assimilation of Large Ore and Flux Particles in Iron Ore Sintering, *Transactions of the Institution of Mining and Metallurgy Section C-Mineral Processing and Extractive Metallurg*y, **101** (1992), C105-C117.

[41] W. J. Jordaan, The Variation of Sinter Strength in the Sinter Bed due to the Mineral Phase Distribution, University of Pretoria, (2002).

[42] M. K. W. Kalenga, Investigation Into the Influence of Magnesia Content, Alumina Content, Basicity and Ignition Temperature on the Mineralogy and Properties of Iron Sinter, University of Pretoria, (2007).

[43] N. Ponghis and A. Poos, Investigations on the Mechanisms Governing Iron Ore Sintering, Ironmaking Conference Proceedings, **36** (1977), 91-101.

[44] H. Kang, S. Choi, W. Yang and B. Cho, Influence of Oxygen Supply in an Iron Ore Sintering Process, *ISIJ International*, **51** (2011), 1065-1071.

[45] L. X. Yang and E. Matthews, Oxidation and Sintering of Magnetite Ore under Oxidising Conditions, *ISIJ International*, **37** (1997), 854-861.

[46] P. R. Dawson, Recent Development in Iron Ore Sintering. II. Research Studies on Sintering and Sinter Quality, *Ironmaking and Steelmaking*, **20** (1993), 137-143.

[47] F. Matsuno, Changes in Mineral Phases during the Sintering of Fe_2O_3-CaO-SiO_2 System, *Transactions of the Iron and Steel Institute of Japan*, **19** (1979), 595-604.

[48] F. Matsuno and T. Hirada, Changes of Mineral Phases during the Sintering of Iron Ore - Lime Stone Systems, *Transactions of the Iron and Steel Institute of Japan*, **21** (1981), 318-325.

[49] S. N. Ahsan, T. Mukherjee and J. A. Whiteman, Structure of fluxed sinter, *Ironmaking and Steelmaking*, **10** (1983), 54-64.

[50] T. R. C. Patrick and R. R. Lovel, Leaching Dicalcium Silicates from Iron Ore Sinter to Remove Phosphorus and Other Contaminants, *ISIJ International*, **41** (2001), 128-135.

[51] S. N. Ahsan, T. Mukherjee and J. A. Whiteman, Structure of fluxed sinter, *Ironmaking and Steelmaking*, **10** (1983), 54-64.

[52] N. Rogers, An Introduction to Our Dynamic Planet, Cambridge University Press, Cambridge, (2008), 146.

[53] C. V. A. Duke and C. D. Williams, Chemistry for Environmental and Earth Sciences, CRC Press, Boca Raton, (2007), 76.

[54] C. E. Loo, L. C. Mackey and B. M. England, Behaviour of Magnesia-Bearing Fluxes during Iron Ore Sintering, *Transactions of the Institution of Mining and Metallurgy Section C-Mineral Processing and Extractive Metallurgy*, **105** (1996), C175-C189.

[55] W. G. Mumme, J. M. F. Clout and R. W. Gable, The Crystal Structure of SFCA-I, $Ca_{3.18}Fe^{3+}_{14.66}Al_{1.34}Fe^{2+}_{0.82}O_{28}$, A Homologue of the Aenigmatite Structure Type, and New Crystal Structure Refinements of ß-CFF, $Ca_{2.99}Fe^{3+}_{14.30}Fe^{2+}_{0.55}O_{25}$ and Mg-free SFCA, $Ca_{2.45}Fe^{3+}_{9.04}Al_{1.74}Fe^{2+}_{0.16}Si_{0.6}O_{20}$, *Neues Jahrbuch für Mineralogie-Abhandlungen*, (1998), 93-117.

[56] N. J. Bristow and A. G. Waters, Role of SFCA in Promoting High-Temperature Reduction Properties of Iron Ore Sinters, *Transactions of the Institution of Mining and Metallurgy Section C-Mineral Processing and Extractive Metallurgy*, **100** (1991), C1-C10.

[57] M. I. Pownceby and J. M. F. Clout, Importance of Fine Ore Chemical Composition and High Temperature Phase Relations: Applications to Iron Ore Sintering and Pelletising, *Transactions of the Institution of Mining and Metallurgy Section C-Mineral Processing and Extractive Metallurgy*, **112** (2003), 44-51.

[58] T. Umadevi, P. Mahapatra and M. Prabhu, Influence of MgO Addition on Microstructure and Properties of Low and High Silica Iron Ore Sinter,

Transactions of the Institution of Mining and Metallurgy Section C-Mineral Processing and Extractive Metallurgy, **122 (**2013), 238-248.

[59] J. McAndrew and J. M. F. Clout, The Nature of SFCA and Its Importance as a Bonding Phase in Iron Ore Sinter, *Proc. of the 4th China-Australia Symp. on the Technology of Feed Preparation for Ironmaking*, Dampier, Australia, (1993), 1.

[60] G. O. Egundebi and J. A. Whiteman, Evolution of Microstructure in Iron Ore Sinter, *Ironmaking and Steelmaking*, **16** (1989), 379-385.

[61] L. H. Hsieh and J. A. Whiteman, Effect of Oxygen Potential on Mineral Formation in Lime-fluxed Iron Ore Sinter, *ISIJ International*, **29** (1989), 625-634.

[62] L. H. Hsieh and J. A. Whiteman, Sintering Conditions for Simulating the Formation of Mineral Phases in Industrial Iron Ore Sinter, *ISIJ International*, **29** (1989), 24-32.

[63] S. Wang, W. Gao and L. Kong, Formation Mechanism of Silicoferrite of Calcium and Aluminium in Sintering Process, *Ironmaking and Steelmaking*, **25** (1998), 296-301.

[64] N. A. S. Webster, M. I. Pownceby, I. C. Madsen and J. A. Kimpton, Effect of Oxygen Partial Pressure on the Formation Mechanisms of Complex Ca-rich Ferrites, *ISIJ International*, **53** (2013), 774-781.

[65] N. A. S. Webster, M. I. Pownceby and I. C. Madsen, In situ X-ray Diffraction Investigation of the Formation Mechanisms of Silico-Ferrite of Calcium and Aluminium-I-type (SFCA-I-type) Complex Calcium Ferrites, *ISIJ International*, **53** (2013), 1334-1340.

[66] N. A. S. Webster, M. I. Pownceby, I. C. Madsen, A. J. Studer, J. R. Manuel and J. A. Kimpton, Fundamentals of Silico-Ferrite of Calcium and Aluminum (SFCA) and SFCA-I Iron Ore Sinter Bonding Phase Formation: Effects of CaO: SiO_2 Ratio, *Metallurgical and Materials Transactions B*, **45** (2014), 2097-2105.

[67] M. B. Turner, S. J. Cronin, R. B. Stewart, M. Bebbington and I. E. M. Smith, Using Titanomagnetite Textures to Elucidate Volcanic Eruption Histories, *Geology*, **36** (2008), 31-34.

[68] Y. Li, Y. Li, and R. J. Fruehan, Formation of Titanium Carbonitride from Hot Metal, *ISIJ International*, **41** (2001), 1417-1422.

[69] A. D. Manshadi, J. Manuel, S. Hapugoda and N. Ware, Sintering Characteristics of Titanium Containing Iron Ores, *ISIJ International*, **54** (2014), 2189-2195.

[70] M. Binnewies and E. Milke, Thermochemical Data of Elements and Compounds, 2nd edition, Wiley-VCH Verlag GmbH, Weinheim, (2002).

[71] G. Wei, Q. Gao, F. Song, Y. He, G. Du and F. Shen, Study on Sintering Experiments with Indonesia Vanadium-bearing Titanomagnetite, Asia Steel International Conference, The Chinese Society for Metals, Beijing, (2012).

[72] H. Du, Principles of Blast Furnace Smelting Vanadium-Bearing Titanomangetite, Science Press, Beijing, (1996).

[73] Z. Yin, J. Li and S. Yang, Sintering Pot Test on Improving TiO_2-containing Ore's Allocated Proportion, *Advanced Materials Research*, **311-313** (2011), 850-853.

[74] T. Paananen and K. Kinnunen, Effect of TiO_2-content on Reduction of Iron Ore Agglomerates, *Steel Research International*, **80** (2009), 408-414.

[75] D. J. Young, High Temperature Oxidation and Corrosion of Metals, Elsevier, Oxford, (2008), 38.

[76] W. Schwenk and A. Rahmel, Theoretical Considerations on Phase Boundary Reactions and Mass Transfer during the Oxidation of Iron. *Oxidation of Metals*, **25** (1986), 293-303.

[77] R. A Button and P. A. Lundh, Mineralogy and Mineral Formation in Iron-ore Sinetr with Addition of Magnetite Fines, *Ironmaking and Steelmaking*, 16 (1989), 151-164.

[78] S. C. Panigrahy, M. J. Rigaud, S. P. Chong and B. Chanda, The Use of Carol Lake Concentrate for Coke Breeze Reduction and LTD Improvement in Sinter Productions, 53rd Ironmaking Conference, AIME Iron and Steel Society, Warrendale, (1994) 523-531.

[79] J. M. F. Clout and J. R. Manuel, Fundamental Investigations of Differences in Bonding Mechanisms in Iron Ore Sinter Formed from Magnetite Concentrates and Hematite ores, *Powder Technology*, **130** (2003), 393-399.

[80] S. P. E. Forsmo, S. E. Forsmo, P. O. Samskog and B. M. T. Björkman, Mechanisms in Oxidation and Sintering of Magnetite Iron Ore Green Pellets, *Powder Technology*, **183** (2008), 247-259.

[81] L. X. Yang, Sintering Fundamentals of Magnetite Alone and Blended with Hematite and Hematite/Goethite Ores, *ISIJ International*, **45** (2005), 469-476.

[82] S. Kelebek, S. Yörük and B. Davis, Characterization of Basic Oxygen Furnace Dust and Zinc Removal by Acid Leaching, *Minerals Engineering*, **17** (2004), 285-291.

[83] J. C. Taylor and A. D. Zunkel, Environmental Challenges for the Lead-Zinc Industry, JOM, 40 (1988), 27-30.

[84] W. J. Rankin and J. B. See, The Alkali Problem in the Blast Furnace, *Minerals Science and Engineering*, **9** (1977), 68-82.

[85] A. F. S. Schoukens, F. Shaw and E. C. Chemaly, The Enviroplas Process for the Treatment of Steel-Plant Dusts, *Journal of the Southern African Institute of Mining and Metallurgy*, **93** (1993), 1-7.

[86] L. M. Southwick, Still No Simple Solution to Processing EAF Dust, *Steel Times International*, **3** (2010), 43-45.

[87] G. Assis, Emerging Pyrometallurgical Processes for Zinc and Lead Recovery from Zinc-Bearing Waste Materials, Zinc and Lead Processing Symposium, The Metallurgical Society of CIM, Calgary, (1998).

[88] Z. H. Trung, F. Kukurugya, Z. Takacova, D. Orac, M. Laubertova, A. Miskufova and T. Havlik, Acidic Leaching Both of Zinc and Iron from Basic Oxygen Furnace Sludge, *Journal of Hazardous Materials*, **192** (2011), 1100-1107.

[89] M. K. Jha, V. Kumar and R. J. Singh, Review of Hydrometallurgical Recovery of Zinc from Industrial Wastes, *Resources, Conservation and Recycling*, **33** (2001), 1-22.

[90] M. R. C. Ismael and J. M. R. Carvalho, Iron Recovery from Sulphate Leach Liquors in Zinc Hydrometallurgy, *Minerals Engineering*, **16** (2003), 31-39.

[91] H. Maczek and R. Kola, Recovery of Zinc and Lead from Electric Furnace Steelmaking Dust at Berzelius, *JOM*, **32** (1980), 53-58.

[92] S. Langova, J. Riplova and S. Vallova, Atmospheric Leaching of Steel-Making Wastes and the Precipitation of Goethite from the Ferric Sulphate Solution, *Hydrometallurgy*, **87** (2007), 157-162.

[93] S. Langova and D. Matysek, Zinc Recovery from Steel-Making Wastes by Acid Pressure Leaching and Hematite Precipitation, *Hydrometallurgy*, **101** (2010) 171-173.

[94] T. Havlík, A. M. Bernardes, I. A. H. Schneider and A. Miskufova, Hydrometallurgical Processing of Carbon Steel EAF dust, *Journal of Hazardous Materials*, **135** (2006), 311-318.

[95] A. J. B. Dutra, P. R. P. Paiva and L. M. Tavares, Alkaline Leaching of Zinc from Electric Arc Furnace Steel Dust, *Minerals Engineering*, **19** (2006), 478-485.

[96] R. L. Nyirenda and A. D. Lugtmeijer, Ammonium Carbonate Leaching of Carbon Steelmaking Dust, Detoxification Potential and Economic Feasibility of A Conceptual Process, *Minerals Engineering*, **6** (1993), 785-797.

[97] O. Ruiz, C. Clemente, M. Alonso and F. J. Alguacil, Recycling of An Electric Arc Furnace Flue Dust to Obtain High Grade ZnO, *Journal of Hazardous Materials*, **141** (2007), 33-36.

[98] I. C. Madsen and N. V. Y. Scarlett, Powder Diffraction: Theory and Practice, edited by R. E. Dinnebier and S. J. L. Billinge, The Royal Society of Chemistry, Cambridge, (2008), 298-331.

[99] Bruker, TOPAS Version 4.2, Bruker AXS Inc., Madison, Wisconsin, USA, (2009).

[100] I. R. Harrowfield, C. M. MacRae and N. C. Wilson, Chemical Imaging in Electron Microprobes, Proceedings of the 27th Annual MAS Meeting, Microbeam Analysis Society, New York, (1993), 547-548.

[101] N. C. Wilson and C. M. MacRae, An Automated Hybrid Clustering Technique Applied to Spectral Data Sets, Microscopy and Microanalysis, 11 (2005), 434-435.

[102] J. L. Pouchou and F. Pichoir, A New Model for Quantitative X-ray Microanalysis. Part 1: Application to the Analysis of Homogeneous Samples, La Recherche Aérospatiale, 3 (1984), 13-38.

[103] J. L. Pouchou and F. Pichoir, "PAP", Procedure for Improved Quantitative Microanalysis, Microbeam Analysis Proceedings, edited by J. T. Armstrong, San Francisco Press, San Francisco, (1985), 104-106.

[104] J. L. Pouchou and F. Pichoir, Quantitative Analysis of Homogeneous or Stratified Microvolumes Applying the Model “PAP”, Electron Probe Quantitation, edited by K. F. J. Heinrich and D. E. Newbury, Plenum Press, New York, (1991) 31-75.

CHAPTER 2. BEHAVIOUR OF NEW ZEALAND IRONSAND DURING IRON ORE SINTERING

Behaviour of New Zealand Ironsand during Iron Ore Sintering

Zhe Wang[1], David Pinson[2], Sheng Chew[2], Harold Rogers[2], Brian J. Monaghan[1], Mark I. Pownceby[3], Nathan A. S. Webster[3], Guangqing Zhang[1]

1. School of Mechanical, Materials and Mechatronic Engineering, University of Wollongong, NSW 2522, Australia

2. BlueScope Technology and Planning, P. O. Box 202 Port Kembla, NSW 2505, Australia

3. CSIRO Mineral Resources Flagship, Private Bag 10, Clayton South, VIC 3169, Australia

Abstract

A New Zealand ironsand sample was characterised by scanning electron microscopy (SEM), X-ray fluorescence (XRF) spectroscopy, qualitative and quantitative X-ray diffraction (XRD), and electron probe microanalysis (EPMA). The titanomagnetite-rich ironsand was added into an industrial sinter blend in the proportion of 5 wt pct and the mixture was uniaxially pressed into cylindrical tablets and sintered in a tube furnace under flowing gas with various oxygen potentials and temperatures to develop knowledge and understanding of the behaviour of titanium during sintering. An industrial sinter with addition of 3 wt pct ironsand was also examined. Both the laboratory and industrial sinters were characterised by optical and scanning electron microscopy. Various morphologies of relict ironsand particles were present in the industrial sinter due to the heterogeneity of sintering conditions, which could be well simulated by the bench-scale sintering experiments. The assimilation of ironsand during sintering in a reducing atmosphere started with the diffusion of calcium into the lattice of the ironsand matrix, and a reaction zone was formed near the boundary within individual ironsand particles where a perovskite phase was generated. With increasing sintering temperature, in a reducing atmosphere ironsand particles underwent further assimilation and most of the titanium moved from the ironsand particles into a glass phase. In comparison, more titanium remained in the original ironsand particles when sintered in air. Ironsand particles are more resistant to assimilation in an oxidising atmosphere.

Key words: Ironsand, Titanomagnetite, Sintering, Iron ore, Titanium.

1. Introduction

Ironsand deposits along the western coast of the North Island of New Zealand are currently mined as iron ores for steel production.[1] The composition of the New Zealand ironsands approximates that of titanomagnetite ($Fe_{3-x}Ti_xO_4$) containing about 60 wt pct iron, 8 wt pct titania (TiO_2) and a small amount of other impurities such as silica, phosphorus and lime.[1-3] Recently, BlueScope's Port Kembla sinter plant has begun incorporating 2-3 wt pct ironsand as a component of its iron ore sinter blend. The ironsand provides a cheaper, alternative source of iron and its incorporation into sinter provides an appropriate method of its utilization in ironmaking as its small particle size precludes direct charging into a blast furnace.[4] The introduction of a minor amount of titanium-bearing burden into blast furnaces has previously been demonstrated to be beneficial through the formation of titanium carbonitride precipitates that can deposit on the hearth lining and, consequently, extend operating campaigns.[5-6]

Limited work[4,7,8] on the addition of titanium-bearing minerals via a sinter plant indicates that a high level of Ti in the sinter mix may reduce productivity, lower sinter strength and result in deterioration of sinter reducibility. In the most comprehensive study, Bristow and Loo[4] examined the effect of addition of an ironsand from New Zealand into two iron ore blends containing 10 pct and 20 pct pisolitic limonite respectively, on the properties of sinter prepared using a pilot scale sintering facility. It was found that addition of up to 2 pct titanomagnetite did not significantly affect the sinter quality however increasing the titanomagnetite levels to greater than 3 pct caused a significant increase in the reduction degradation index (RDI) of the sinters. It was postulated that the addition of titanium decreased the fracture toughness of glass phase which is the weakest phase in a sinter and would increase the vulnerability of the sinter to crack propagation, thereby resulting in deterioration in sinter RDI.

Limited work[4,7,8] on the addition of titanium-bearing minerals via a sinter plant indicates that a high level of Ti in the sinter mix may reduce productivity, lower sinter strength and result in deterioration of sinter reducibility. In the most comprehensive study, Bristow and Loo[4] examined the effect of addition of an ironsand from New Zealand into two iron ore blends containing 10 pct and 20 pct pisolitic limonite

respectively, on the properties of sinter prepared using a pilot scale sintering facility. It was found that addition of up to 2 pct titanomagnetite did not significantly affect the sinter quality however increasing the titanomagnetite levels to greater than 3 pct caused a significant increase in the reduction degradation index (RDI) of the sinters. It was postulated that the addition of titanium decreased the fracture toughness of glass phase which is the weakest phase in a sinter and would increase the vulnerability of the sinter to crack propagation, thereby resulting in deterioration in sinter RDI.

2. Experimental Procedure

Bench-scale sintering tests using iron ore mixes containing 5 wt pct ironsand were carried out. The sintered samples were characterised by optical microscopy and scanning electron microscopy with energy dispersive X-ray spectroscopy (SEM/EDS) analyses.

2.1 Raw Materials and Preparation

The starting materials for the bench-scale iron ore sintering experiments were a bulk iron ore blend, limestone, dolomite, silica sand, manganese ore, cold return fines (CRF) and ironsand from New Zealand. All components were supplied by BlueScope Ltd. The major chemical compositions of the raw materials are listed in Table 1. Each raw material component (except the ironsand) was crushed and screened to less than 200 μm. These materials were then mixed in the proportion corresponding to that of BlueScope's bulk sinter blend before the ironsand was added and mixed thoroughly to ensure homogeneity. The final raw material mixture contained: iron ore blend 61.7 wt pct, limestone 9.7 wt pct, dolomite 1.8 wt pct, silica sand 0.1 wt pct, CRF 21.7 wt pct and ironsand 5.0 wt pct. The overall basicity (CaO/SiO_2 mass ratio) of the mixture was 2.0. The final sinter blend was pressed into cylindrical tablets of 5 mm diameter and ~5 mm height for the sintering experiments. Each tablet weighed ~0.3 g.

Table 1. The major chemical compositions of raw materials, wt pct.

Raw material	Total Fe	CaO	SiO_2	Al_2O_3	MgO	TiO_2	Loss on ignition
Iron ore blend	58.46	2.77	5.46	1.67	0.58	0.09	
Limestone	0.15	54.08	1.48	0.35	0.37		43.1
Dolomite	0.58	29.92	1.16	0.28	20.11		46.3
Silica sand	0.49	1.58	92.4	1.71	0.23		1.3
Ironsand*	58.28	0.59	2.34	3.78	3.06	7.95	-2.5

* Based on XRF analysis. Table 2 lists more detailed chemical composition.

2.2 Bench-scale Sintering

A schematic of the sintering apparatus is shown in Figure 1. The setup utilises a vertical tube furnace with a working tube of 55 mm internal diameter through which a gas mixture of controlled composition is continuously passed. A type R thermocouple was inserted from furnace bottom with its tip located below the sample crucible to monitor the sintering temperature. Experiments were conducted at a range of temperatures (1523, 1548, 1573 and 1598 K [1250, 1275, 1300 and 1325 ℃]) typical for iron ore sintering. The gas atmospheres include a 1 pct CO - 24 pct CO_2 - 75 pct Ar mixture which gives an equilibrium pO_2 of $2.9x10^{-6}$ kPa (1523 K [1250 ℃]), $5.9x10^{-6}$ kPa (1548K [1275 ℃]), $1.2x10^{-5}$ kPa (1573 K [1300 ℃]), and $2.3x10^{-5}$ kPa (1598 K [1325 ℃]). A pO_2 of 0.5 and 5 kPa was achieved by mixing Ar and air, and pO_2 of 21 kPa by using air.

To conduct the experiments, the furnace was preheated to a designated temperature, and then purged with the desired gas mixture for at least 20 min. The crucible with the specimen tablet(s) was then placed in the hot zone of the furnace. After sintering for the desired time (between 5 and 20 min), the samples were then rapidly removed from the hot zone to the cool top part of the furnace for quenching in the sintering atmosphere.

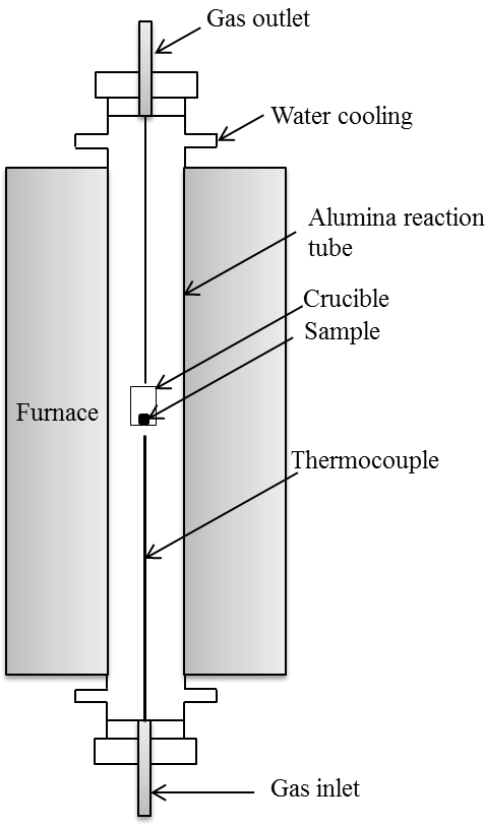

Figure 1. Schematic of the sintering apparatus.

2.3 Characterisation of Raw Materials and Sintered Samples

A detailed structure and compositional analysis of the original ironsand was conducted using combined SEM, XRF, qualitative and quantitative XRD and EPMA techniques. The sintered samples as well as an industrial sinter with the addition of 3 wt pct of ironsand were subjected to optical microscopy and SEM/EDS analysis to observe and characterise the sintering behaviour of the ironsand.

2.3.1 Optical and SEM/EDS Analyses

The sintered samples were mounted in epoxy resin in preparation for optical and SEM analysis. After curing, the basal part of each sample mount was sectioned to expose a fresh surface cross-section. The newly exposed surface was polished to a 1 μm finish for optical microscopic observation (Leica DM6000 Optical Microscope). The polished

sample was then carbon coated prior to analysis by field – emission scanning electron microscopy (FESEM, JEOL JSM – 7001F) operated at 15 kV.

2.3.2 X-Ray Fluorescence (XRF) Spectroscopy

Bulk chemical analysis of the ironsand sample was carried out by XRF. A glass disk was prepared from ~0.4 g of finely ground, oven dried sample powder and ~4 g of 12:22 lithium tetraborate:metaborate flux using standard methods. The resulting glass disc was analysed on a Philips PW2404 XRF system using an ilmenite-specific control program developed by Philips and algorithms developed by CSIRO.

2.3.3 Qualitative and Quantitative Phase Analysis via X-ray Diffraction

Powder X-ray diffraction (XRD) data were collected for the ironsand in Bragg-Brentano geometry using a Philips X'Pert diffractometer, fitted with a Cobalt long-fine-focus tube operated at 40 kV and 40 mA and a curved graphite post-diffraction monochromator. Data were collected over the range $3° \leq 2\theta \leq 140°$ in steps of 0.01°, with a counting time of 5 s at each step. Qualitative phase analysis was carried out using HighScore Plus (Version 3.0.5).[9]

A Rietveld refinement-based approach to quantitative phase analysis (QPA)[10] was performed using TOPAS (Version 4.2).[11] In order to determine the absolute phase concentrations via the QPA, the ironsand sample was mixed with an ultrapure and highly crystalline corundum (α-Al_2O_3; Baikalox Alumina Polishing Powder, Type GE6) internal standard.

2.3.4 Electron Probe Microanalysis (EPMA)

Electron Probe Microanalysis (EPMA) was conducted on the ironsand sample. Two types of EPMA information were obtained. Initially, the ironsand sample was mapped using a high resolution Field Emission Gun (FEG) equipped EPMA (JEOL 8500F Hyperprobe). This was done in order to: 1) determine the distribution of major and

minor mineral phases within the sample[12-13] and, 2) examine the chemical homogeneity of the titanomagnetite grains. Following mapping by FEG-EPMA, the samples were examined by quantitative EPMA techniques using a JEOL 8900 Superprobe to determine the composition of the titanomagnetite grains. The operating conditions for each of the techniques and the instruments are described separately below.

EPMA Mapping

The JEOL Hyperprobe microanalyser used for electron microprobe mapping is equipped with five wavelength dispersive (WD) spectrometers. The sample particles were uniformly dispersed in epoxy resin, mounted into a 25 mm round block and polished flat at a final diamond paste cutting size of 1μm. The polished sample was then carbon coated.

The above prepared sample was mapped over a grid of analysis points covering 2 x 2 mm using a combination of WD and energy dispersive (ED) spectroscopic techniques. The elements mapped using the WD spectroscopic techniques were Fe, Nb, Cr, V and Ti. Standards used to calibrate the EPMA WD spectrometers prior to mapping were: hematite (Fe_2O_3), niobium metal (Nb), rutile (TiO_2), synthetic yttrium vanadate (YVO_4) and synthetic eskolaite (Cr_2O_3). Elements that were not measured by WD spectroscopy were measured using two energy-dispersive (ED) spectrometers operating in parallel. Operating conditions for the microprobe during mapping were an accelerating voltage of 15 kV, a beam current of 100 nA, a step size of 2 μm (in x and y), and a counting time of 30 ms per step. The choice of step size was based on a compromise between maximising the number of particles analysed and ensuring any fine-grained mineral phases were located.

Following mapping, the element distribution data obtained by mapping were manipulated using the software package CHIMAGE[14] which incorporates an automated clustering algorithm that identifies chemically alike phases[15]. These phases were then overlaid onto the mapped region to provide a "phase-patched" map showing the distribution of all chemical/mineral phases within the mapped area.

Quantitative EPMA

Approximately 500 randomly selected Ti-bearing grains were analyzed using a JEOL 8900 Superprobe to assess the distribution of major and minor elements. The analysis position within each grain was also random. For the quantitative analyses, the microprobe was operated at 15 kV and 40 nA and the electron beam defocused to 10 μm (to account for any within-grain inhomogeneity). Counting times were 20 s on the main peak and 10 s on the background. The suite of elements analyzed included Al, Cr, Mn, Mg, Ti, V, Fe, Si and Nb. Oxygen was calculated by difference, based on valence. All analysis positions were verified as being homogeneous and flat by viewing the secondary electron image of the area to be analyzed (at 5000x magnification). Elemental analyses were corrected for atomic number (Z), absorption (A) and fluorescence (F) using the PAP procedure of Pouchou and Pichoir.[16-18]

3. Results

3.1 Characterisation of the Ironsand

3.1.1 Bulk Composition

Table 2 lists the bulk composition of the ironsand as determined by XRF analysis. The ironsand contained 7.95 wt pct TiO_2 and ~83 wt pct Fe_2O_3 (total Fe content equivalent). Major impurities in the bulk concentrate included: Al_2O_3 3.78 wt pct, MgO 3.06 wt pct, SiO_2 2.34 wt pct, V_2O_5 0.607 wt pct, and MnO 0.638 wt pct. The impurities aluminium, vanadium, manganese, and magnesium were typically associated with the titanomagnetite grains, occurring as solid solution components within the lattice. The other impurity elements, including some aluminium, were more typically associated with gangue mineral grains such as aluminosilicates (e.g. pyroxenes, feldspars and clays), quartz and apatite.

Table 2. Summary of XRF assay data and EPMA results (from 508 grains) for the ironsand.

Oxide	XRF Assay†	EPMA titanate dataset‡
TiO_2	7.95	8.54
Fe_2O_3	83.33*	83.35*
Cr_2O_3	0.045	0.072
Nb_2O_5	<DL	0.002
V_2O_5	0.607	0.51
MnO	0.638	0.74
Al_2O_3	3.78	3.48
CaO	0.590	n.d.
MgO	3.06	3.09
SiO_2	2.34	0.272
ZrO_2	0.011	n.d.
P_2O_5	0.077	n.d.
K_2O	0.024	n.d.
ZnO	0.086	n.d.
U (ppm)	20	n.d.
Th (ppm)	<DL	n.d.
Total	102.54	100.06

† Detection limits are 0.005 wt pct except for MgO, Cr_2O_3, U and Th where the detection limits are; 0.01 wt pct, 0.002 wt pct, 10 ppm and 10 ppm, respectively.

‡ data excludes any impurity grains (e.g. quartz, aluminosilicates, etc.) that are present in the sample.

^ n.d. = not determined.

* calculated assuming all Fe is present as Fe^{3+}

3.1.2 Ironsand Morphology

Figures 2 (a) and (b) present two optical micrographs of original ironsand particles. The two morphological types present include homogeneous particles and those with exsolution lamellae, respectively. Cocker *et al.*[1] examined New Zealand ironsands using EPMA and found that homogeneous titanomagnetite particles that were relatively rich in Ti, (containing up to 8.2 wt pct TiO_2), accounted for 90 to 95 vol pct of the ironsands. In the particles exhibiting the exsolution lamellae structure, the lighter regions of variable thickness in a trellis-like pattern were of hematite-ilmenite

composition with an overall high TiO_2 content of 13.1 wt pct, while the titanomagnetite host was relatively low with about 1.5 wt pct TiO_2.

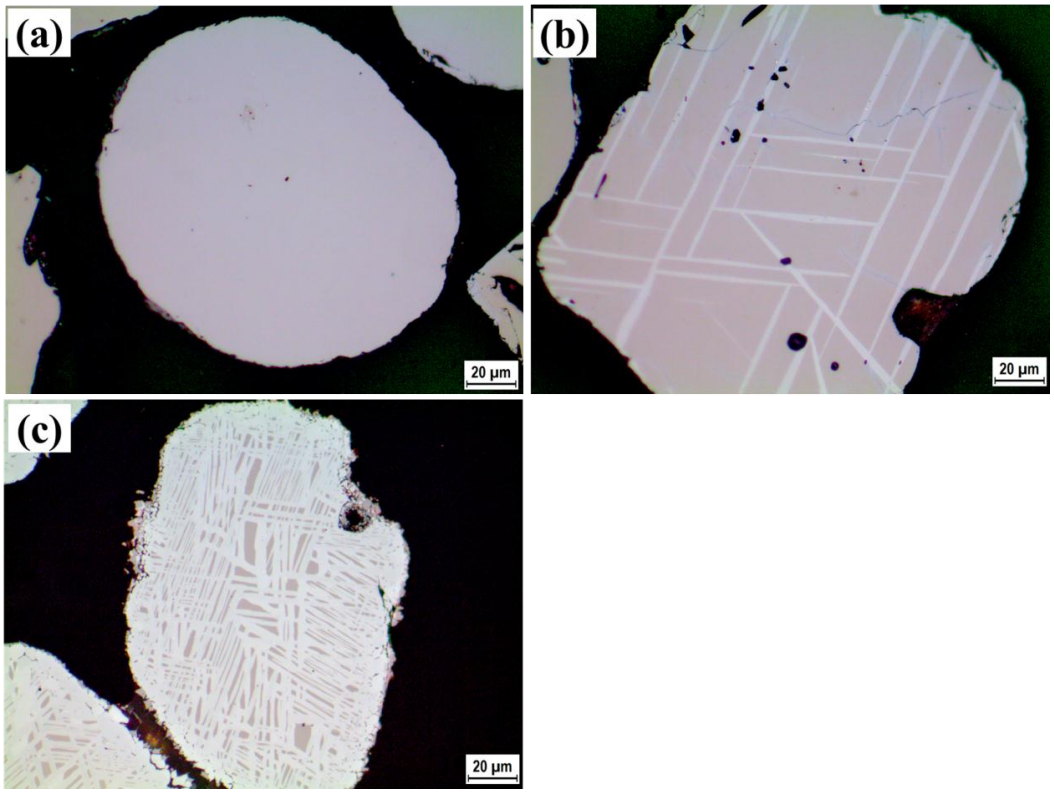

Figure 2. Optical micrographs of typical ironsand particles. Image (a) shows a homogeneous titanomagnetite particle (uniform pink). Image (b) is a titanomagnetite particle with thick hematite-ilmenite (white bands) exsolution lamellae. Image (c) shows that ironsand particles heated in air at 1473K (1200 ℃) for 5 min exhibiting an increase in the amount of exsolution lamellae present.

The optical micrograph of a typical ironsand particle after heating in air at 1473 K (1200 ℃) for 5 min is presented in Figure 2(c). After heating, the coarsened hematite-ilmenite exsolution lamellae were present in the majority of ironsand particles. High-temperature oxidation of Fe^{2+} to Fe^{3+} in titanomagnetite produces vacancies in octahedral sites of the {111} crystal planes, allowing increased diffusion of Ti to these regions which led to the formation of hematite-ilmenite lamellae (1-10 µm) along the original {111} planes of the titanomagnetite host.[19] The extent of oxidation of the titanomagnetite particle is determined by kinetics. Wright[20] reported that virtually complete oxidation of ironsand to titanohematite was achieved on heating in air at 1073 K (800 ℃) for 2 h.

3.1.3 XRD

Qualitative phase analysis showed that the ironsand contained a spinel phase which, based on the EPMA analysis, was designated titanomagnetite, an intermediate member of the isomorphous series of solid solutions of magnetite ($FeFe_2O_4$) and ulvöspinel (Fe_2TiO_4), with a nominal composition of $Fe_{2.75}Ti_{0.25}O_4$ (ICDD card no. 01-075-1374). Peaks for ilmenite ($FeTiO_3$, 29-0733), hematite (Fe_2O_3, 33-0664) and quartz (SiO_2, 33-1161) were also observed. For the Rietveld refinement-based QPA, the crystal structure data of Bosi *et al.*[21], Wechsler and Prewitt[22], Blake *et al.*[23], Lager *et al.*[24] and Brown *et al.*[25] were used for titanomagnetite, ilmenite, hematite, quartz and corundum, respectively. Figure 3 shows the Rietveld refinement output for the ironsand/corundum mixture; the insert shows clearly the peaks from the crystalline phases. The absolute phase abundances were 84.1, 1.7, 3.0 and 0.5 wt pct for titanomagnetite, ilmenite, hematite and quartz, respectively. Therefore, there was 10.7 wt pct unidentified material, comprised mainly of the pyroxene, aluminosilicates, apatite and feldspar phases as identified by EPMA.

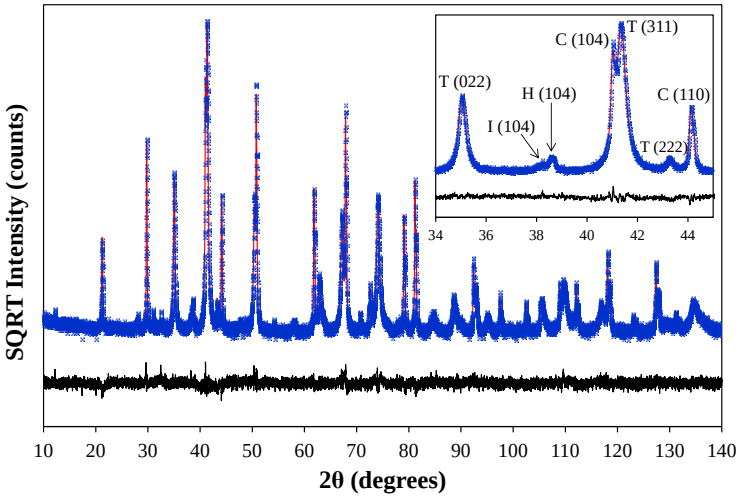

Figure 3. Rietveld refinement fit for the XRD data collected for the ironsand/corundum mixture. Experimental data are shown as crosses, the calculated pattern as a solid line and the difference pattern as a solid line below. R_{wp} = 9.14; R_{exp} = 7.05. The inset shows the range 34° ≤ 2θ ≤ 45°, with reflections from titanomagnetite (T), ilmenite (I) and hematite (H) annotated on the plot. C = the corundum internal standard.

3.1.4 EPMA Mapping

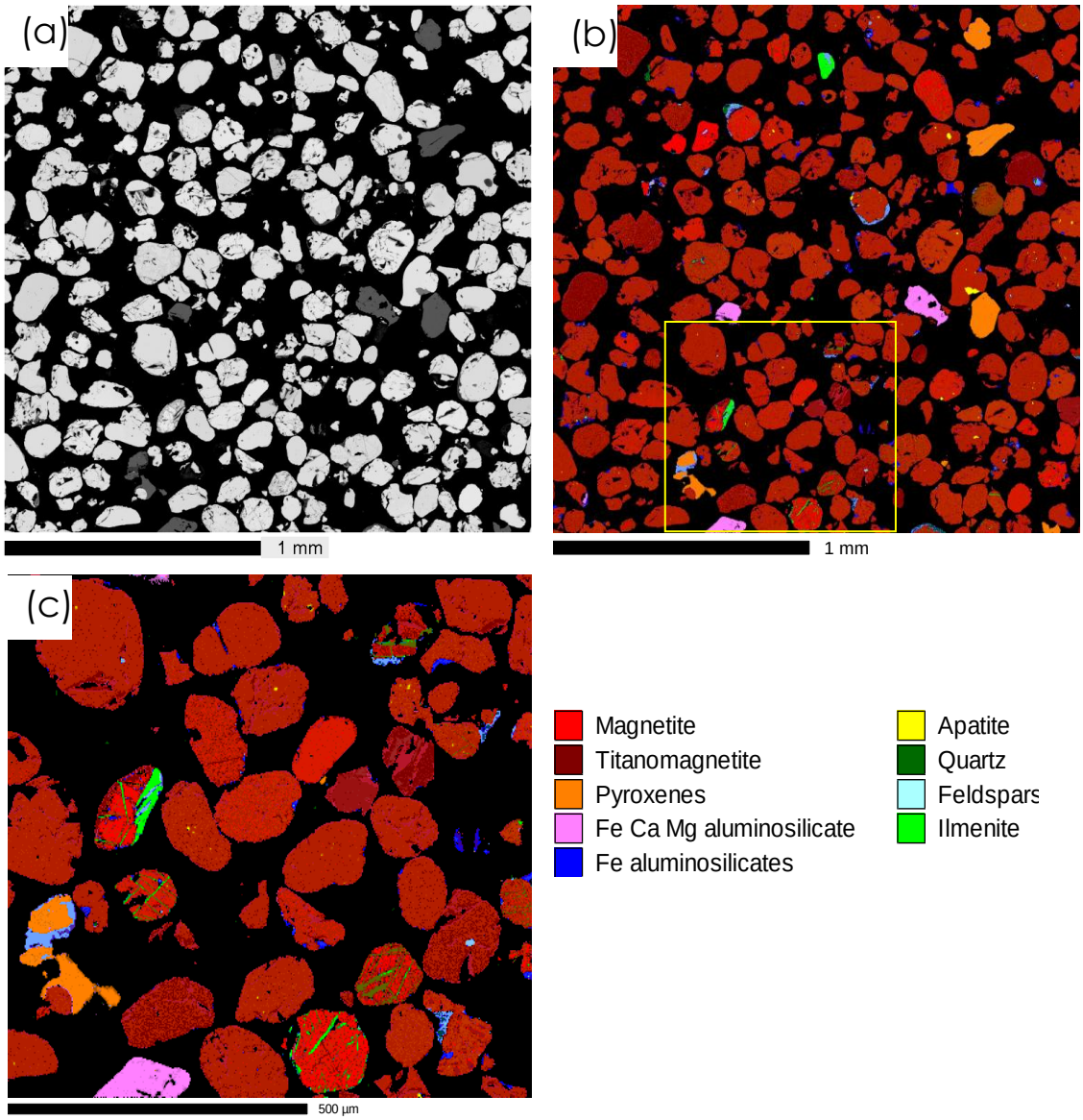

Figure 4. EPMA mapping results for the ironsands. Image (a) is a BSE image of the mapped area. Titanomagnetite grains appear bright in BSE contrast while gangue aluminosilicate grains are darker. Image (b) is the phase distribution map for the area shown in the BSE image. Image (c) is a magnified view (boxed region shown in image (b)) highlighting the Ti-rich lamellae within individual magnetite and titanomagnetite particles.

The results from the EPMA mapping are shown in Figure 4 in the form of (a) a BSE image showing all grains within the mapped area, and (b) a map showing the types and

distribution of phases within the mapped area. Figure 4(c) is a magnified view (boxed region shown in image (b)) highlighting the Ti-rich lamellae within individual magnetite and titanomagnetite particles. The sample comprises >80-85 pct titanomagnetite with associated gangue minerals including ilmenite, pyroxenes (a mixture of enstatite and diopside), unidentified Fe/Ca/Mg and Fe-rich aluminosilicates and minor to trace amounts of quartz, apatite, and feldspar. The majority of gangue mineral grains are largely fully liberated except for the feldspars and Fe-rich aluminosilicate which are present as pore-fill or coatings on titanomagnetite.

3.1.5 Quantitative EPMA

To characterise the composition of the titanomagnetite component of the New Zealand ironsand, quantitative EPMA analyses on individual Ti-rich grains within the sample were undertaken. A comparison of the bulk assay determined via XRF for these samples with the bulk average analyses is provided in Table 2.

To examine variation in the composition of the Ti-rich grains, the EPMA data were plotted on a TiO_2 versus Fe_3O_4 scatter plot (Figure 5). The data lie on an extended composition range from 0 pct TiO_2 (Fe-oxide, magnetite or hematite, dominated compositions) to ~53 pct TiO_2 (ilmenite) with a cluster of data points centered close to 7-8 pct TiO_2 and 83-85 pct Fe_3O_4 corresponding to titanomagnetite. Major impurities within the titanomagnetite grains consisted of, on average, Al_2O_3 3.48 wt pct, MgO 3.09 wt pct, MnO 0.74 wt pct and V_2O_5 0.51 wt pct.

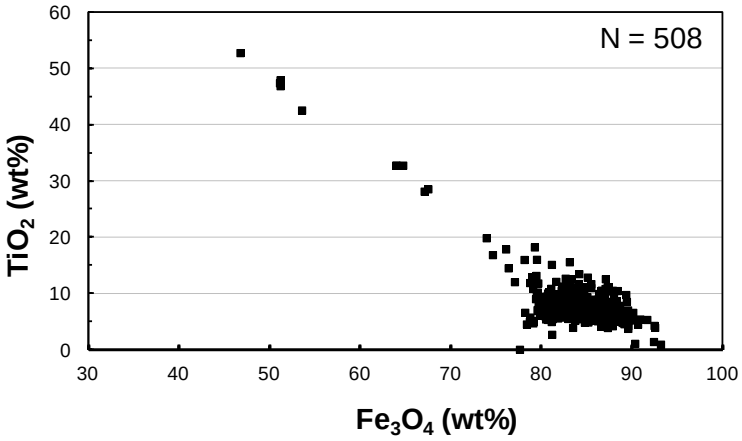

Figure 5. Quantitative EPMA results showing the relationship between Fe_3O_4 and TiO_2 in the Ti-containing grains. Titanomagnetite compositions plot as a cluster centered about 8 wt pct TiO_2, 85 wt pct Fe_3O_4. More Ti-rich compositions represent possible ilmenite and altered titanomagnetite components (alteration is usually associated with leaching of Fe).

3.2 Characterization of Relict Ironsand in Industrial Sinter

Figure 6 presents the optical micrographs of two relict ironsand particles taken from two pieces of an industrial sinter which are assumed to have experienced different sintering conditions. It is known that the temperature and gas atmosphere during the sintering process is far from homogeneous. Generally, during the heating stage, iron oxides adjacent to the coke particles are sintered at a higher temperature and lower oxygen partial pressure, and therefore are easier to reduce to magnetite. In contrast, primary hematite particles present after sintering have remained separated and relatively far from the coke. During the cooling stage, any magnetite particles adjacent to open pores are easily oxidised to secondary hematite, while other materials that are distant from open pores may still be present in an atmosphere of low oxygen potential and remain in their reduced form.[26]

Figure 6(a) shows a typical ironsand particle sintered in a relatively oxidizing atmosphere as indicated by the abundance of secondary hematite in the surrounding solid. The particle can be identified by its characteristic morphology with the internal structure having the typical lamellae texture similar to that given in Figure 2. The

boundary of the ironsand particle however became less distinct with the lamellae-textured core surrounded by a layer of smaller, secondary hematite crystals. The oxidation of the ironsand particle resulted in the development of the coarsened hematite-ilmenite lamellae. Figure 6(b) shows another typical ironsand particle in the industrial sinter, where a clear boundary with surrounding silicate (glass) phase and magnetite crystals can be seen. The lack of hematite and abundance of associated magnetite indicated that the ironsand particle experienced relatively reducing sintering conditions. In this case a magnetite-rich rim was present around the periphery of the ironsand particle as a result of reduction (although this process was not complete as demonstrated by the presence of a more oxidised core region).

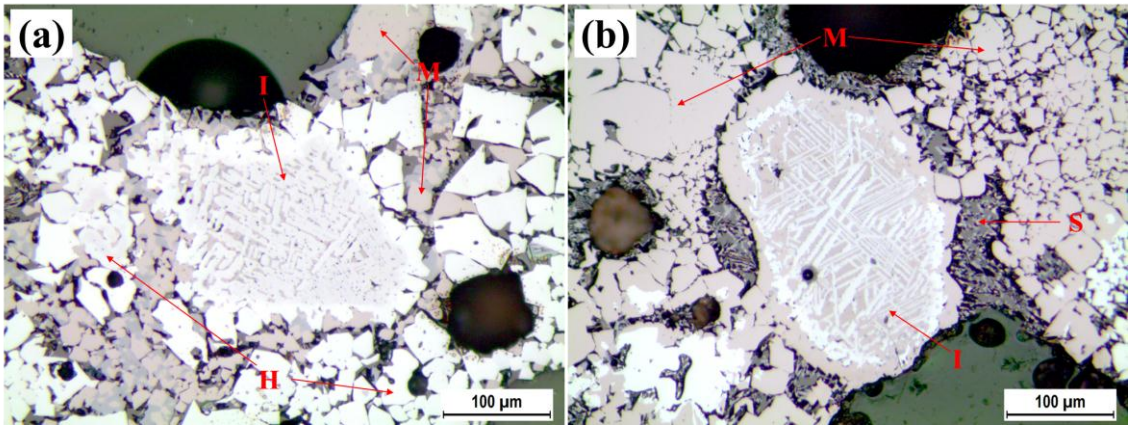

Figure 6. Optical micrographs of two typical relict particles of New Zealand ironsand in the industrial sinter. Image 6(a) indicates a relatively oxidizing environment whereas image 6(b) shows results from a more reducing environment. H: Hematite; M: Magnetite; S: Silicates; I: Ironsand.

Figure 7 shows a BSE image and element distribution maps of a lightly reacted particle of ironsand in industrial sinter. In this example, exsolution took place in the interior of the particle causing enrichment of Ti in the titanohematite phase and incorporation of Mg and Al in the titanomagnetite host. Meanwhile, the periphery was reduced forming a magnetite rim that was richer in iron but had less Ti, Mg, and Al in comparison to the interior. These elements diffused outwards and entered the surrounding silicate phase. Upon solidification, Mg entered into crystallised magnetite leaving a silicate phase with little Mg. It is also noted that a phase rich in Ti and Ca was distributed between the core

of the ironsand particle and its reduced magnetite periphery layer. A phase with a similar composition was observed adjacent to a void in the particle where Ca and Ti contents were high. These small zones were described as being perovskite phase, $CaTiO_3$, incorporating some silica (with Si content 0.4-1.4 wt pct, mostly less than 1 wt pct).

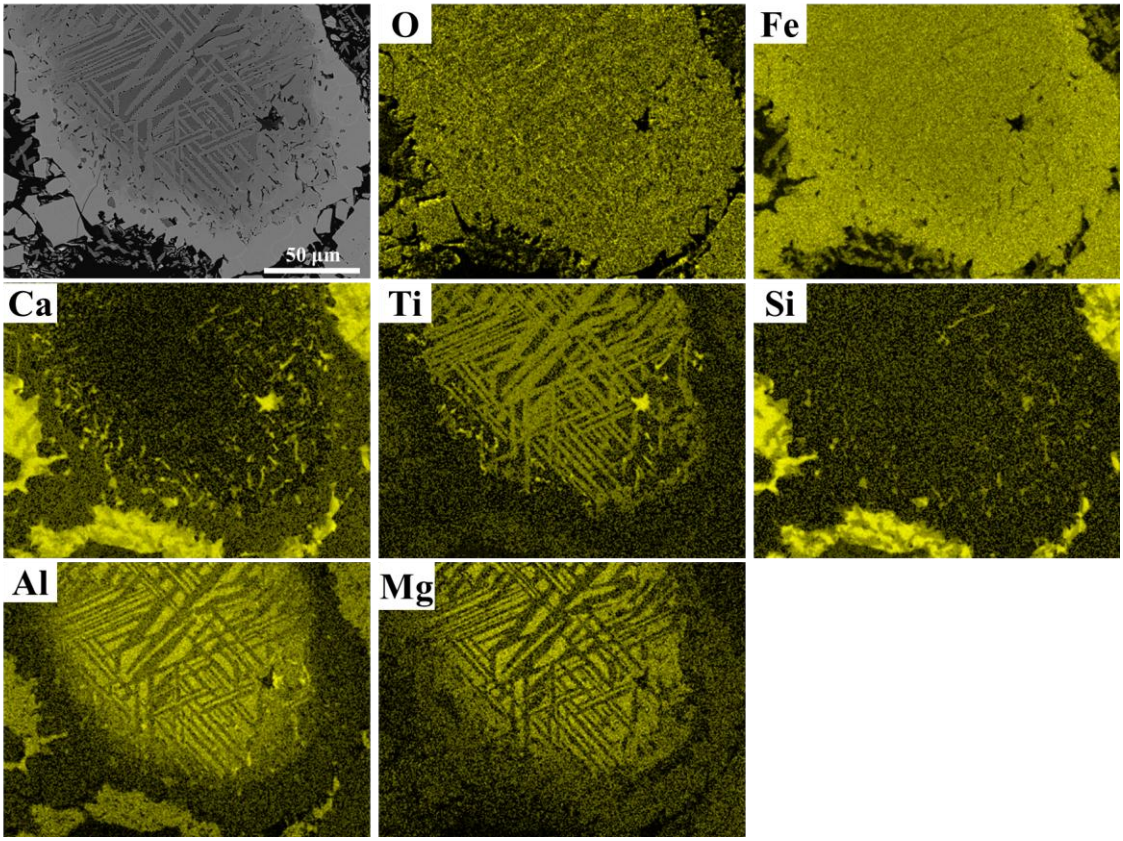

Figure 7. BSE image and EDS mapping of a typical relict ironsand particle in the industrial sinter.

Figure 8 shows a BSE image and element distribution maps from a region of industrial sinter that was distant from relict ironsand particles. The columnar SFCA phase was associated with magnetite and glassy phase in this region. Most Ti was concentrated in the glassy phase. Point analysis by EDS showed that the slag phase consisted of 31.8 wt pct calcium, 17.8 wt pct silicon, 9.83 wt pct iron and 2.97 wt pct titanium. The titanium content in the slag phase was slightly higher than that obtained by Bristow and Loo[4] who used a similar amount of ironsand addition. Mg was concentrated in the magnetite phase but Al was selectively concentrated in the SFCA phase.

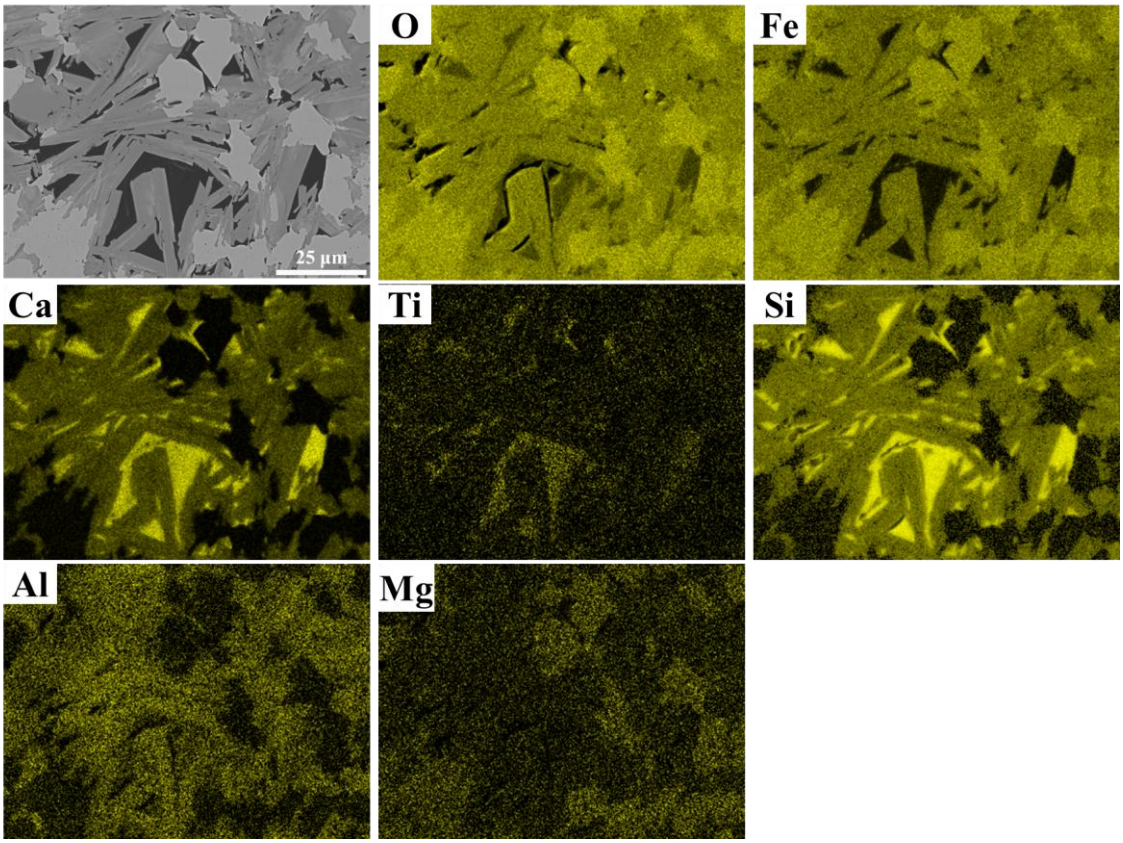

Figure 8. BSE image and EDS mapping of matrix phases in the industrial sinter. The BSE image shows typical textures exhibited by SFCA (medium grey phase), slag (or glass phase – darkest phase, rich in Ca and Si and also with elevated Ti) and magnetite (brightest phase).

3.3 Bench-scale Sintering of Iron Ore Mixes Containing New Zealand Ironsand

To better understand the behaviour of New Zealand ironsand during sintering, an iron ore blend with 5 wt pct of ironsand was sintered under different conditions (i.e. variable T and pO_2) and the specimens examined by optical microscopy and SEM**.** Here, the focus is exclusively on the behaviour of the ironsand during the sintering process. A quantitative examination of the formation of mineral phases will be reported separately.

Figure 9 shows the effect of sintering temperature and gas atmosphere on the extent of sintering. The extent of coalescence of particles in the starting raw mixture increased gradually with increasing sintering temperature.

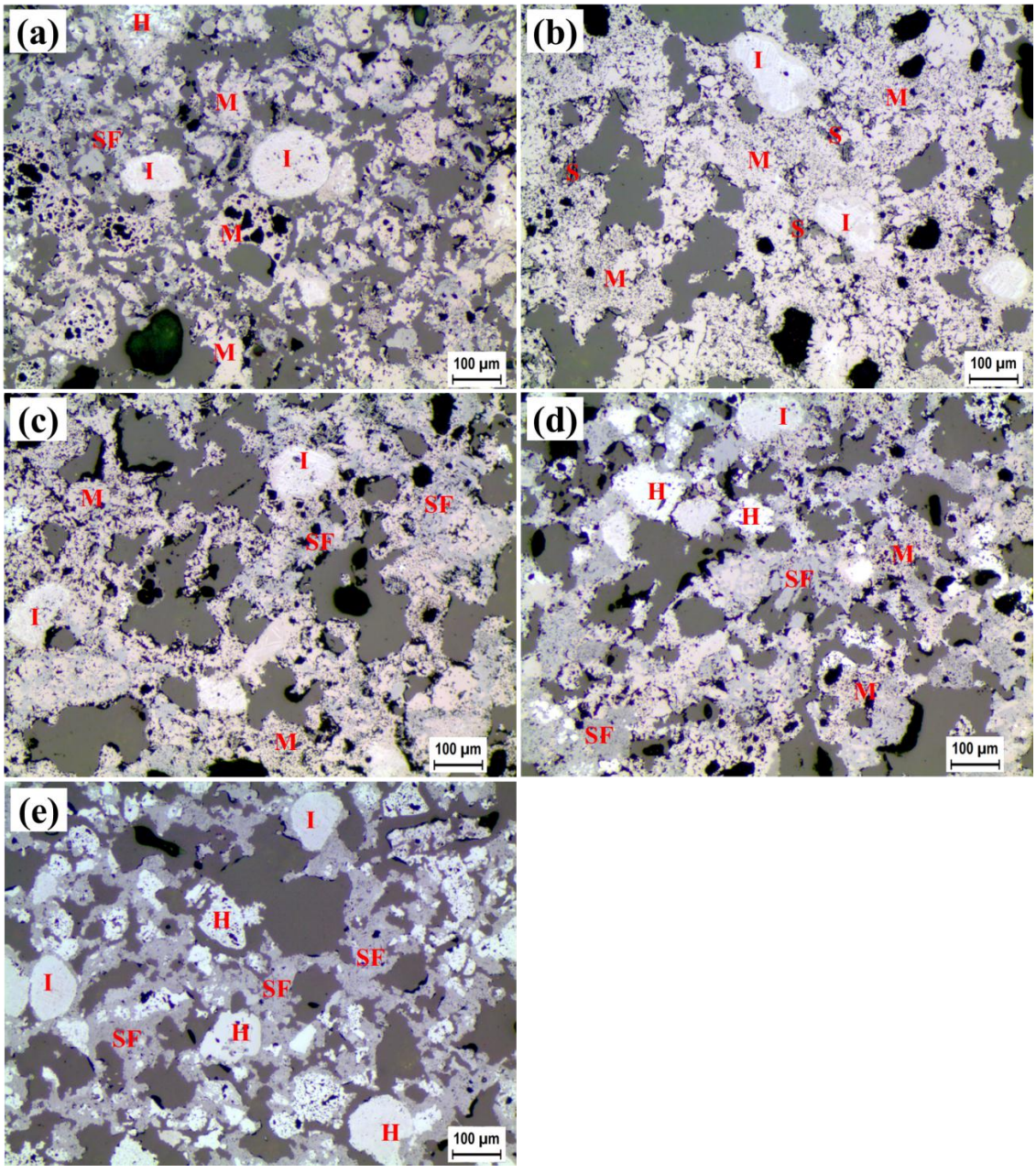

Figure 9. Optical micrographs of specimens sintered for 4 min at different temperatures in various gas atmospheres. H: Hematite; M: Magnetite; SF: SFCA; S: Silicates; I: Ironsand. (a) 1 pct CO, 1523 K (1250 ℃); (b) 1 pct CO, 1573 K (1300 ℃); (c) 0.5 pct O_2, 1573 K (1300 ℃); (d) 5 pct O_2, 1573 K (1300 ℃); (e) Air, 1573 K (1300 ℃).

Figure 9(a) shows the microstructure of a sample sintered at 1523 K (1250 ℃) for 4 min in a gas mixture containing CO 1 pct, CO_2 24 pct, and Ar 75 pct. There was distinct aggregation of the sample and reactions between the fine particles resulted in the generation of SFCA in addition to the reduction of almost all hematite into magnetite. At this temperature the assimilation of oxide materials was incomplete, leaving a large proportion of only partially reacted iron ore and flux particles. Secondary magnetite crystals which were segregated from melt phase were rarely found in the specimen. The major change of the ironsand was exsolution of a titanohematite phase to form the lamellae texture. Interaction of the ironsand particles with other components was also not obvious.

When the sintering temperature was increased to 1573 K (1300 ℃) (Figure 9(b)), it was found that more significant aggregation of fine particles took place, forming fewer but larger pores. The specimen was dominated by polycrystalline magnetite distributed in a continuous silicate matrix. As expected, no SFCA was observed in the specimen. A layer on the periphery of the ironsand particles was reduced to magnetite with which assimilation took place and caused some boundaries to become vague. Figures 9(c-e) present the microstructure of samples heated at 1573 K (1300 ℃) for 4 min in the gas atmospheres with pO_2 = 0.5, 5 and 21 kPa, respectively. Consistent with the recent results of Webster *et al*.[27,28], increasing O_2 partial pressure resulted in more SFCA. In the sample sintered in air (Figure 9(e)), SFCA was the dominant phase with significant amounts of hematite. Magnetite was rarely observed under these conditions. In all of the samples, ironsand boundaries were clearly visible although intimately bonded with surrounding phases.

Figure 10 consists of four optical reflected light images of typical ironsand particles in samples sintered under the different conditions. The morphology of the relict ironsand particle in the sample sintered at 1523 K (1250 ℃) in a gas atmosphere with pO_2 = 0.5 kPa for 20 min (Figure 10(a)) was similar to that in the industrial sinter shown in Figure 6(b). The ironsand particles were reduced in the periphery and bonded with surrounding magnetite without complete assimilation. Increasing sintering temperature to 1573 K (1300 ℃) resulted in complete reduction of the titanohematite phase because

the lamellar texture completely disappeared. Only the contour of the ironsand particles could be identified (the oval in Figure 10(b)).

Different morphologies of ironsand particles can be found in samples sintered in air, as shown in Figures 10 (c) and (d). In these experiments, the presence of the ironsand particles is much easier to identify due to remaining titanohematite lamellae structure, although the bonding between them and surrounding oxides increased with increasing sintering temperature. As shown in Figure 10(d), a significant amount of SFCA phase was formed at 1573 K (1300 ℃) in air, although no SFCA phase was detected in a mixture with 0.5 pct O_2 at the same temperature.

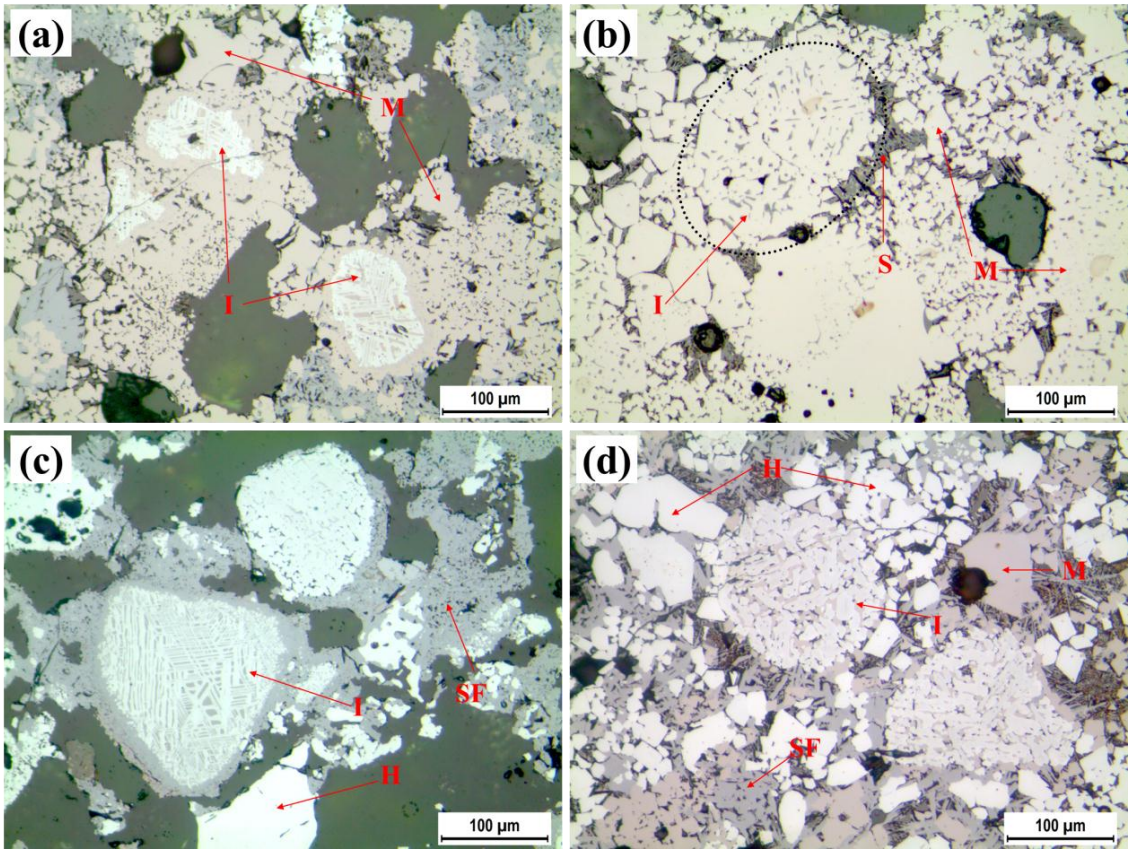

Figure 10. Optical micrographs of typical ironsand particles in specimens sintered at different temperatures for 20 min in different gas atmospheres. (a) 0.5 pct O_2, 1523 K (1250 ℃); (b) 0.5 pct O_2, 1573 K (1300 ℃); (c) Air, 1523 K (1250 ℃); (d) Air, 1573 K (1300 ℃).

Figure 11 shows a typical ironsand particle in the sample heated at 1523 K (1250 ℃) for 20 min in a gas atmosphere with pO_2 = 0.5 kPa. A reaction zone, which contained a high level of Ca and Ti and a relatively low level of Fe between the core with the characteristic lamellae structure and the reduced magnetite periphery layer, was established. This zone was similar to that observed in the industrial sinter shown in Figure 7, but with a more established intermediate layer which was attributed to the extended sintering time that allowed more CaO diffusion into the particle interior.

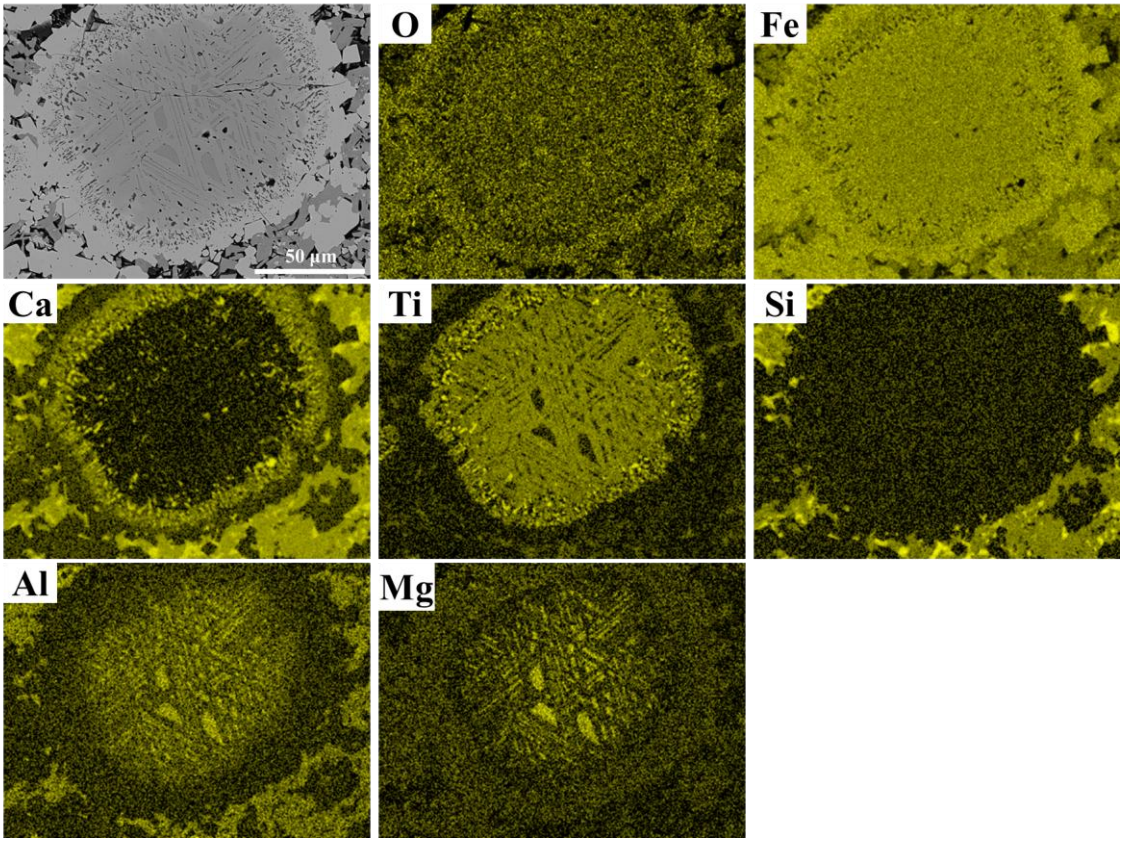

Figure 11. BSE image and EDS mapping of a typical relict ironsand particle in a specimen sintered at 1523 K (1250 ℃) for 20 min in the gas atmosphere with pO_2 = 0.5 kPa.

A detailed EDS analysis across the reaction zone of the same ironsand particle was performed. The compositions of different points presented in Figure 12 across the reaction zone and beyond are listed in Table 3. Points 1 and 2 represent the phase composition of the Ti-lean titanomagnetite matrix and the Ti-rich hematite-ilmenite lamellae within the relict ironsand, respectively. The dark, finely distributed areas

within the reaction zone as represented by points 3 and 4 were identified to be a complex perovskite phase containing Fe in addition to CaO and TiO_2 which was also found in Figure 7. Point 5 was from the magnetite rim of the ironsand particle which characteristically contained some CaO and MgO. Additional phases surrounding the ironsand particle included silicate glass (points 6 and 7), secondary magnetite (point 8) and SFCA (points 9 and 10). Besides in the relict ironsand particle, titanium was also found in the silicate phase (3-4 wt pct) and SFCA (about 0.5 wt pct) in close proximity to the relict ironsand particle.

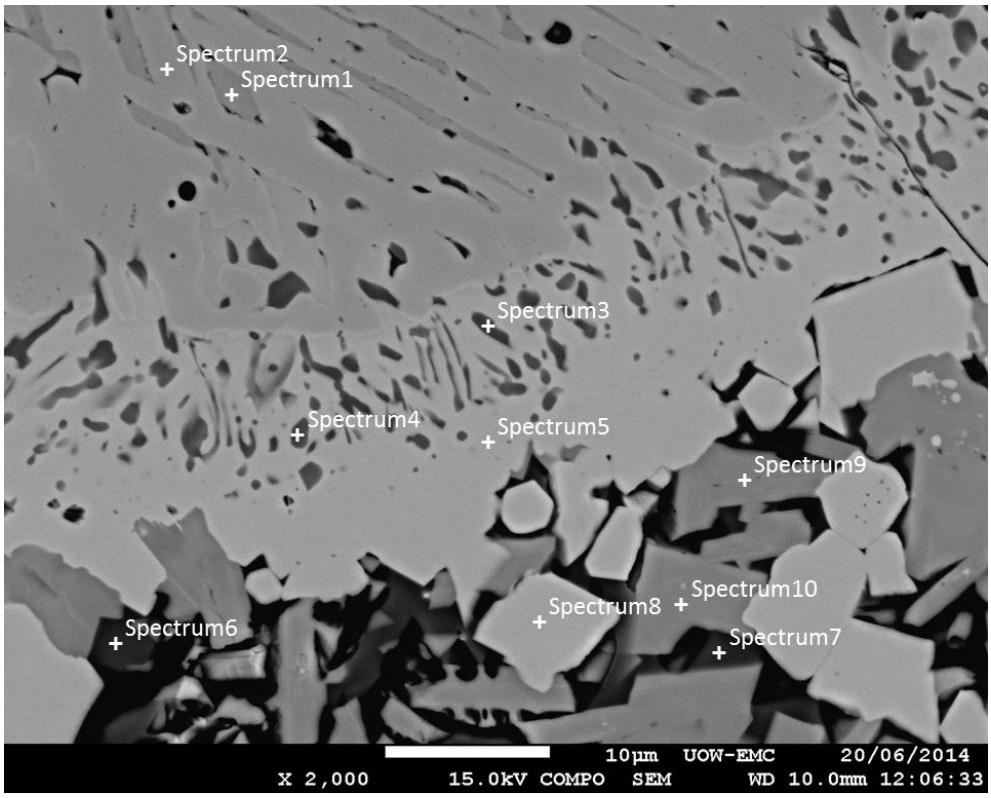

Figure 12. The BSE image of the reaction zone of a typical ironsand particle in a sample heated at 1523 K (1250 ℃) for 20 min in the gas atmosphere with pO_2 = 0.5 kPa.

Table 3. Elemental composition (wt pct) of grains marked in Figure 12 and corresponding phases.

Point no.	Fe	Ca	Ti	Si	Al	Mg	Phase identified
1	64.7	0.3	1.1	0.1	4.5	4.2	Titanomagnetite
2	64.2	0.1	6.6	0.1	1.9	1.2	Titanohematite
3	19.9	21.7	23.1	0.2	0.4	0.1	Perovskite
4	27.1	19.4	19.4	0.1	0.4	0.3	Perovskite
5	72.2	1.6	0.3	0.1	0.8	1.2	Magnetite
6	12.2	30.1	3.4	16.2	2.9	0.2	Silicate (glass)
7	13.7	29.3	4.1	15.8	2.0	0.1	Silicate (glass)
8	74.5	0.9	0.2	0.1	0.7	1.2	Secondary magnetite
9	54.2	10.9	0.7	3.4	3.0	0.4	SFCA
10	55.1	10.8	0.5	3.3	2.8	0.4	SFCA

It was recognised that during sintering, when the solid CaO or a silicate melt was in contact with an ironsand particle, TiO_2 diffused outwards while CaO diffused towards the center of the particle. When the CaO was accumulated to some concentration, it combined with TiO_2 due to their chemical affinity[29] to form the perovskite phase that was finely distributed in the reaction zone of an ironsand particle. The ironsand surface was attacked by the silicate melt and gradually dissolved into the melt. On cooling, secondary magnetite or SFCA phase was segregated from the melt phase making the particle boundary ambiguous.

Figure 13 shows the BSE image and EDS mapping of a typical relict ironsand particle in a specimen sintered at 1573 K (1300 ℃) for 20 min in a gas atmosphere with pO_2 = 0.5 kPa. On the BSE image, the ironsand particle can only be identified by its rounded contour and texture, although the boundary had substantially disappeared. However, the presence of perovskite phase as characterised by bright dots on the Ti distribution gave evidence that it was an ironsand particle. Silicate melt penetrated into the matrix of ironsand particles, which enhanced their assimilation. The glass phase present inside the ironsand particle had a similar composition to that outside, containing about 3.5 wt pct of Ti. In comparison, the magnetite matrix of the ironsand relict contained less than 0.2

wt pct of Ti. The dispersed perovskite phase remaining in the core of the ironsand relict showed that the assimilation of the ironsand particle was not complete.

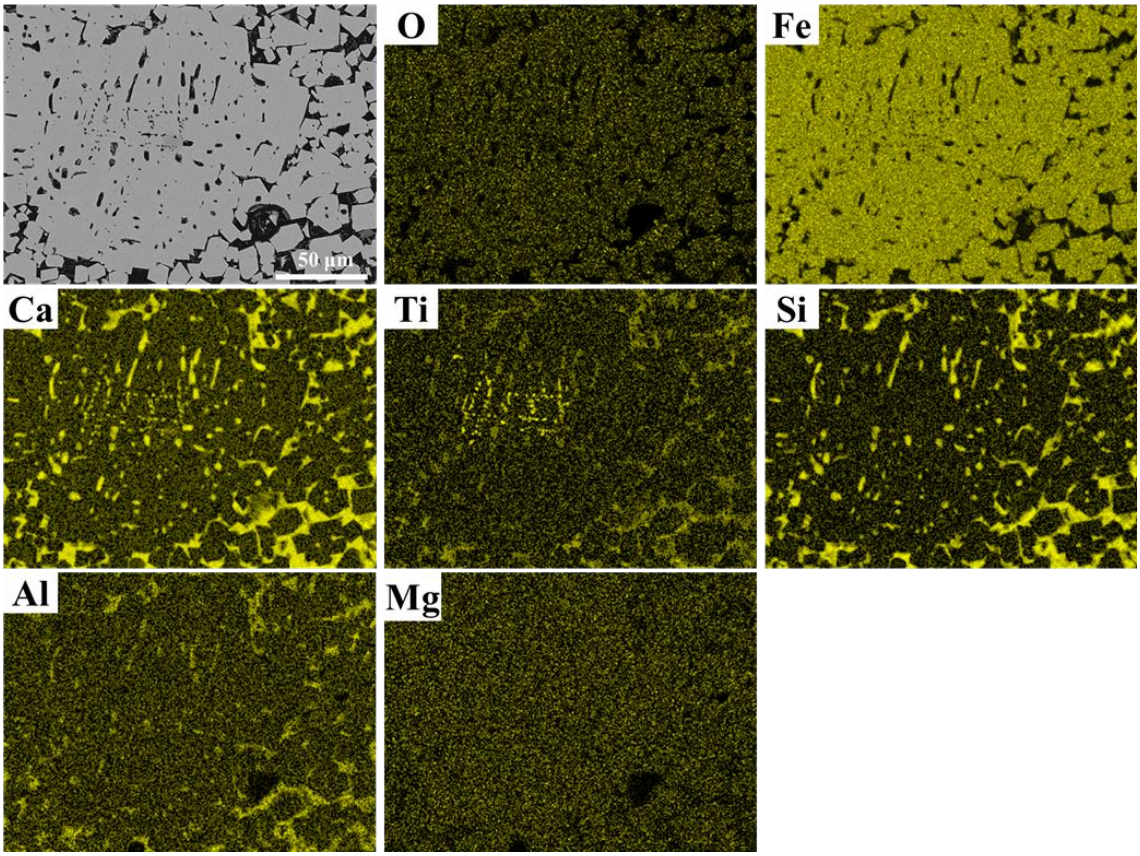

Figure 13. BSE image and EDS mapping of a typical relict ironsand particle in a specimen sintered at 1573 K (1300 ℃) for 20 min in a gas atmosphere with pO_2 = 0.5 kPa.

Figure 14 presents the BSE image and the distribution of the main elements Fe, Ca, Ti, Mg and Al of an ironsand particle in a specimen sintered in air at 1573 K (1300 ℃) for 20 min. The distribution of Si appeared identical to that of Ca. Unlike the sample sintered under otherwise the same conditions but lower pO_2 (Figure 13), the assimilation of ironsand with other oxides was limited. Penetration of Ca reached the center of the particle but it was only distributed in the finely fragmented areas associated with Si, Al and less iron which belong to silicate and SFCA phases. There were two phases with the lamellae structure of ironsand particle, as indicated by the Ti rich and Mg rich lamella which were titanohematite and titanomagnetite, respectively. There also existed secondary hematite and magnetite, SFCA and silicate phases around the relict ironsand

particle, and only 0.5 wt pct titanium was present in the silicate phase. There was no reaction zone containing dispersed Ca and Fe perovskite phase as was found in ironsand particles sintered in the reducing atmosphere (Figures 11 and 13). In a high oxygen partial pressure atmosphere, the reductive melting of SFCA was suppressed[27] and TiO_2 was stabilised in the titanohematite phase which also inhibited transfer of Ti out of the ironsand particles.

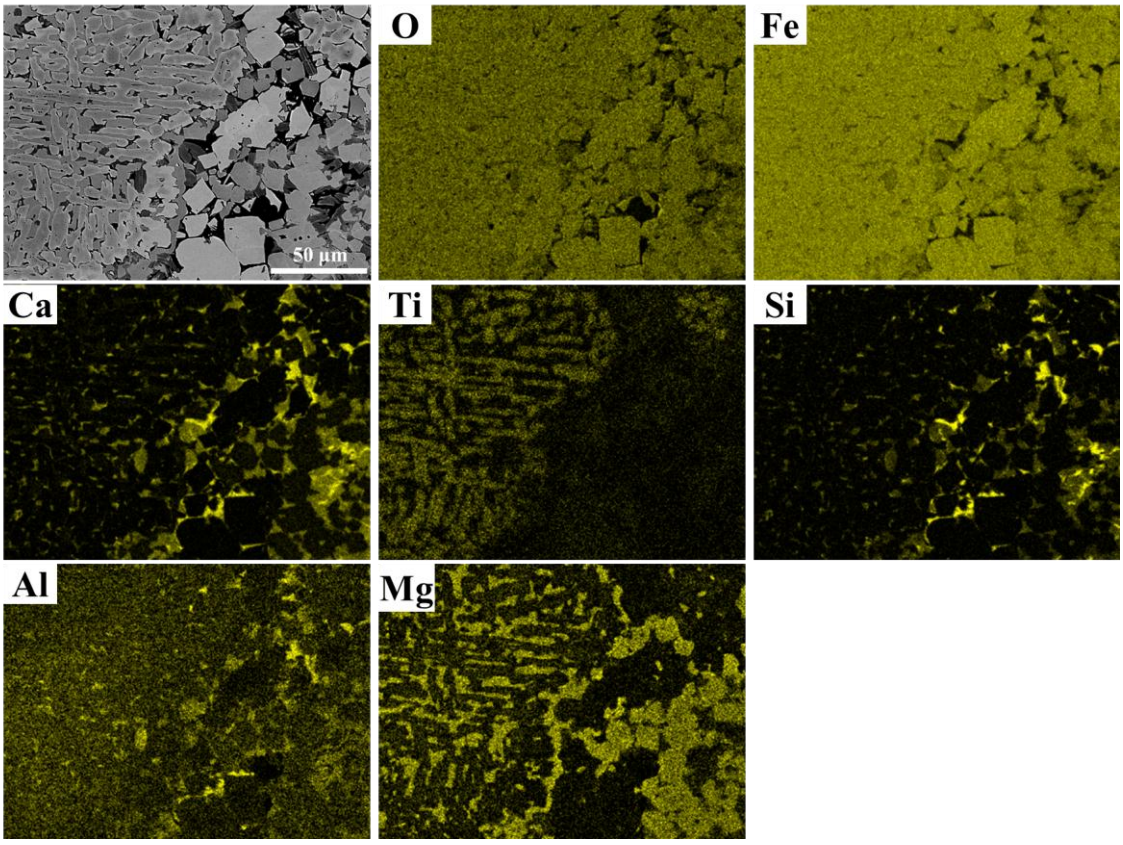

Figure 14. BSE image and EDS mapping of a typical relict ironsand particle in a specimen sintered at 1573 K (1300 ℃) for 20 min in air.

4. Discussion

In an industrial iron ore sintering process, ironsand particles experience heating, solid reaction, melting and cooling phenomena. The detailed behaviour of an ironsand particle depends on the solid particles in contact with it, as well as the heating history

and the prevailing gas atmosphere. Due to the changes of conditions as sintering progresses, the particles also behave differently during sintering.

New Zealand ironsand is primarily present in a titanomagnetite form. Depending on the oxygen potential of the surrounding atmosphere when it is heated, formation of titanohematite exsolution texture can take place to different extents. Along with this process, elemental redistribution takes place. It was observed in SEM images that Ti tended to concentrate in the titanohematite phase while its content in the titanomagnetite became lower. In contrast, Al and Mg were selectively concentrated in the titanomagnetite phase (Figures 7, 11 and 14).

When the oxygen potential was low enough, the titanohematite phase decomposed to magnetite while Ti was segregated from the phase. According to SEM analysis results (Figure 12 and Table III), the Ti content in the magnetite rim formed from an ironsand particle was only 0.25 wt pct. Ti was either combined with Ca diffused from outside particles to form a perovskite phase, or diffused into the adjacent silicate phase.

Although the ironsand particles are small, they generally retained their shape after both industrial and laboratory sintering, illustrating that they are more resistant to high temperature sintering reactions than traditional iron ores. This is especially true for particles which experienced high oxygen potential conditions (Figure 14) where lack of assimilation was particularly obvious and most of the Ti remained in the original ironsand particles. In comparison, ironsand particles which experienced more reducing conditions underwent more assimilation during sintering.

The investigation of the phase formation during sintering[27] showed that the formation and melting of a low melting point phase $CaFe_2O_3$ promoted further sintering by enhanced mass transfer between solid and liquid phases. Although the diffusion of Ca^{2+} to Fe_3O_4 decreased the melting point of Fe_3O_4, Ti existing in the lattice of ironsand can stabilise the system of $CaO\text{-}TiO_2\text{-}FeOx$[30] and hinder further dissolution of the ironsand particles. This is illustrated in Figure 15 where the $CaO\text{-}TiO_2\text{-}FeOx$[30] phase diagram indicates that the liquidus temperature increases gradually with the introduction of TiO_2

along the tie-line from CaO·Fe_2O_3 (initial melt in iron ore sintering mainly originated from the formation of calcium ferrite) to CaO·TiO_2 (blue line in Figure 15).

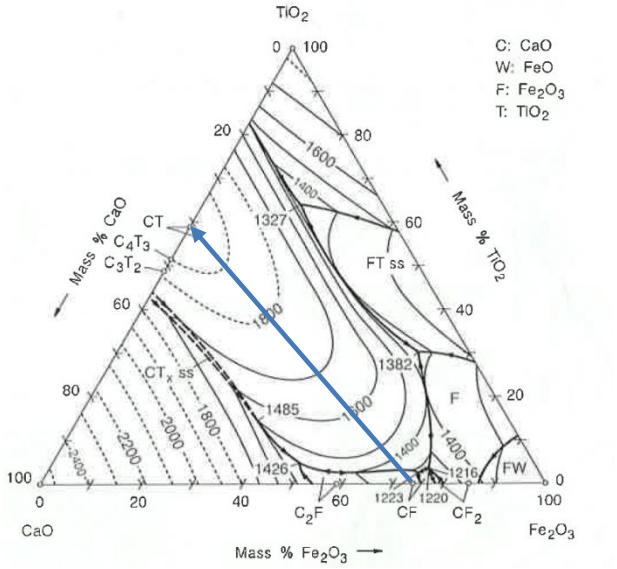

Figure 15. Liquidus temperature of CaO-TiO_2-FeOx system.[30]

During cooling, the molten phase segregates into different phases. It is shown in Figures 13 and 14 that Ti preferably remained in the glass phase, while its content in the secondary magnetite, hematite and SFCA were relatively low. This was also confirmed by the elemental distribution in an industrial sinter as presented in Figure 8.

5. Conclusion

In this study, detailed characterization of a raw New Zealand ironsand concentrate and relict ironsand particles in an industrial sinter with 3 wt pct ironsand was conducted. Following these characterization studies, bench-scale sintering experiments were carried out to investigate in detail, the behaviour of ironsand during sintering to gain a better understanding of the sintering performance of titanomagnetite. The main results obtained are as follows.

(1) Ironsand had greater resistance to assimilation than traditional iron ores.

(2) The relict ironsand particles in industrial sinter presented varied morphologies due to the spatial non-uniformity of sintering conditions. These can be well simulated by bench-scale sintering experiments, since the range of bench-scale experimental conditions employed in this study have been shown to produce relict ironsand morphologies consistent with the industrial sinter.

(3) A relatively reducing atmosphere promoted the assimilation of ironsand into a liquid phase. The assimilation of ironsand during sintering in a reducing atmosphere started from the diffusion of calcium from the sinter blend into the lattice of the ironsand matrix. This in turn further decreased the melting point of titanomagnetite and accelerated the assimilation rate of ironsand particles. A reaction zone was formed near the boundary within ironsand particles where a perovskite phase was generated as a result of the reaction between TiO_2 and CaO.

(4) When sintering at higher temperatures in a reducing atmosphere, ironsand particles underwent more assimilation. Along with the progress of assimilation, Ti in the perovskite phase was redistributed into glass and magnetite phases with the concentration in the former significantly higher than in the latter.

(5) More Ti remained in original ironsand particles in a relatively oxidizing atmosphere, which was attributed to the high oxygen partial pressure suppressing the melting of SFCA and stabilizing TiO_2 in titanohematite.

Acknowledgements

The project is financially supported by the BlueScope Steel Metallurgical Centre. Zhe Wang is a recipient of University of Wollongong Deputy Vice Chancellor's Special Scholarship and International Postgraduate Tuition Award. Steve Peacock and Barry Halstead of the CSIRO are acknowledged for their XRF and XRD measurements. This research used FESEM JEOL JSM-7001F funded by the Australian Research Council (ARC) – Linkage, Infrastructure, Equipment and Facilities (LIEF) grant (LE0882613) located at the UOW Electron Microscopy Centre.

References

[1] H. A. Cocker, J. L. Mauk, H. Rogers, A. B. Padya and J. Ogiliev, Where is the Titanium in the Ironsands? - Ti Partitioning in the Magnetic Fraction, Proceedings of the AusIMM New Zealand Branch 43rd Annual Conference, AusIMM New Zealand Branch, Alexandra, (2010), 165-174.

[2] J. B. Wright, Iron-titanium Oxides in Some New Zealand Ironsands, *New Zealand Journal of Geology and Geophysics*, **7** (1964), 424-444.

[3] J. B. Wright and J. F. Lovering, Electron-probe Micro-analysis of the Iron-titanium Oxides in some New Zealand Ironsands, *Mineralogical Magazine*, **35** (1965), 604-621.

[4] N. J. Bristow and C. E. Loo, Sintering Properties of Iron Ore Mixes containing Titanium. *ISIJ International*, **32** (1992), 819-828.

[5] I. F. Carmichael and J. Lowering, *Steel Times*, **209** (1981), 416.

[6] Y. Li, Y. Li, and R. J. Fruehan, Formation of Titanium Carbonitride from Hot Metal, *ISIJ International*, **41** (2001), 1417-1422.

[7] T. Paananen and K. Kinnunen, The Effect of Titanium on Reduction Degradation of Iron Ore Agglomerates, Iron Ore Conference 2007, AusIMM, (2007), 361-376.

[8] Z. Yin, J. Li and S. Yang, Sintering Pot Test on Improving TiO_2-containing Ore's Allocated Proportion, *Advanced Materials Research*, **311-313** (2011), 850-853.

[9] PANalytical HighScore Plus Version 3.0.5, PANalytical B. V., Almelo, The Netherlands, (2012).

[10] I. C. Madsen and N. V. Y. Scarlett, Powder Diffraction: Theory and Practice, edited by R. E. Dinnebier and S. J. L. Billinge, Royal Society of Chemistry, Cambridge, (2008), 298-331.

[11] Bruker, TOPAS Version 4.2, Bruker AXS Inc., Madison, Wisconsin, USA, (2009).

[12] M. I. Pownceby, C. M. MacRae and N. C. Wilson, Electron Microprobe Mapping – a Diagnostic Tool for Ilmenite Characterisation, International Heavy Minerals Conference, AusIMM, Fremantle, (2001), 69-74.

[13] M. I. Pownceby, C. M. MacRae and N. C. Wilson, Mineral Characterisation by EPMA Mapping, *Minerals Engineering*, **20** (2007), 444-451.

[14] I. R. Harrowfield, C. M. MacRae and N. C. Wilson, Chemical Imaging in Electron Microprobes, Proceedings of the 27th Annual MAS Meeting, Microbeam Analysis Society, New York, (1993), 547-548.

[15] N. C. Wilson and C. M. MacRae, An Automated Hybrid Clustering Technique Applied to Spectral Data Sets, *Microscopy and Microanalysis*, **11** (2005), 434-435.

[16] J. L. Pouchou and F. Pichoir, A New Model for Quantitative X-ray Microanalysis. Part 1: Application to the Analysis of Homogeneous Samples, *La Recherche Aérospatiale*, **3** (1984), 13-38.

[17] J. L. Pouchou and F. Pichoir, "PAP", Procedure for Improved Quantitative Microanalysis, Microbeam Analysis Proceedings, edited by J. T. Armstrong, San Francisco Press, San Francisco, (1985), 104-106.

[18] J. L. Pouchou and F. Pichoir, Quantitative Analysis of Homogeneous or Stratified Microvolumes Applying the Model "PAP", Electron Probe Quantitation, edited by K. F. J. Heinrich and D. E. Newbury, Plenum Press, New York, (1991) 31-75.

[19] M. B. Turner, S. J. Cronin, R. B. Stewart, M. Bebbington and I. E. M. Smith, Using Titanomagnetite Textures to Elucidate Volcanic Eruption Histories, *Geology*, **36** (2008), 31-34.

[20] J. B. Wright, Heating Experiments on New Zealand Ironsands and the Presence of Pseudobrookite, *New Zealand Journal of Geology and Geophysics*, **10** (1967), 659-665.

[21] F. Bosi, U. Halenius and H. Skogby, Crystal Chemistry of the Magnetite-ulvöspinel Series. *American Mineralogist*, **94** (2009), 181-189.

[22] B. A. Wechsler and C. T. Prewitt, Crystal Structure of Ilmenite ($FeTiO_3$) at High Temperature and at High Pressure, *American Mineralogist*, **69** (1984), 176-185.

[23] R. Blake, R. Hessevick, T. Zoltai and L. Finger, Refinement of the hematite structure, *American Mineralogist*, **51** (1966), 123-129.

[24] G. A. Lager, J. D. Jorgensen and F. J. Rotella, Crystal Structure and Thermal Expansion of α-quartz SiO_2 at Low Temperature, *Journal of Applied Physics*, **53** (1982), 6751-6756.

[25] A. S. Brown, M. A. Spackman and R. J. Hill, The Electron Distribution in Corundum. A Study of the Utility of Merging Single-crystal and Powder Diffraction Data, *Acta Crystallographica Section A*, **49** (1993), 513-527.

[26] A. K. Biswas, Principles of Blast Furnace Ironmaking: Theory and Practice, Cootha Publishing House, Brisbane, (1981), 194.

[27] N. A. S. Webster, M. I. Pownceby, I. C. Madsen and J. A. Kimpton, Effect of Oxygen Partial Pressure on the Formation Mechanisms of Complex Ca-rich Ferrites, *ISIJ International*, **53** (2013), 774-781.

[28] N. A. S. Webster, M. I. Pownceby, I. C. Madsen, A. J. Studer, J. R. Manuel and J. A. Kimpton, Fundamentals of Silico-Ferrite of Calcium and Aluminum (SFCA) and SFCA-I Iron Ore Sinter Bonding Phase Formation: Effects of CaO: SiO_2 Ratio, *Metallurgical and Materials Transactions B*, **45** (2014), 2097-2105.

[29] M. Binnewies and E. Milke, Thermochemical Data of Elements and Compounds, 2nd edition, Wiley-VCH Verlag GmbH, Weinheim, (2002).

[30] K. C. Mills, Slag Atlas, 2nd edition, Verlag Stahleisen GmbH, D-Düsseldorf, (1995), 131.

CHAPTER 3. EFFECT OF SINTERING CONDITIONS ON THE FORMATION OF MINERAL PHASES DURING IRON ORE SINTERING

Effect of Sintering Conditions on the Formation of Mineral Phases during Iron Ore Sintering

Zhe Wang[1], David Pinson[2], Sheng Chew[2], Brian J. Monaghan[1], Mark I. Pownceby[3], Nathan A.S. Webster[3], Harold Rogers[2], Guangqing Zhang[1]

1. School of Mechanical, Materials and Mechatronic Engineering, University of Wollongong, NSW 2522, Australia
2. BlueScope Technology and Planning, P.O. Box 202 Port Kembla, NSW 2505, Australia
3. CSIRO Mineral Resources Flagship, Private Bag 10, Clayton South, VIC 3169, Australia

Abstract

Silico-ferrites of calcium and aluminium (SFCA and SFCA-I) are desirable phases in a high quality iron ore sinter product. The effects of temperature, CaO/SiO_2 ratio, sintering gas atmosphere and cooling procedure on the phase composition of sintered specimens from an industrial sinter blend were examined with focus on the formation of SFCA phases. The proportions of mineral phases in specimens sintered at 1250 - 1325℃ were quantitatively examined using image analysis. Although SFCA and SFCA-I can be formed at low temperatures by solid state reactions, they are most likely to be formed by crystallization of the silicate melt in a relatively oxidising gas atmosphere in an industrial sintering process. Maintaining a high oxygen partial pressure favours the formation of SFCA and SFCA-I, either via solid state reactions or from a melt. This is attributed to hematite being available as a reactant for SFCA formation. Similarly, increasing CaO/SiO_2 ratio provides more CaO as a reactant for SFCA formation and promotes its formation.

Key words: Sintering, Iron ore, Silico-ferrites of calcium and aluminium, phase composition

1. Introduction

In industrial iron ore sintering, the combustion of coke breeze supplies the necessary heat to achieve partial melting of raw materials. It also produces a locally relatively reducing atmosphere within the sinter bed during the heating stage. Once the peak temperature has been reached, the agglomerated semi-molten material then slowly cools under an atmosphere with higher partial pressure of oxygen [1, 2]. The final sinter mainly contains primary and secondary hematite, magnetite, complex calcium-rich ferrite(s) and glassy silicate phases. Their relative proportion depends on the sintering conditions, such as temperature, sinter mix composition, oxygen partial pressure, basicity (CaO/SiO_2 mass ratio) and sintering time, which are controlled by operating parameters such as sinter blend composition, coke breeze rate, humidity, windbox pressure, bed height and sinter strand speed.

Attempts have been made by many investigators to study how various mineral phases, particularly the complex calcium ferrites, are developed in a sinter. Matsuno [3] and Matsuno and Harada [4] conducted sintering experiments under equilibrated oxidising conditions which do not correspond to the real sintering process. Similarly, Ahsan et al. [5] attempted to deduce the sintering mechanism from the structure of industrial sinters. However, little information was obtained as to how initial and intermediate phases were developed during the sintering process.

A more detailed study by Sasaki and Hida [6] concluded that complex calcium ferrites such as SFCA-I, an Fe-rich phase of silico-ferrite of calcium and aluminium with a characteristic acicular texture, are present in iron ore sinter if the temperature remained below 1300 ℃. If however, the temperature of sintering exceeded 1300 ℃, the early formed SFCA-I would breakdown to a calcium silicate melt and either Fe_3O_4 at low oxygen partial pressure (pO_2) or Fe_2O_3 at high pO_2. Upon cooling, Sasaki and Hida [6] observed that a different complex calcium ferrite (now termed SFCA), crystallised. This was distinguished from SFCA-I by its coarse-grained columnar crystal morphology, and its lower Fe and higher Si content.

To examine the effect of oxygen partial pressure on sinter phase formation, Hsieh and

Whiteman [7, 8] conducted experiments in which small tablet specimens made from powdered materials were rapidly heated in a tube furnace under controlled gas atmospheres to a temperature in the range 1180 - 1255 ℃. They found that a medium pO_2 value of $5x10^{-3}$ atm maximised the formation of complex calcium ferrites in the heating stage. In the cooling stage, magnetite could be oxidised to hematite and also react with the silicate melt to produce a large amount of columnar calcium ferrite (SFCA).

Wang et al. [9] terminated the sintering process during pot tests and analysed specimens taken in different layers by optical microscopy and scanning electron microscopy (SEM). They found that the high temperature oxidation zone in the sintering process was very important for SFCA formation. A longer residence time in this zone was critical for improving sinter quality, especially in the sintering of magnetite.

The CaO/SiO_2 mass ratio, or basicity, of the sinter blend has also been shown to be a key factor governing mineral phase formation and sinter microstructure. A CaO/SiO_2 ratio greater than 1.8 to 2.0 favours the formation of complex calcium ferrites, while a lower basicity favours the formation of calcium silicate and glassy phases [3-5]. In a separate study, Egundebi and Whiteman [10] proposed that the effects of time, temperature, and composition on the evolution of mineral phases in sinters were associated with change in the viscosity of the melt. High viscosity melts sintered at low temperatures (<1300 ℃) and short sintering times produced assemblages consisting of SFCA-I, calcium silicates, glass and relict hematite whereas high sinter temperatures (>1300 ℃) and long sintering times produced SFCA, calcium silicates, glass, magnetite and hematite.

Recently, Webster et al. [11] examined the formation of SFCA and SFCA-I phases during heating and cooling of synthetic iron ore sinter mixtures in the temperature range 25 to 1350 ℃ at a fixed pO_2 of $5x10^{-3}$ atm, variable alumina contents between 1-10 wt% and a heating rate of 10 ℃/min using *in situ* X-ray diffraction (XRD). They reported that initially Fe_2O_3 reacted with CaO at temperature 771 ℃ to form calcium ferrite C_2F ($Ca_2Fe_2O_5$). The C_2F phase then reacted further with Fe_2O_3 to produce calcium ferrite

CF ($CaFe_2O_4$) at temperatures in the range 968-979 ℃. SFCA-I formation occurred at temperatures 1054-1119 ℃, preceding SFCA formation which occurred between 1107 and 1164 ℃. The changing temperature ranges in SFCA-I and SFCA formation reflected the difference in alumina contents, with high alumina content increasing the temperature range over which SFCA-I was stable before the formation of SFCA, and stabilising SFCA to higher temperatures before it incongruently melted to produce the assemblage Fe_3O_4 + melt. Further *in situ* studies by Webster et al. [12] examined the effect of oxygen partial pressure on SFCA and SFCA-I formation, and showed that if the pO_2 was too low, SFCA-I would not form, whereas both were stable under an oxidising regime. Webster et al [13] also investigated the effect of basicity on SFCA and SFCA-I formation and found that higher basicity favoured the formation of SFCA-I.

Sintering is a complex process and investigations to further elucidate reaction mechanisms and the effects of processing parameters will continue into the future. Further adding to the complexity is the recent introduction of titanium-containing ironsand as a component of the sinter blend. In a separate paper [14], the behaviour of New Zealand ironsand during sintering under various temperature and oxygen partial pressure was examined. The objective of the present work is to investigate the effect of sintering conditions on the formation of mineral phases during iron ore sintering. The effects of the raw material composition, gas atmosphere, heating temperature and cooling condition on the formation of mineral phases in sinter are examined.

2. Experimental Procedure

2.1 Sample Preparation

The starting materials for the iron ore sintering experiments were: a bulk iron ore blend, limestone, dolomite, silica sand, manganese ore, cold return fines (CRF) and New Zealand ironsand, supplied by BlueScope Ltd. The chemical compositions of the raw materials are reported in ref. [14]. Each raw material component, except the New Zealand ironsand, was crushed and screened to less than 200 μm in size. These

materials were then mixed in the proportion corresponding to that of BlueScope's bulk sinter blend.

Five separate sinter blends were prepared with the CaO/SiO_2 ratio varied from 1.5 to 4.0 so as to examine the effect of basicity on sinter phase formation. To these blends, 5 wt% of the ironsand was added and mixed to ensure homogeneity. The blend compositions are listed in Table 1. The final blends were pressed into cylindrical tablets of 5 mm diameter and ~5 mm height for sintering experiments, each weighing ~0.3 g.

Table 1. Composition of the sinter blends with different CaO/SiO_2 ratio, wt%.

CaO/SiO_2 ratio	Iron ore blend	Limestone	Dolomite	Silica sand	CRF	Ironsand
1.5	64.0	6.5	1.9	0.1	22.5	5.0
2.0	61.7	9.7	1.8	0.1	21.7	5.0
3.0	59.4	12.9	1.8	0.1	20.8	5.0
4.0	57.1	16.0	1.7	0.1	20.0	5.0
5.0	53.0	21.8	1.6	0.1	18.6	5.0

2.2 Sintering

A schematic of the laboratory sintering apparatus used in this study is described in detail elsewhere [14]. The setup is based on a vertical tube furnace with a working diameter of 55 mm through which a gas mixture of controlled composition can be continuously passed. Experiments were conducted at a range of temperatures typical for iron ore sintering (1250, 1275, 1300 and 1325 ℃) and a range of gas compositions as shown in Table 2, for 4 min duration. For each experiment the furnace was preheated to a designated temperature, and then purged with the relevant gas mixture for at least 20 min before a crucible with the specimen tablets was suspended in the hot zone of the furnace. After sintering for the desired time, the samples were then cooled following one of two procedures: (1) rapid cooling, where the crucible was directly lifted to the cold top end of the furnace tube, and (2) slow cooling, where the crucible was first lifted to a location in the furnace where the temperature was 1160 ℃, and held there for 2.5 min before being lifted to the cold top end. The gas mixture was switched to purging air

when the sample was lifted to the 1160 ℃ location.

Table 2. The composition of gases used in the heating stage of sintering experiments.

Identification	CO	CO_2	O_2	Ar	N_2
1% CO	1	24	0	75	0
0.5% O_2	0	0	0.5	99.5	0
5% O_2	0	0	5	95	0
Air	0	0	21	0	79

2.3 Microstructure Analysis

The sintered tablets were mounted in epoxy resin, cut perpendicular to the top surface, and then polished for optical microscopic and SEM analysis. The optical microscopic images were obtained in reflected light using Leica Phase Expert software. Different phases (hematite, magnetite and SFCA) as well as pores in the samples were identified by regions of homogeneous reflectivity. The various key phases were then differentiated by coloured overlays (e.g. Figure 1) to show their distribution, and the volumetric

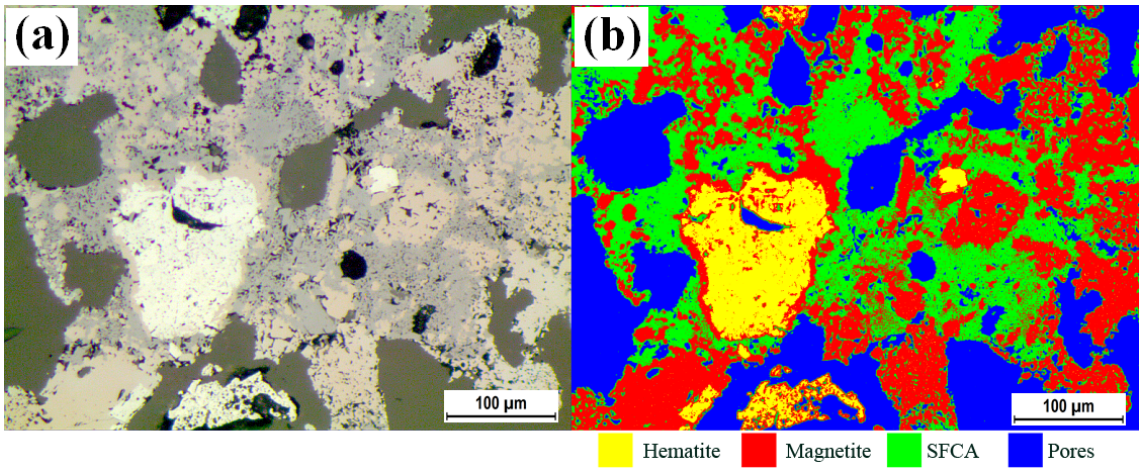

Figure 1. Processing of the optical microscopic images of sinter samples. The sample used for illustration had a CaO/SiO_2 ratio of 2.0 and was sintered at 1300 ℃ for 4 min in a gas mixture of 5% O_2 and 95% argon. (a) Original reflected light optical microscopic image; (b) the same image processed using the Leica Phase Expert software for determination of the phase proportion.

fractions of the phases present in the sinter were determined using the software. The relative errors of the volume fractions of SFCA and magnetite phases are in the range of ±5% of the corresponding values. This error is much smaller for the hematite phase, due to its sharp contrast with other phases. The silicate phase in a sintered sample was difficult for the software to distinguish from pores due to their similar contrast, so it was not included in the relative phase composition of the samples.

3. Experimental Results

3.1 Effects of Sintering Temperature and CaO/SiO_2 Ratio

To examine the effects of temperature and CaO/SiO_2 ratio (B) on sinter phase formation during heating, the ironsand-doped samples with different basicities (B = 1.5, 2.0, 2.5, 3.0 and 4.0) were heated at different temperatures (1250, 1275, 1300 and 1325 ℃) for 4 min in various gas mixtures (Table 2) followed by rapid cooling.

Figure 2 shows the optical images of samples with B = 2.0 sintered at different temperatures in a gas mixture containing 1% CO, 24% CO_2 and 75% Ar. As shown in Figure 2(a), in the sample sintered at 1250 ℃, a significant amount (25.0%) of SFCA was formed. Under these conditions, most of the hematite was converted to magnetite (67.3%), although a small amount (7.7%) of unreacted hematite still remained. There was distinct aggregation and reaction of the finer ore grains resulting in the generation of sinuous pores, however at this temperature the assimilation of oxide materials was incomplete, leaving a large proportion of partially reacted iron ore and flux particles. There was little interaction of the ironsand particles with the other components with individual ironsand particles remaining largely unreacted.

When the sintering temperature was increased to 1275 ℃ (Figure 2(b)), the fine iron ore particles began to be assimilated through reaction with the flux components resulting in almost no discrete iron ore particles remaining. Relict hematite was not detected, and the amount of SFCA formed reached a maximum (38.2%). Note that the image analysis results only report data for total SFCA (i.e. SFCA and SFCA-I) – the distinction

between SFCA and SFCA-I can be made on a textural basis or by assessing powder X-ray diffraction data (i.e. SFCA and SFCA-I have distinct powder diffraction patterns [11]), but is difficult using optical microscopy due to similarity in their compositions resulting in similar reflectivities. Although the sample showed evidence of considerable reaction between components, the notable exception was the ironsand particles. While showing some evidence of reactive rims and partial assimilation, the bulk of the ironsand particles appeared to remain relatively inert during sintering.

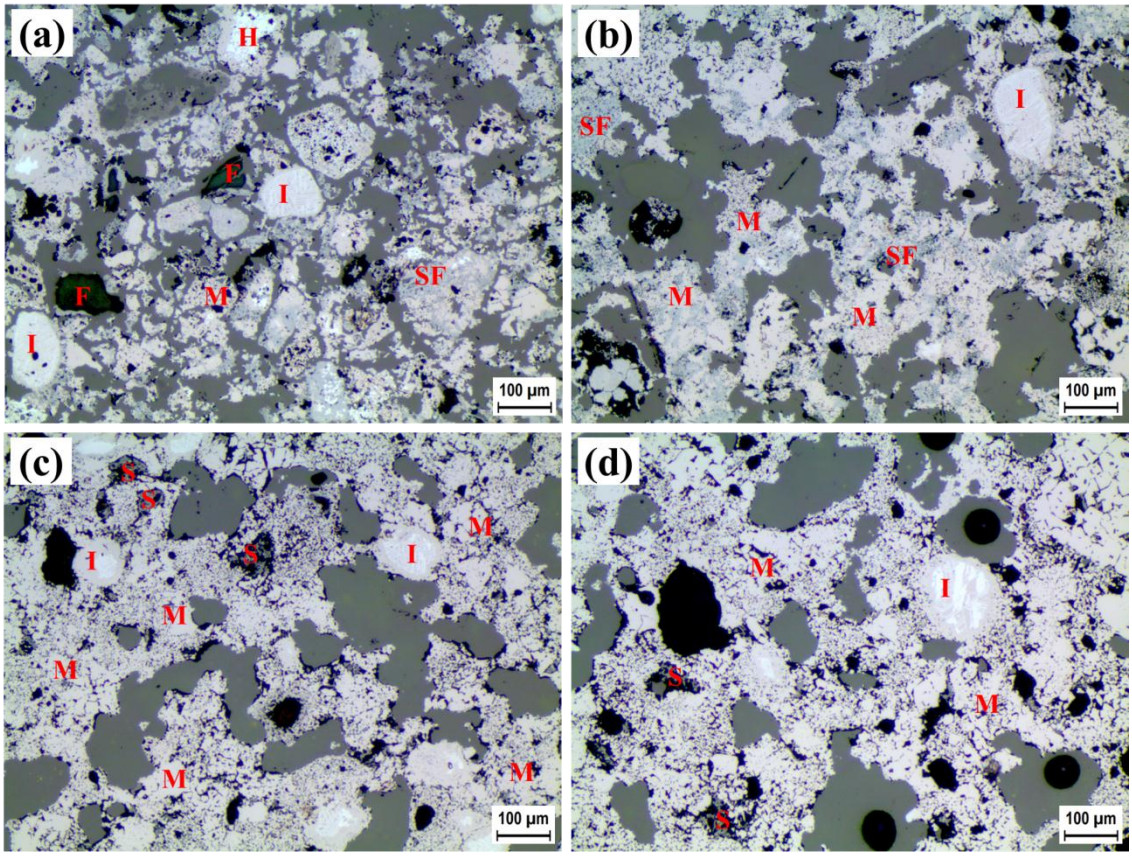

Figure 2. Optical reflected light and corresponding phase images of specimens with CaO/SiO_2 ratio = 2.0 sintered at different temperatures for 4 min in a gas mixture containing 1% CO, 24% CO_2 and 75% argon followed by rapid cooling. H: Hematite; M: Magnetite; SF: SFCA; S: Silicates; I: Ironsand; F: Relict Flux. (a)1250 ℃; (b) 1275 ℃; (c) 1300 ℃; (d) 1325 ℃.

The major phase (93.6%) present in the sample sintered at 1300 ℃ (Figure 2(c)) was magnetite, with textural evidence of secondary crystallised magnetite. Minor (6.4%)

associated hematite was also present, however these were primarily relict hematite particles encapsulated inside magnetite particles. SFCA was less common and an interstitial silica-rich phase was also present. The ironsand still remained as large, mostly unassimilated particles.

Further increasing the sintering temperature to 1325 ℃ (Figure 2(d)) resulted in the disappearance of hematite and SFCA, accompanied by concomitant increases in the amounts of magnetite and the silica-rich phase. Relict ironsand particles were still discernible as characterised by the presence of hematite exsolution lamellae in the cores. Even at this high temperature the original contours/shape of the ironsand particles remained clearly visible, although individual grains were intimately bound with other sinter components.

Figure 3 shows the volumetric percentage of SFCA (total) in specimens with B = 2.0 sintered at different temperatures and under different gas atmospheres, followed by rapid cooling. In general, at the same sintering temperature, more SFCA was formed in specimens sintered in gases with a higher pO_2. In experiments at higher pO_2 (21% and 5% O_2) atmospheres, the amount of SFCA increased with increasing sintering temperature from 1250 ℃ to 1300 ℃. Beyond 1300 ℃ the amount of SFCA formed was significantly reduced. In comparison, in less oxidising or reducing conditions (0.5% O_2 or 1% CO), the total SFCA content reached maxima at 1275 ℃ before becoming much less at higher temperatures.

Figure 4 presents the proportion of the three major phases, hematite, magnetite and total SFCA within specimens of varying basicity sintered at 1275 ℃ and 1300 ℃ and under two different gas atmospheres (0.5% and 5% O_2, respectively), followed by rapid cooling. Overall, even though the temperature and pO_2 were different, the proportion of all three phases followed similar trends with changing basicity. As the CaO/SiO_2 ratio increased from 1.5 to 4.0, the content of SFCA increased, and there was a concomitant decrease in the amounts of both hematite and magnetite.

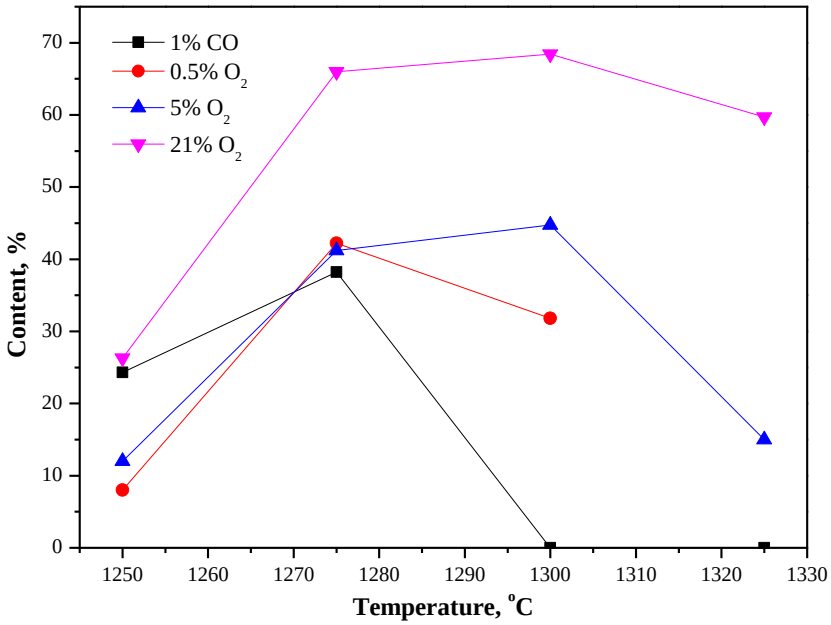

Figure 3. Effect of sintering temperature on SFCA content formed in specimens with CaO/SiO_2 ratio = 2.0 sintered in different gas atmospheres for 4 min followed by rapid cooling.

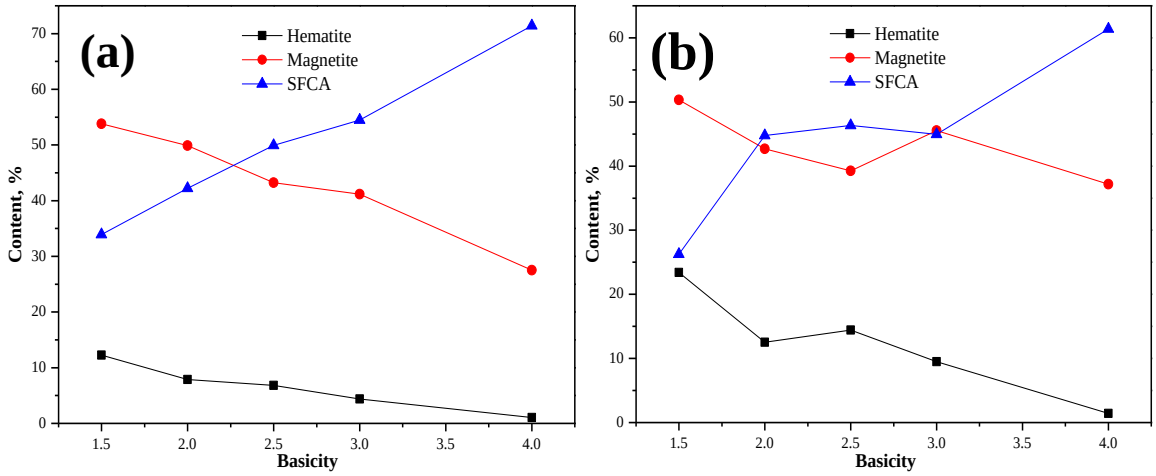

Figure 4. The phase composition of specimens with different CaO/SiO_2 ratio sintered under two different conditions for 4 min followed by rapid cooling. (a) Sintered at 1275 ℃ in gas with 0.5% O_2; (b) Sintered at 1300 ℃ in gas with 5% O_2.

3.2 Effect of Sintering Gas Atmosphere

The previous results illustrating the effects of heating and CaO/SiO_2 ratio on phase formation also indicated a pronounced effect of the gas atmosphere. To examine this

further, Figure 5 shows the measured phase abundance in samples that were sintered in each of the four gas atmospheres (Table 2), followed by fast cooling. Data are shown for three conditions: T = 1275 ℃, B = 2.0; T = 1300 ℃, B = 2.0; and T = 1300 ℃, B = 1.5. The results indicate that the SFCA (total) and hematite contents both increased with increasing oxygen potential in the system, while the magnetite content decreased sharply. For example, SFCA was rarely detected in the sample with B = 1.5 sintered in a gas mixture containing 1 vol% CO-24 vol% CO_2 at 1300 ℃, while the content of SFCA increased to >50% when the equivalent mixture was sintered in air. The specimen with B = 2.0 sintered at 1275 ℃ also increased in total SFCA content by nearly 30% as the gas atmosphere became progressively more oxidising. It should be noted, however, that the sample already contained a high amount of SFCA when sintered in a gas mixture containing 1 vol% CO-24 vol% CO_2.

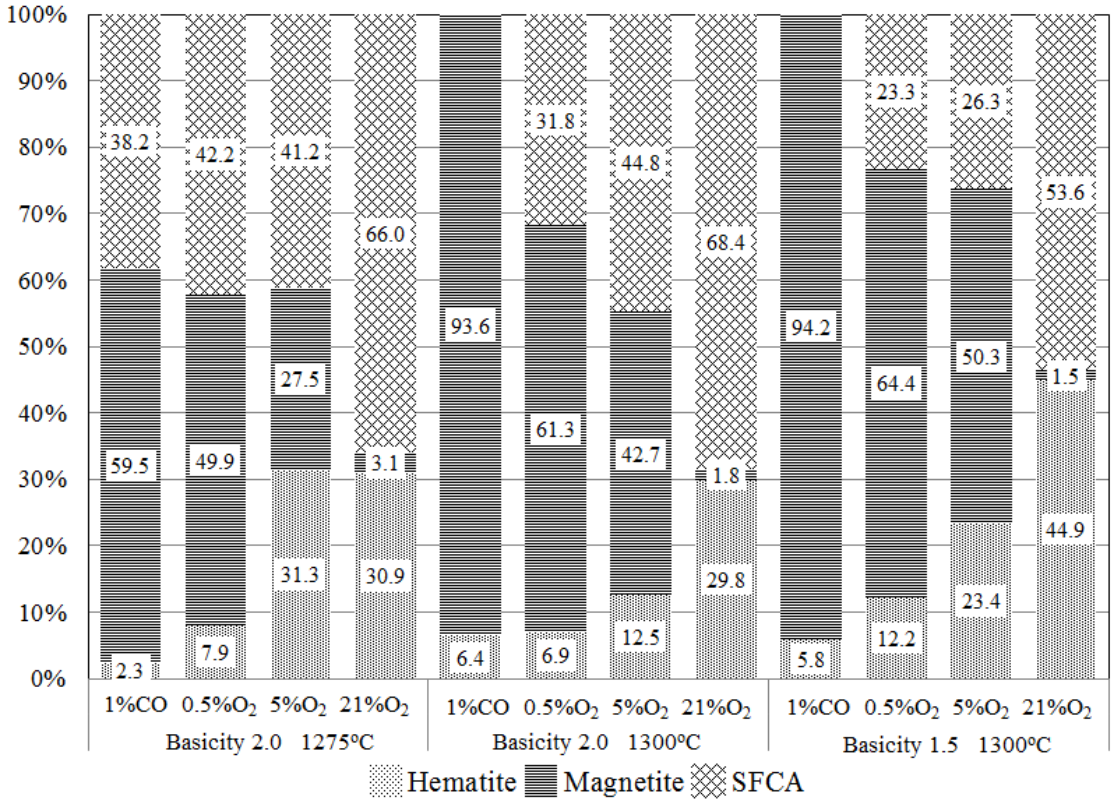

Figure 5. The phase composition of specimens sintered in different gas atmospheres for 4 min followed by rapid cooling.

3.3 Effect of Oxidation during Cooling

The effect of oxidation on the sinter phase assemblage was examined by comparing the final phase assemblage between samples that were rapidly quenched, with those that were subject to a slower cooling profile. Figure 6 compares the phase compositions of the sinter specimens with B = 2.0 and sintered under four different gas atmospheres at 1300 ℃, followed by either a rapid cooling or a slow cooling procedure. The results indicated that, for specimens sintered in air there was a negligible difference between rapid and slow cooling, with phase assemblages remaining approximately constant. In comparison, for samples sintered under more reducing gas atmospheres there was a large difference between samples cooled at different rates. For rapidly cooled samples, the content of magnetite increased significantly with decreasing oxygen potential in the sintering gas mixture. However, this magnetite was almost totally eliminated during

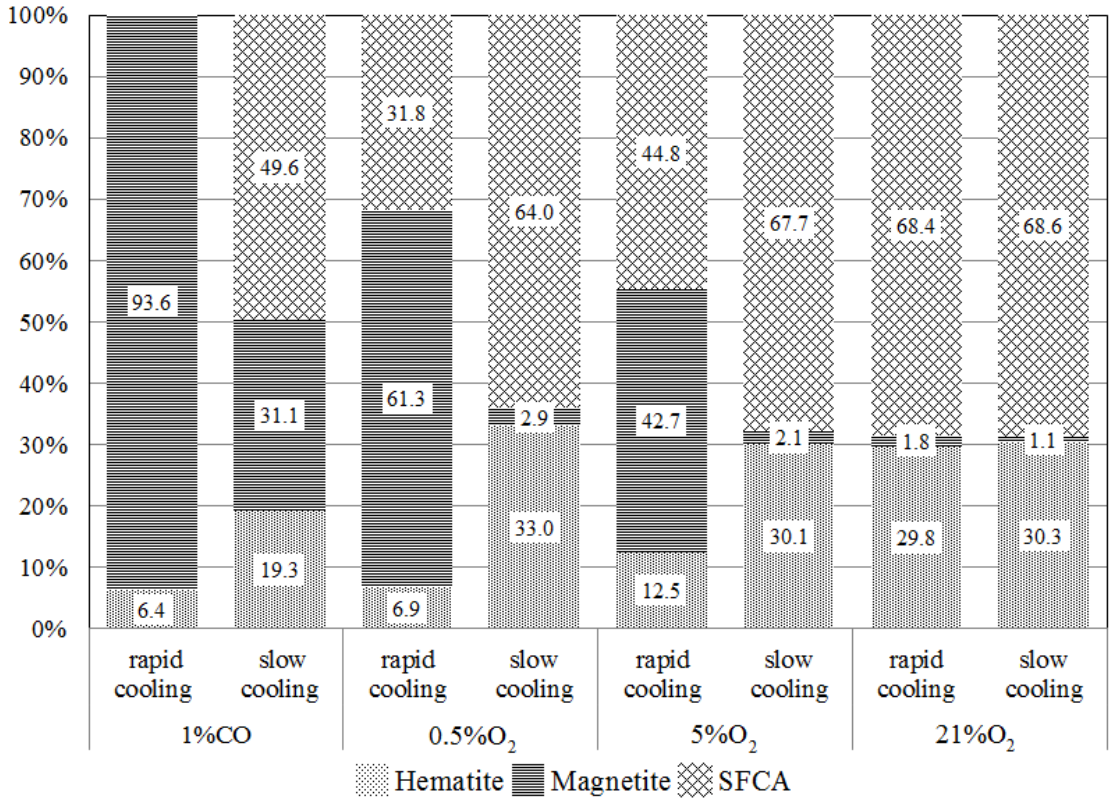

Figure 6. Effect of cooling procedure on the phase composition of samples sintered in different atmospheres. All samples are with CaO/SiO_2 ratio = 2.0 and sintered at 1300 ℃ for 4 min.

slow cooling for the sintered samples with 0.5% and 5% O_2. Correspondingly, the contents of SFCA and hematite both increased during slow cooling, and reached levels similar to those observed when the sample was sintered in air. For example, in the sample sintered in the gas mixture containing 0.5% O_2, up to 61.3% of magnetite was obtained by rapid cooling, whereas the amount decreased to only 2.9% following the slow cooling procedure. At the same time, the content of SFCA increased from 31.8 to 64.0%, and hematite from 6.9 to 33.0%.

4. Discussion

SFCA (including SFCA-I) is a calcium ferrite based mineral phase with aluminium and silicon. Considering the heating and cooling cycle of sintering, its formation starts with solid state reaction during heating:

$$CaO + Fe_2O_3 = CaFe_2O_4 \quad (1)$$

where calcium from the flux initially diffuses into the iron ore particles to form a new phase, $CaFe_2O_4$ (CF) [15, 16]. As well, $Ca_2Fe_2O_5$ (C_2F) can form when enough calcia is available, and recent work by Webster *et al* [11] indicates that in synthetic sinter mixtures, C_2F forms before CF. The pure $CaFe_2O_4$ phase has a melting point of 1216 ℃ while $Ca_2Fe_2O_5$ melts at 1449 ℃ [17]. Due to the relative difficulty of solid state diffusion, formation of a localised melt enhances mass transfer and further reaction remarkably. Impurities such as silica and alumina within the sinter blend participate in additional reactions with the early formed ferrites resulting in the formation of SFCA phases.

In a relatively reducing gas atmosphere, decomposition of hematite to magnetite may take place:

$$6Fe_2O_3 = 4Fe_3O_4 + O_2 \quad (2)$$

Ignoring any kinetic impediment, whether Reaction (2) takes place is determined by temperature and the prevailing pO_2 for the reaction. In a CO and CO_2 containing gas, the equilibrium pO_2 may be determined by the thermodynamics of Reaction (3):

$$2CO_2 = 2CO + O_2 \quad (3)$$

Figure 7 presents the equilibrium values of pO_2 for Reactions (2) and (3) in the 1% CO-24% CO_2-75% Ar gas atmosphere calculated using the thermodynamic data from [17]. It can be seen that the equilibrium pO_2 of the gas is six orders of magnitude lower than that of Reaction (2), which makes decomposition of hematite a highly favoured reaction throughout the temperature range examined in the investigation. The extent of this reaction is determined by kinetics. A pO_2 of 0.5 kPa is not enough to suppress the decomposition of hematite in the temperature range investigated. Below 1230 and 1290 ℃, Reaction (2) is suppressed by applying a pO_2 of 5 kPa (5% O_2 in gas) and 21 kPa (air), respectively.

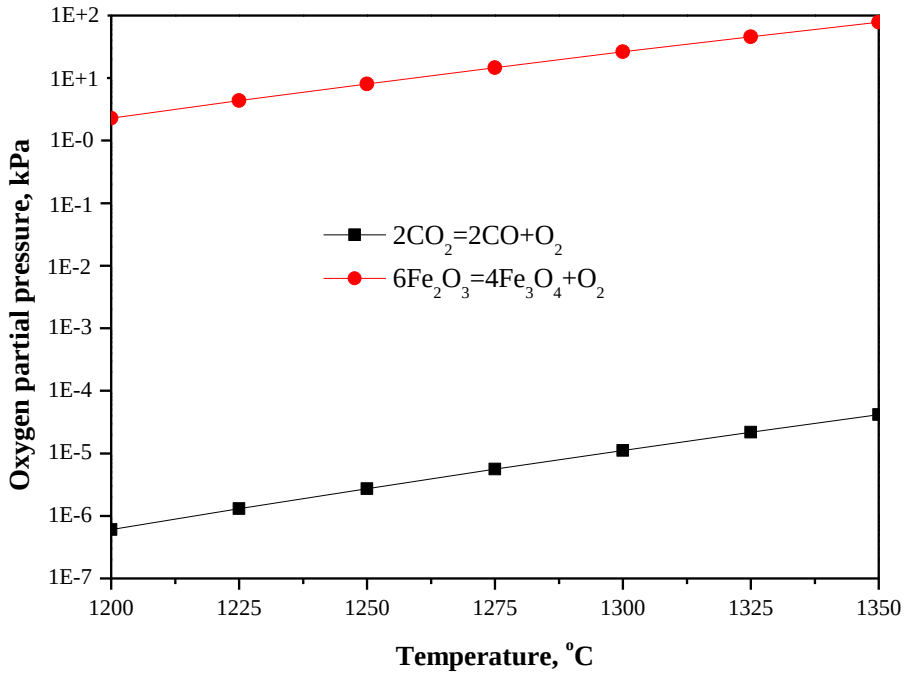

Figure 7. Equilibrium partial pressures of O_2 for Reactions (2) and (3) in the 1% CO-24% CO_2-75% Ar gas atmosphere.

Dissolution of limited amounts of silica and alumina in the CF and C_2F phases decreases their melting temperatures, as in the case of the formation of SFCA phases. The formation of a melt from SFCA could be caused by two different reasons: (1) a physical melting process without a chemical reaction involved, or (2) reduction of Fe^{3+} to Fe^{2+} in SFCA which affects its stability. A synthetic SFCA was prepared containing

77.4 wt% Fe_2O_3, 14.1 wt% CaO, 3.6 wt% SiO_2 and 5.0 wt% Al_2O_3. The synthetic SFCA and a chemically pure hematite sample were tested by TG-DSC analysis at a ramping rate of 10 ℃/min in argon and in air using high-purity alumina crucibles with an internal diameter of 5 mm. Figure 8 shows the TG-DSC patterns of hematite and synthetic SFCA heated at 800 – 1450 ℃ in air. It is noted that the SFCA sample started to lose weight at 1220 ℃ in air, which was significantly lower than the temperature the hematite started to lose weight, which was measured to be at 1335 ℃. A smaller total weight loss was detected in the SFCA sample, indicating that less Fe_2O_3 was decomposed in the SFCA sample in comparison with that in the hematite sample. During this heating process, the hematite sample did not melt because the maximum temperature (1450 ℃) of the test is much lower than the melting points of pure hematite and magnetite. For the SFCA sample, however, besides decomposition of Fe_2O_3 in SFCA phase, a melt is believed to have been generated due to the larger heat flow in the DSC pattern accompanying the weight loss. The total heat flow calculated from SFCA curve was 0.365 J/mgFe_2O_3, while the total heat flow calculated from hematite curve was only 0.240 J/mgFe_2O_3.

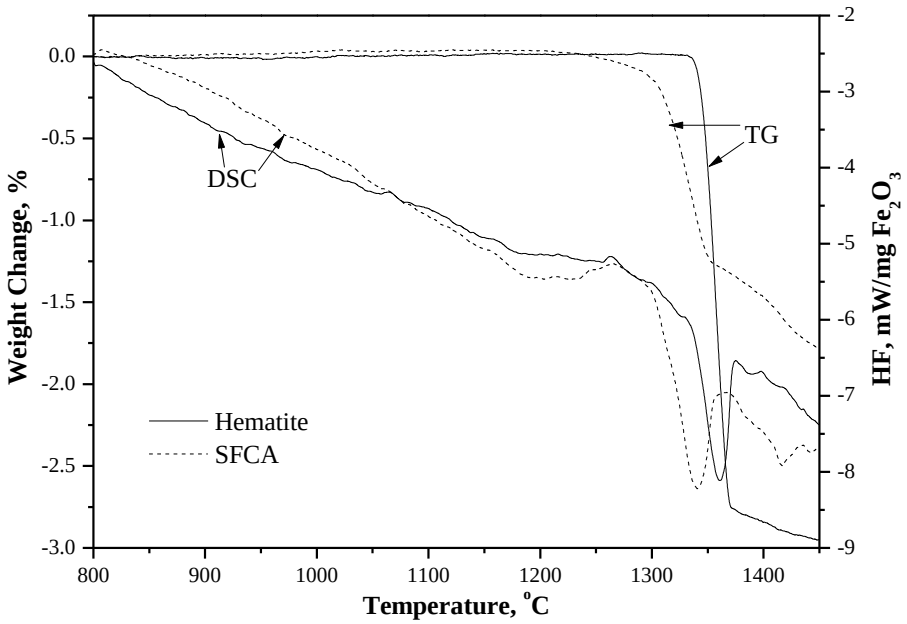

Figure 8. TG-DSC patterns of pure hematite and a synthetic SFCA sample heated in the temperature range of 800-1450 ℃ in air. The temperature ramping rate was 10 ℃/min.

In an argon atmosphere, the SFCA sample started to lose its weight from 1190 ℃ and the low but close temperatures of SFCA decomposition in argon and air may illustrate that it was favoured thermodynamically due to reduced activity of magnetite when dissolved in a melt, and the rate was controlled by the kinetics of conversion of Fe_2O_3 in SFCA to magnetite accompanied by formation of a melt.

The synthetic SFCA was also heated at a rate of 10 ℃ min^{-1}, under a flow of air. The content of SFCA was examined by *in situ* XRD and the XRD data was collected over the range $10° \leq 2\theta \leq 120°$ continuously throughout heating, with individual datasets collected for 0.5 min. The use of the diffractometer and high-temperature chamber in an iron ore sinter phase context has been described previously [11, 12]. In this case, however, the concentration of the gas exiting the high-temperature stage was measured using a Thermo Scientific VG PROLAB Benchtop QMS. It is observed that a spike in the O_2 concentration occurred corresponding with a decrease in the SFCA scale factor (i.e. the decomposition of SFCA), which is interpreted as being indicative of the reduction of Fe^{3+} in the SFCA crystal structure to Fe^{2+}.

In the sintering process, when a specimen is heated to a temperature sufficient to form a liquid phase, the melt will convert to a glassy phase and secondary magnetite during cooling in a reducing atmosphere, or form SFCA phase and secondary hematite if enough cooling time is provided in an oxidising atmosphere.

The nominally isothermal sintering process was practically a rapid heating process, with a heating rate significantly faster than that used by Webster et al. [11]. According to Figure 2(a), both SFCA and SFCA-I were present in the bonding matrix of the specimen sintered at 1250 ℃ in an atmosphere of 1% CO-24% CO_2 followed by rapid cooling. The contours of the original particles remained indicating a lack of assimilation, although a small portion of magnetite was identified as having been crystallised from a melt (secondary magnetite) which means that local melting took place during sintering (e.g. in areas close to a flux particle where the local CaO/SiO_2 ratio was very high). At this relatively low temperature, SFCA and SFCA-I were formed via solid state reactions among iron ore, flux, and alumina and silica impurities. It can be expected that the

magnetite phase in this sintered sample was from the decomposition and melting of SFCA and, mostly, from decomposition of hematite. The presence of hematite phase encapsulated in the magnetite particles shows that its decomposition was still incomplete. A lack of glassy phase is an indication of insignificant melting of SFCA.

An increase in temperature from 1250 to 1275 ℃ resulted in the formation of more SFCA phase (Figure 2(b)). The increase of SFCA-I amount was less significant than SFCA due to the lower thermal stability of the former. Secondary magnetite particles were also observed in this sample, meaning that a significant amount of melt phase was formed during heating.

A further increase in temperature to 1300 and 1325 ℃ almost completely eliminated SFCA whereas there was a significant increase in the amount of magnetite and glassy silicate phases. At these temperatures, SFCA phases are unstable, and incongruently melt to form the assemblage of magnetite and a melt [11]. As shown in Figures 2 (c) and (d), the amount of secondary magnetite also increased along with increasing temperature, indicating more severe melting of SFCA at these temperatures. Rare hematite was found located inside the iron ore matrix surrounded by magnetite. This hematite residue was not reduced to magnetite due to lack of exposure to the gas atmosphere.

As shown in Figures. 3 and 5, increasing the partial pressure of O_2 in the sintering gas atmosphere significantly increased the content of SFCA in a sinter specimen because it increased the stability of SFCA at higher temperatures, which is consistent with the observation by Webster et al. [12]. When the temperature went beyond 1300 ℃, the pO_2 was not high enough to fully suppress the decomposition of SFCA, resulting in decreased SFCA content in the sinter samples. This brought about a maximum SFCA content at a temperature which increased with increasing pO_2.

It is also noted that, although a higher pO_2 favoured SFCA formation by solid-state reaction at lower temperatures e.g. 1250 ℃, the assimilation of original blend particles was better with a more reducing gas atmosphere. According to the CaO-Fe_2O_3-FeO

phase diagram [18], FeO fluxes calcium ferrite phases to form melt at lower temperatures, which promotes mass transfer and assimilation reactions between solid particles via the melt.

Figure 9 presents the optical microscopic images of the specimens with a CaO/SiO_2 ratio of 2.0 subjected to sintering at 1300 ℃ for 4 min with changing gas atmosphere. In a gas with 0.5% O_2, the sinter consisted of mainly primary and secondary magnetite; SFCA content was low and hematite was rarely found. As discussed above, SFCA was unstable under these temperature and O_2 conditions. Increasing O_2 to 5% resulted in more SFCA being formed, and some secondary hematite (which was formed by crystallisation of silicate melt during cooling) was identified together with primary hematite and magnetite. In the sample sintered in air, SFCA was the dominant phase with significant content of hematite; magnetite was rarely observed. Because the melting of SFCA was accompanied by reduction of Fe_2O_3 in this phase to magnetite, reoxidation of the latter must have taken place in order to form secondary hematite and SFCA phases during cooling in air.

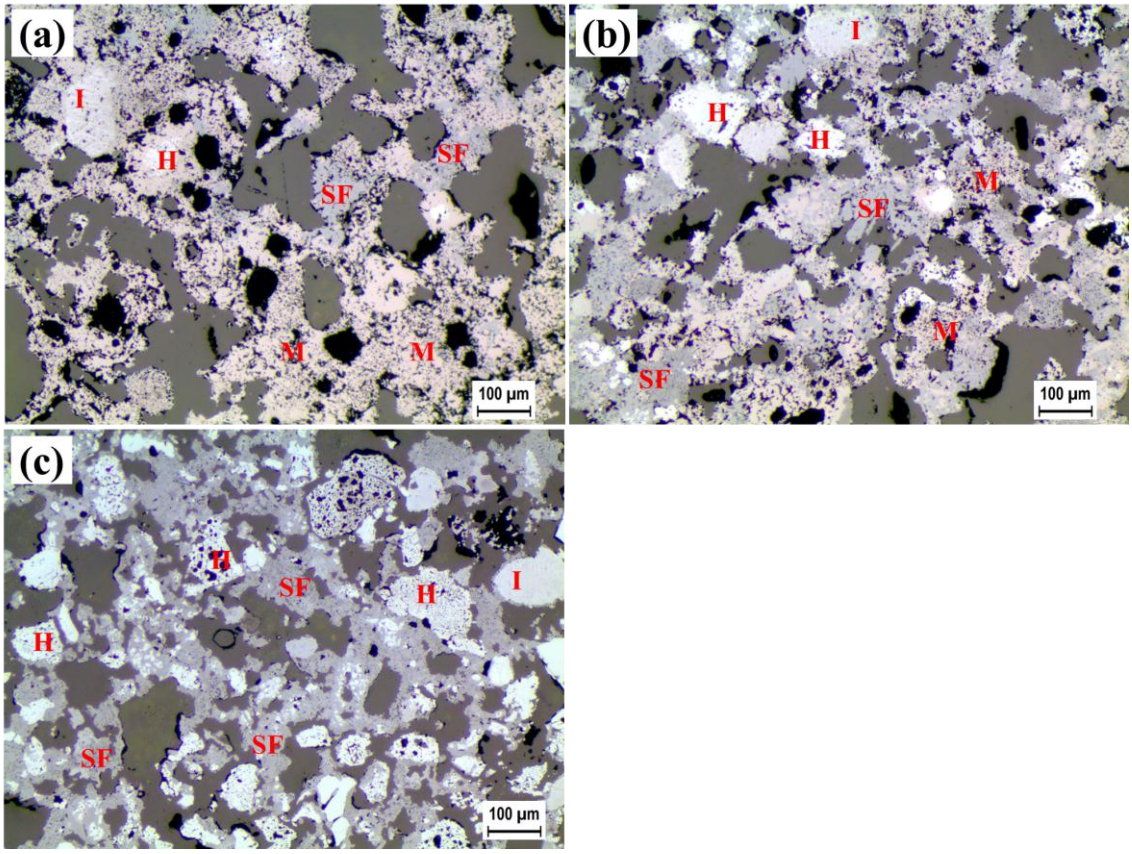

Figure 9. Microstructure of specimens with CaO/SiO_2 ratio = 2.0 sintered in different gas atmosphere at 1300 ℃ for 4 min. (a) 0.5% O_2; (b) 5% O_2; (c) Air.

High basicity favours formation of SFCA, as demonstrated by Figure 4. As shown in Reaction (1), increasing the content of CaO (as formed by decomposition of limestone) enhances the formation kinetics of calcium ferrite by solid state reaction at low temperatures; at high temperatures when SFCA is crystallised from a melt phase, a high concentration of CaO also favours formation of SFCA via thermodynamics and kinetics. As a result, the content of SFCA increased consistently with increasing the CaO/SiO_2 ratio of the sinter blend at different sintering conditions.

As shown in Figure 6, slow cooling of sintered specimens in air resulted in large increases in the SFCA content of a sinter especially for those sintered in a more reducing gas atmosphere. Furthermore, the morphology of sinter oxidised during cooling was different from that produced during the heating stage of sintering. Figure 10 compares the microstructure of two specimens with CaO/SiO_2 = 2.0 sintered in a gas with 0.5% O_2 at 1275^{o}C for 4 min followed by fast cooling and slow cooling. It

can be seen that the coalescence extent of the sample after slow cooling (Figure 10(b)) increased significantly compared to the sample experienced rapid cooling (Figure 10(a)). Also, the sample after slow cooling was dominated by hematite, SFCA and SFCA-I and contained almost no magnetite phase (main phase in the sample followed by rapid cooling).

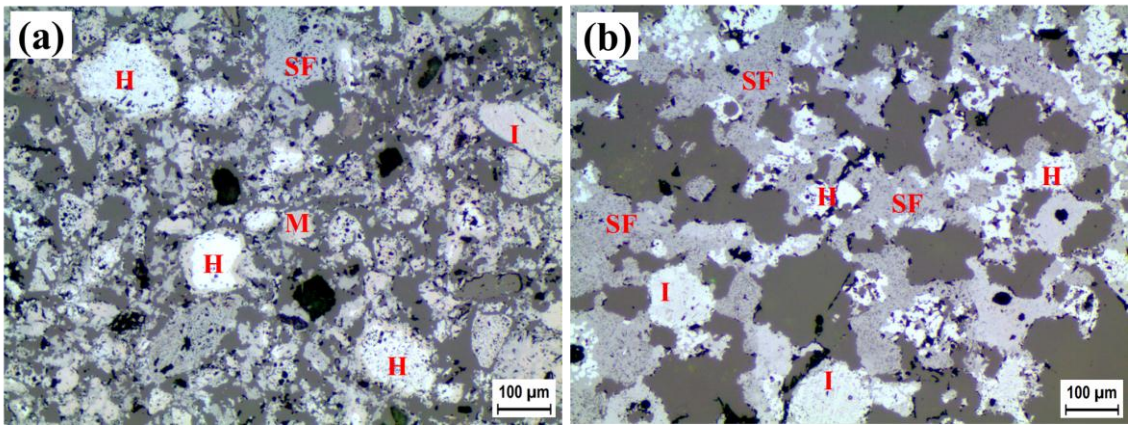

Figure 10. Microstructure of specimens with CaO/SiO_2 ratio = 2.0 sintered in a gas atmosphere with 0.5% O_2 at 1275 ℃ for 4 min followed by different cooling procedures. (a) Rapid cooling; (b) Slow cooling.

The morphology of a commercial sinter supplied by BlueScope Ltd. was also examined in this study. This sinter contained approximately 23% SFCA (total), 6% primary hematite, 31% secondary hematite, 25% magnetite and 15% silicates. Figures 11(a) and (b) show typical microstructures from the exterior and interior of lumps of this commercial sinter, respectively. The exterior of the sinter has similar morphology to that of laboratory sinter following the slow cooling procedure presented in Figure 10(b) in that hematite and acicular SFCA-I are dominant phases. In comparison, a large amount of magnetite and interstitial silicates but rare columnar SFCA were observed in the interior of this commercial sinter, which is similar to the laboratory sinter sintered in a reducing atmosphere as shown in Figures 2 (c) and (d). It is known that the reaction conditions in an industrial iron ore sintering process are heterogeneous. Generally, in the heating stage the iron ore particles are in a more reducing atmosphere, while in the cooling stage, the particles adjacent to the gas flow channels are subject to a highly oxidising atmosphere.

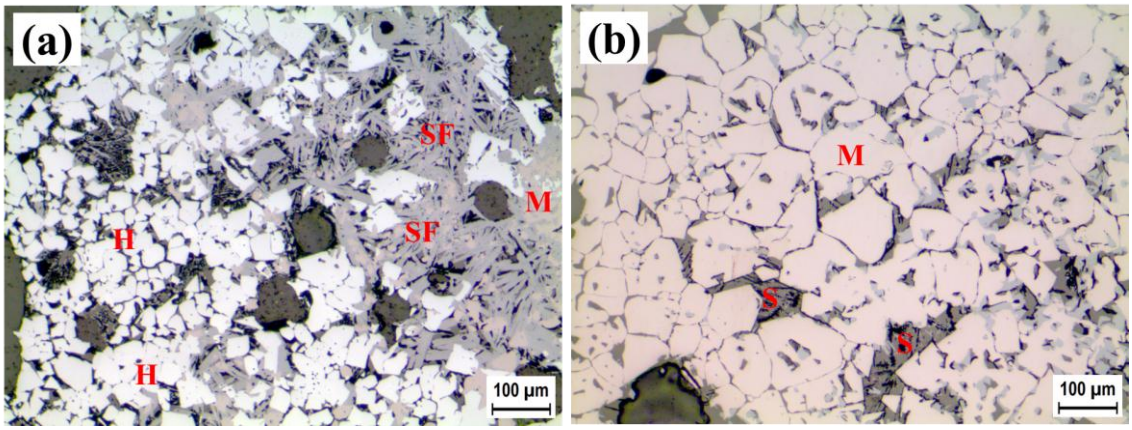

Figure 11. Typical microstructure of a commercial sinter. (a) Exterior and (b) interior of sinter lumps.

In this investigation, the smaller size of raw material particles and continuous void generated during heating in addition to the relatively small tablets used benefit the diffusion of gas mixture inside a specimen. Therefore the reactions in laboratory sinter were more homogeneous and susceptible to a greater influence of the prevailing gas atmosphere. Accurately controlled experimental conditions and uniform reactions during sintering however are helpful to reduce the uncertainty and better investigate the effects of sintering conditions on the final mineralogy of sinter.

From the above similarity in the microstructure of commercial sinter shown in Figure 11 with that obtained in the laboratory presented in Figure 10(b), as well as the similarity in the changing patterns of the sintering conditions, it can be recognised that the SFCA phase in commercial sinter is most likely formed by heating the sinter blend in a relatively reducing atmosphere followed by cooling in an oxidising atmosphere. The relatively fine microstructure of SFCA-I formed in the laboratory specimen as shown in Figure10(b) compared with commercial sinter was probably influenced by the sudden reduction of temperature by 100 ℃ during the oxidation stage of slow cooling which generates a lot of SFCA (or SFCA-I) nuclei. In comparison, melt in the commercial process is gradually cooled which may generate less SFCA nuclei which grow into a lesser number of coarse crystals of SFCA-I. Further examination of the formation of mineral phases during cooling and solidification is in progress.

5. Conclusions

(1) The content of SFCA phase was significantly affected by temperature. In the temperature range of 1250 – 1300 ℃, SFCA formation was enhanced by increasing temperature. Further increasing sintering temperature promoted the Fe^{3+} in the SFCA crystal structure to Fe^{2+} and consequent decomposition of SFCA.

(2) Sintering at a low temperature generated SFCA by solid state reactions. At high temperatures, SFCA was produced during cooling via crystallisation from a silicate melt. Slow cooling in an oxidising gas atmosphere strongly promoted formation of SFCA.

(3) Increasing CaO/SiO_2 ratio and oxygen partial pressure favour the formation of SFCA phase. A high oxygen partial pressure suppressed conversion of hematite into magnetite, and so promoted formation of SFCA.

(4) A typical microstructure of SFCA bonding phase composed of acicular SFCA-I and hematite in the commercial sinter was formed by crystallisation from a silicate melt formed in the heating stage with relatively low oxygen partial pressure during cooling in an oxidising gas atmosphere.

Acknowledgements

The project is financially supported by the BlueScope Steel Metallurgical Centre Projects Grant. Zhe Wang is a recipient of University of Wollongong Deputy Vice Chancellor's Special Scholarship and International Postgraduate Tuition Award. The authors would like to acknowledge the Electron Microscopy Center (EMC) at University of Wollongong for SEM/EDS analysis.

References

[1] A. K. Biswas, Principles of Blast Furnace Ironmaking: Theory and Practice, Cootha Publishing House, Brisbane, (1981), 194.

[2] P. R. Dawson, J. Ostwald, K. M. Hayes, Influence of Alumina on Development of Complex Calcium Ferrites in Iron Ore Sinters, *Transactions of the Institution of Mining and Metallurgy Section C-Mineral Processing and Extractive Metallurgy*, **94** (1985), C71-C78.

[3] F. Matsuno, Changes in Mineral Phases during the Sintering of Fe_2O_3-CaO-SiO_2 System, *Transactions of the Iron and Steel Institute of Japan*, **19** (1979), 595-604.

[4] F. Matsuno and T. Hirada, Changes of Mineral Phases during the Sintering of Iron Ore - Lime Stone Systems, *Transactions of the Iron and Steel Institute of Japan*, **21** (1981), 318-325.

[5] S. N. Ahsan, T. Mukherjee and J. A. Whiteman, Structure of fluxed sinter, *Ironmaking and Steelmaking*, **10** (1983), 54-64.

[6] M. Sasaki and Y. Hida, Consideration on the Properties of Sinter from the Point of Sintering Reaction, *Tetsu-to-Hagane*, **68** (1982), 563-571.

[7] L. H. Hsieh and J. A. Whiteman, Sintering Conditions for Simulating the Formation of Mineral Phases in Industrial Iron Ore Sinter, *ISIJ International*, **29** (1989), 24-32.

[8] L. H. Hsieh and J. A. Whiteman, Effect of Oxygen Potential on Mineral Formation in Lime-fluxed Iron Ore Sinter, *ISIJ International*, **29** (1989), 625-634.

[9] S. Wang, W. Gao and L. Kong, Formation Mechanism of Silicoferrite of Calcium and Aluminium in Sintering Process, *Ironmaking and Steelmaking*, **25** (1998), 296-301.

[10] G. O. Egundebi and J. A. Whiteman, Evolution of Microstructure in Iron Ore Sinter, *Ironmaking and Steelmaking*, **16** (1989), 379-385.

[11] N. A. S. Webster, M. I. Pownceby, I. C. Madsen and J. A. Kimpton, Silico-ferrite of Calcium and Aluminum (SFCA) Iron Ore Sinter Bonding Phases: New Insights into their Formation during Heating and Cooling, *Metallurgical and Materials Transactions B*, **43** (2012), 1344-1357.

[12] N. A. S. Webster, M. I. Pownceby, I. C. Madsen and J. A. Kimpton, Effect of Oxygen Partial Pressure on the Formation Mechanisms of Complex Ca-rich Ferrites, *ISIJ International*, **53** (2013), 774-781.

[13] N. A. S. Webster, M. I. Pownceby, I. C. Madsen, A. J. Studer, J. R. Manuel and J. A. Kimpton, Fundamentals of Silico-Ferrite of Calcium and Aluminum (SFCA) and SFCA-I Iron Ore Sinter Bonding Phase Formation: Effects of CaO: SiO_2 Ratio, *Metallurgical and Materials Transactions B*, **45** (2014), 2097-2105.

[14] Z. Wang, D. Pinson, S. Chew, H. Rogers, B. J. Monaghan, M. I. Pownceby, N. A. S. Webster and G. Zhang, Behaviour of New Zealand Ironsand during Iron Ore Sintering, *submitted to Metallurgical and Materials Transactions B*, (Chapter 2).

[15] X. Guo and Y. Ono, Kinetics of Calcium Ferrites Formation from CaO and Fe_2O_3 in Solid State, Memoirs of the Faculty of Engineering, Kyushu University, **52** (1992), 7-17.

[16] J. W. Jeon, S. M. Jung and Y. Sasaki, Formation of Calcium Ferrites under Controlled Oxygen Potentials at 1273 K, *ISIJ International*, **50** (2010), 1064-1070.

[17] M. Binnewies and E. Milke, Thermochemical Data of Elements and Compounds, 2nd edition, Wiley-VCH Verlag GmbH, Weinheim, (2002).

[18] K. C. Mills, Slag Atlas, 2nd edition, Verlag Stahleisen GmbH, D-Düsseldorf, (1995), 59.

CHAPTER 4. INTERACTION OF NEW ZEALAND IRONSAND AND FLUX MATERIALS

Interaction of New Zealand Ironsand and Flux Materials

Zhe Wang[1], David Pinson[2], Sheng Chew[2], Harold Rogers[2], Brian J. Monaghan[1], Guangqing Zhang[1]

1. School of Mechanical, Materials and Mechatronic Engineering, University of Wollongong, NSW 2522, Australia
2. BlueScope Technology and Planning, P.O. Box 202 Port Kembla, NSW 2505, Australia

Abstract

New Zealand ironsand is mined for steel production. Its composition approximates that of titanomagnetite ($Fe_{3-x}Ti_xO_4$) containing about 60 wt% iron and 8 wt% titania. The ironsand provides an alternative source of iron to conventional iron ores. Its addition into a sinter blend is an established method of utilisation in ironmaking. Knowledge of the interaction between ironsand and flux materials during sintering is helpful to understand the sintering mechanism of titanomagnetite. In this study, two-layer interaction couples between ironsand and flux materials (CaO, MgO and dolomite) were prepared and sintered in an atmosphere of pO_2 = 0.5 kPa in the temperature range of 1200 – 1300 ℃ for different times. When the ironsand was sintered with MgO, Mg^{2+} ions significantly diffused into the lattice of ironsand, which stabilised the system of FeOx-MgO and hindered the assimilation of ironsand particles. During the sintering of ironsand with CaO, a reaction zone consisting of perovskite and calcium ferrite formed between the two layers. In comparison, a reaction zone consisting of perovskite, MgO-FeO solid solution and calcium ferrite occurred during the sintering of ironsand with dolomite. Increasing sintering temperature significantly enhanced the penetration of calcium ferrite into the dolomite layer; whereas the perovskite phase and MgO-FeO solid solution remained at higher sintering temperatures due to their relatively high melting points.

Key words: Sintering, ironsand, Titanomagnetite, Dolomite, Calcia, Magnesia.

1. Introduction

Ironsand deposits along the west coast of New Zealand's North Island, including these at Waikato North Head and Taharoa, are mined for iron and steel production [1]. The composition and microstructure of New Zealand ironsand have been intensively examined. Although the composition of ironsand is partially dependant on origin/location, it approximates that of titanomagnetite ($Fe_{3-x}Ti_xO_4$) containing about 60 wt% iron and 8 wt% titania (TiO_2) [1-3]. The major impurities in the ironsand include Al_2O_3, MgO, SiO_2, V_2O_5, and MnO. The impurities aluminium, vanadium, manganese, and magnesium are typically associated with the titanomagnetite grains, occurring as solid solution components within the lattice. The other impurity elements, including part of the aluminium, are more typically associated with gangue mineral grains such as aluminosilicates (e.g. feldspars and clays), quartz and apatite [4].

New Zealand ironsand grains can be divided into two types: homogeneous grains and grains that contain exsolution lamellae. Cocker et al. [1] examined New Zealand ironsand using electron microprobe analyses and found that homogeneous titanomagnetite particles accounted for 90 to 95 vol% and were relatively rich in Ti, containing up to 8.2 wt% TiO_2. The exsolution lamellae appearing as bands of variable thickness in a trellis-like pattern were of hematite-ilmenite composition with an overall high TiO_2 content of 13.1 wt%, while the titanomagnetite host was relatively lean in Ti (about 1.5 wt% TiO_2). High-temperature oxidation of Fe^{2+} to Fe^{3+} in titanomagnetite can produce vacancies in octahedral sites of the {111} crystal planes, which allows increased diffusion of Ti into these regions and leads to the formation of hematite-ilmenite lamellae (1-10 μm) along the original {111} planes of the titanomagnetite host [5].

The ironsand provides an alternative source of iron to conventional iron ores. Its small particle size precludes direct charging into a blast furnace but its incorporation into sinter provides an appropriate method for its utilisation in ironmaking [6]. The behaviour of ironsand during iron ore sintering has been examined previously [4]. It was reported that the assimilation of ironsand during sintering in a reducing atmosphere started from the diffusion of calcium into the lattice of the ironsand matrix, which

further decreased the melting point of titanomagnetite and accelerated the melting rate of ironsand particles. A reaction zone was formed within the ironsand particle where a perovskite phase was generated as the result of the reaction between TiO_2 and CaO.

This paper is focused on characterising the interaction between ironsand and flux materials (CaO, MgO and dolomite) to gain a better understanding of the sintering mechanism of titanomagnetite.

2. Experimental Procedure

2.1 Sample Preparation

The starting materials used in the interaction experiments were: New Zealand ironsand and three fluxes including synthetic calcia, CaO (Sigma Aldrich, reagent grade); synthetic magnesia, MgO (Sigma Aldrich, 99%, <325 mesh) and dolomite. The synthetic CaO powder was calcined at 1000 ℃ for 2 h. Ironsand and dolomite were supplied by BlueScope Ltd. and the chemical compositions examined by X-ray fluorescence (XRF) were reported previously [7]. Detailed characterisation of the ironsand has been presented elsewhere [4]. Dolomite was crushed and screened to a particle size smaller than 38 μm before use.

The interaction couple between ironsand and each flux material used in this work was prepared as follows. 0.5 g ironsand particles were first placed in a die with a diameter of 8 mm and pressed into a substrate in a uniaxial hydraulic press by applying 20 kN of pressure for 2 min. Then 0.3 g of each flux material powder, in turn, was placed into the same die and pressed with the ironsand substrate into an interaction couple by applying 20 kN of pressure for 2 min.

2.2 Sintering

The sintering apparatus has been described previously[4]. The setup is based on a vertical tube furnace with a working diameter of 55 mm through which a gas mixture of

controlled composition can be continuously passed. Experiments were conducted at different temperatures (1200, 1250, 1300 and 1325 ℃) in an atmosphere of pO_2 = 0.5 kPa (representative of industrial iron ore sintering pO_2 [8]) maintained by an oxygen-nitrogen mixture. The furnace was preheated to a designated temperature, and then purged with the gas mixture for at least 20 min before a crucible with the interaction couples was suspended in the hot zone of the furnace. After sintering for a desired time, the samples were cooled rapidly by lifting the crucible to the cold top end of the furnace tube in order to avoid any possible transformation due to slow cooling.

2.3 Microstructure Analysis

After cooling to room temperature, the specimens were vacuum infiltrated by epoxy resin, and after hardening, sectioned perpendicular to the ironsand-flux interface. The section was ground and polished to a 1μm finish for optical microscopic observation (Leica DM6000 Optical Microscope). The polished samples were then coated with carbon prior to analysis by scanning electron microscopy (SEM, JEOL JCM-6000) operated at 15 kV. The thickness of the reaction layers reported represents an average of 12 measurements of the layers.

3. Results and Discussion

3.1 Interaction between Ironsand and MgO

The interaction couples between ironsand and MgO were sintered in an atmosphere of pO_2 = 0.5 kPa in the temperature range of 1200 – 1300 ℃ for different times. Figure 1 presents the back-scattered electron (BSE) images of typical ironsand particles in direct contact with the MgO layer in the interaction couples sintered under different conditions. The BSE image of the interface marked in Figure 1(b) is shown in Figure 1(c) at a higher magnification. These sintered ironsand particles remained intact and there was no obvious morphology change due to the reaction between ironsand and MgO. There was some evidence of bonding (see the area inside the circle in Figure 1 (b)) at 1300 ℃, likely due to a reaction with a silicate phase. This was not observed in the sample

sintered at 1250 ℃ (Figure 1(a)).

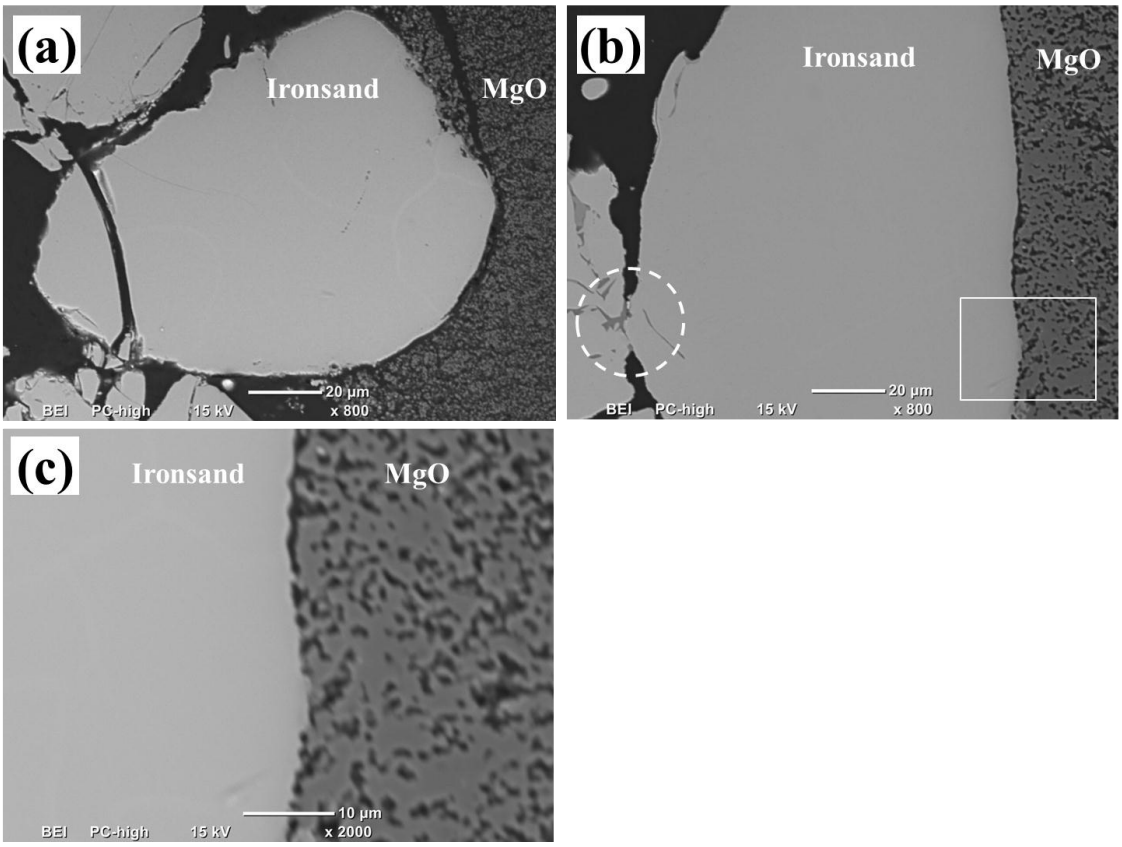

Figure 1. Back-scattered electron (BSE) images of typical ironsand particles close to the MgO layer in the interaction couples between ironsand and MgO sintered under different conditions. (a) 1250 ℃, 4 min; (b) 1300 ℃, 8 min; (c) 1300 ℃, 8 min, high magnification.

Figure 2 shows the chemical composition across the interface between ironsand and MgO flux in a sample sintered at 1200 ℃ for 4 min. Approximately 9 wt% Mg and 5 wt% Fe were present in the ironsand matrix and MgO layer, respectively. The original ironsand particles contained about 3 wt% Mg in the titanomagnetite phase according to SEM/EDS analysis. The lack of concentration gradients of Mg within the titanomagnetite particle and iron in MgO indicate that the diffusion of Mg and Fe ions was fast. In comparison, a very small amount of Ti (0.3 wt%) was found in the magnesia layer near the interface. This may be the result of the low diffusivity of Ti^{4+} in the ironsand and MgO phases.

Generally, one ion may take the place of another to form a solid-solution series if the difference between their ionic radii does not exceed 15% of the radius of the smaller ion [9]. The ionic radius of Fe^{2+} ion is 92 pm which is close to that of Mg^{2+} ion (86 pm). Due to their similar atomic size and identical charge, Fe^{2+} ions can replace Mg^{2+} ions without distorting the overall structures of minerals such as in olivine and spinel [10]. In this study, during sintering at a high temperature, Mg^{2+} ions from MgO diffused into the lattice of titanomagnetite to form $MgFe_2O_4$ - Fe_3O_4 solid solution, and simultaniously Fe^{2+} ions diffused in the opposite direction into MgO. Only very limited Ti^{4+} ions (about 0.25 wt%) diffused into MgO. This is likely due to the difference in its ionic radius (74pm) and valency.

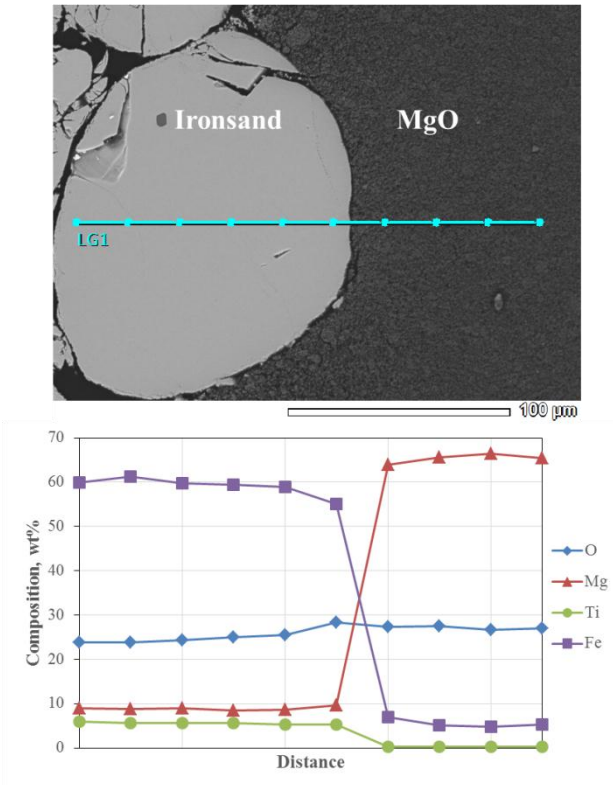

Figure 2. BSE image and the chemical composition near the interface between ironsand and MgO layers in a sample sintered at 1200 ℃ for 4 min.

Figure 3 presents a BSE image of typical ironsand particles in a sample sintered at 1300 ℃ for 8 min, and the chemical compositions at different points marked in Figure 3 are listed in Table 1. It should be noted that when an elemental content is less than 1 wt%, the number is only indicative due to the accuracy limits of EDS analysis. Points

1 and 2 represent the relict titanomagnetite particles in which the Mg content increased to over 8 wt%. Besides enhanced diffusion of ions, the higher sintering temperature also improved the sintering of ironsand particles. As shown in Figure 3, although the contour of each ironsand particle remained intact, they were bonded together by silicate phase (Points 3 and 4). During sintering at the high temperature, a small amount of silicate phase with low melting point was generated and melted due to the presence of impurities in the original ironsand, which was beneficial to the aggregation of ironsand particles. It is noted that the silicate phase contained approximately 7 wt% of Mg and Ca. The diffusion of Mg to the contacts between ironsand particles is likely to assist the formation of a liquid silicate phase.

However, significant diffusion of Mg^{2+} ions into the Fe_3O_4 lattice of ironsand can stabilise the system of FeOx-MgO and hinder the dissolution of ironsand particles. As shown in Figure 4, the liquidus temperature of the FeOx-MgO system [11] increases gradually with increasing MgO content.

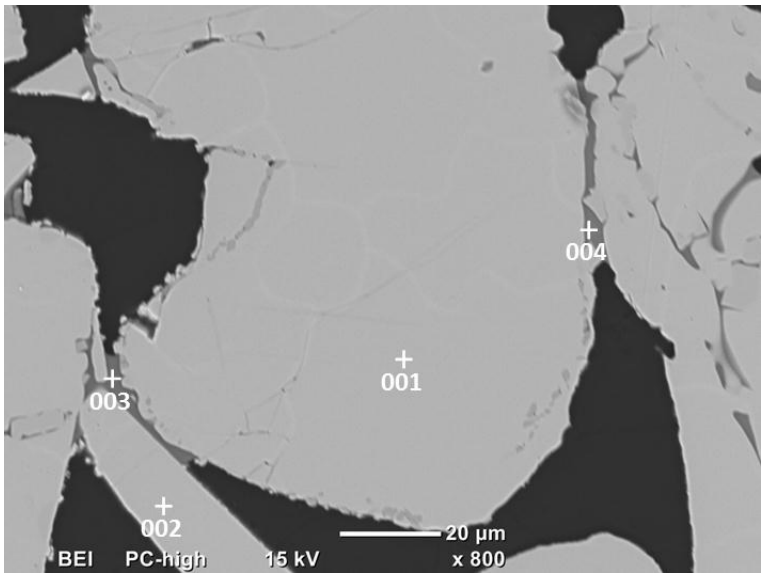

Figure 3. BSE images of typical ironsand particles in the interaction couples between ironsand and MgO sintered at 1300 ℃ for 8min.

Table 1. Elemental compositions (wt%) at the points marked in Figure 3 and corresponding phases.

Point no.	Fe	Ca	Ti	Mg	Si	Al	Phase identified
1	62.0	0.1	5.2	8.1	0.1	1.9	Titanomagnetite
2	61.5	0.1	5.5	8.7	0.2	2.1	Titanomagnetite
3	12.3	7.6	3.2	7.6	22.5	6.9	Silicate
4	12.2	7.8	3.8	7.3	23.6	6.6	Silicate

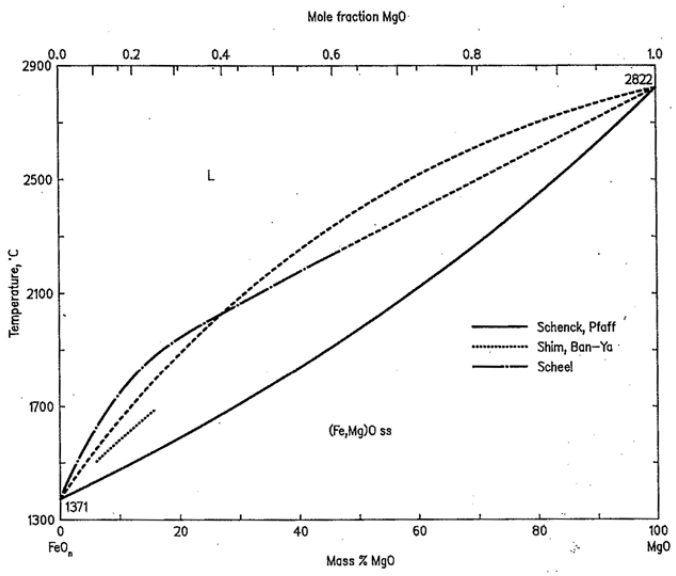

Figure 4. Liquidus temperature of FeOx-MgO system [11].

3.2 Interaction between Ironsand and CaO

The interaction couples between ironsand and CaO were sintered in an atmosphere of pO_2 = 0.5 kPa in the temperature range of 1200 – 1325℃ for different times. The microstructure of formed mineral phases was examined by optical microscope and SEM/EDS.

A reaction zone between the ironsand and CaO layers was generated in the specimens during sintering in this study. Figure 5 presents the BSE images of the interface between the ironsand and CaO layer sintered under different conditions. As shown in Figure 5(a), a reaction zone with a width of approximately 3 μm was formed at the boundary of

ironsand particles and CaO sintered at 1200 ℃ for 4 min. The reaction zone thickness increased with increasing sintering time (see Figure 5(b)), showing a reaction zone of thickness of ~12 μm after 20 min. A morphological change of the reaction zone with sintering temperature was also observed. Figure 5(c) shows the interface between the ironsand and CaO layers in samples sintered at 1250 ℃ for 4 min and the thickness of the reaction zone increased to approximately 8 μm. When sintered at 1300 ℃ for 4 min, the average thickness of the reaction zone increased significantly to about 30 μm, as shown in Figure 5(d).

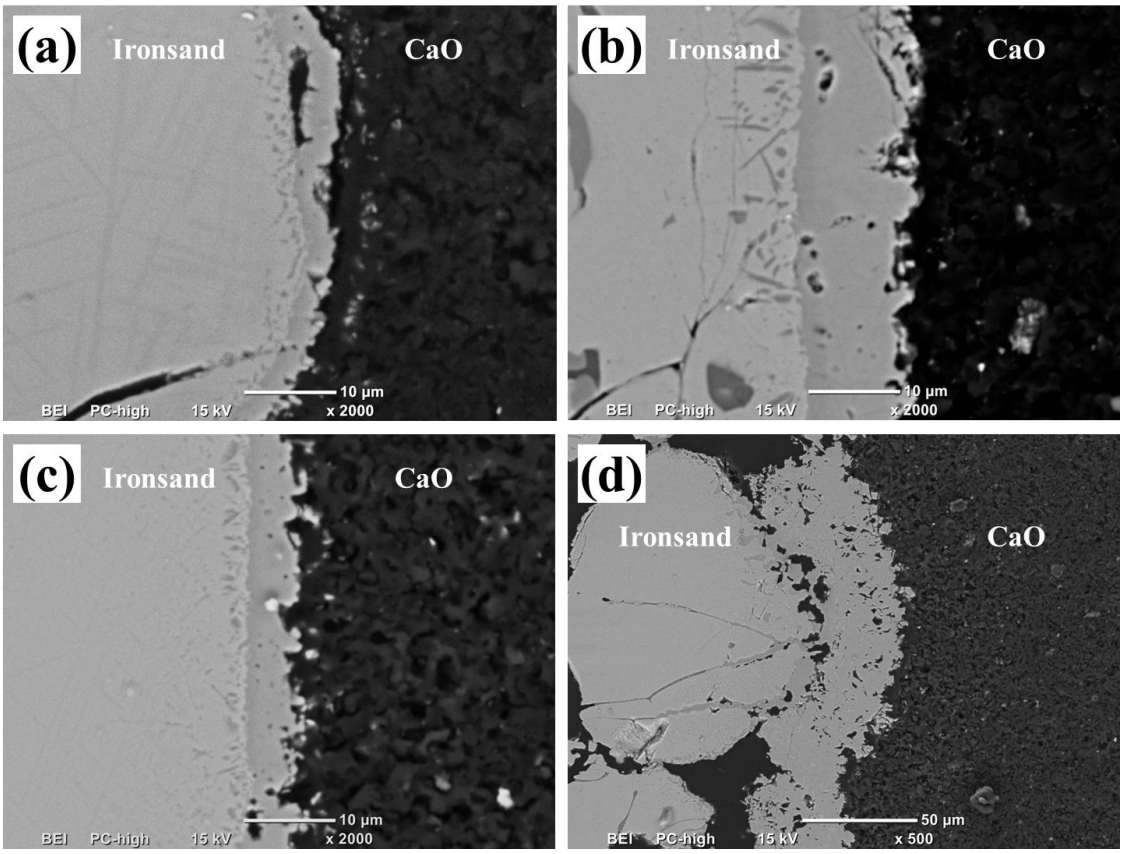

Figure 5. BSE images of the interaction couples of ironsand and CaO sintered under different conditions. (a) 1200 ℃, 4 min; (b) 1200 ℃, 20 min; (c) 1250 ℃, 4 min; (d) 1300 ℃, 4 min.

Figure 6 shows the BSE image and elemental distribution of a reaction zone between ironsand and CaO in a specimen heated at 1200 ℃ for 20 min. The chemical compositions at different points presented in Figure 6 were examined by EDS analysis and are listed in Table 2. The reaction zone contained a high concentration of Ca which

was relatively uniformly distributed. However it can be noted from the distributions of Fe and Ti that there was a narrow band within the reaction zone next to the titanomagnetite matrix, corresponding to a band in the BSE image with a slightly darker colour. EDS analysis shows that the band (point 3) had a distinct composition from the major part of the reaction zone (points 4 and 5), but was the same as those distributed dark areas (point 2) within the titanomagnetite matrix. As shown in Table 2, the major part of the reaction zone was dominated by a calcium ferrite phase containing about 27 wt% Ca and 36 wt% iron, while the Ti-rich subzone and the distributed dark areas in the titanomagnetite matrix were complex perovskite phase of Fe and Ca, containing 16-24 wt% of Ti. Point 6 proved to be in the lime layer, which also contained low levels of iron (3.71 wt%). Problems in sample preparation resulted in some loss of CaO. As a result the CaO side of the ironsand-CaO couple shown in Fig 6 was not in the same plane as the other part of the sample, making the absolute signal strength of Ca in this area weaker.

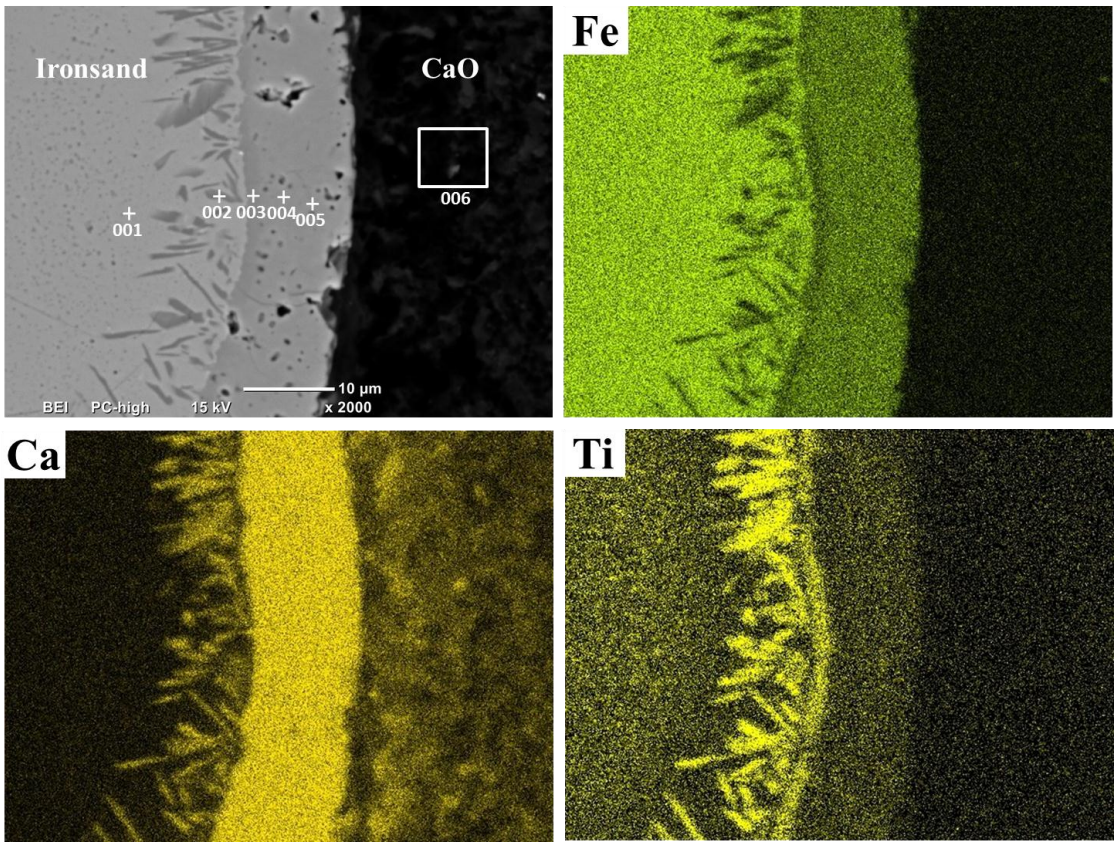

Figure 6. BSE image and EDS mapping of a reacted zone between ironsand and CaO in a specimen sintered at 1200 ℃ for 20 min.

Table 2. Elemental composition (wt%) of grains marked in Figure 6 and corresponding phases.

Point no.	Fe	Ca	Ti	Mg	Si	Al	Phase identified
1	63.8	1.0	2.48	3.5	0.3	2.7	Titanomagnetite
2	14. 5	24.0	23.6	0.3	0.4	0.6	Perovskite
3	22.3	27.7	16.0	0.2	2.8	1.4	Perovskite
4	35.7	27.4	1.3	0.2	0.8	2.0	Calcium ferrite
5	36.2	27.0	1.2	0.4	0.3	1.4	Calcium ferrite
6	3.7	57.9	0.1	2.0	0.6	0.1	CaO

It is known that the reactions between CaO and Fe_2O_3 and TiO_2 are favoured thermodynamically which can be presented as follows:

$$CaO\,(s) + Fe_2O_3\,(s) = CaFe_2O_4\,(s) \quad (1)$$

$$\Delta G^{o} = -29519 - 9.93T\ (J)$$

$$CaO\,(s) + TiO_2\,(s) = CaTiO_3\,(s) \quad (2)$$

$$\Delta G^{o} = -80150 - 6.47T\ (J)$$

The standard Gibbs free energy changes of the reactions were calculated using data from the ref. [12] in the range of 1200 to 1325 ℃. Thermodynamically, the reaction between TiO_2 and CaO is favoured over that between Fe_2O_3 and CaO.

When the interaction couples of ironsand and CaO were sintered, Ca^{2+} ions from CaO diffused into the lattice of Fe_3O_4, while Fe^{2+}, Fe^{3+} and Ti^{4+} ions from ironsand diffused in the opposite direction into CaO. As a result, a reaction zone which was rich in Ca, Fe and Ti was generated between the two layers. Due to a low diffusivity of Ti^{4+}, it was accumulated near the titanomagnetite matrix boundary and combined with relatively mobile Ca and formed the perovskite phase.Ca also diffused inside the titanomagnetite matrix and formed distributed perovskite phase where the Ti content was much higher than the average after Fe diffused away. Meanwhile, a calcium ferrite phase was formed close to the CaO layer due to the reaction between CaO and iron oxides and the relatively higher diffusion rates of Fe^{2+} and Fe^{3+}.

Figure 7 shows the BSE image and EDS mapping of an interaction couple between ironsand and CaO heated at 1300 ℃ for 20 min. A coarsened reaction zone was observed around the interface of the two layers whose development may have been affected by separation from the ironsand layer. The Ti rich and Fe rich bands in the reaction zone can be clearly identified from the Fe and Ti distributions. A part of Fe-rich subzone was penetrated into CaO layer, which was repeated in specimens sintered at this severe sintering condition, but was never observed in other conditions. This excludes the possibility of mixing ironsand particles into the CaO layer, and penetration of Fe into CaO was through diffusion of Fe. It can also been seen that Ca penetrated deeply into the ironsand layer and distributed between the titanomagnetite particles.

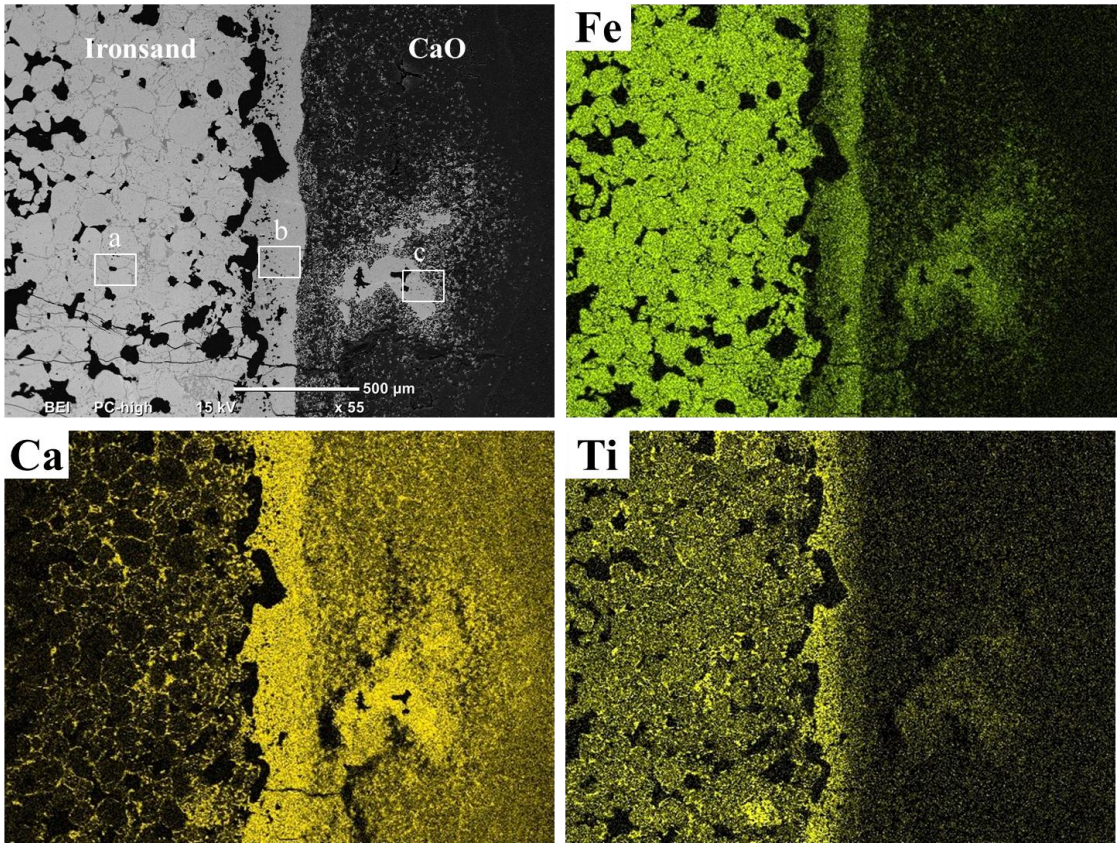

Figure 7. BSE image and EDS mapping of an interaction couple between ironsand and CaO sintered at 1300 ℃ for 20 min. The details of the small areas marked as a, b and c are presented in Figure 8.

The BSE images of three different typical areas in Figure 7 are shown in Figure 8 with higher magnification. The chemical compositions at different points presented in Figure

8 obtained by EDS analysis are summarised in Table 3. Figure 8(a) represents the microstructure of the ironsand layer after sintering. Although ironsand boundaries were still clearly seen, they were intimately bonded by perovskite phase (Points 3 and 4) and a lesser amount of silicate phase (Point 5). The reaction zone presented in Figure 8(b) consisted of perovskite (Points 6 and 7) and calcium ferrite (Points 8 and 9) phases. Small amounts of iron oxides were also finely distributed in the reaction zone represented by Points 10 and 11. Figure 8(c) shows the microstructure of calcium ferrite penetrated into the CaO layer. A lot of calcium ferrite particles were aggregated together (as represented by Point 12) as well as finely distributed in the CaO layer (Point 13).

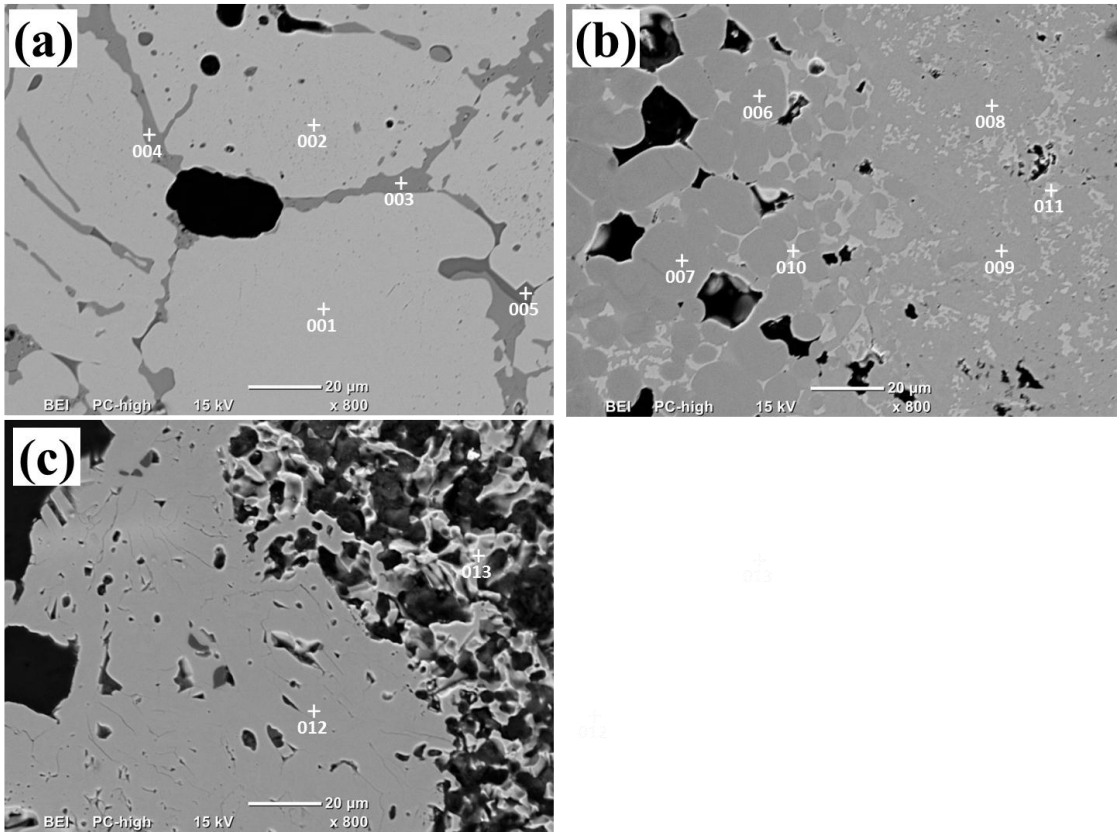

Figure 8. The higher magnification BSE images of the areas marked in Figure 7.

Table 3. Elemental composition (wt%) of grains marked in Figure 8 and corresponding phases.

Point no.	Fe	Ca	Ti	Mg	Si	Al	Phase identified
1	71.4	0.7	3.5	1.6	0.3	1.5	Titanomagnetite
2	69.4	1.1	4.4	1.4	0.5	1.6	Titanomagnetite
3	12.0	27.8	23.7	0.3	1.0	0.7	Perovskite
4	10.8	27.2	26.0	0.2	0.8	0.6	Perovskite
5	11.8	30.1	3.8	0.5	13.2	3.6	Silicate
6	29.0	29.4	9.4	0.4	1.6	1.1	Perovskite
7	26.9	28.2	10.7	0.5	1.4	1.0	Perovskite
8	36.6	28.6	2.4	0.4	0.8	1.4	Calcium ferrite
9	37.6	28.9	2.3	0.3	0.9	1.6	Calcium ferrite
10	65.5	3.6	0.5	4.4	0.2	1.7	Iron oxides
11	66.1	3.7	0.7	4.3	0.3	1.6	Iron oxides
12	37.3	28.6	1.8	0.7	0.6	1.4	Calcium ferrite
13	31.4	24.9	1.6	1.1	0.5	1.4	Calcium ferrite

Enhanced sintering conditions (higher temperature and longer sintering time) significantly enhanced the assimilation and correspondingly resulted in a coarsened reaction zone. The formation of low melting point calcium ferrite phase in the Fe-rich subzone greatly promoted mass transfer and futher penetration of calcium ferrite into the CaO layer. In contrast, the TiO_2-rich subzone became wider and did not melt since TiO_2 stablised the system of CaO-TiO_2-FeOx [11] and hindered its further dissolution, as illustrated in Figure 9. The liquidus temperature increases gradually with the introduction of TiO_2 along the tie-line from CaO·Fe_2O_3 (mono calcium ferrite) to CaO·TiO_2 (perovskite).

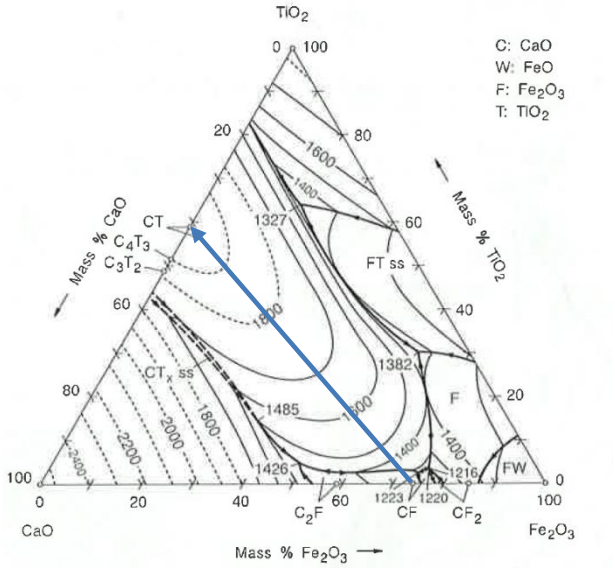

Figure 9. Liquidus temperature of CaO-TiO_2-FeOx system [11].

3.3 Interaction between Ironsand and Dolomite

Investigation of the decomposition of dolomite showed that under CO_2 the reaction takes place in two distinct stages. Dolomite decomposes into calcite and magnesium oxide in the range of 550 – 800 ℃ (Reaction 3), and then calcite dissociates (Reaction 4) in the range of 900 – 960 ℃.

$$CaMg(CO_3)_2\,(s) = CaCO_3\,(s) + MgO\,(s) + CO_2\,(g) \quad (3)$$

$$CaCO_3\,(s) = CaO\,(s) + CO_2\,(g) \quad (4)$$

As a result, the interaction between ironsand and dolomite layers practically involved ironsand with CaO and MgO. This was investigated in an atmosphere of pO_2 = 0.5 kPa in the temperature range of 1200 – 1325 ℃ for different times. The morphological changes of the interaction couples with sintering temperature and time were observed, as shown in Figure 10. A reaction zone was formed between the two layers with an average thickness of 3.8 μm after sintering at 1200 ℃ for 4 min, as shown in Figure 10(a). Its interface towards the dolomite face was sometimes jagged, but with no sharp edges or straight sides. The thickness of the reaction zone increased to about 13 μm as sintering time increased to 20 min (Figure 10(b)). Figure 10(c) shows the reaction zone in a specimen sintered for 4 min at 1250 ℃ with an average thickness of 7.8 μm. It is

common in Figures 10 (a) through (c) that some of the reaction product was penetrated into the dolomite layer, which became extreme in Figure 10(d) where the specimen was sintered at 1300 ℃ for 4 min. The formation of reaction zone was significantly enhanced with a distinct increase in the average thickness to over 100 μm. The reaction zone consisted of several different subzones as shown by their difference in brightness.

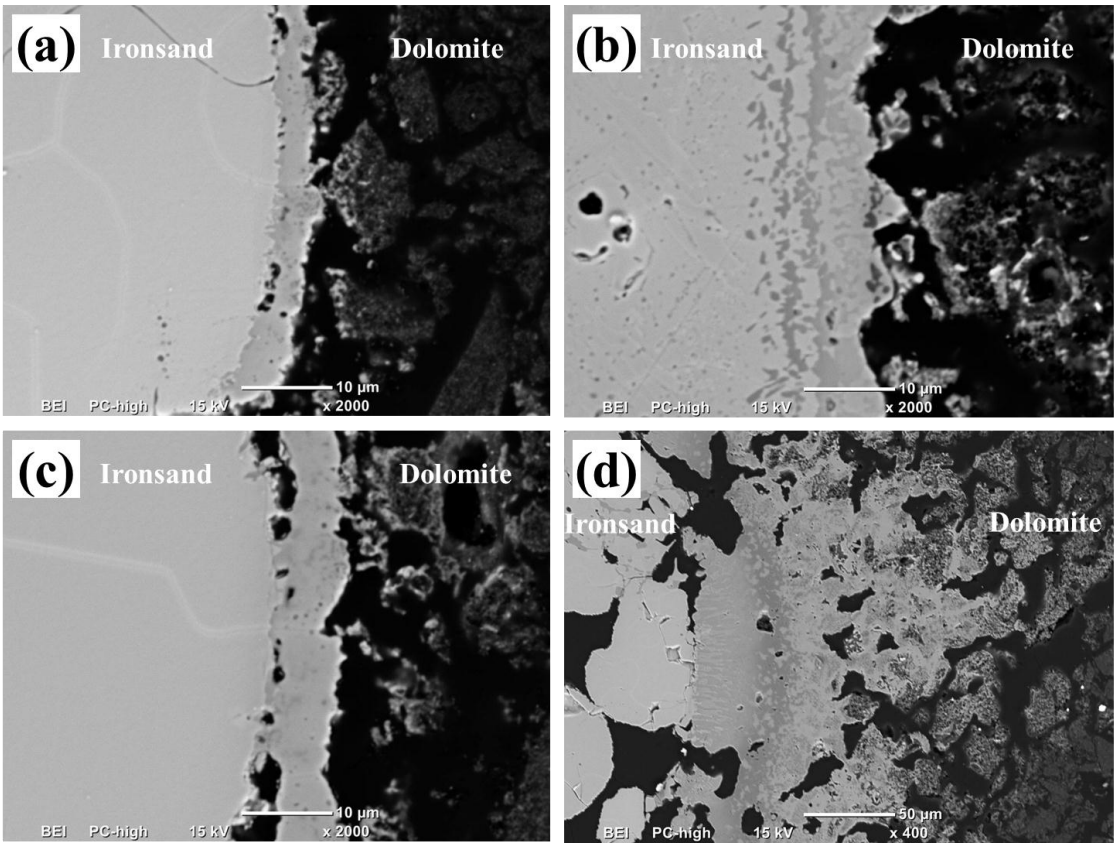

Figure 10. BSE images of the interaction couples of ironsand and dolomite sintered under different conditions. (a) 1200 ℃, 4 min; (b) 1200 ℃, 20 min; (c) 1250 ℃, 4 min; (d) 1300 ℃, 4 min.

Figure 11 shows the BSE images and EDS mapping of the interaction couple between ironsand and dolomite heated at 1300 ℃ for 20 min. Discrete titanomagnetite particles with very limited Ca and Mg concentrations were present within the ironsand layer. A coarsened (diffused edge on the dolomite side) reaction zone with broad penetration of Fe and Ti into the dolomite layers was observed. From the elemental distribution of the reaction zone, Fe, Ca, Ti and Mg were non-uniformly distributed. At least three subzones can be identified, one being the broadest part which penetrated into the

dolomite layer and contained high levels of Fe and Ca, while another was close to the unreacted ironsand layer with relatively high Ti and Ca contents, which formed a discontinuous boundary on the ironsand layer. Between these two subzones was a band appearing similar to the perovskite band observed in the sintered ironsand and CaO reaction couple, but containing significant amount of Mg.

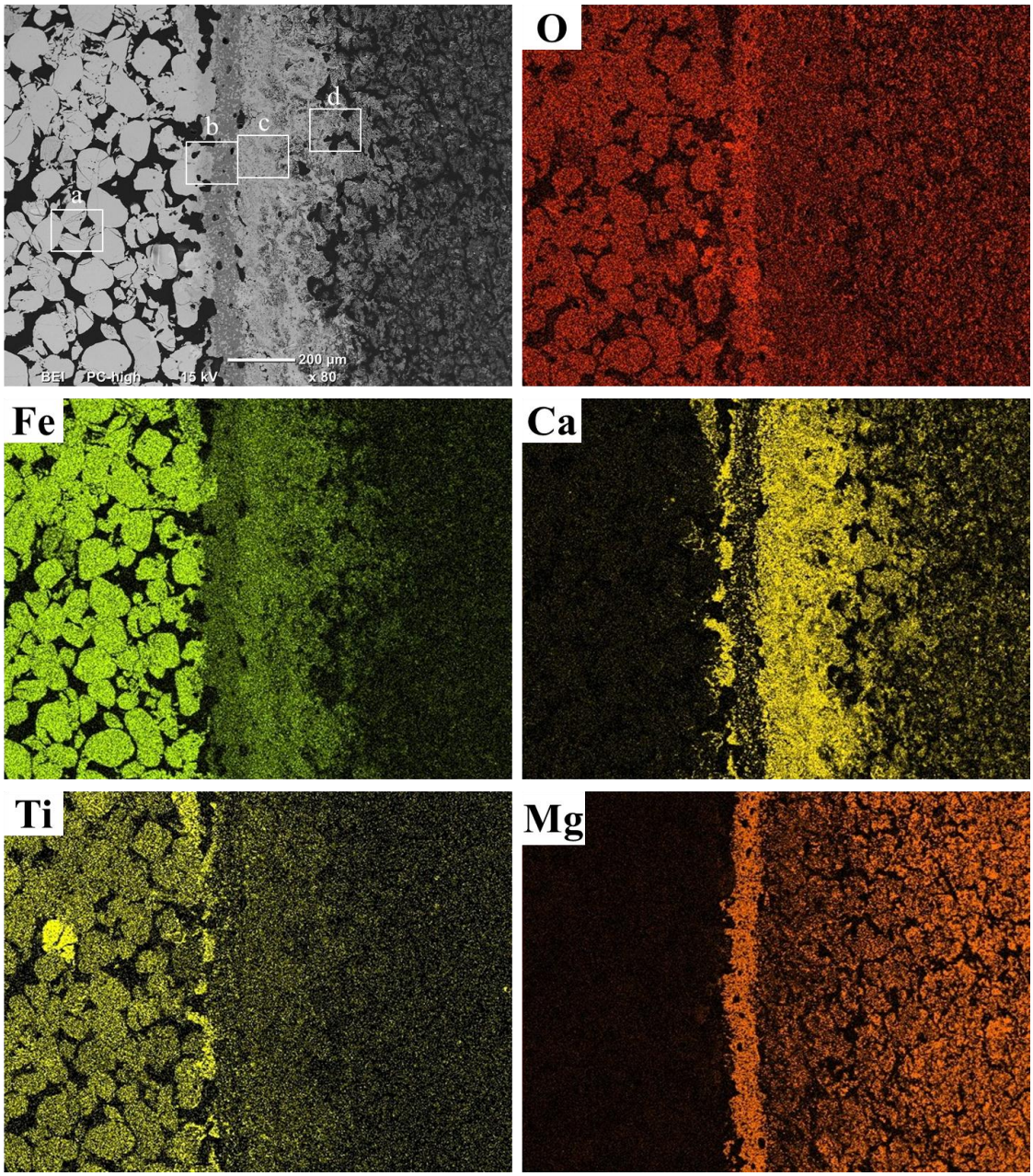

Figure 11. BSE image and EDS mapping of an interaction couple between ironsand and dolomite sintered at 1300 ℃ for 20 min. The detailed information in areas a through d is presented in Figure 12.

Figure 12 shows the BSE images of four different typical areas in Figure 11 at higher magnification. The chemical compositions at different points marked in Figure 12 were examined by EDS analysis and summarised in Table 4. As shown in Figure 12(a), the morphology of the ironsand layer after sintering at 1300 ℃ for 20 min was very similar to that occurring in sintered reaction couples of ironsand and MgO (Figure 3). The ironsand particles remained intact and were weakly bonded by narrow necks. A small amount of silicate bonding phase (Points 3 and 4) contained relatively low concentrations of Ca and Mg, indicating that the assimilation between the ironsand particles which were located several particles away from the interface was not affected by the presence of dolomite. The concentrations of Mg and Ca in the relict titanomagnetite particles (Points 1 and 2) were also hardly changed.

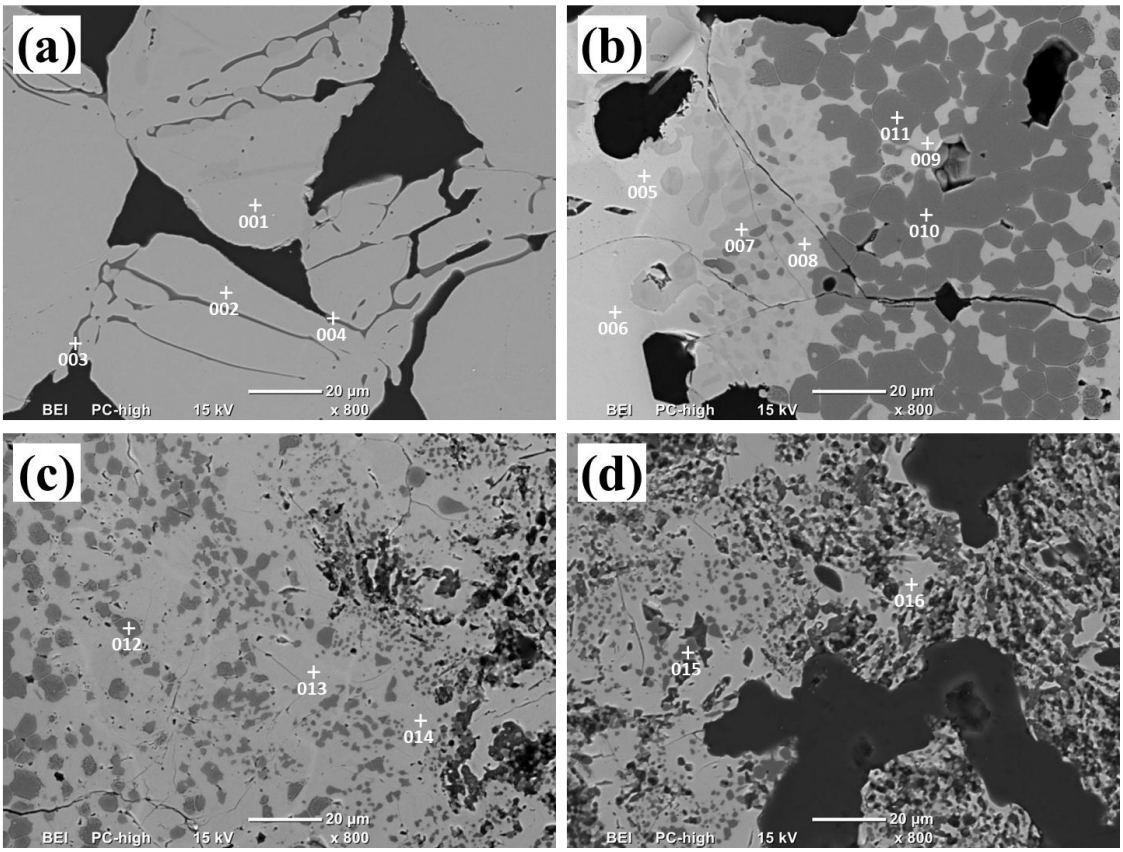

Figure 12. BSE images of phases marked in Figure 11.

Table 4. Elemental composition (wt%) of grains marked in Figure 12 and corresponding phases.

Point no.	Fe	Ca	Ti	Mg	Si	Al	Phase identified
1	65.9	0.4	5.6	3.0	0.3	1.9	Titanomagnetite
2	68.1	0.2	4.8	2.6	0.3	1.4	Titanomagnetite
3	21.0	3.5	4.3	1.9	20.9	5.8	Silicate
4	16.7	5.7	5.2	1.6	22.8	7.3	Silicate
5	65.3	1.3	1.1	7.0	0.4	1.7	Titanomagnetite
6	67.5	0.5	1.5	4.1	0.3	1.6	Titanomagnetite
7	12.4	26.5	22.4	1.1	0.6	0.9	Perovskite
8	20.4	27.4	15.4	1.7	1.5	1.2	Perovskite
9	25.5	27.3	10.4	1.7	0.9	0.9	Perovskite
10	25.9	0.3	0.5	42.0	0.4	0.8	MgO-FeO
11	24.5	0.8	0.7	44.7	0.3	0.9	MgO-FeO
12	24.4	0.6	0.4	43.4	0.4	1.1	MgO-FeO
13	33.7	28.2	3.8	2.1	1.0	1.4	Calcium ferrite
14	36.9	28.7	1.8	1.8	0.5	1.3	Calcium ferrite
15	6.2	0.7	0.4	59.7	0.4	0.4	MgO-FeO
16	36.7	28.4	2.3	2.3	0.6	1.2	Calcium ferrite

Figure 12(b) shows the microstructure of the Ti-rich subzone and Mg-rich subzone in samples sintered at 1300 ℃ for 20 min. The Ti-rich subzone marked by Point 7 and next to the titanomagnetite (Points 5 and 6) proved to be complex perovskite phase containing some Fe. The phase with brightness between perovskite and titanomagnetite (Point 8), which was also found to be distributed in the dark grey area (Point 9), was another form of perovskite containing less Ti but more Fe. The Mg-rich band shown in Figure 11 was seen to consist of round dark grey grains (Points 10 and 11), and contained mainly MgO-FeO solid solution. The microstructure of the subzone rich in Fe and Ca is presented in Figure 12(c), which was found, as expected, to mainly consist of calcium ferrite (Points 13 and 14) but also contained discrete fine particles of MgO-FeO solid solution (Point 12). Figure 12(d) shows the penetration of calcium ferrite particles

into the dolomite layer. A large amount of fine calcium ferrite particles and MgO-FeO particles (Point 15) were distributed in the dolomite layer.

The mechanisms of phase formation in the interaction couple of ironsand and dolomite can be summarised in Figure 13. During sintering, Mg^{2+} and Ca^{2+} ions from the dolomite (MgO and CaO) layer diffused towards the ironsand layer, while Fe^{2+}, Fe^{3+} and Ti^{4+} ions from ironsand diffused in the opposite direction into MgO and CaO. Consequently, the reaction zone which was rich in Ca, Fe, Mg and Ti was generated between the two layers. Because Ti^{4+} diffused at a slower rate than $Fe^{2+}$and Fe^{3+}, a perovskite phase was formed as a result of reaction between CaO and accumulated TiO_2 close to the relict ironsand layer. This perovskite acted as a barrier to the diffusion of Mg^{2+} ions, which accumulated next to the perovskite layer and combined with Fe to form a FeO-MgO solid solution. Shown in Figure 12 (a), the contents of Mg in slicate bonding phase and ironsand were low, since the prescence of perovskite phase hindered the diffusion of Mg into ironsand layer. In contrast, in sintered ironsand-MgO couple shown in Figure 3, Mg significantly diffused into ironsand layer and benefited the generation of silicate bonding phase. This FeO-MgO solid solution hindered the further diffusion of CaO towards the ironsand layer. Finally, further phase formation was due to the relatively higher diffusion rates of Fe^{2+} and Fe^{3+} through the perovskite and MgO-FeO solution barriers, and Fe and Ca combined to form calcium ferrite phase close to the CaO-MgO layer. This mechanism explains why Mg and Ca can individually diffuse into the titanomagnetite matrix and even penetrate deeply into the ironsand layers, but little of them enter into the ironsand layer from the MgO-CaO mixture. It also shows that the assimilation process mainly developed in the direction of the MgO-CaO layer through the diffusion of Fe.

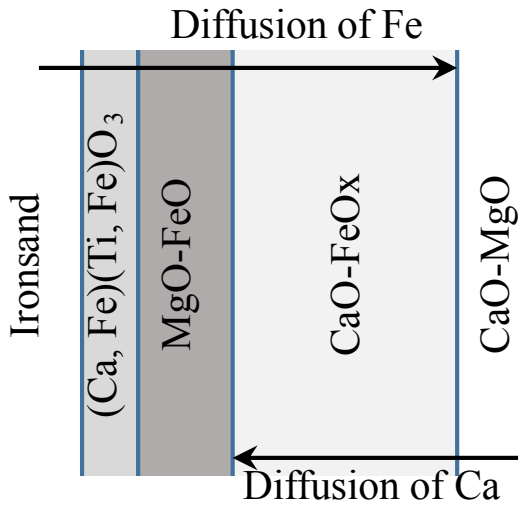

Figure 13. A diffusion model describing phase formation during sintering of an interaction couple between ironsand and dolomite.

With the increase in sintering temperature, the calcium ferrite phase with low melting point in the Fe-rich subzone firstly started to melt and promoted the futher spread of calcium ferrite into the dolomite layer, as shown in Figure 11. The perovskite phase and MgO-FeO solid solution remained stable at the higher sintering temperature due to their relatively higher melting points.

4. Conclusions

In this study, the reaction couples between ironsand and flux materials (CaO, MgO and dolomite) were sintered in an atmosphere of pO_2 = 0.5 kPa in the temperature range of 1200 - 1300 ℃ for different times. The main conclusions are as follows.

(1) Mg^{2+} ions significantly diffused into the lattice of ironsand when the ironsand was sintered with MgO, which stabilised the system of FeOx-MgO and hindered the assimilation of ironsand particles.

(2) During sintering of ironsand with CaO, a reaction zone consisting of perovskite and calcium ferrite occurred between the two layers. When sintered at higher temperature (1300 ℃), the ironsand particles were intimately bonded by mainly perovskite and a

lesser amount of silicate phases. Partial melting of calcium ferrite phase greatly promoted mass transfer and futher penetration of calcium ferrite into the CaO layer.

(3) In terms of sintering of ironsand with dolomite, perovskite and calcium ferrite were also generated in the reaction zone. A MgO-FeO solid solution was formed close to the perovskite phase, since the formation of perovskite phase hindered the further diffusion of Mg^{2+} ions into the ironsand layer. Increasing sintering temperature significantly enhanced the penetration of calcium ferrite phase into the dolomite layer; whereas the perovskite phase and MgO-FeO solid solution remained at high sintering temperature due to their relatively higher melting points which hindered penetration of Ca and Mg into the ironsand layer and suppressed the bonding between ironsand particles.

Acknowledgements

The project is financially supported by the BlueScope Steel Metallurgical Centre Projects Grant. Zhe Wang is a recipient of University of Wollongong Deputy Vice Chancellor's Special Scholarship and International Postgraduate Tuition Award. The authors would like to acknowledge the Electron Microscopy Center (EMC) at University of Wollongong for SEM/EDS analysis.

References

[1] H. A. Cocker, J. L. Mauk, H. Rogers, A. B. Padya and J. Ogiliev, Where is the Titanium in the Ironsands? - Ti Partitioning in the Magnetic Fraction, Proceedings of the AusIMM New Zealand Branch 43rd Annual Conference, AusIMM New Zealand Branch, Alexandra, (2010), 165-174.

[2] J. B. Wright, Iron-titanium Oxides in Some New Zealand Ironsands, *New Zealand Journal of Geology and Geophysics*, **7** (1964), 424-444.

[3] J. B. Wright and J. F. Lovering, Electron-probe Micro-analysis of the Iron-titanium Oxides in some New Zealand Ironsands, *Mineralogical Magazine*, **35** (1965), 604-621.

[4] Z. Wang, D. Pinson, S. Chew, H, Rogers, B. J. Monaghan, M. I. Pownceby, N. A. S. Webster and G. Zhang, Behaviour of New Zealand Ironsand during Iron Ore Sintering, *submitted to Metallurgical and Materials Transactions B*, (Chapter 2).

[5] M. B. Turner, S. J. Cronin, R. B. Stewart, M. Bebbington and I. E. M. Smith, Using Titanomagnetite Textures to Elucidate Volcanic Eruption Histories, *Geology*, **36** (2008), 31-34.

[6] N. J. Bristow and C. E. Loo, Sintering Properties of Iron Ore Mixes containing Titanium. *ISIJ International*, **32** (1992), 819-828.

[7] Z. Wang, D. Pinson, S. Chew, B. J. Monaghan, M. I. Pownceby, N. A. S. Webster, H. Rogers and G. Zhang, Effect of Sintering Conditions on the Formation of Mineral Phases during Iron Ore Sintering, *to be submitted*, (Chapter 3).

[8] L. H. Hsieh and J. A. Whiteman, Effect of Oxygen Potential on Mineral Formation in Lime-fluxed Iron Ore Sinter, *ISIJ International*, **29** (1989), 625-634.

[9] N. Rogers, An Introduction to Our Dynamic Planet, Cambridge University Press, Cambridge, (2008), 146.

[10] C. V. A. Duke and C. D. Williams, Chemistry for Environmental and Earth Sciences, CRC Press, Boca Raton, (2007), 76.

[11] K. C. Mills, Slag Atlas, 2nd edition, Verlag Stahleisen GmbH, D-Düsseldorf, (1995).

[12] M. Binnewies and E. Milke, Thermochemical Data of Elements and Compounds, 2nd edition, Wiley-VCH Verlag GmbH, Weinheim, (2002).

CHAPTER 5. EFFECT OF ADDITION OF MILL SCALE ON SINTERING OF IRON ORES

Effect of Addition of Mill Scale on Sintering of Iron Ores

Zhe Wang[1], David Pinson[2], Sheng Chew[2], Brian J. Monaghan[1], Mark I. Pownceby[3], Nathan A.S. Webster[3], Harold Rogers[2], Guangqing Zhang[1]

1. School of Mechanical, Materials and Mechatronic Engineering, University of Wollongong, NSW 2522, Australia
2. BlueScope Technology and Planning, P. O. Box 202 Port Kembla, NSW 2505, Australia
3. CSIRO Mineral Resources Flagship, Private Bag 10, Clayton South, VIC 3169, Australia

Abstract

Iron-rich (65-70% total Fe) mill scale generated during processing by steel mills can potentially be recycled by using it as a ferrous raw material in the sintering process. The effect of mill scale addition on the phase formation of sintered specimens from an industrial sinter blend containing 0-15 wt% mill scale was examined and the mineral phases formed during sintering under various conditions (T = 1250-1325 ℃ and gas compositions of pO_2 0.5, 5 and 21 kPa) were quantitatively measured. For samples sintered in air (pO_2 = 21 kPa), there was negligible effect of mill scale addition on the phases formed. The oxidation of the mill scale was complete and phases such as Silico-Ferrite of Calcium and Aluminium (SFCA), SFCA-I, and hematite dominated. Under lower oxygen partial pressures (pO_2 = 0.5 or 5 kPa) and throughout the temperature range examined, the mill scale was converted to magnetite, with the extent of reaction controlled by the hematite-magnetite conversion kinetics. When sintered in the gas mixture with pO_2 = 5 kPa, an increase in the mill scale content from 0 to 15 wt% resulted in a decrease of hematite and total SFCA phases and a corresponding increase in the amount of magnetite formed. The oxidation of wustite in mill scale to magnetite decreased partial pressure of O_2 and increased sintering temperature, which promoted the decomposition of hematite.

Key words: Mill scale, Sintering, Iron ore, Phase composition.

1. Introduction

Mill scale is a waste product containing wustite (FeO), magnetite (Fe_3O_4) and hematite (Fe_2O_3) that is formed on the surface of steel as a result of oxidation of the metal that occurs during continuous casting, reheating and hot rolling operations [1]. Mill scale is a valuable ferrous raw material, containing 65 - 70% iron [2] and often recycled through the sintering process [3].

During iron ore sintering, iron ore fines are mixed with limestone and coke breeze. The combustion of coke breeze supplies the necessary heat to achieve partial melting and reaction of the raw materials. It also produces a locally, relatively reducing atmosphere within the sinter bed during the heating stage. Once peak temperatures are reached, the agglomerated, semi-molten material slowly cools under a relatively oxidising atmosphere [4, 5]. The mill scale contains a high amount of Fe and low amounts of silica and alumina. Thus, recycling it through the sintering process reduces consumption of raw material like iron ore and limestone.

A further advantage in the use of mill scale is that as it is assimilated during sintering, the oxidation of wustite or magnetite provides a small fuel offset to the sintering process leading to a potential saving of fuel coke since the oxidation reactions of wustite and magnetite are exothermic [3]. The oxidation of magnetite ore to reduce coke consumption has been demonstrated by several investigators. Button and Lundh [6], using an ore blend containing 30 wt% magnetite in pot tests, found that compared to the 100 wt% hematite ore blend, the maximum sintering temperature at a given coke rate was about 60℃ higher, which was equivalent to about 0.75 wt% coke breeze. Panigrahy et al. [7] studied the effect of blending 7 and 23 wt% of magnetite (Carol Lake concentrate) on the sintering of hematite ore in pilot scale test. It was found that a 10 wt% coke breeze saving was achieved by blending 23 wt% of magnetite.

Although there have been a number of sintering and oxidation of magnetite ore studies [8-11], there have not been many focused on understanding the effect of mill scale addition on the sintering process largely due to the complexity of the raw materials and variation of sintering conditions.

JSW Steel Ltd [3] in India conducted pot grate sintering experiments to investigate the influence of mill scale addition on sintering. The mill scale in the sinter mix was varied from 0 to 70 kg/t-sinter. It was shown that the FeO content of the sinter increased with the increase in mill scale addition, and sinter productivity decreased with an increase in the amount of mill scale addition due to a decrease in sinter bed permeability. The sinter strength initially increased and reached a maximum at mill scale addition of 40-50kg/t-sinter and declined afterwards. It was also found that the reduction degradation index and reducibility of the sinter decreased with the increase in mill scale addition which was attributed the increase in FeO content. In their sinter pot investigation, El-Hussiny et al. [12] similarly found that replacement of the initial iron ore concentrate with 5 wt% mill scale increased the overall sinter strength, but the productivity decreased due to mill scale addition. This distinction in conclusions on the productivity change is likely caused by the difference in the physical form of the mill scale used.

In this study, a mill scale sample was characterised using optical microscope and quantitative XRD followed by laboratory sinter assimilation tests designed to understand the effect of various levels of mill scale addition on the formation of mineral phases during iron ore sintering.

2. Experimental Procedure

2.1 Sintering Experiments

The starting materials for the iron ore sintering experiments were: a bulk iron ore blend, limestone, dolomite, manganese ore, cold return fines (CRF) and mill scale. All materials were supplied by BlueScope Ltd. Table 1 presents the chemical compositions of the raw materials as determined by XRF analysis. Each raw material component was crushed and screened to smaller than 200 μm. These were then mixed in the proportion corresponding to that of BlueScope Ltd's bulk sinter blend. To assess the effect of mill scale on sinter phase formation, four separate sinter blends were prepared with the mill scale contents varied from 0 to 15 wt%. The resulting sinter blend compositions are

given in Table 2. These blends were pressed into ~0.3 g cylindrical tablets of 5 mm diameter and ~5 mm height for the sintering experiments.

Table 1. The chemical compositions of raw materials, wt%.

Raw material	Total Fe	CaO	SiO_2	Al_2O_3	MgO	Mn	Loss on ignition
Iron ore blend	56.6	2.63	5.31	1.44	0.81	0.14	8.3
Limestone	0.11	54.22	0.9	0.32	0.49	0.02	43.6
Dolomite	1.21	29.04	1.69	0.3	19.65	0.12	45.7
Manganese ore	5.4	0.06	5.4	3.5	0.1	49.2	12.9
Mill scale	71	0.16	0.88	0.07	0.15	0.61	--

Table 2. Compositions of the sinter blends with different mill scale contents, wt%.

No.	Iron ore blend	Mill scale	CRF	Limestone	Dolomite	Mn ore
M0	66.8	0	20.1	8.2	1.4	0.4
M5	61.9	5	20.1	8.2	1.4	0.4
M10	57	10	20.1	8.2	1.4	0.4
M15	52.1	15	20.1	8.2	1.4	0.4

A schematic diagram of the sintering apparatus and procedure used has been described in detail elsewhere [13]. The setup is based on a vertical tube furnace with a working tube of 55 mm internal diameter through which a gas mixture of controlled composition was continuously passed. Experiments were conducted over a range of temperatures typical of iron ore sintering (1250, 1275, 1300 and 1325 ℃) and three gas compositions of pO_2 0.5, 5 and 21 kPa respectively. The furnace was preheated to a designated temperature, and then purged with the reactive gas mixture for at least 20 min prior to hanging a crucible containing the sinter tablet in the hot zone of the furnace. After sintering for 4 minutes, the samples were then cooled following one of two procedures: (1) rapid cooling by which the crucible was directly lifted to the cold top end of the furnace tube, and (2) slow cooling by which the crucible was first raised to a location at 1160 ℃ for 2.5 min before being further raised to the cold top end; the gas mixture was switched to purging air at the time the sample was lifted to the 1160 ℃ location.

The sintered tablets were mounted in epoxy resin and cut perpendicular to the top surface, and then polished for examination using optical microscopy and scanning electron microscopy (SEM). The optical microscopic digital images were obtained in reflected light and analysed using Leica Phase Expert software. Different phases (hematite, magnetite, and SFCA) as well as sample porosity were identified on the basis of homogeneous reflectivity. The principle of phase determination used by Phase Expert and an error analysis for the determination of phase composition of sinter samples are discussed in detail elsewhere [14]. One point to note is that Phase Expert cannot distinguish between the silicate phase and sample pores due to similar reflectivities and therefore the presence of any silicate phase was not included in the determination of the mineral phases within the sintered samples. Another limitation of the software is that it cannot effectively discriminate between the two SFCA microtypes, SFCA and SFCA-I, therefore these phases are reported as the sums of both.

2.2 Interaction Experiments

To investigate the detailed behaviour of mill scale particles during iron ore sintering, the mill scale was crushed and screened to obtain a particle size 425-600 μm. This sized mill scale was mixed with sample M0 (<200 μm) shown in Table 2 in a weight ratio of 1:9 and compressed into Ø5mm x 5mm tablets. The tablets were then sintered at different temperatures in the vertical furnace in the gas mixture containing 0.5 % O_2 and 99.5 % argon (i.e. pO_2 = 0.5kPa). After sintering for the required time, the samples were then cooled following the same procedures as used in the sintering experiments. The sintered tablets were mounted in epoxy resin and prepared for optical microscopic and SEM analysis.

3. Experimental Results

3.1 Characterization of Mill Scale

As shown in Table 1, the mill scale contained approximately 91 wt% FeO (total Fe content equivalent). Major impurities included: SiO_2 0.88 wt%, CaO 0.16 wt%, MgO

0.15 wt%, Al_2O_3 0.07 wt%, and Mn 0.61 wt%.

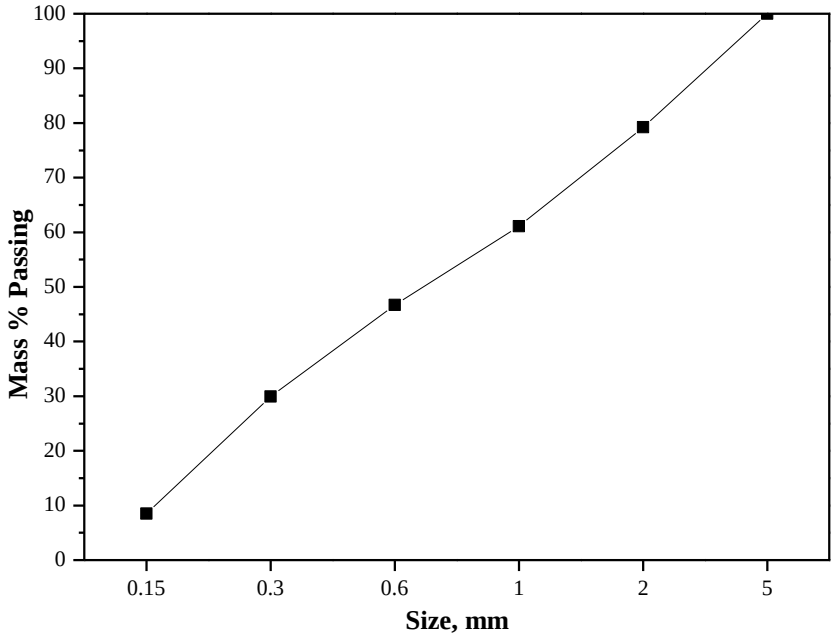

Figure 1. Cumulative size distribution of the mill scale sample prior to crushing.

Figure 1 shows the size distribution of the mill scale particles which was obtained by screening prior to crushing. It is indicated that they were 100% minus 5 mm and around 80 wt% was smaller than 2 mm. These mill scale particles are too fine for direct use in a blast furnace and so incorporation into sinter provides an appropriate method for its utilisation in ironmaking. Quantitative XRD analysis of the mill scale sample was conducted and Figure 2 shows the Rietveld fit of XRD data collected (Co Kα radiation). It indicates that the mill scale consists of approximately 53 wt% wustite, 35 wt% magnetite, 10 wt% hematite, 1 wt% goethite and 1 wt% green rust (i.e. $Fe_2O_3.H_2O$).

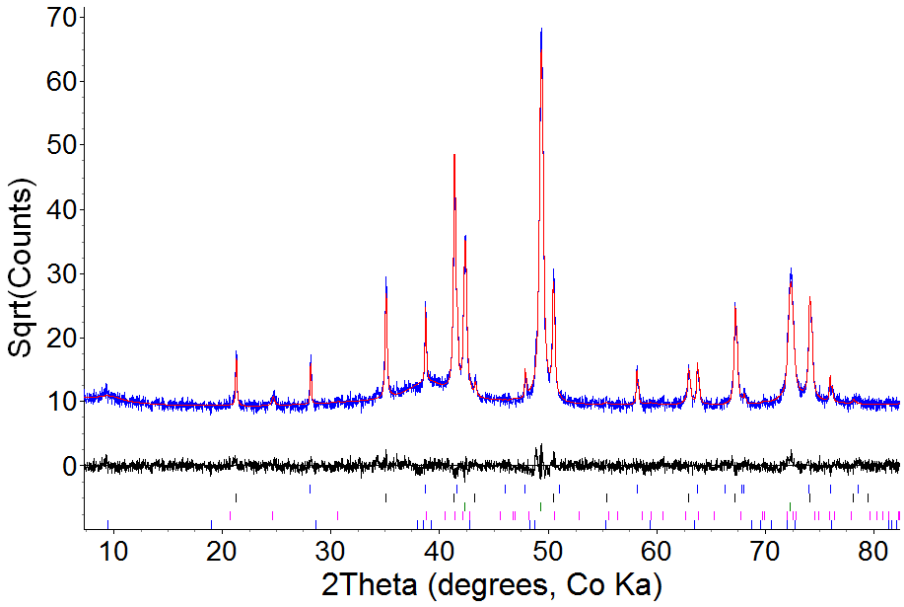

Figure 2. Rietveld fit of XRD data collected (Co Kα radiation) for the mill scale. Experimental data are shown as a scattered blue solid line, the calculated pattern the smooth red solid line, and the difference pattern the black solid line below. The vertical lines are the Bragg reflection markers for (top to bottom) hematite, magnetite, wustite, goethite and green rust.

Figure 3 presents a micrograph (reflected light) of a typical mill scale particle. The particle contains three layers of iron oxide. The hematite layer (white) is very thin and the middle layer displays the pinkish colour characteristic of magnetite under reflected light. The thickest layer is wustite (uniform mid-grey). Hydrated iron oxide phases could not be observed in this image. The results agree well with those in the literature [1, 15-17] where it has been shown that at temperatures above 570 ℃ the oxidation of iron in air leads to the formation of multi-layered scales consisting of wustite, magnetite, and hematite in that sequence, and with wustite being adjacent to the original metal. The much greater mobility of defects within wustite causes this layer to be very thick compared with the magnetite and hematite layers. Schwenk and Rahmel [16] found that the relative thickness of wustite : magnetite : hematite are in the ratio of roughly 95:4:1 at 1000 ℃. At temperatures below 570 ℃, wustite does not form and magnetite is found adjacent to the metal.

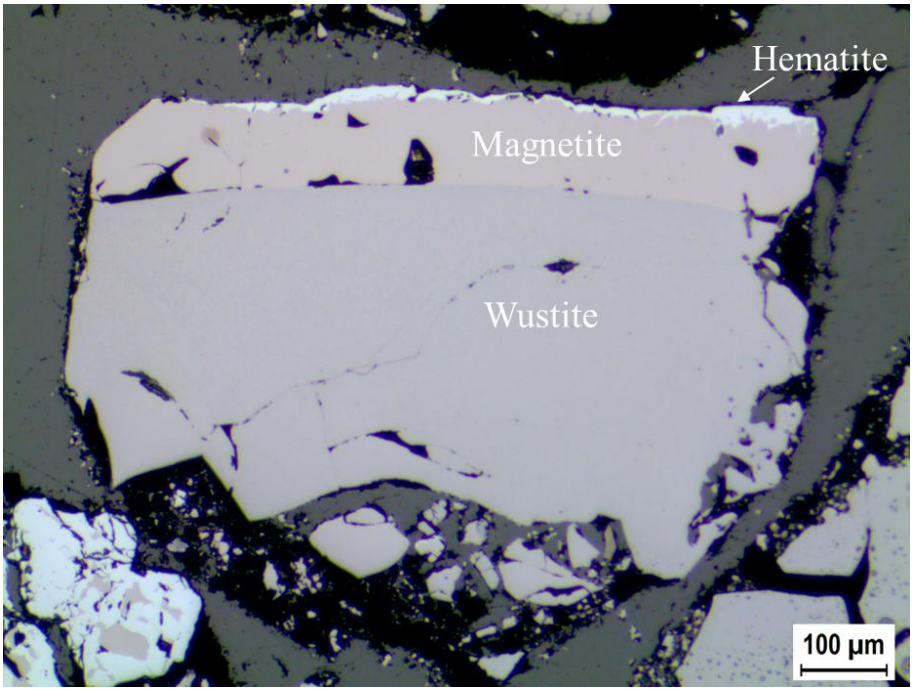

Figure 3. Optical microscope image of a typical mill scale particle showing the presence of the three iron oxides wustite, magnetite and hematite.

3.2 Formation of Mineral Phases during Sintering

3.2.1 Effect of Sintering Temperature and Gas atmosphere

Figure 4 shows optical images from the samples with 5 wt% mill scale sintered at 25 ℃ intervals between 1250 – 1325 ℃ for 4 min at pO_2 = 0.5 kPa, followed by rapid cooling. As shown in Figure 4(a), in the sample sintered at 1250 ℃, most of the hematite was converted to magnetite, and little unreacted hematite remained. SFCA was also formed. Image analysis showed that the fractions of hematite, magnetite and SFCA present were 15.7, 70 and 14.3 %, respectively. There was distinct aggregation and reaction of the finer ore grains resulting in the generation of sinuous pores, however at this temperature the assimilation of oxide materials was not complete, leaving a large proportion of only partially reacted iron ore and flux particles.

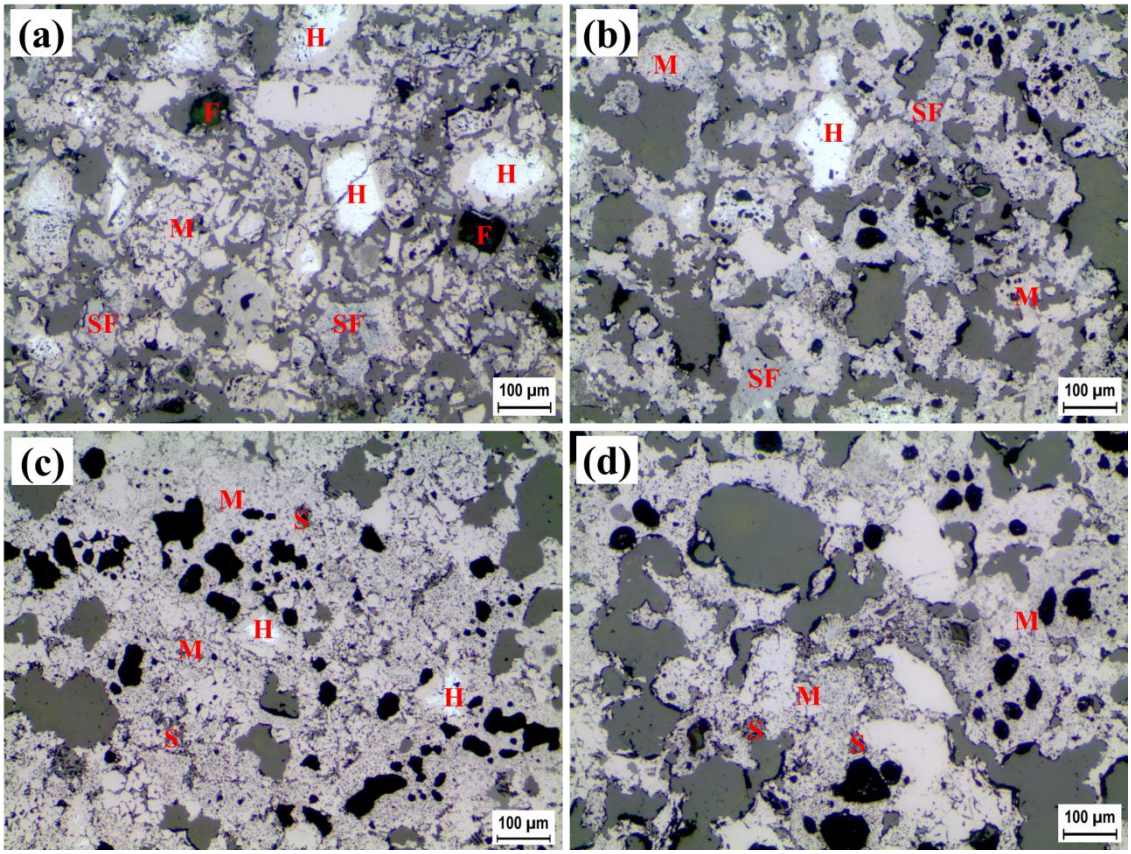

Figure 4. Optical reflected light images of specimens with 5 wt% mill scale sintered at different temperatures for 4 min in a gas mixture containing 0.5% O_2 and 99.5% argon followed by rapid cooling. H: Hematite; M: Magnetite; SF: SFCA; S: Silicates; F: Relict flux. (a) 1250 ℃; (b) 1275 ℃; (c) 1300 ℃; (d) 1325 ℃.

When the sintering temperature was increased to 1275 ℃ (Figure 4(b)), the amount of SFCA formed reached a maximum (27.5%) and minor primarily relict hematite particles (7.0%) were encapsulated inside magnetite phase (65.6%). Almost no discrete iron ore particles remained due to the assimilation of the fine iron ore particles through reaction with the flux components. The major phase present in the sample sintered at 1300 ℃ (Figure 4(c)) was magnetite (94.6%) with only 5.4% hematite. The SFCA phase was rarely detected and an interstitial silica-rich phase was present. Further increasing the sintering temperature to 1325 ℃ (Figure 4(d)) resulted in the hematite and SFCA almost disappearing completely accompanied by increases in the amounts of magnetite and silica-rich phase. It is also noted that the larger pores were generated in the sample since higher sintering temperature resulted in the more enhanced aggregation of fine

particles.

Figure 5 shows the volumetric percentage of total SFCA in specimens with 5% mill scale sintered at 1250 - 1325 ℃ in different gas atmospheres for 4 min, followed by rapid cooling. In general, at the same sintering temperature, more SFCA was formed in specimens sintered in gases with a higher pO_2 (5% and 21% O_2). At these pO_2 values, the amount of SFCA increased with increasing sintering temperature from 1275 ℃ to 1300 ℃ but significantly decreased beyond 1300 ℃. In comparison, in less oxidising conditions (0.5% O_2), the total SFCA content reached a maximum at 1275 ℃ before decreasing at higher temperatures. This trend is consistent with what was found in the previous work on sintering of iron ore with addition of ironsand [14].

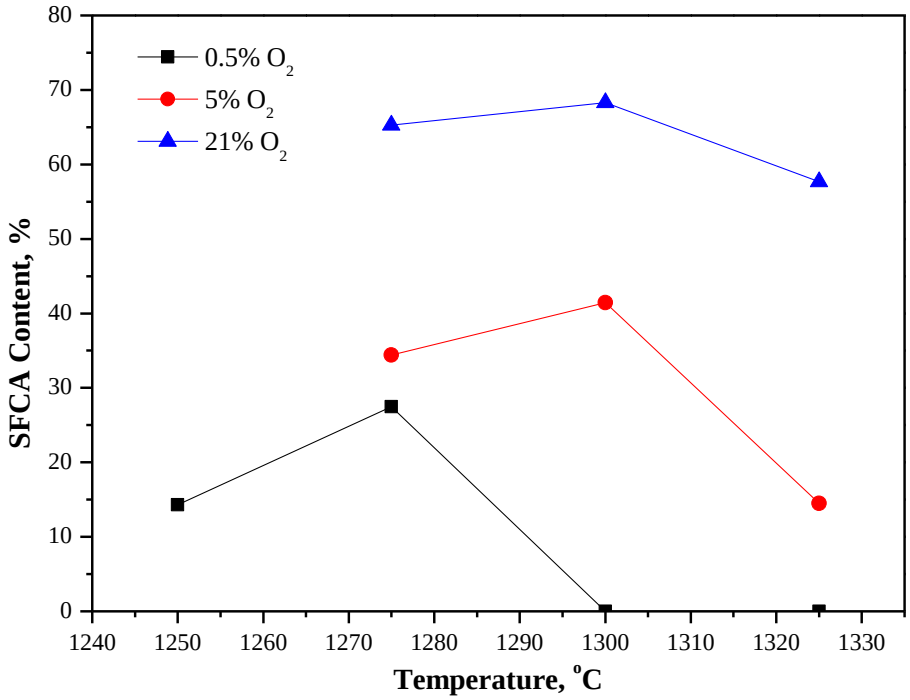

Figure 5. Effect of sintering temperature and gas atmosphere on the total SFCA content formed in specimens with 5% mill scale sintered for 4 min followed by rapid cooling.

3.2.2 Effect of Mill Scale Content

Air, 1300 ℃

When sintered in air, the effect of mill scale content on the sinter mineral phase composition was negligible. Figure 6 compares the microstructures of the M0 and M15 samples sintered in air at 1300 ℃ for 4 min followed by rapid cooling. The mineralogy and microstructure of the two samples were similar and dominated by hematite and SFCA. This was typical for all mill scale additions under these conditions. It was found that although the content of mill scale in the samples was changed from 0 to 15 wt%, the fractions of different phases, as identified by Phase Expert, of the sintered samples were all similar comprising 30-38% hematite, 60-68% SFCA, with little magnetite and silicate.

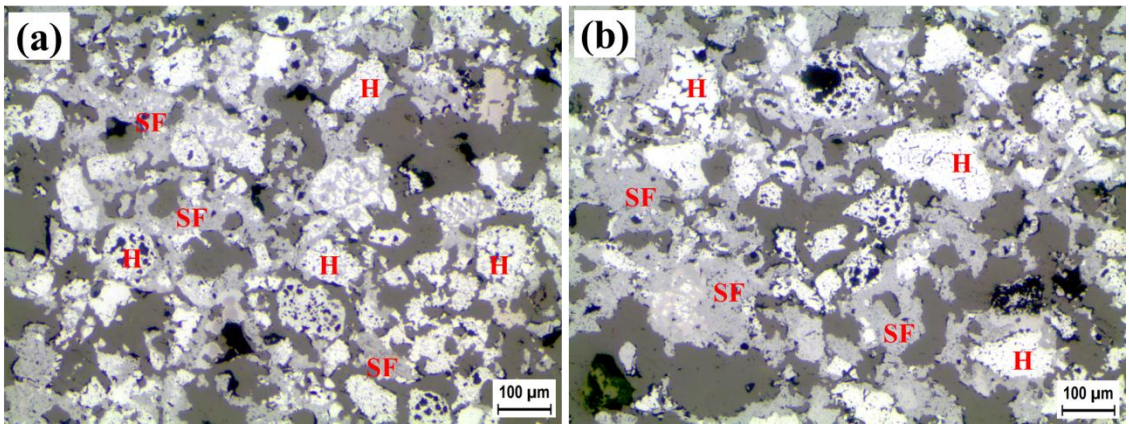

Figure 6. Optical reflected light images of specimens with different mill scale contents sintered at 1300 ℃ in air for 4 min followed by rapid cooling. (a) M0; (b) M15.

5% O_2, 1300°C

Figure 7 presents the microstructures of samples with different mill scale contents sintered at 1300 ℃ in a gas mixture containing 5% O_2 and 95% argon for 4 min with rapid cooling. The measured phase compositions are presented in Figure 8. Generally, as the content of mill scale increased from 0 to 15 wt%, the content of magnetite increased while the amounts of SFCA and hematite decreased simultaneously. As shown in Figure 7(a), in the sample sintered without mill scale addition, a significant amount (41.4%) of SFCA was formed. The fractions of hematite and magnetite were 19.2 and 39.5%, respectively. When 5 wt% mill scale was added into the sinter blend (Figure 7(b)), the amount of SFCA remained unchanged, but the content of hematite decreased to 7.7% and magnetite became the major phase (50.9%). Further increasing

the content of mill scale to 10 and 15 wt% resulted in sharp increase in the amount of magnetite >85% while those of hematite and SFCA further decreased to about 10 and 5%, respectively. It is inferred that the wustite initially present in the mill scale was oxidised to magnetite. The mill scale particles in sintered specimens were not discernible because the mill scale size was similar to other components in the sinter blend (Figure 7(c)).

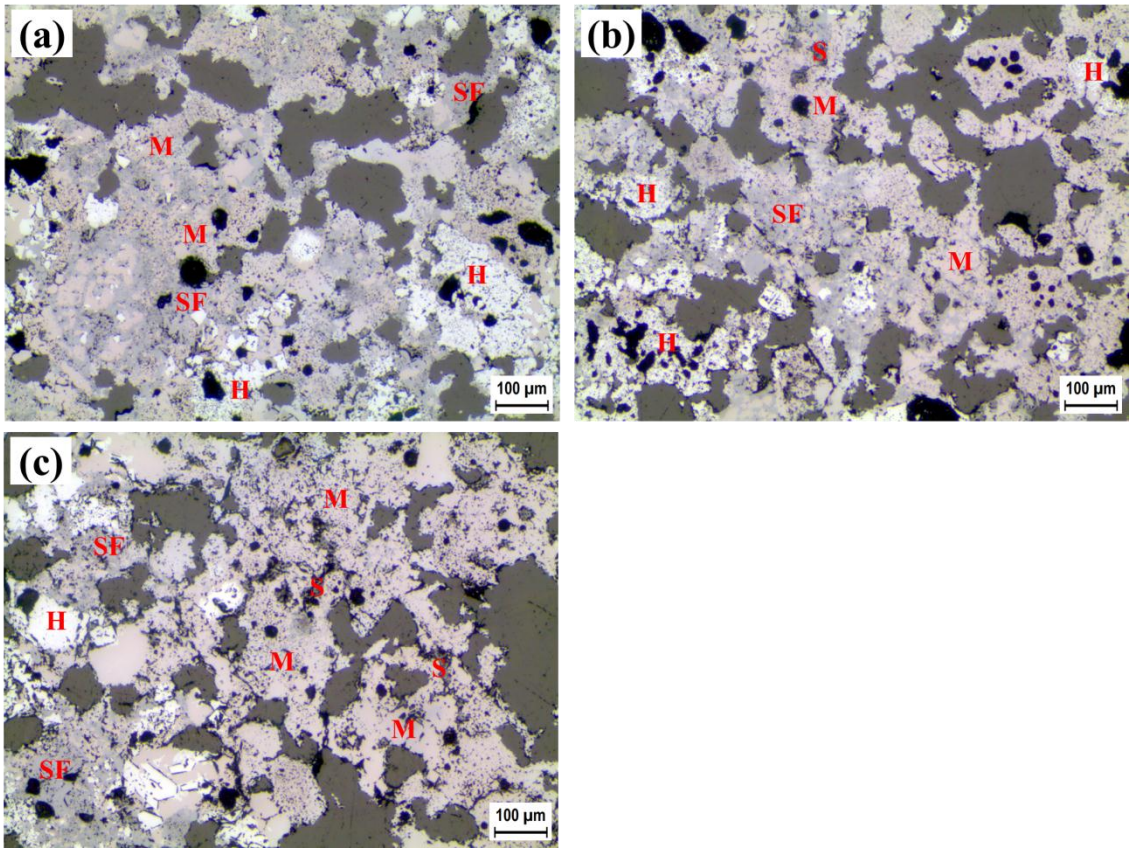

Figure 7. Optical reflected light images of specimens with different mill scale contents sintered at 1300 ℃ in a gas mixture containing 5% O_2 and 95% argon for 4 min followed by quick cooling. (a) M0; (b) M5; (c) M15.

Figure 8 shows the phase compositions in specimens with varying mill scale contents sintered at 1300 ℃ at pO_2 = 5 kPa for 4 min followed by either slow or rapid cooling in air. Slow cooling in air converted magnetite, the dominant phase in the rapidly cooled specimens, to additional SFCA and hematite phases. The magnetite was almost totally eliminated during slow cooling of the samples containing 0 and 5 wt% mill scale; while

only 9.4 and 6.9 % magnetite was left in the sintered samples which had 10 and 15 wt% mill scale addition, respectively.

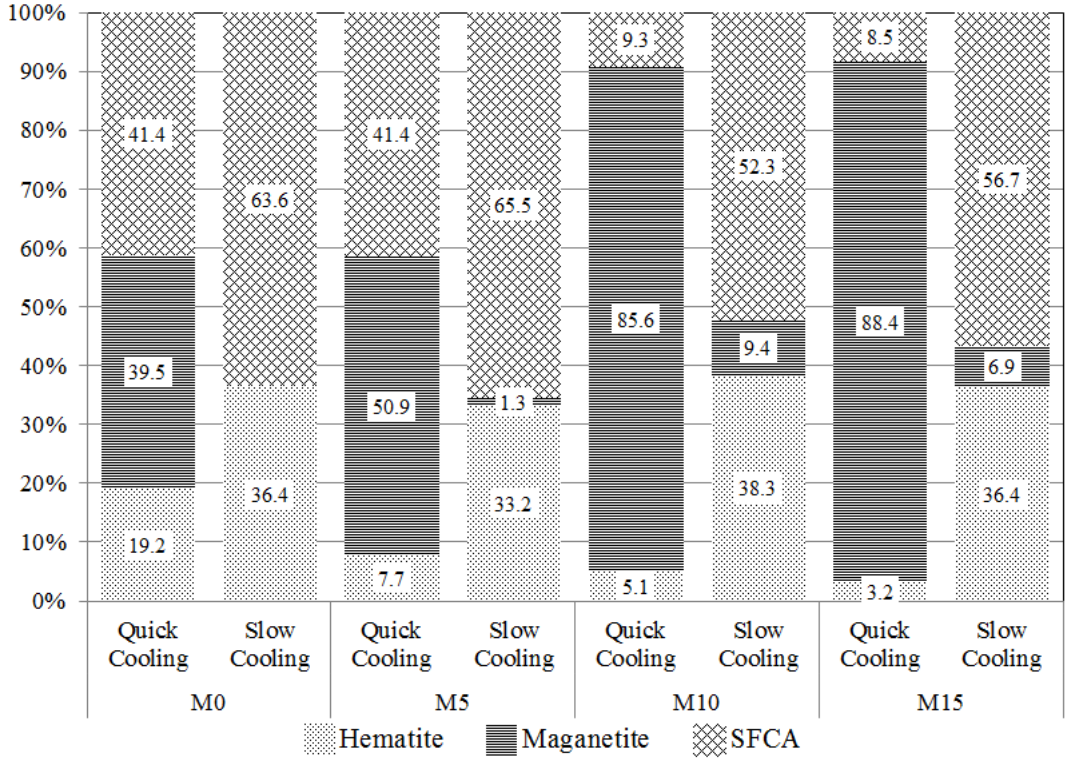

Figure 8. The phase composition of specimens with different mill scale levels sintered at 1300 ℃ at pO_2 = 5 kPa for 4 min, followed by two different cooling procedures.

0.5%O_2, 1300℃

Figure 9 compares the morphology of specimens with and without mill scale addition sintered at 1300 ℃ for 4 min in a less oxidising atmosphere (0.5% O_2) and then followed by two different cooling procedures. As shown in Figure 9(a), during the heating stage, the predominant phases in the quenched sample without mill scale addition were magnetite and silicates. Small fractions of hematite were also present. The addition of 15% mill scale resulted in almost complete elimination of hematite, and more importantly, less aggregation (Figure 9(b)). The fine grained hematite particles were converted to magnetite with little obvious sintering effect. The effect of mill scale on the extent of sintering was also reflected by the change of the porosity of the sintered specimens (Figure 10). After sintering at 1300 ℃ in pO_2 = 0.5 kPa for 4 min followed by rapid cooling, the specimen without mill scale showed a porosity of 36%. The

porosity increased gradually with increasing content of mill scale and reached a maximum of 62% which is in the range of the porosity of packed particles without sintering.

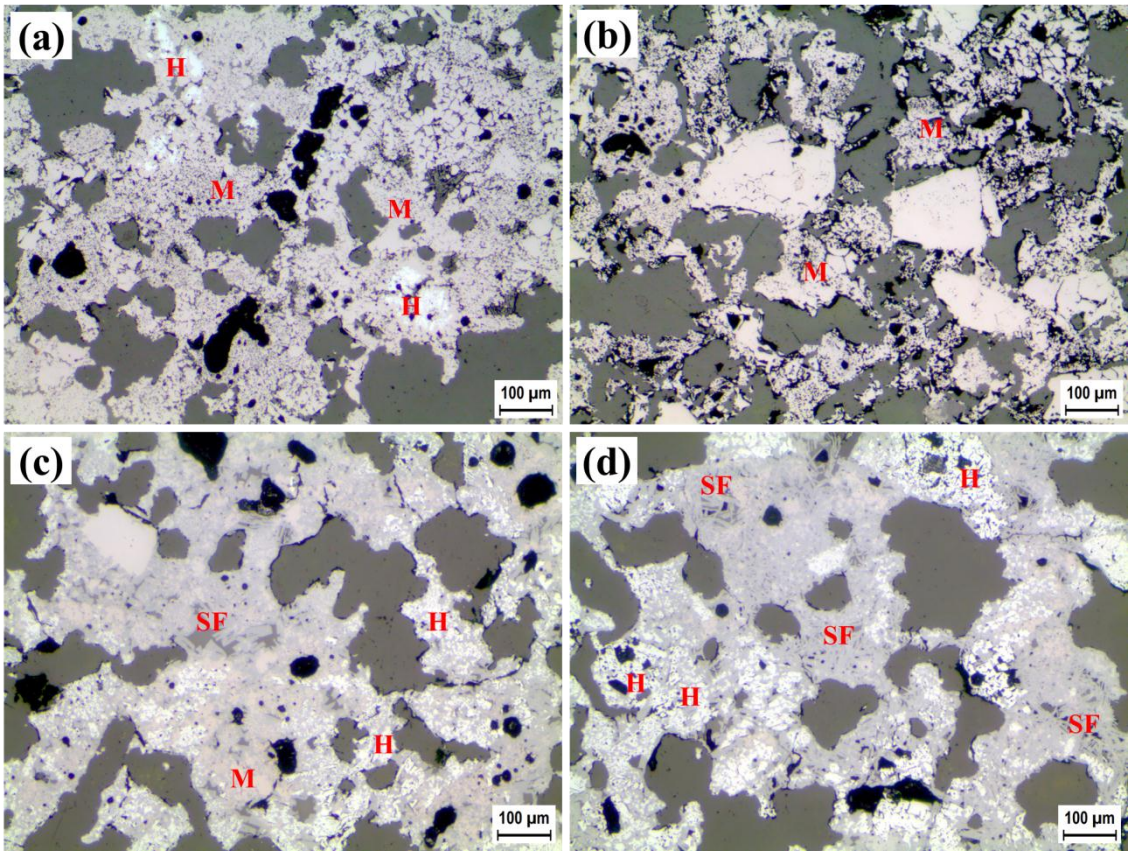

Figure 9. Optical reflected light images of specimens with and without mill scale addition sintered at 1300 ℃ in a gas mixture containing 0.5% O_2 and 99.5% argon for 4 min and then followed by two different cooling procedures. (a) M0, rapid cooling; (b) M15, rapid cooling; (c) M0, slow cooling; (d) M15, slow cooling.

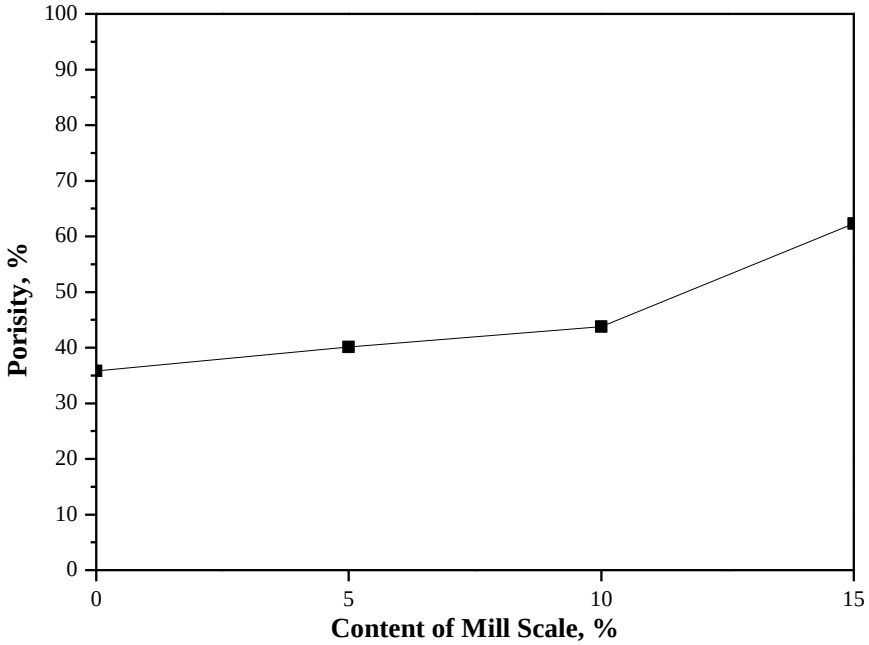

Figure 10. The porosity of specimens with different mill scale additions sintered at 1300 ℃ in pO_2 = 0.5 kPa for 4 min followed by rapid cooling.

As shown in Figures 9(c) and 9(d), the slow cooling procedure totally changed the microstructures of the sintered samples with 0 and 15 wt% mill scale. Both specimens were well sintered with a dense solid matrix and large pores, and with a large amount of SFCA phase present. Figure 11 presents the mineral compositions in specimens over a range of mill scale contents sintered at 1300 ℃ in pO_2 = 0.5 kPa for 4 min followed by slow cooling in air. As the mill scale content was increased from 0 to 15 wt%, the content of SFCA increased while the magnetite content decreased concomitantly. The content of hematite increased within 10 wt% of mill scale addition however beyond this range, the increase was offset by its consumption in the formation of SFCA. The changes of the microstructure and mineral composition when switching from rapid cooling to slow cooling procedures were attributed to the oxidation of magnetite during the cooling stage which was benefited by the high porosity in the specimens with higher mill scale contents. Thus, the hematite and SFCA phases were mainly formed during slow cooling in air when oxygen was readily able to diffuse into the interior of the specimen tablets. From Figures 9(c) and (d) it can be seen most of the hematite and magnetite present were crystallised secondary phases identified by the euhedral crystal

shapes, showing that melting and crystallisation occurred along with the oxidation reactions during the slow cooling stage.

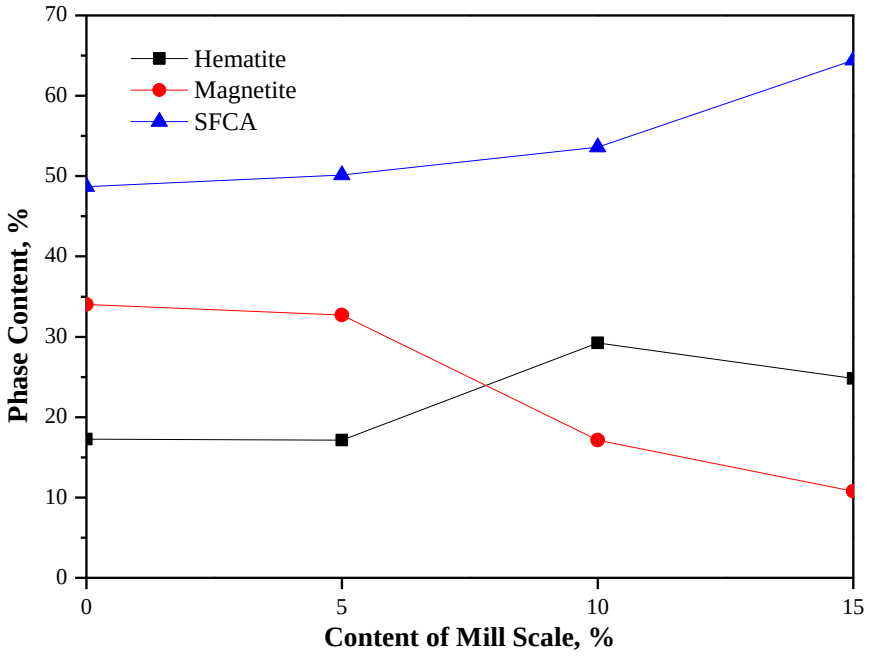

Figure 11. The phase composition of specimens with different mill scale additions sintered at 1300 ℃ in pO_2 = 0.5 kPa for 4 min followed by slow cooling in air.

3.2.3 Effect of Oxidation during Cooling

The previous results illustrating the effects of mill scale content on the formation of mineral phases also indicated a pronounced effect caused by oxidation during cooling. The effect of oxidation was further examined by comparing the final compositions of specimens subject to both rapid and slow cooling. Figure 12 compares the phase compositions in sinter specimens with 5 wt% mill scale and sintered under three different gas atmospheres at 1300 ℃, followed by either a rapid or a slow cooling procedure. The results indicated that, for specimens sintered in air (21% O_2) there was a negligible difference between rapid and slow cooling, with nearly the same phase composition present in both samples. In comparison, for samples sintered under less oxidising gas atmospheres, there was a large difference in mineral composition between samples cooled using the two different procedures. For the rapidly cooled samples, the content of magnetite increased significantly with decreasing oxygen potential in the

sintering gas mixture. In comparison, magnetite was almost totally eliminated during slow cooling for the specimen sintered with 5% O_2. Correspondingly, the contents of SFCA and hematite both increased during slow cooling, close to the levels observed when the sample was sintered in air. In the specimen sintered in 0.5 vol%O_2 - 99.5 vol% argon, up to 94.6% of magnetite was obtained by rapid cooling. The amount of magnetite sharply decreased to only 32.7% following the slow cooling procedure. At the same time, the content of SFCA and hematite increased to 50.2% and 17.1%, respectively.

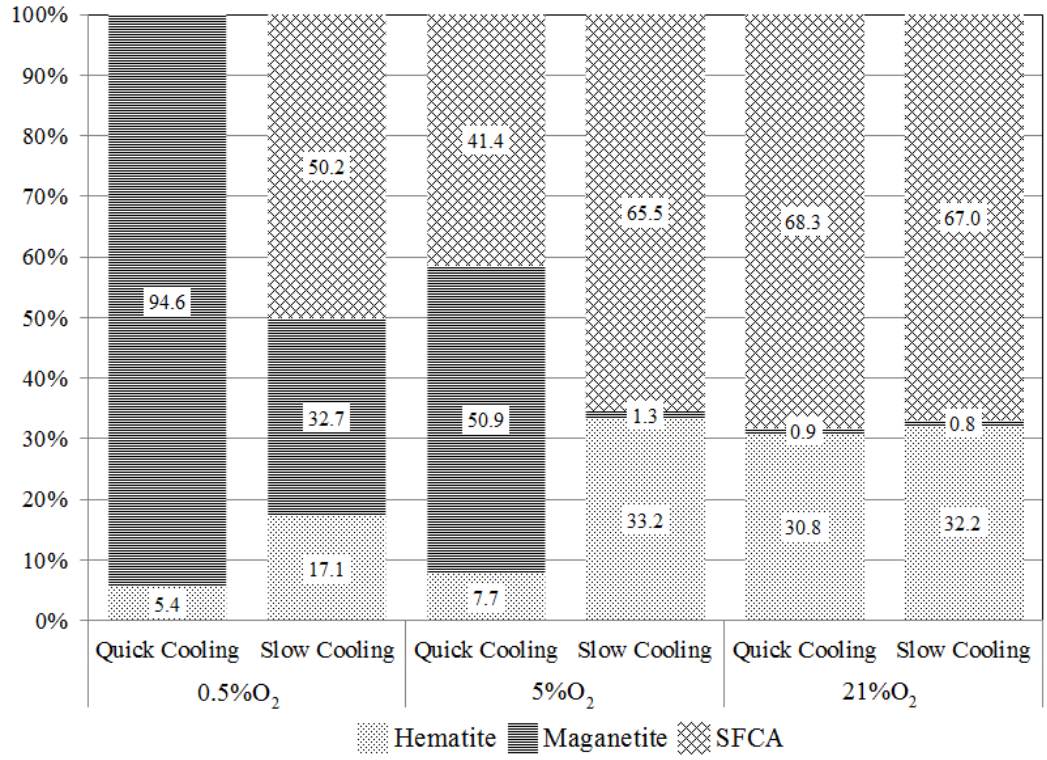

Figure 12. Effect of cooling procedure on the phase composition of samples sintered in different atmospheres. All samples are with 5 wt% mill scale and sintered at 1300 ℃ for 4 min.

3.3 Interaction between Mill Scale and Other Components

Further experiments were carried out to examine the behaviour of mill scale during sintering using larger mill scale particles (425-600 μm). Figure 13 (a) shows the optical reflected light image of a typical mill scale particle in specimens sintered at 1275 ℃ for

4 min and then cooled rapidly. The fine iron ore particles began to be assimilated through reaction with the flux components resulting in almost no discrete iron ore particles remaining, which is in agreement with the results of a previous investigation with New Zealand ironsand [14]. While showing some evidence of partial assimilation, the original contour of the mill scale particle remained clearly visible. Magnetite rims formed around wustite particles were generally observed. Figure 13(b) shows similar image of a typical mill scale particle sintered under the same conditions as Figure 13(a) but cooled slowly in air. A large amount of SFCA was produced during slow cooling in air and intimately bound with mill scale particles. The wustite in the mill scale was completely oxidised and part was oxidised to hematite which grew as lumpy and needle-like crystals.

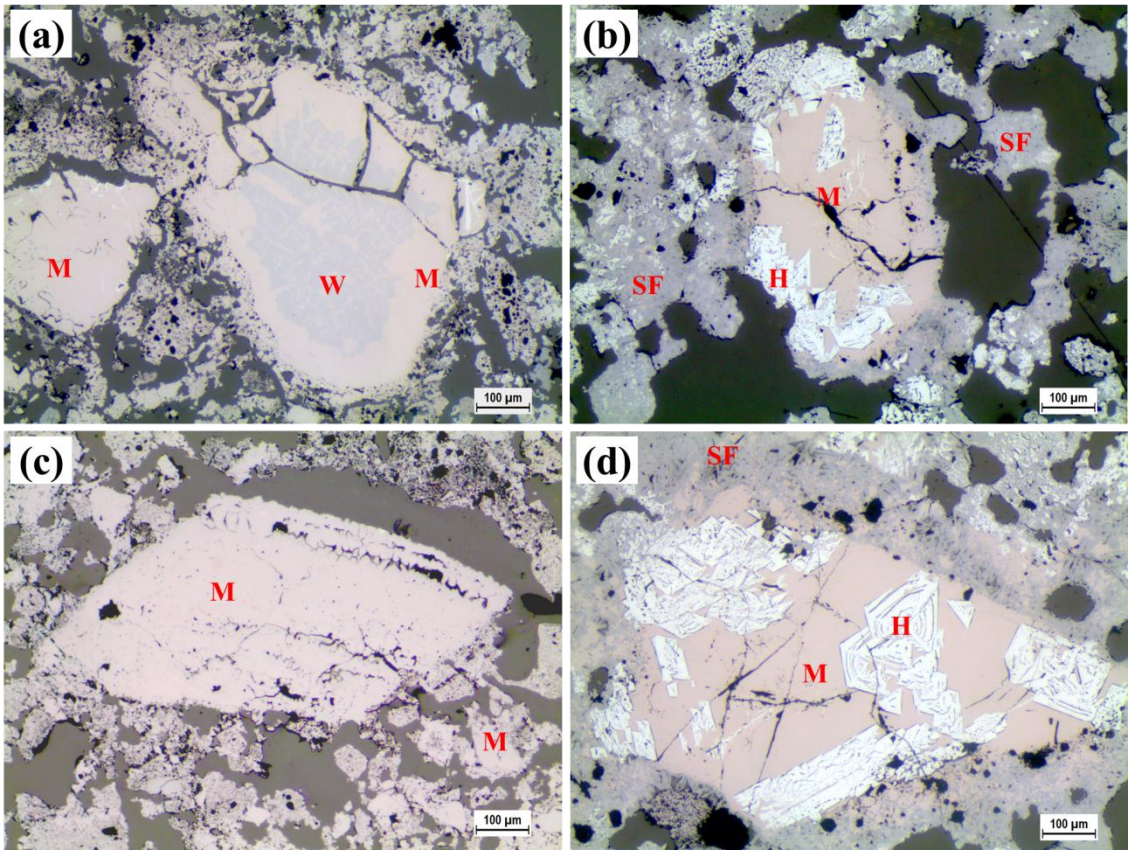

Figure 13. Optical reflected light images of typical mill scale particles in specimens sintered at different temperatures for 4 min in a gas mixture containing 0.5% O_2 and 99.5% argon followed by different cooling procedures. (a) 1275 ℃, rapid cooling; (b) 1275 ℃, slow cooing in air; (c) 1300 ℃, rapid cooling; (d) 1300 ℃, slow cooing in air.

Figure 13(c) shows the optical reflected light image of a typical mill scale particle in specimens sintered at 1300 ℃ for 4 min and then cooled rapidly. The original morphology of the mill scale particle remains clear with little assimilation evident, which is consistent with that observed at 1275 ℃ (Figure 9(b)). After slow cooling in air (Figure 13(d)), a large amount of hematite was present in the matrix of mill scale particles. These were surrounded by SFCA bonding phase which increased in content during cooling.

4. Discussion

As shown in Figure 13, the mill scale particles consisting of mainly wustite had a strong tendency to be oxidised to magnetite even in less oxidising atmospheres, and further to hematite in highly oxidising atmospheres. The oxidation reactions of wustite in mill scale are as follows:

$$3FeO\ (s) + 1/2O_2\ (g) = Fe_3O_4\ (s) \quad (1)$$

$$2Fe_3O_4(s) + 1/2O_2\ (g) = 3Fe_2O_3(s) \quad (2)$$

The equilibrium partial pressures of Reactions (1) and (2) are presented in Figure 14. Wustite is unstable under sintering conditions and can be oxidised when the oxygen partial pressure is greater than ~10^{-7} kPa which is well below that used in the current investigation, reverting to either magnetite or hematite. Hematite becomes unstable when the sintering temperature is high enough resulting in the reverse reaction of Reaction (2) to take place. Wang et al. [18] demonstrated the occurrence of hematite decomposition in the preheating zone of a sinter pot test by measuring the increase in the amount of Fe^{2+} in the blend in this zone. The equilibrium oxygen partial pressure of Reaction (1) is 14.7 and 26.2 kPa at 1275 and 1300 ℃, respectively. Due to the large difference between the equilibrium partial pressures of Reactions (1) and (2), there is always a tendency of conversion of co-existing wustite and hematite to magnetite by oxygen transfer even in an inert gas.

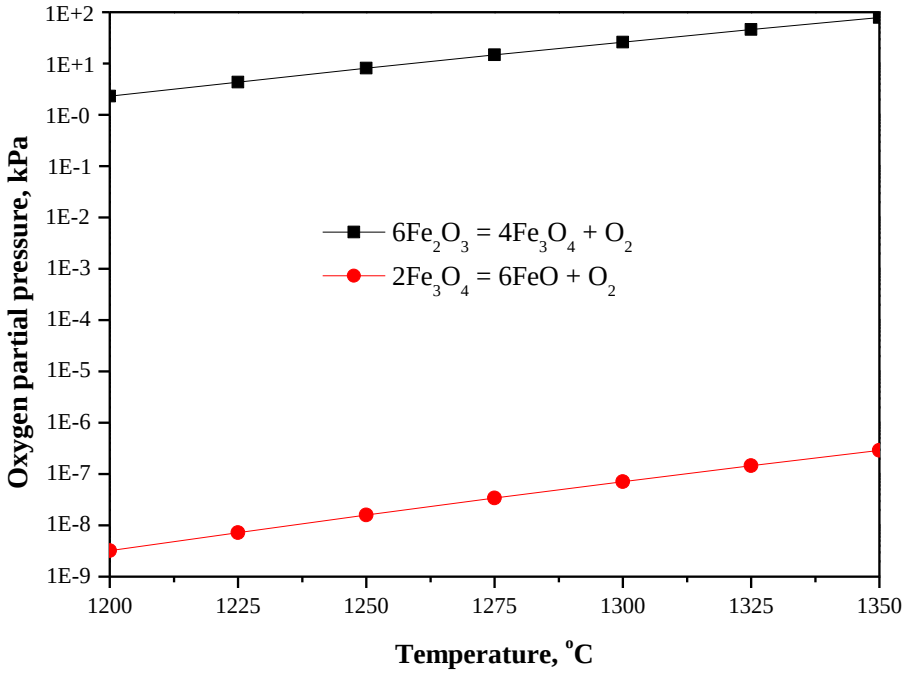

Figure 14. Equilibrium partial pressures of O_2 for Reactions (1) and (2).

As shown in Figure 8, by sintering at 1300 ℃ at pO_2 = 5 kPa for 4 min, near 40% magnetite was formed due to reverse Reaction (2) in a specimen without mill scale. This indicated that the effective partial pressure of oxygen inside the tablet was higher than 5 kPa in the atmosphere used. Addition of 5 wt% of mill scale increased the magnetite content by 11.4% while increasing the mill scale content to 10wt% further increased the magnetite content by near 35%. These results show that consumption of oxygen in the gas phase by the oxidation of mill scale created a locally less oxidising environment which promoted conversion of hematite to magnetite.

During sintering with fine mill scale particles as shown in Figure 4, the mill scale was completely oxidised into magnetite at all temperatures tested in an atmosphere with pO_2 =0.5 kPa. Using particles of larger size as shown in Figure 13, however, revealed that the oxidation of wustite proceeded via a magnetite rim with a thickness of less than 100 μm at 1275 ℃. The oxidation reaction involved diffusion of oxygen via the magnetite lattice to the wustite-magnetite interface which may be the controlling step of the reaction. A finer particle size is beneficial to the conversion of wustite into magnetite and further conversion to hematite in a more oxidising atmosphere such as during the slow cooling stage (Figures 13 (b) and 13(d)).

SFCA phases are desired in high quality sinter due to their role in improving sinter reducibility and reduction degradation index. Specifically, SFCA phases are calcium ferrite based mineral phases with dissolved alumina and silica. The formation of SFCA starts with the solid state reaction:

$$CaO\ (s) + Fe_2O_3\ (s) = CaFe_2O_4\ (s) \quad (3)$$

where calcium from the flux initially diffuses into the iron ore particles to form a new phase, $CaFe_2O_4$ (CF). As well, $Ca_2Fe_2O_5$ (C_2F) can form when enough calcia is available. Pure $CaFe_2O_4$ has a melting point of 1216 ℃ while $Ca_2Fe_2O_5$ melts at 1449 ℃. Due to the relative difficulty in solid diffusion, formation of a localised melt enhances mass transfer and further reaction remarkably. Impurities such as silica and alumina within the sinter blend participate in additional reactions with the early formed ferrites resulting in the formation of SFCA phases.

It is well recognised that SFCA only forms from hematite [11, 19]. In a relatively reducing gas atmosphere however, decomposition of hematite to magnetite takes place as the reverse reaction of Reaction (2), as discussed above. Factors which enhance decomposition of hematite affect the formation of SFCA negatively, whereas those factors which help to retain hematite favour the formation of SFCA. However, the SFCA formed at low temperatures will be melted when heated to high temperatures, such as above 1300 ℃. This can take place by two different mechanisms: (1) a physical phase change without a chemical reaction involved, and (2) a reduction of Fe_2O_3 in SFCA which affects its stability. Because a much higher temperature is required for the first mechanism, the second is most likely the dominant mechanism in sintering.

As shown in Figure 5, increasing the partial pressure of O_2 in the sintering gas atmosphere significantly increased the content of SFCA in a sinter specimen because it increased the stability of SFCA to higher temperatures, which is consistent with the observation by Webster et al. [20]. However, when the temperature went beyond 1300 ℃, the pO_2 in air is insufficient to fully suppress the decomposition of SFCA, resulting in decreased SFCA content in the sinter samples. Thus, the maxima of SFCA content were formed, and the peak temperature increased with increase of pO_2.

The addition of mill scale had a more significant effect on the mineral phase formation at lower oxygen partial pressures. Changing mill scale addition from 0 to 15 wt% had a negligible effect on the sintering in air (Figure 6). The oxidation of mill scale was complete and SFCA was the dominant phase with a significant content of hematite throughout the temperature range examined. In the gas mixture with pO_2 = 5 kPa, the decomposition of hematite to magnetite is favoured thermodynamically when sintering temperature is higher than 1267 ℃. As shown in Figures 7 and 8, increasing mill scale content from 0 to 15 wt% resulted in a decrease of both hematite and SFCA phase with correspondingly more magnetite formation. At pO_2 = 0.5 kPa, sintering was obvious in a sample without mill scale (Figure 9(a)), although the content of SFCA was low. The addition of 15 wt% of mill scale (Figure 9(b)) resulted in a sample with little evidence for sintering having occurred. In this sample, the wustite in mill scale promoted the reduction of hematite quickly into magnetite which hindered the formation of calcium ferrites and preliminary liquid phase, and the aggregation of fine particles.

It seems, however, that the lack of sintering during the heating stage is not an issue if the sample is exposed to a high oxygen content atmosphere, as demonstrated by the results from specimens slowly cooled in air. The SFCA and hematite contents of a specimen sintered in a less oxidising gas atmosphere and then cooled in air became close to that sintered in air. The porous structure generated during heating stage is beneficial to the diffusion of oxygen inside a specimen when cooled slowly in air, and promotes the formation of secondary hematite and SFCA.

In industrial sintering, the sinter blend experiences different stages with varying temperature and gas atmospheres. Although overall, a sinter bed is in an oxidising atmosphere, the oxygen content beneath the combustion zone can be well below 10%, and the local oxygen content in the combustion zone can be much lower than the average level. This causes inhomogeneity of sintering. Figure 15 shows that in an industrial sinter, the material close to the edge of a sinter lump was high in SFCA and hematite content (more oxidising), but the interior (less oxidising) was mainly secondary magnetite and silicate phases with little SFCA and hematite generated/remaining.

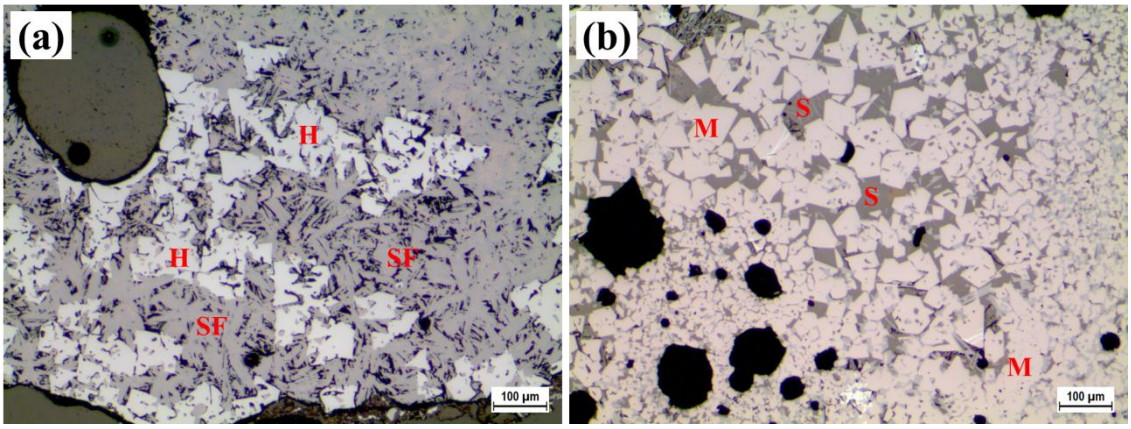

Figure 15. Typical microstructure of an industrial sinter. (a) Exterior and (b) interior of sinter lumps.

Based on the observations in this study, mill scale is a suitable sinter blend component with very low impurity contents. Addition of mill scale into a sinter blend, especially in significant amount such as above 5 wt%, may however affect the formation of mineral phases during the heating stage. Nonetheless, if appropriate measures are taken so that the magnetite formed during heating is allowed to be sufficiently oxidised during the cooling stage, the contents of SFCA and hematite will not be significantly changed and the quality of sinter can be maintained. Reducing the suction pressure of a sinter grate may reduce the cooling rate and promote the formation of SFCA. Recycling of hot air from the cooling section to the sintering section not only reduces fuel consumption but also reduces the cooling rate of sinter which may also promote formation of SFCA.

5. Conclusions

In order to examine the effect of mill scale addition on the formation of minerals during iron ore sintering, small tablets of sinter specimens containing 0-15 wt% mill scale were heated in controlled gas atmospheres. The results obtained are summarised as follows:

(1) When samples with 0-15% mill scale were sintered in a high oxidizing atmosphere (air) followed by rapid cooling, there was negligible effect of mill scale addition on the phase formation within sinter. The oxidation of mill scale was complete and SFCA and

hematite were the dominant phases throughout the temperature range examined in this study.

(2) In the gas mixture with pO_2 = 5 kPa and during heating stage, an increase in mill scale content from 0 to 15 wt% resulted in a decrease in the amount of hematite and SFCA phase and a corresponding increase in magnetite formation.

(3) In sintered samples with 15 wt% of mill scale in a gas with pO_2 = 0.5 kPa followed by rapid cooling, a low sintering extent was obtained within the samples. In contrast, slow cooling of sintered specimens in air resulted in an increase of the hematite and SFCA contents.

Acknowledgements

The project is financially supported by a BlueScope Steel Metallurgical Centre Projects Grant. Zhe Wang is a recipient of a University of Wollongong Deputy Vice Chancellor's Special Scholarship and International Postgraduate Tuition Award. The authors would like to acknowledge the Electron Microscopy Centre (EMC) at University of Wollongong for SEM/EDS analysis.

References

[1] N. Birks, G. H. Meier, and F. S. Pettit, Introduction to the High Temperature Oxidation of Metals, 2nd edition, Cambridge University Press, Cambridge, (2006), 83.

[2] T. Umadevi, M. G. S. Kumar, P. C. Mahapatra, T. M. Babu and M. Ranjan, Recycling of Steel Plant Mill Scale via Iron Ore Pelletisation Process, *Ironmaking and Steelmaking*, **36** (2009), 409-415.

[3] T. Umadevi, A. Brahmacharyulu, P. Karthik, P. C. Mahapatra, M. Prabhu and M. Ranjan, Recycling of Steel Plant Mill Scale via Iron Ore Sintering Plant, *Ironmaking and Steelmaking*, **39** (2012), 222-227.

[4] A. K. Biswas, Principles of Blast Furnace Ironmaking: Theory and Practice, Cootha Publishing House, Brisbane, (1981), 194.

[5] P. R. Dawson, J. Ostwald, K. M. Hayes, Influence of Alumina on Development of Complex Calcium Ferrites in Iron Ore Sinters, *Transactions of the Institution of Mining and Metallurgy Section C-Mineral Processing and Extractive Metallurgy*, **94** (1985), C71-C78.

[6] R. A Button and P. A. Lundh, Mineralogy and Mineral Formation in Iron-ore Sinetr with Addition of Magnetite Fines, *Ironmaking and Steelmaking*, **16** (1989), 151-164.

[7] S. C. Panigrahy, M. J. Rigaud, S. P. Chong and B. Chanda, The Use of Carol Lake Concentrate for Coke Breeze Reduction and LTD Improvement in Sinter Productions, 53rd Ironmaking Conference, AIME Iron and Steel Society, Warrendale, (1994) 523-531.

[8] L. X. Yang and E. Matthews, Oxidation and Sintering of Magnetite Ore under Oxidising Conditions, *ISIJ international*, **37** (1997), 854-861.

[9] J. M. F. Clout and J. R. Manuel, Fundamental Investigations of Differences in Bonding Mechanisms in Iron Ore Sinter Formed from Magnetite Concentrates and Hematite ores, *Powder Technology*, **130** (2003), 393-399.

[10] S. P. E. Forsmo, S. E. Forsmo, P. O. Samskog and B. M. T. Björkman, Mechanisms in Oxidation and Sintering of Magnetite Iron Ore Green Pellets, *Powder Technology*, **183** (2008), 247-259.

[11] L. X. Yang, Sintering Fundamentals of Magnetite Alone and Blended with Hematite and Hematite/Goethite Ores, *ISIJ International*, **45** (2005), 469-476.

[12] N. A. E. Hussiny, F. M. Mohamed and M. E. H. Shalabi, Recycling of Mill Scale in Sintering Process, *Science of Sintering*, **43** (2011), 21-31.

[13] Z. Wang, D. Pinson, S. Chew, H, Rogers, B. J. Monaghan, M. I. Pownceby, N. A. S. Webster and G. Zhang, Behaviour of New Zealand Ironsand during Iron Ore Sintering, *submitted to Metallurgical and Materials Transactions B*, (Chapter 2).

[14] Z. Wang, D. Pinson, S. Chew, B. J. Monaghan, M. I. Pownceby, N. A. S. Webster, H. Rogers and G. Zhang, Effect of Sintering Conditions on the

Formation of Mineral Phases during Iron Ore Sintering, *to be submitted*, (Chapter 3).

[15] M. H. Davies, M. T. Simnad and C. E. Birchenall, On the Mechanism and Kinetics of the Scaling of Iron, *Transactions of the ASME*, **3** (1951), 889-896.

[16] W. Schwenk and A. Rahmel, Theoretical Considerations on Phase Boundary Reactions and Mass Transfer during the Oxidation of Iron. *Oxidation of Metals*, **25** (1986), 293-303.

[17] D. J. Young, High Temperature Oxidation and Corrosion of Metals, Elsevier, Oxford, (2008), 38.

[18] S. Wang, W. Gao and L. Kong, Formation Mechanism of Silicoferrite of Calcium and Aluminium in Sintering Process, *Ironmaking and Steelmaking*, **25** (1998), 296-301.

[19] L. H. Hsieh and J. A. Whiteman, Effect of Oxygen Potential on Mineral Formation in Lime-fluxed Iron Ore Sinter, *ISIJ International*, **29** (1989), 625-634.

[20] N. A. S. Webster, M. I. Pownceby, I. C. Madsen and J. A. Kimpton, Effect of Oxygen Partial Pressure on the Formation Mechanisms of Complex Ca-rich Ferrites, *ISIJ International*, **53** (2013), 774-781.

CHAPTER 6. MINERAL PHASE FORMATION AND ZINC REMOVAL DURING SINTERING OF FILTER CAKE WASTES

Mineral Phase Formation and Zinc Removal during Sintering of Filter Cake Wastes

Zhe Wang[1], David Pinson[2], Sheng Chew[2], Brian J. Monaghan[1], Harold Rogers[1,2], Guangqing Zhang[1]

1. School of Mechanical, Materials and Mechatronic Engineering, University of Wollongong, NSW 2522, Australia
2. BlueScope Technology and Planning, P. O. Box 202 Port Kembla, NSW 2505, Australia

Abstract

A large amount of filter cake wastes are produced from the gas cleaning systems of blast furnace (BF) ironmaking and basic oxygen furnace (BOF) steelmaking processes. The filter cake wastes cannot be directly recycled through the ironmaking process due to the high zinc contents and are therefore, predominantly, stockpiled. The storage of filter cake wastes presents a long-term environmental issue but also an opportunity to extract or recover the iron content, motivating a search for processes or technologies to allow their cost-effective recycling. In this study, two filter cake wastes from BlueScope Ltd. were sintered at 1100 – 1300 ℃ in argon and air to evaluate the effects of temperature, gas atmosphere and carbon content on the mineral phase formation and zinc removal of sintered filter cake specimens. The fine particles in filter cake can be well aggregated by bonding phases (calcium ferrites and silicates) during sintering due to the presence of flux materials, CaO and SiO_2, in the filter cake. A degree of zinc removal was also achieved during sintering by reduction of ZnO to zinc vapour by carbon or metallic iron in the filter cake.

Key words: Filter cake; Sintering; Mineral phase formation; Zinc removal; Recycling.

1. Introduction

Steelmaking plants generate a significant amount of flue dusts. These dusts are removed from the off-gases of blast furnaces (BF), basic oxygen furnaces (BOF) and electric arc furnaces (EAF) either in the form of dry dusts by dry separation methods, or in the form of sludge or filter cake from wet separation methods [1]. Typically the off-gases are ducted to scrubbers for cleaning so that the cleaned gas can be reused within the steelworks and the collected dusts can be dewatered for stockpiling (or further processing) in the form of filter cake.

These flue dusts usually contain large amounts of iron as well as varying amounts of zinc. The low vaporization temperature of zinc leads to its accumulation in the dusts in the off-gases from the iron and steelmaking furnaces [2]. Mineralogical analyses [1] show the presence of zinc in oxide forms, such as zincite (ZnO) and franklinite ($ZnFe_2O_4$). Iron is found mostly as hematite (Fe_2O_3), magnetite (Fe_3O_4), wustite (FeO), franklinite and metallic iron. Typically, EAF dust contains a higher level of zinc (about 15-30%) compared to BF and BOF dusts (1-5%). The levels of zinc in the flue dusts hinder their direct utilization by iron and steelmaking processes. Zinc in the flue dusts recirculates in the plants, causing refractory failure and scaffold formation [1].

Storage of these dusts presents a long-term environmental concern, motivating the search for processes or technologies to allow their recycling. Attempts have been made by many investigators to recycle the flue dusts generated from the iron and steelmaking processes, however information on the treatment of BF and BOF dusts is limited. Processes investigated include pyrometallurgical [1, 3-6], hydrometallurgical [7-9] and hybrid processes [10-12], the latter involving a combination of bio-leaching, hydrometallurgical and pyrometallurgical stages. After significant effort in process development, the problem is still not well resolved [6]. The majority of the pyrometallurgical processes to remove zinc from the dusts are based on high temperature reduction and volatilisation followed by gas phase recovery. ZnO and $ZnFe_2O_4$ in the dust are reduced by C, CO or H_2 to Zn vapour. Depending on the process, Zn may be recovered as elemental Zn in liquid form in condensers [5] or in solid form as ZnO in baghouses [3, 6].

Attempts to briquette filter cake for recycling were conducted by BlueScope and trial production of briquettes was carried out at pilot plant scale in 2004 and 2005, but these attempts were unsuccessful due to the low strength of the briquettes produced [13]. Alternatively, utilisation of the existing iron ore sintering facility may be an attractive way to agglomerate fine particles of filter cake into the sinter which can be used in BF ironmaking or directly added into BOF as an iron source and coolant. However, little information is available for the mineral phase formation and the behaviour of zinc containing filter cake in the sintering process. This paper investigates the sintering behaviour of the filter cake under different sintering conditions including the zinc removal.

2. Experimental Procedure

Two types of filter cake wastes were used in this study. A BOF filter cake sample and a mixture (MIX) filter cake sample. The MIX sample represents a 3:1 blend of both BOF and BF filter cake.

These filter cake samples were dried in an oven at 110 ℃ for 48 hours before being crushed and screened to < 200 μm. After drying they were then pressed into ~1.0 g cylindrical tablets of 8 mm diameter and ~10 mm height for sintering experiments.

Sintering of the filter cake samples was carried out under an argon atmosphere in a vertical tube furnace and in air in a muffle furnace in the temperature range of 1100 - 1300 ℃ (50 ℃ increments) for 5 minutes typical for iron ore sintering. A schematic of the vertical tube furnace has been described in detail elsewhere [14]. The internal diameter of the working tube was 55 mm. The furnace was preheated to a designated temperature, and then purged with argon for at least 20 minutes prior to hanging a crucible containing the sinter tablet in the hot zone of the furnace. After sintering for 5 minutes, the samples were rapidly cooled by raising the crucible to the cold top end of the furnace tube. In the muffle furnace, a sample was placed on an alumina plate and sintered in a static air atmosphere for 5 minutes.

The sintered tablets were mounted in epoxy resin, cut perpendicular to the top surface and then polished for optical microscopy (Leica DM6000) and field – emission scanning electron microscopy (FESEM, JEOL JSM – 7001F) analysis.

The original filter cakes and sintered samples were analysed by X-ray diffraction (XRD, MMA, GBC Scientific Equipment, Braeside, Australia). The carbon content in sintered samples was measured by LECO analysis (SC-444 DR Carbon/Sulphur Determinator). The zinc content of samples was analysed by Inductively Coupled Plasma - Optical Emission Spectrometry (ICP-OES). About 0.1 g of crushed sintered sample was digested into a solution consisting of 6 mL HCl, 2 mL HNO_3 and 2 mL H_2O_2. After filtration through 0.1μm glass fibre filter, the solution was then diluted to an appropriate concentration for analysis.

3. Results

3.1. Characterisation of Filter Cake Samples

The chemical composition of the two filter cake samples measured by X-Ray Fluorescence spectroscopy (XRF) is given in Table 1. Quite similar chemical compositions can be found for these two samples; both contain 53-56 wt% iron and about 2 wt% of zinc. The contents of other impurities, CaO, MgO, SiO_2, and Al_2O_3 are also similar. A major difference between the two samples is in their carbon content. It is significantly higher in the MIX filter cake (3.14 wt%) compared with the BOF filter cake (0.85 wt%). This increased carbon level results from the presence of coke dust from the coke used in the BF process.

Table 1. Chemical compositions of two filter cake waste materials.

Sample	Fe	SiO_2	Al_2O_3	CaO	Mn	MgO	TiO_2	Zn	Free C
BOF	55.70	1.46	0.16	6.31	0.80	2.79	0.04	2.28	0.85
MIX	53.70	1.84	0.40	6.28	0.72	2.79	0.06	2.01	3.14

Figure 1 shows the XRD patterns of the two filter cake samples. The main mineral phases present were similar, including hematite Fe_2O_3, magnetite Fe_3O_4, wustite FeO, metallic iron Fe, limestone $CaCO_3$ and carbon C. Based on relative intensity of the peaks, it is noted that carbon content of the MIX sample was higher than that in the BOF sample, which is consistent with the XRF results. A further difference in the filter cake samples is that the MIX sample contained more metallic iron than the BOF filter cake.

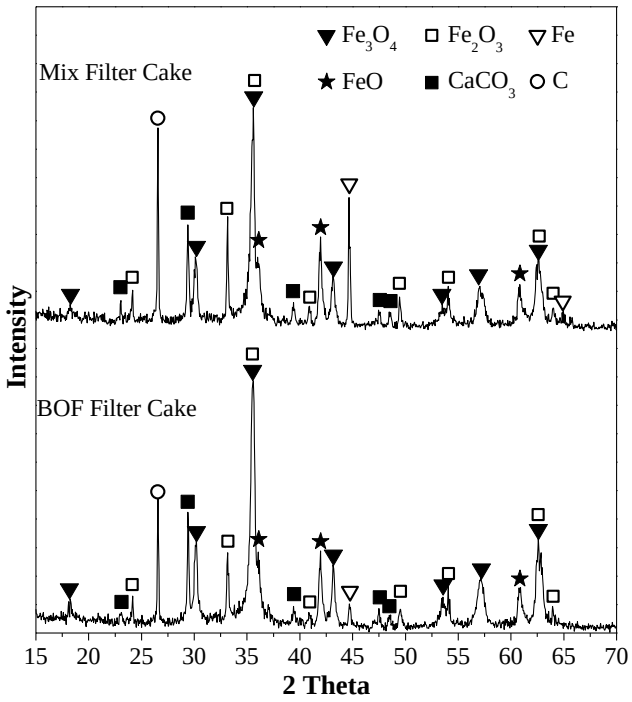

Figure 1. The XRD patterns of the filter cake samples.

3.2. Sintering of Filter Cake Samples

The XRD patterns of the MIX samples sintered in static air in the temperature range of 1100 - 1300 ℃ (50 ℃ increments) for 5 minutes are presented in **Figure 2**. No metallic iron, carbon or limestone were detected by XRD in the sintered samples; the major phases identified were magnetite and wustite in all of the sintered samples. Hematite was detected in the sample sintered at 1100 ℃; its peaks became very weak after sintering at 1150 ℃ and disappeared when sintered at 1200 ℃ and higher temperatures.

A small amount of silico-ferrite of calcium and aluminium (SFCA) can be identified among all the XRD patterns of the sintered MIX samples.

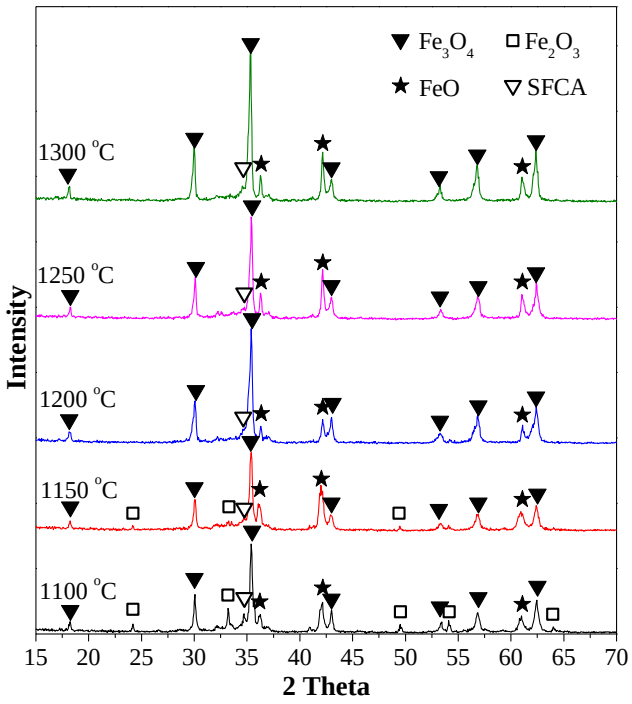

Figure 2. XRD patterns of MIX samples sintered in the temperature range of 1100 - 1300 ℃ for 5 minutes in a muffle furnace.

Figure 3 represents the morphology of the MIX samples calcined at 1100 - 1300 ℃ for 5 minutes in the muffle furnace. The sintering extent of the MIX samples increased gradually with increasing sintering temperature. The pressed tablets changed their shape and expanded when sintered at higher temperatures, causing an increase in porosity. The tablets heated at 1250 and 1300 ℃ all fractured into several pieces during sintering.

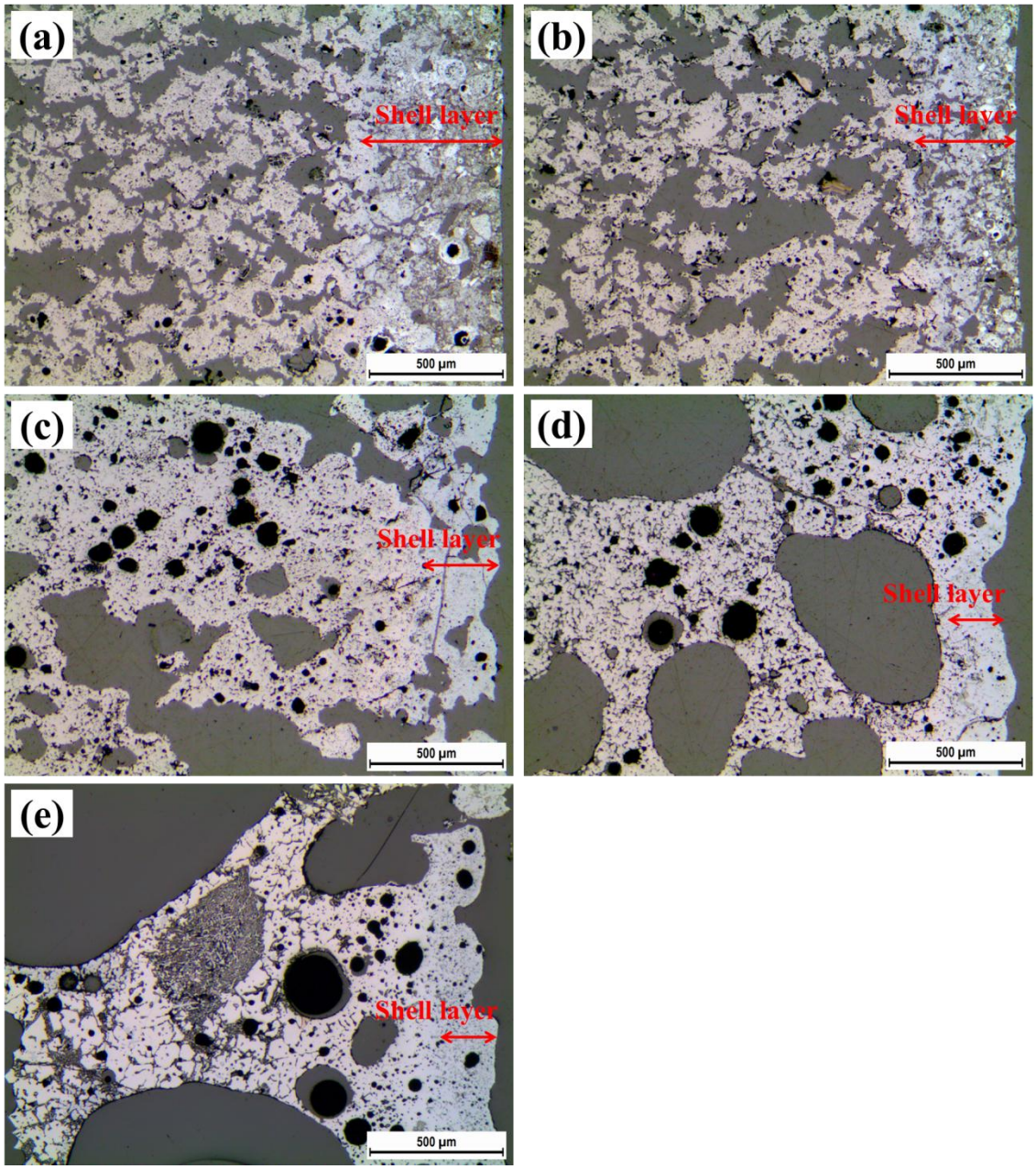

Figure 3. Optical microscope images of MIX samples sintered in the temperature range of 1100 - 1300 ℃ for 5 minutes in a muffle furnace. (a) 1100 ℃; (b) 1150 ℃; (c) 1200 ℃; (d) 1250 ℃; (e) 1300 ℃.

In each case a "shell" layer formed around the boundary of each tablet in which the mineral phases present differed from those in the sample interior. This layer (visible by its different colour from the interior) was about 500 µm thick for the sample sintered at 1100 ℃ (see Figure 3(a)) and became thinner when the sintering temperature was increased. In the shell of samples sintered at 1100 ℃ and 1150 ℃ (Figures 3(a) and 3(b)),

the assimilation of oxide materials was not complete, leaving a large proportion of only partially reacted filter cake particles. In comparison, most of the fine particles of filter cake in the interior were aggregated resulting in the formation of large pores inside the samples. As shown in Figures 3(c), 3(d) and 3(e), the shell layers of samples sintered at 1200, 1250 and 1300 ℃ were thinner but denser, and the aggregation of particles in them was complete, resulting in almost no discrete filter cake particles remaining.

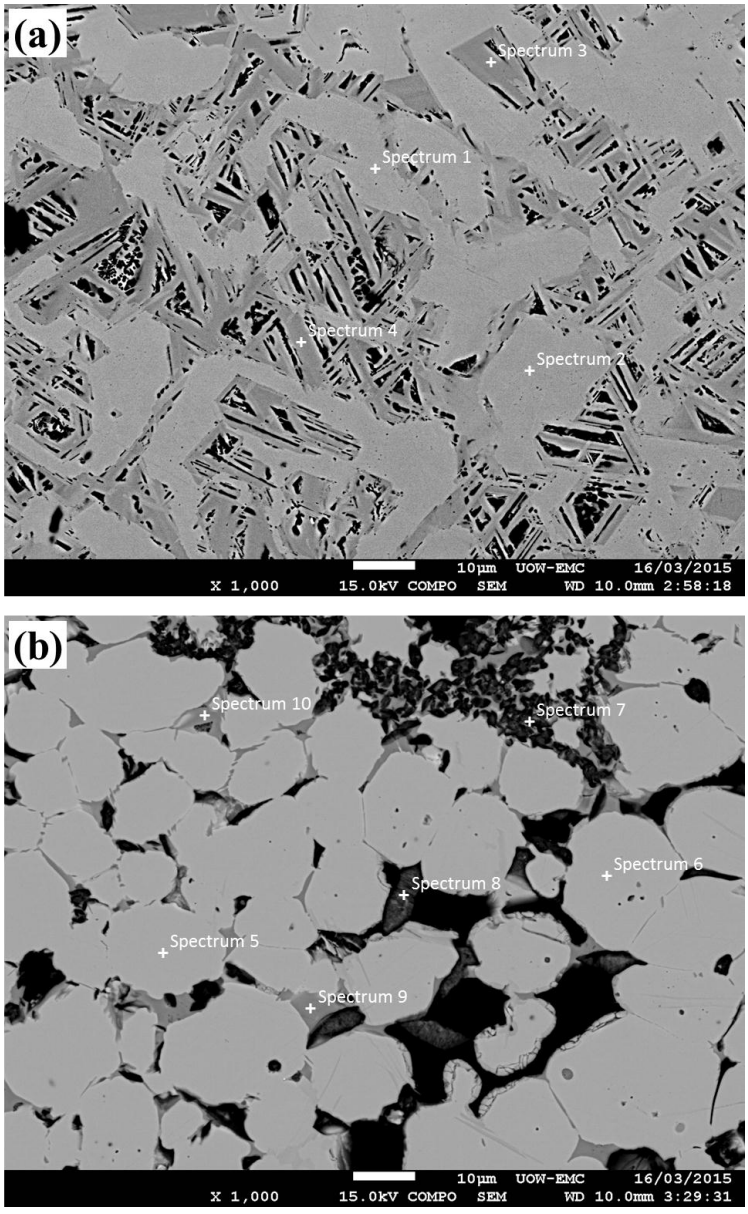

Figure 4. Back-scattered electron (BSE) images of mineral phases in MIX samples sintered at 1250 ℃ for 5 minutes in a muffle furnace. (a) Exterior; (b) Interior.

The mineral phases in different regions of sintered tablets were further analysed by SEM/EDS. Figures 4(a) and 4(b) show the back-scattered electron (BSE) images of the exterior and interior of a MIX sample sintered at 1250 ℃ for 5 minutes in a muffle furnace, respectively. The compositions at different points in Figure 4, as analysed by energy dispersive X-ray spectroscopy (EDS), are listed in Table 2. It should be noted that when an elemental content is less than 1 wt%, the number is only indicative due to the accuracy limits of EDS analysis. A large number of iron oxide particles associated with columnar SFCA were present in the shell of this sample, as shown in Figure 4(a). The phase associated with points 1 and 2 containing about 64 wt% iron and 7 wt% zinc represented a solid solution of zinc ferrite ($ZnFe_2O_4$) and magnetite (Fe_3O_4). These oxide particles were bonded by columnar SFCA (points 3 and 4). In comparison, as shown in Figure 4(b), well aggregated iron oxide particles (points 5 and 6) were present in the interior of the sample associated with dicalcium silicate (points 7 and 8) as well as a small amount of dicalcium ferrite (points 9 and 10). A very low concentration of zinc (about 0.35 wt%) was found in these iron oxide phases which were identified as magnetite and wustite by XRD analysis (Figure 2).

Table 2. Elemental composition (wt%) of grains marked in Figure 4 and corresponding phases.

Point no.	Fe	Ca	Si	Al	Mg	Zn	Phase identified
1	63.4	3.7	0.08	0.2	2.0	7.1	Zn-rich iron oxides
2	64.4	3.6	0.02	0.2	2.3	6.5	Zn-rich iron oxides
3	59.3	14.5	0.2	0.2	0.3	1.5	SFCA
4	59.6	14.0	0.1	0.2	0.2	1.6	SFCA
5	73.2	2.0	0.07	0.3	2.6	0.4	Zn-poor iron oxides
6	72.7	2.5	0.2	0.3	2.6	0.4	Zn-poor iron oxides
7	4.9	40.1	20.3	0.01	0.1	0.2	Dicalcium silicate
8	2.1	48.0	18.4	0.04	0.05	0.4	Dicalcium silicate
9	36.2	33.2	1.0	3.5	0.07	0.3	Dicalcium ferrite
10	36.2	32.8	0.9	3.9	0.05	0.5	Dicalcium ferrite

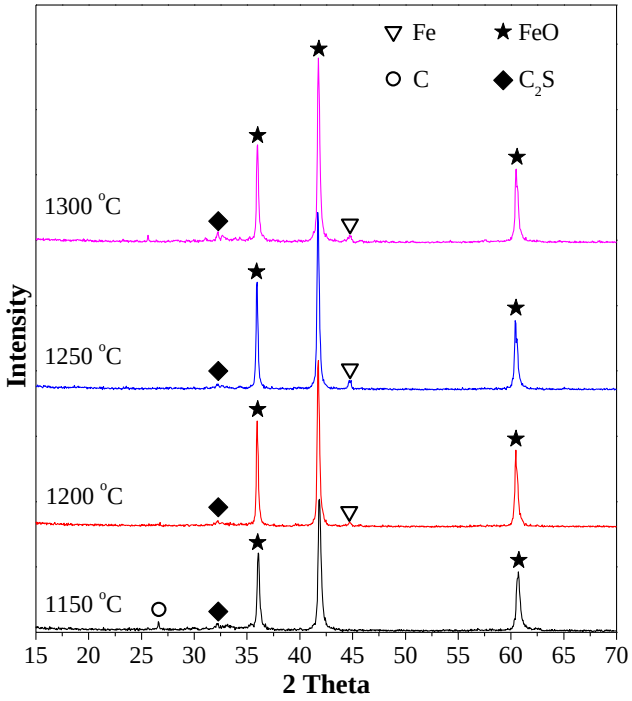

Figure 5. XRD patterns of MIX samples sintered in the temperature range of 1150 - 1300 ℃ for 5 minutes in argon with a flow rate of 1.5L/min. C_2S-dicalcium silicate.

To examine the effect of gas atmosphere on the sintering behaviour of the filter cake samples, the MIX samples were heated in the temperature range of 1150 - 1300 ℃ for 5 minutes in a vertical furnace in argon with a flow rate of 1.5 L/minute. None of the MIX tablets sintered in argon fractured and the original as-pressed shape of the tablets persisted. From the XRD patterns of these sintered samples presented in Figure 5, it is noted that the sintered MIX samples in argon were dominated by a wustite phase; a small amount of metallic iron was also present within samples sintered at higher temperatures (1200 - 1300 ℃). A weak carbon peak was only detected in the sample sintered at 1150 ℃; a small amount of dicalcium silicate was identified by XRD in all the samples. Optical microscope and SEM analysis show that these mineral phases were uniformly distributed in these sintered samples. Figure 6 shows a typical BSE image of the MIX samples sintered in argon at 1300 ℃ for 5 minutes. This figure shows the dispersed metallic iron in the wustite matrix and the dicalcium silicate phase.

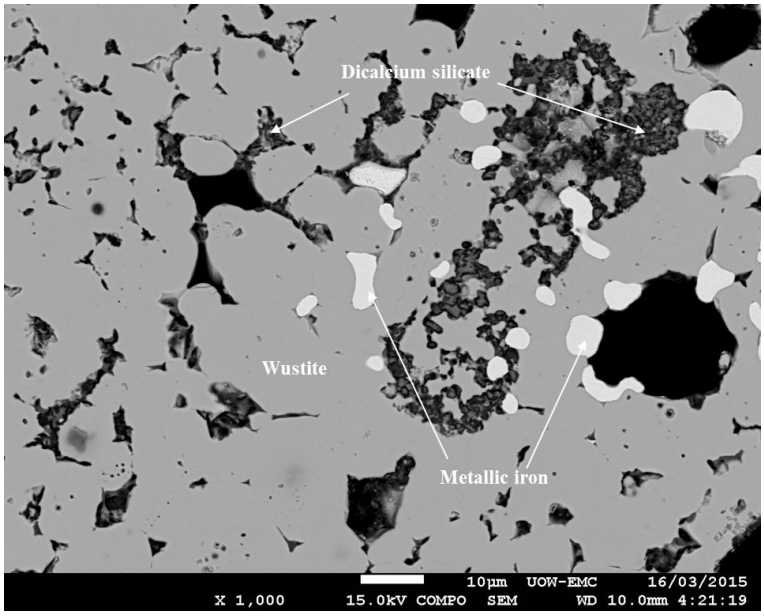

Figure 6. BSE image of phases in MIX samples sintered at 1300℃ for 5 minutes in argon with a flow rate of 1.5 L/min.

To examine the influence of carbon content on the sintering behaviour of filter cake samples, the BOF filter cake samples (containing less carbon, Table 1) were heated in air (muffle furnace) and in argon with a flow rate of 1.5 L/min (vertical furnace) in the temperature range of 1100 - 1300℃ for 5 minutes. None of the BOF tablets sintered in air fractured and the original as-pressed shape remained. Compared with the MIX filter cake, a similar but thicker shell structure was identified in the BOF tablets sintered in air. The mineral phases of these sintered BOF samples were examined by XRD analysis (Figure 7 (a)). It can be seen that the BOF samples sintered in air at 1100 and 1150℃ were dominated by magnetite, hematite and SFCA but no wustite which was present in a significant amount in the MIX samples sintered under the same conditions. As the sintering temperature increased, the content of magnetite increased gradually with a corresponding decrease in the contents of hematite and SFCA.

No shell structure was observed in BOF filter cake samples sintered in argon, and the distribution of mineral phases within these samples was relatively uniform. The XRD analysis (Figure 7(b)) showed that magnetite and wustite were the dominant phases in the BOF samples sintered in argon. The $CaFe_3O_5$ phase peak intensity, though not pronounced, appeared to decrease with increasing sintering temperature. The carbon

phase was only observed in the 1150 ℃ sintered sample. The metallic iron found in the MIX samples sintered in argon was not present in the BOF samples. This is likely a result of the relatively oxidising conditions of the sintered BOF filter cake, as the high carbon concentration levels in the MIX samples provided a more reducing atmosphere than that of the BOF samples.

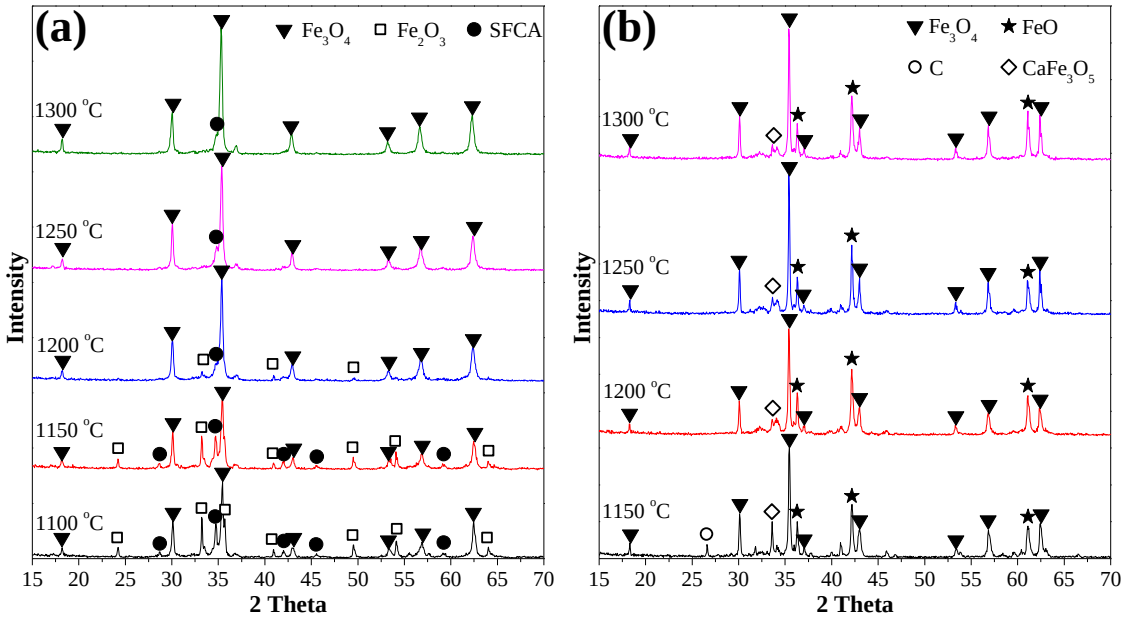

Figure 7. XRD patterns of BOF samples sintered (a) in air (muffle furnace) and (b) in argon with a flow rate of 1.5L/min (vertical furnace) in the temperature range of 1100 - 1300 ℃ for 5 minutes.

3.3. Zinc Removal from Filter Cake Samples

The zinc contents of filter cake samples sintered under different conditions were analysed by ICP-OES. The effects of temperature, gas atmosphere and carbon content on the zinc removal of sintered filter cake sample are shown in Figure 8.

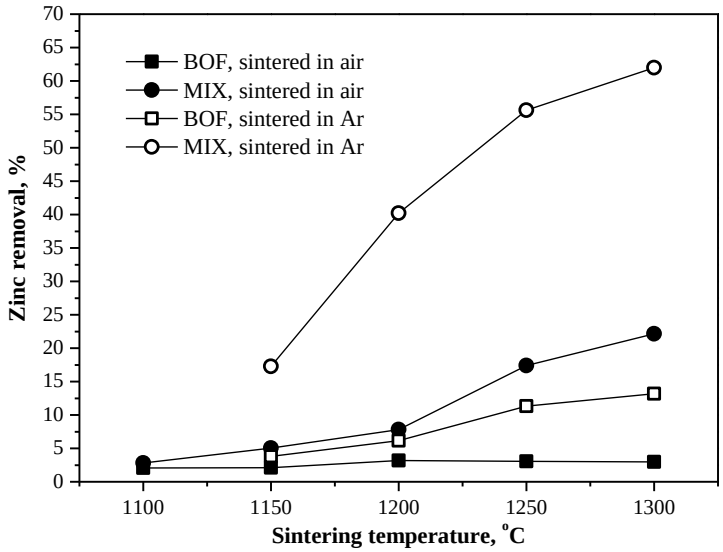

Figure 8. Zinc removal of filter cake samples sintered under different conditions.

In general, increasing the sintering temperature improved the zinc removal rate of sintered filter cake samples except for the BOF filter cake samples sintered in air where the effect of temperature on zinc removal was negligible. At 1150 ℃, the zinc removal of MIX sample sintered in Ar was less than 20%. It increased to 55% at 1250 ℃ and achieved 62% at 1300 ℃.

For each filter cake sample sintered in the temperature interval of 1100 - 1300 ℃, removal of zinc in argon was higher than in air. The zinc removal of the MIX sample sintered in air at 1300 ℃ was only 22%, which is 40% lower than that achieved in argon. For BOF filter cake, the zinc removal after sintering in argon and in air at 1300 ℃ was 13% and 3%, respectively.

4. Discussion

4.1 Mineral Phase Formation

The mineral phases present in the sintered filter cake tablets are summarised in Table 3. It can be seen that the predominant phases of the sintered samples are very different although the starting materials had very similar metal oxide compositions. These variations are mainly attributed to the differences in carbon and metallic iron contents in

the original filter cake samples and the sintering environment for the inner and outer areas of the tablet in addition to the sintering temperature used.

Table 3. Phase Composition of MIX and BOF filter cake samples sintered in air and argon in the temperature range of 1100 - 1300 ℃.

Sample	Gas atmosphere	Sintering temperature, ℃				
		1100	1150	1200	1250	1300
MIX	Air	Magnetite Hematite Wustite SFCA	Magnetite Wustite Hematite SFCA	Magnetite Wustite SFCA	Magnetite Wustite SFCA	Magnetite Wustite SFCA
MIX	Argon		Wustite C_2S Carbon	Wustite C_2S Iron	Wustite C_2S Iron	Wustite C_2S Iron
BOF	Air	Magnetite Hematite SFCA	Magnetite Hematite SFCA	Magnetite Hematite SFCA	Magnetite SFCA	Magnetite SFCA
BOF	Argon		Magnetite Wustite $CaFe_3O_5$ Carbon	Magnetite Wustite $CaFe_3O_5$	Magnetite Wustite $CaFe_3O_5$	Magnetite Wustite $CaFe_3O_5$

When the MIX filter cake tablets were sintered in air, the combustion of carbon and decomposition of calcium carbonate took place by Reactions (1) and (2), respectively:

$$C\ (s) + O_2\ (g) = CO_2\ (g) \qquad (1)$$

$$\Delta G^{o} = -\ 394597 - 1.226T\ (J)$$

$$CaCO_3\ (s) = CaO\ (s) + CO_2\ (g) \qquad (2)$$

$$\Delta G^{o} = 161621 - 138.5T\ (J)$$

The standard Gibbs free energy changes of the reactions in this paper were calculated using available data [15] in the range of 773K to 1773K (500 ℃ to 1500 ℃). The Boudouard reaction (3) is highly favoured thermodynamically within the temperature range of sintering experiments in this investigation.

$$C\ (s) + CO_2\ (g) = 2CO\ (g) \qquad (3)$$

$$\Delta G^{o} = 168284 - 172.9T\ (J)$$

Reaction (2) and other reactions in argon atmospheres generated a small amount of gases, which escaped from the MIX tablets easily without damaging the tablets. As a result, the MIX tablets sintered in argon showed only shrinkage. The MIX tablets sintered in air swelled or even broke due to rapid release of gas from the combustion of carbon, Reaction (1). Figure 9 presents the carbon loss in the MIX and BOF filter cakes after sintering in air and argon. It is noted that when sintered at temperatures below 1250 ℃, carbon was consumed at a much higher rate in air than in argon.

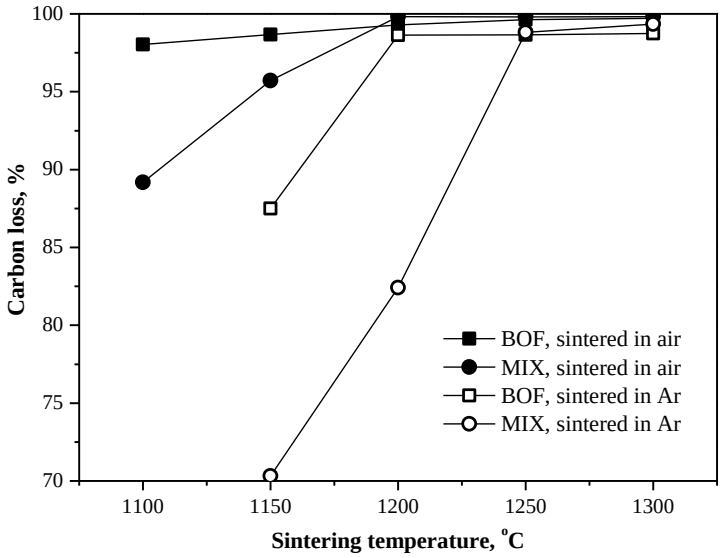

Figure 9. Carbon loss of filter cake samples sintered under different conditions.

A more reducing atmosphere in the interior of the tablets can be inferred due to the fact that the reducing gas produced from carbon combustion (a combination of reactions (1) and (3)) diffused outwards. As shown in Figure 3, a higher extent of aggregation of particles was likely achieved in the interior of sintered tablets, probably since the heat released from the carbon combustion was accumulated internally, leading to a higher interior temperature than the exterior.

Figure 10 shows the stability of the oxides of iron as a function of temperature and oxygen pressure [16]. It can be seen that higher temperature and lower pO_2 benefit the reduction of hematite to magnetite, wustite and even metallic iron.

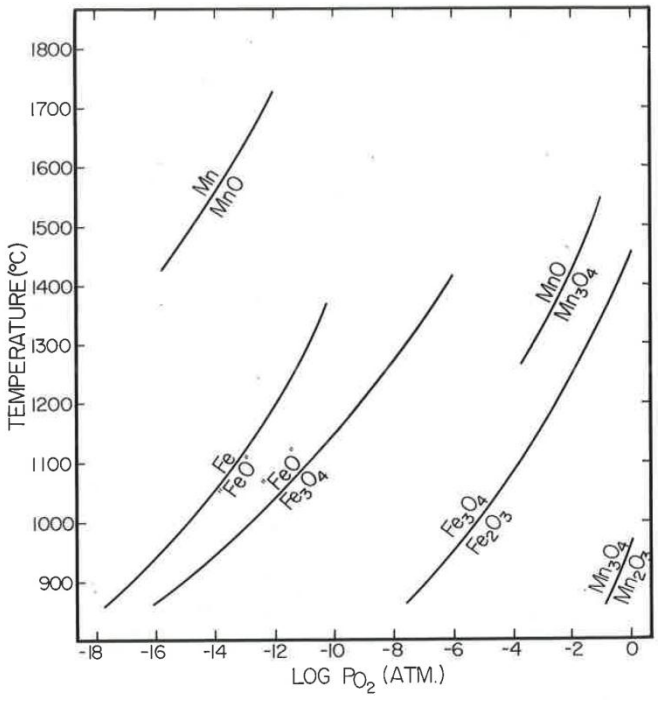

Figure 10. Stability of the oxides of iron as a function of temperature and oxygen pressure [16].

The MIX samples sintered in air showed different phases in the interior and exterior of the tablets. When sintered in air, combustion of carbon by reaction (1) caused diffusion of oxygen inwards, while heat released from the reaction transferred towards the surface of the tablets. These processes resulted in higher temperature and a more reducing atmosphere in the interior which prevented iron from oxidising to hematite. Only wustite and magnetite were observed in the interior. In comparison, the shell of sintered MIX tablets mainly consisted of magnetite associated with SFCA, as shown in Figures 3 and 4. SFCA phases (including SFCA-I) are key bonding materials of industrial iron ore sinter. $CaFe_2O_4$ (CF) can be formed as the precursor phase of SFCA through solid state reaction:

$$CaO\,(s) + Fe_2O_3\,(s) = CaFe_2O_4\,(s) \qquad (4)$$

$$\Delta G^{o} = -29519 - 9.929T\ (J)$$

where calcium from the flux initially reacts with hematite to form the new phase, CF. Formation of $Ca_2Fe_2O_5$ (C_2F) is also possible when enough lime is available. Impurities

such as silica and alumina reacted with these early formed ferrites to form SFCA phases.

No formation of SFCA was observed in the interior of tablets sintered in air. Although a small amount of hematite was present in the original filter cake, the high temperature and low pO_2 conditions in the interior of the tablets led to the reduction of hematite into magnetite (Reaction (5)) and correspondingly suppressed the formation of SFCA.

$$6Fe_2O_3\ (s) = 4Fe_3O_4\ (s) + O_2\ (g) \quad (5)$$
$$\Delta G^{o} = 479433 - 293.6T\ (J)$$

During iron ore sintering, the mass ratio of CaO to SiO_2 of the sinter blend is known to be a key factor governing mineral phase formation and sinter microstructure. A ratio greater than 1.8 to 2.0 favours the formation of SFCA phases, while a lower ratio favours the formation of calcium silicate and glassy phases [17-19]. The BOF and MIX filter cakes used in this investigation have ratio between 3.41 and 4.32, therefore the formation of SFCA phases observed in the sintered filter cake samples was highly favoured.

When the MIX filter cake tablets were sintered in argon, the carbon and metallic iron in the filter cake created a more reducing sintering atmosphere. Wustite was the main phase and an amount of metallic iron was produced when the samples were sintered at temperatures higher than 1200 ℃. The formation of wustite and iron can mainly be shown in Reactions (6) – (8).

$$3Fe_2O_3\ (s) + C\ (s) = 2Fe_3O_4\ (s) + CO\ (g) \quad (6)$$
$$\Delta G^{o} = 126343 - 233.7T\ (J)$$

$$Fe_3O_4\ (s) + C\ (s) = 3FeO\ (s) + CO\ (g) \quad (7)$$
$$\Delta G^{o} = 186429 - 190.9T\ (J)$$

$$FeO\ (s) + C\ (s) = Fe\ (s) + CO\ (g) \quad (8)$$
$$\Delta G^{o} = 150265 - 151.6T\ (J)$$

Under this reducing atmosphere, calcium ferrites could not be formed, and silicates were formed instead.

Compared to the MIX filter cake, the BOF filter cake contained less carbon reductant, so less reduction took place when the BOF samples were sintered in both air and argon. Similar to the MIX filter cake, a shell structure was identified in the BOF tablets sintered in air, with more hematite and SFCA present in the shell layers after sintering at and below 1200 ℃. The interior was mainly magnetite; wustite that dominated within the air-sintered MIX samples was not detected in the interior of air-sintered BOF samples. This is because sufficiently strong reducing conditions could not be generated from the low carbon and metallic iron contents.

In terms of the BOF samples sintered in argon, the dominant phases were magnetite and wustite, and no metallic iron was present. It is noted that $CaFe_3O_5$ phase identified by XRD analysis was distributed around iron oxide particles as a bonding phase in these samples. In general, $CaFe_3O_5$ is not a common phase identified in iron ore sinter but could be generated with the reaction between Fe_3O_4 and CaO [20].

4.2 Zinc Removal

During sintering of filter cake samples, carbon within the samples acted as a reductant. Zinc oxide in filter cake was reduced to zinc vapour (Zn (g)) by Reaction (9).

$$ZnO\ (s) + C\ (s) = CO\ (g) + Zn\ (g) \quad (9)$$

$$\Delta G^{o} = 356434 - 291.2T\ (J)$$

Like carbothermal reduction of other metal oxides [21-23], the above reaction proceeds via the gas phase. CO reacts with ZnO to form Zn vapour and CO_2, and the latter, further reacts with carbon to regenerate CO (Boudouard reaction (3)).

Zinc oxide could also be reduced by metallic iron by Reaction (10)

$$ZnO\ (s) + Fe\ (s) = Zn\ (g) + FeO\ (s) \quad (10)$$

$$\Delta G^{o} = 206170 - 139.6T \text{ (J)}$$

Figure 11 presents the partial pressure of zinc vapour in equilibrium with ZnO and CO calculated from Reaction (9) at various CO pressures and temperatures. The equilibrium partial pressure of zinc vapour following Reaction (10) and the saturation vapour pressure of liquid zinc are also shown in the figure. Both Reactions (9) and (10) are thermodynamically favoured in a wide range of reaction conditions. For instance, at 1000 ℃ and CO partial pressure of 10 kPa, equilibrium zinc vapour pressure in Reactions (9) and (10) reaches approximately 400kPa and 10kPa, respectively.

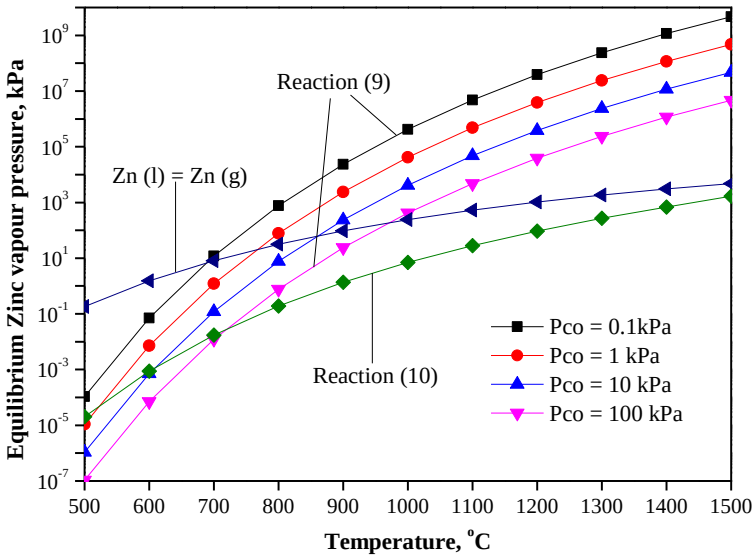

Figure 11. Equilibrium partial pressures of zinc vapour in Reactions (9) and (10).

The experimental results show that the gas atmosphere has an important influence on the potential for zinc removal. For experiments in argon, the reduced zinc vapour diffused out of tablets and was removed from the filter cakes. In the experiments in air, zinc vapour generated in the tablet interior diffused outwards. In the exterior of the tablets, zinc vapour was oxidised as follows.

$$Zn(g) + \tfrac{1}{2} O_2 = ZnO \qquad (11)$$

$$\Delta G^{o} = -469808 + 204.4T \text{ (J)}$$

$$Zn(g) + \tfrac{1}{2} O_2(g) + Fe_2O_3 = ZnFe_2O_4 \qquad (12)$$

$$\Delta G^{o} = -483479 + 193.1T \text{ (J)}$$

Figure 12 presents the partial pressure of zinc vapour in equilibrium with ZnO or $ZnFe_2O_4$ calculated from reactions (11) and (12) under different oxygen partial pressures at different temperatures. The equilibrium zinc vapour pressure decreases significantly with decreasing temperature and increasing oxygen partial pressure. Both Reactions (11) and (12) are thermodynamically favoured over a fairly wide range of reaction conditions. For Reaction (11), a pO_2 of 1 kPa suppresses the equilibrium zinc vapour pressure to the order of 10^{-4} to 10^{-2} kPa in the sintering temperature range of this work; the equilibrium zinc pressure is an order of magnitude lower for Reaction (12).

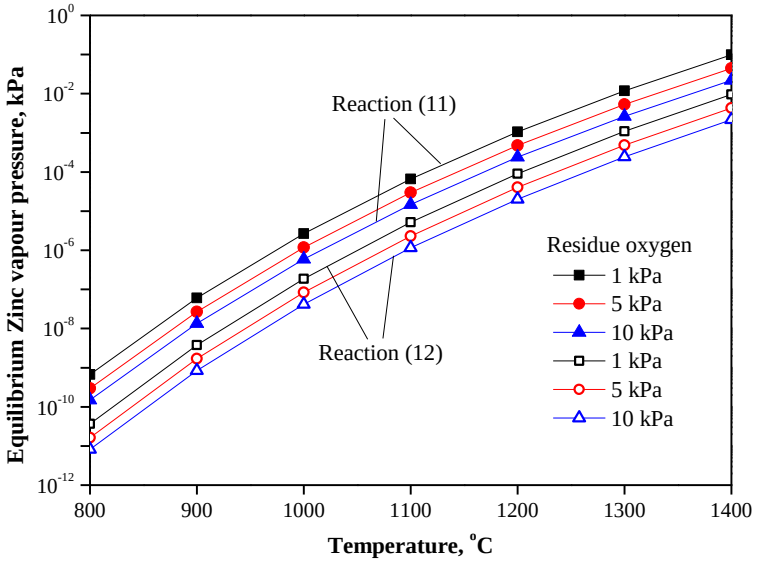

Figure 12. Equilibrium partial pressures of zinc vapour in Reactions (11) and (12).

It has been demonstrated that the oxidation of zinc vapour cannot occur in the gas phase due to the lack of crystallisation sites. In an investigation on the reduction of zinc oxide from manganese furnace dust, Shen et al. [24] observed that oxidation of zinc only took place on the crucible wall or contained materials rather than in the gas phase. Weidenkaff et al. [25] concluded that oxidation of zinc vapour by oxygen is heterogeneous and, in the absence of nucleation sites, zinc vapour and oxygen gas coexist in a metastable state.

In the present investigation, zinc vapour formed by reduction of zinc oxide in tablets diffused outwards and was removed from the tablets when sintered in argon. When sintered in air, an oxidising atmosphere was present at the exterior of tablets due to the

inward diffusion of O_2, and zinc vapour was oxidised and doped in the magnetite substrate forming a zinc ferrite-magnetite solid solution. Particularly during sintering at higher temperatures (1250 and 1300 ℃), the fracturing of samples provided more opportunities with zinc vapour to react with O_2 and consequently form the zinc ferrite-magnetite solid solution. This resulted in migration of zinc vapours to the exterior of tablets as observed in Figures 3 and 4. As shown by the thermodynamics of reactions (11) and (12), the combination of ZnO with iron oxide phases stabilises ZnO and makes it less prone to reduction reactions.

The significant difference in zinc removal from two filter cake samples shown in Figure 8 can be attributed to their difference in carbon and metallic iron contents. The removal of zinc in MIX filter cake was more complete than that in BOF filter cake, since the MIX filter cake had higher carbon and metallic iron contents which were available as reductants for ZnO reduction. Argon was more beneficial to zinc removal than air by maintaining a more reducing atmosphere. The zinc removal from the MIX sample sintered in air was still higher than that of the BOF sample sintered in argon, which demonstrates the critical importance of a reductant such as carbon in the sample. Also, it is worthwhile to note that the filter cake samples used in this investigation contained significantly lower content of metallic iron than when freshly generated from steelmaking processes. Further investigation on the sintering behaviour of the filter cakes containing more metallic iron and with added carbon is in progress.

5. Conclusions

A mixture of blast furnace filter cake and basic oxygen steelmaking filter cake (MIX filter cake) and a pure basic oxygen steelmaking filter cake (BOF filter cake) were sintered at different temperatures (100-1300°C) in argon and in air. The sintering extent of both filter cake samples increased with increasing sintering temperature.

When sintered in air, filter cake particles showed greater aggregation in the interior than in the exterior of sintered tablets, because the heat released from the combustion of carbon in the filter cake likely led to a higher temperature in the interior. SFCA and

ZnO containing magnetite phases were formed in the external layer of the tablets, while internal phases were magnetite and wustite.

When sintered in argon, mineral phases were evenly distributed in the samples due to the absence of carbon combustion. The dominant phases were magnetite, wustite, and metallic iron. SFCA was not present in the filter cake samples sintered in argon due to the relatively reducing sintering conditions.

Removal of zinc was observed during the sintering of filter cake samples, which was enhanced by increasing the contents of carbon and metallic iron as well as using a reducing gas atmosphere. Zinc oxide in filter cake was reduced to zinc vapour by carbon or metallic iron in filter cake. During sintering in argon, the reduced zinc vapour diffused out of the tablets and was removed from the filter cake. In comparison, when sintered in air, the zinc vapour formed in the interior diffused to the exterior of tablets where it was oxidised and doped in the magnetite substrate forming a zinc ferrite-magnetite solid solution.

Acknowledgements

The project is financially supported by the BlueScope Steel Metallurgical Centre Projects Grant. Zhe Wang is a recipient of University of Wollongong Deputy Vice Chancellor's Special Scholarship and International Postgraduate Tuition Award. The authors would like to acknowledge the assistance of Prof. Long Nghiem and Mr. Hung Cong Duong at University of Wollongong for ICP-OES analysis. This research used FESEM JEOL JSM-7001F funded by the Australian Research Council (ARC) – Linkage, Infrastructure, Equipment and Facilities (LIEF) grant (LE0882613) located at the UOW Electron Microscopy Centre.

References

[1] R. L. Nyirenda, The Processing of Steelmaking Flue-Dust: A Review, *Minerals Engineering*, **4** (1991), 1003-1025.

[2] S. Kelebek, S. Yörük and B. Davis, Characterization of Basic Oxygen Furnace Dust and Zinc Removal by Acid Leaching, *Minerals Engineering*, **17** (2004), 285-291.

[3] K. Meyer, Pelletizing of Iron Ores, Springer-Verlag, (1980), 52.

[4] A. F. S. Schoukens, F. Shaw and E. C. Chemaly, The Enviroplas Process for the Treatment of Steel-Plant Dusts, *Journal of the Southern African Institute of Mining and Metallurgy*, **93** (1993), 1-7.

[5] L. M. Southwick, Still No Simple Solution to Processing EAF Dust, *Steel Times International*, **3** (2010), 43-45.

[6] G. Assis, Emerging Pyrometallurgical Processes for Zinc and Lead Recovery from Zinc-Bearing Waste Materials, Zinc and Lead Processing Symposium, The Metallurgical Society of CIM, Calgary, (1998).

[7] Z. H. Trung, F. Kukurugya, Z. Takacova, D. Orac, M. Laubertova, A. Miskufova and T. Havlik, Acidic Leaching Both of Zinc and Iron from Basic Oxygen Furnace Sludge, *Journal of Hazardous Materials*, **192** (2011), 1100-1107.

[8] M. K. Jha, V. Kumar and R. J. Singh, Review of Hydrometallurgical Recovery of Zinc from Industrial Wastes, *Resources, Conservation and Recycling*, **33** (2001), 1-22.

[9] M. R. C. Ismael and J. M. R. Carvalho, Iron Recovery from Sulphate Leach Liquors in Zinc Hydrometallurgy, *Minerals Engineering*, **16** (2003), 31-39.

[10] E. A. Vestola, M. K. Kuusenaho, H. M. Närhi, O. H. Tuovinen, J. A. Puhakka, J. J. Plumb and A. H. Kaksonen, Acid Bioleaching of Solid Waste Materials from Copper, Steel and Recycling Industries, *Hydrometallurgy*, **103** (2010), 74-79.

[11] O. Bayat, E. Sever, B. Bayat, V. Arslan and C. Poole, Bioleaching of Zinc and Iron from Steel Plant Waste using Acidithiobacillus Ferrooxidans, *Applied Biochemistry and Biotechnology*, **152** (2009), 117-126.

[12] P. Fu and Q. Zhang, Investigation on Steelmaking Dust Recycling and Iron Oxide Red Preparing, *Journal of University of Science and Technology Beijing, Mineral, Metallurgy, Material*, **15** (2008), 24-28.

[13] Bluescope Health, Safety, Enviroment and Community Report 2004, BlueScope Ltd., http://hsecreport.bluescopesteel.com/environment/waste-case-studies.html

[14] Z. Wang, D. Pinson, S. Chew, H. Rogers, B. J. Monaghan, M. I. Pownceby, N. A. S. Webster and G. Zhang, Behaviour of New Zealand Ironsand during Iron Ore Sintering, *submitted to Metallurgical and Materials Transactions B*, (Chapter 2).

[15] M. Binnewies and E. Milke, Thermochemical Data of Elements and Compounds, 2nd edition, Wiley-VCH Verlag GmbH, Weinheim, (2002).

[16] A. Muan and E. F. Osborn, Phase Equilibria among Oxides in Steelmaking, Addison-Wesley Publishing Company, Inc., (1965), 33.

[17] F. Matsuno, Changes in Mineral Phases during the Sintering of Fe_2O_3-CaO-SiO_2 System, *Transactions of the Iron and Steel Institute of Japan*, **19** (1979), 595-604.

[18] F. Matsuno and T. Hirada, Changes of Mineral Phases during the Sintering of Iron Ore - Lime Stone Systems, *Transactions of the Iron and Steel Institute of Japan*, **21** (1981), 318-325.

[19] S. N. Ahsan, T. Mukherjee and J. A. Whiteman, Structure of fluxed sinter, *Ironmaking and Steelmaking*, **10** (1983), 54-64.

[20] J. W. Jeon, S. M. Jung and Y. Sasaki, Formation of Calcium Ferrites under Controlled Oxygen Potentials at 1273 K, *ISIJ International*, **50** (2010), 1064-1070.

[21] R. Kononov, O. Ostrovski, and S. Ganguly, Carbothermal solid state reduction of manganese ores: 2. Non-isothermal and isothermal reduction in different gas atmospheres, *ISIJ International*, **49** (2009), 1107-1114.

[22] J. Li, et al., Low-temperature synthesis of aluminium carbide, *ISIJ International*, **51**(2011), 870-877.

[23] M. A. Dewan, G. Zhang, and O. Ostrovski, Carbothermal reduction of titania in different gas atmospheres, *Metallurgical and Materials Transactions B*, **40** (2009), 62-69.

[24] R. Shen, G. Zhang, M. Dell'Amico, P. Brown and O. Ostrovski, Reduction of Zinc Oxide in Manganese Furnace Dust with Tar, *ISIJ international*, **46** (2006), 8-13.

[25] A. Weidenkaff, A. Steinfeld, A. Wokaun, P. O. Auer, B. Eichler and A. Reller, Direct Solar Thermal Dissociation of Zinc Oxide: Condensation and

Crystallisation of Zinc in the Presence of Oxygen, *Solar Energy*, **65** (1999), 59-69.

CHAPTER 7. CONCLUSIONS AND RECOMMENDATIONS

7.1 Conclusions

The aim of the project was to investigate the sintering behaviour of three kinds of unconventional ferrous materials (New Zealand ironsand, mill scale and filter cake wastes) and assess the feasibility of their utilization by sintering. The effect of sintering conditions on the formation of mineral phases during iron ore sintering was also studied to gain better understanding of sintering mechanism. The results in each section are summarised as follows.

7.1.1 Behaviour of New Zealand Ironsand during Iron Ore Sintering

A detailed characterisation shows that the New Zealand ironsand sample used in this study contained about 60 wt% iron, 7.95 wt% TiO_2 and a small amount of other impurities. Major impurities in the bulk concentrate included: Al_2O_3 3.78 wt%, MgO 3.06 wt%, SiO_2 2.34 wt%, V_2O_5 0.607 wt%, and MnO 0.638 wt%. The impurities aluminium, vanadium, manganese, and magnesium are typically associated with the titanomagnetite grains, occurring as solid solution components within the lattice. The other impurity elements, including part of aluminium, are more typically associated with gangue mineral grains such as aluminosilicates (e.g. pyroxenes, feldspars and clays), quartz and apatite.

The relict ironsand particles in industrial sinters doped with 3wt% New Zealand ironsand presented different morphologies due to the heterogeneity of sintering conditions. These can be well simulated by bench-scale sintering experiments.

A relatively reducing atmosphere benefited the melting of ironsand into a liquid phase. The assimilation of ironsand during sintering in a reducing atmosphere started from the diffusion of calcium into the lattice of the ironsand matrix. This in turn further decreased the melting point of titanomagnetite and accelerated the melting rate of

ironsand particles. A reaction zone was formed near the boundary within ironsand particles where a perovskite phase was generated as a result of the reaction between TiO_2 and CaO. With increasing sintering temperature, in a reducing atmosphere ironsand particles underwent more assimilation and most of the Ti moved from the ironsand particles into a glass phase.

More Ti remained in original ironsand particles in a relatively oxidising atmosphere, which is attributed to the high oxygen partial pressure which suppresses the melting of SFCA and stabilises TiO_2 in titanohematite.

It is also observed that New Zealand ironsand had greater resistance to assimilation than traditional iron ores.

7.1.2 Effect of Sintering Conditions on the Formation of Mineral Phases during Iron Ore Sintering

The content of SFCA phase formed during iron ore sintering was significantly affected by temperature. In the temperature range of 1250 – 1300 ℃, SFCA formation was enhanced by increasing temperature. Further increasing sintering temperature promoted the Fe^{3+} in the SFCA crystal structure to Fe^{2+} and consequent decomposition of SFCA.

Sintering at a low temperature generated SFCA by solid state reactions. At high temperatures, SFCA was produced during cooling via crystallisation from a silicate melt. A slow cooling in an oxidising gas atmosphere strongly promoted formation of SFCA.

Increasing CaO/SiO_2 ratio and oxygen partial pressure favour the formation of SFCA phase. A high oxygen partial pressure suppressed conversion of hematite into magnetite, and so promoted formation of SFCA.

A typical microstructure of SFCA bonding phase composed of acicular SFCA-I and hematite in the commercial sinter was formed by crystallisation from a silicate melt

formed in the heating stage with relatively low oxygen partial pressure during cooling in an oxidising gas atmosphere.

7.1.3 Interaction of New Zealand Ironsand and Flux Materials

Mg^{2+} ions can easily diffuse into the lattice of ironsand significantly, when the ironsand was sintered with MgO. Mg presented in the ironsand can stabilise the system of FeOx-MgO and hinder the dissolution of ironsand particles.

During sintering of ironsand with CaO, a reaction zone consisting of perovskite and calcium ferrite occurred between two layers. When sintered at higher temperature (1300 ℃), the ironsand particles intimately bonded by mainly perovskite and less amount of silicate phases. Partial melting of calcium ferrite phase greatly promoted mass transfer and further penetration of calcium ferrites into CaO layer.

In terms of sintering of ironsand with dolomite, similar perovskite and calcium ferrites were also generated in the reacted zone. A MgO-FeO solid solution was formed close to perovskite phase, since the formation of perovskite phase hindered the further diffusion of Mg^{2+} ions into ironsand layer. Increasing sintering temperature significantly improved the penetration of calcium ferrite phase into dolomite layer; while the perovskite phase and MgO-FeO solid solution remained at high sintering temperature due to their relatively higher melting points which hindered penetration of Ca and Mg into the ironsand layer and suppressed the bonding between ironsand particles.

7.1.4 Effect of Addition of Mill Scale on Sintering of Iron Ores

When samples with 0-15% mill scale were sintered in a high oxidizing atmosphere (air), there was negligible effect of mill scale addition on the phases formed during sintering. The oxidation of the mill scale was complete and phases such as SFCA, SFCA-I, and hematite were dominant throughout the temperature range (1250-1325 ℃) examined in this study.

Under lower oxygen partial pressures (pO_2 = 0.5 or 5 kPa) and throughout the temperature range examined, the mill scale was converted to magnetite, with the extent of reaction controlled by the hematite-magnetite conversion kinetics. When sintered in the gas mixture with pO_2 = 5 kPa, an increase in the mill scale content from 0 to 15 wt% resulted in a decrease of hematite and total SFCA phases and a corresponding increase in the amount of magnetite formed. The oxidation of wustite in mill scale to magnetite decreased partial pressure of O_2 and increased sintering temperature, which promoted the decomposition of hematite.

Mill scale is a suitable sinter blend component with very low impurity contents. Although addition of mill scale into a sinter blend affected the formation of mineral phases during the heating stage, if appropriate measures are taken so that the magnetite formed during heating is allowed to be sufficiently oxidised during the cooling stage, the contents of SFCA and hematite will not be significantly changed and the quality of sinter can be maintained.

7.1.5 Mineral Phase Formation and Zinc Removal during Sintering of Filter Cake Wastes

When the filter cake samples were sintered in air, filter cake particles were aggregated better in the interior than in the exterior of sintered tablets, because the heat released from the combustion of carbon of the filter cake was accumulated internally which led to a higher temperature in the interior. SFCA and ZnO containing magnetite phases were formed in the external layer of a tablet, while internal phases were magnetite and wustite.

For the filter cake samples sintered in argon, mineral phases were evenly distributed in samples due to absence of carbon combustion. The dominant phases were magnetite, wustite, and metallic iron. SFCA was not present in the filter cake samples sintered in argon due to the relatively reducing sintering condition.

Removal of zinc was observed during the sintering of filter cake samples which was

enhanced by increasing of sintering temperature and carbon content as well as using a reducing gas atmosphere. Zinc oxide in filter cake was reduced to zinc vapour by carbon or metallic iron in filter cake. During sintering in argon, the reduced zinc vapour diffused out of the tablets and was removed from the filter cake. In comparison, when sintered in air, the zinc vapour formed in the interior diffused to the exterior of tablets where it was oxidised and zinc ferrite was generated due to the reaction of zinc, iron oxides and oxygen, resulting in migration of zinc to the exterior of tablets.

7.2 Recommendations

The effect of different sintering conditions on mineral phase formation of iron ore sinter has been studied. More detailed sintering experiments are worthwhile to be performed to identify the influence of oxidation during cooling stage of sintering, which is helpful to gain better understanding of sintering mechanism.

A certain amount of zinc removal was obtained during the sintering of filter cake wastes. Carbon content in the sintering tablets is a critical factor for zinc removal. Also, it is worthwhile to note that the filter cake samples used in this investigation contained significantly lower contents of metallic iron than freshly generated from steelmaking processes. Further investigation on the sintering behaviour of the filter cakes containing more metallic iron and with added carbon is recommended.